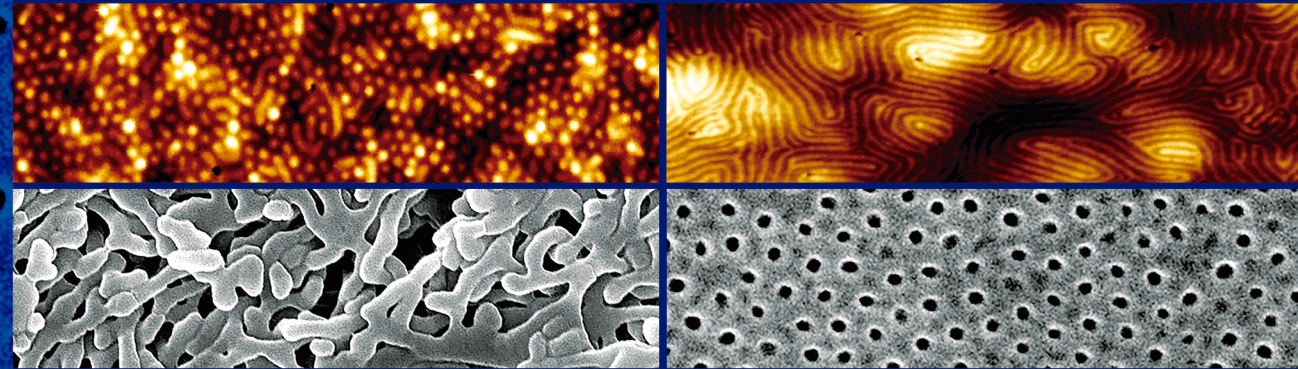


# Thermo-responsive block copolymers

Synthesis, self-assembly and membrane development



Thermo-responsive block copolymers

Merve Mocan Çetintaş

Merve Mocan Çetintaş

## Propositions

1. The synthesis of a systematic series of block copolymers is not required to obtain one specific morphology.  
(this thesis)
2. Polystyrene-poly(*N*-isopropylacrylamide) block copolymers are suitable polymers to produce nano-, isoporous and fully reversible thermo-responsive membranes.  
(this thesis)
3. To prevent Schlenk ampoules from breaking during a freeze-thaw cycle, one should apply a thermal shock.
4. The productivity of an employee coming from a Mediterranean country increases when he/she starts working in the Netherlands.
5. A key strategy to solve a complex question is to average over many possible answers.
6. The tolerance of Eurasian people should be explored more to decrease the tension between different cultures.
7. Gardening must be a mandatory course at schools.

Propositions belonging to the thesis entitled:

**“Thermo-responsive block copolymers: Synthesis, self-assembly and membrane development”**

Merve Mocan Çetintaş

Wageningen, 2 June 2017

# **Thermo-responsive block copolymers**

Synthesis, self-assembly and  
membrane development

Merve Mocan Çetintaş

## **Thesis committee**

### **Promotor**

Prof. Dr F.A.M. Leermakers  
Personal chair at Physical Chemistry and Soft Matter  
Wageningen University & Research

### **Co-promotor**

Dr M.M.G. Kamperman  
Associate professor, Physical Chemistry and Soft Matter  
Wageningen University & Research

### **Other members**

Prof. Dr H. Zuilhof, Wageningen University & Research  
Prof. Dr B. van der Wal, Wageningen University & Research  
Prof. Dr F. Picchioni, University of Groningen, the Netherlands  
Dr E. Mendes, Delft University of Technology, the Netherlands

This research was conducted under the auspices of the Graduate School VLAG (Advanced studies in Food Technology, Agrobiotechnology, Nutrition and Health Sciences).

# Thermo-responsive block copolymers

Synthesis, self-assembly and  
membrane development

Merve Mocan Çetintaş

## Thesis

submitted in fulfillment of the requirements for the degree of doctor

at Wageningen University

by the authority of the Rector Magnificus,

Prof. Dr A.P.J. Mol,

in the presence of the

Thesis Committee appointed by the Academic Board

to be defended in public

on Friday 2 June 2017

at 11 a.m. in the Aula.

Merve Mocan Çetintaş

Thermo-responsive block copolymers: Synthesis, self-assembly and membrane development

178 pages.

PhD thesis, Wageningen University, Wageningen, NL (2017)

With references, with summaries in English and Turkish

ISBN: 978-94-6343-158-3

DOI: 10.18174/411467

*Do not say I wouldn't even harm a fly, the fly would be harmed from that 'even'  
Saying a word requires wisdom; comprehending it, a human.*

*Karıncayı bile incitmem deme, 'bile'den incinir karınca  
Söz söylemek irfan ister, anlamak insan.*

*Fuzûlî*

*To Mustafa Kemal Atatürk and all our martyrs ...*



## CONTENTS

<b>Chapter 1: Introduction</b> .....	<b>1</b>
1.1 Scope of the thesis.....	2
1.2 Synthesis of block copolymers.....	2
1.2.1 Types of controlled/living polymerizations.....	3
1.2.2 Reversible-addition-fragmentation-transfer polymerization.....	4
1.3 Block copolymer self-assembly.....	6
1.3.1 Block copolymer phase diagram.....	7
1.3.2 Mesophases obtained from block copolymers.....	7
1.4 Block copolymer membranes.....	10
1.4.1 Block copolymer thin films.....	10
1.4.2 Self-assembly and non-solvent induced phase separation method.....	11
1.4.3 Stimuli-responsive block copolymer membranes.....	13
1.5 Aim and outline of the thesis.....	14
References.....	16
<b>Chapter 2: Free-standing thermo-responsive nanoporous membranes from high molecular weight PS-PNIPAM block copolymers</b> .....	<b>21</b>
2.1 Abstract.....	22
2.2 Introduction.....	22
2.3 Experimental Section.....	24
2.3.1 Materials.....	24
2.3.2 Synthesis procedures.....	25
2.3.2.1 Synthesis of <i>S,S'</i> -bis( <i>a,a'</i> -dimethyl- <i>a''</i> -acetic acid) trithiocarbonate.....	25
2.3.2.2 Synthesis of PS macro-RAFT agents.....	25
2.3.2.3 Synthesis of PS- <i>b</i> -PNIPAM- <i>b</i> -PS copolymers.....	26
2.3.2.4 Synthesis of PNIPAM macro-RAFT agents.....	26
2.3.2.5 Synthesis of PS- <i>b</i> -PNIPAM copolymers.....	26
2.3.3 Reaction parameters.....	27
2.3.4 Membrane preparation.....	28
2.3.5 Characterization.....	28
2.3.6 Permeability experiments.....	29

2.4 Results and Discussion .....	30
2.4.1 Synthesis and optimization of homopolymers and copolymers .....	30
2.4.2 Membrane fabrication by SNIPS.....	35
2.4.3 Permeability measurements .....	38
2.5 Conclusions .....	40
References .....	41
Appendix.....	45

**Chapter 3: Microphase segregation of diblock copolymers studied by the self-consistent field theory of Scheutjens and Fleer ..... 51**

3.1 Abstract .....	52
3.2 Introduction.....	53
3.2.1 SF-SCF characteristics and parameters .....	57
3.3 Results .....	59
3.3.1 Box size adjustment for free energy optimization.....	59
3.3.1.1 The lamellar phase .....	61
3.3.1.2 The hexagonal phase .....	62
3.3.1.3 Various mesophases that require three-gradient SF-SCF .....	64
3.3.2 Systematic dependences.....	69
3.3.3 The stability of various mesophases.....	74
3.4 Discussion.....	78
3.5 Conclusions .....	80
References .....	81
Appendix .....	85

**Chapter 4: Self-assembly of PS-*b*-PNIPAM-*b*-PS block copolymer thin films via selective solvent annealing ..... 91**

4.1 Abstract .....	92
4.2 Introduction.....	92
4.3 Experimental Section .....	94
4.3.1 Materials .....	94
4.3.2 Synthesis procedures.....	95
4.3.2.1 Synthesis of PS macro-RAFT agents.....	95
4.3.2.2 Synthesis of PS- <i>b</i> -PNIPAM- <i>b</i> -PS copolymers .....	95

4.3.3 Polymer characterization .....	96
4.3.4 Bulk film preparation .....	96
4.3.5 Thin film preparation .....	97
4.3.6 Atomic force microscopy (AFM) .....	97
4.3.7 Small angle X-ray scattering (SAXS) .....	97
4.3.8 Grazing incidence small angle X-ray scattering (GISAXS) .....	98
4.4 Results and Discussion .....	98
4.4.1 Bulk morphology .....	100
4.4.2 As-spun samples .....	100
4.4.3 Solvent annealing.....	101
4.4.3.1 Solvent annealing with pure solvents .....	101
4.4.3.2 Solvent annealing with selective solvent mixtures .....	104
4.4.3.2.1 Methanol-tetrahydrofuran.....	104
4.4.3.2.2 Methanol-toluene .....	109
4.5 Conclusions .....	112
References .....	113
Appendix.....	118

**Chapter 5: Systematic variation of membrane casting parameters to control the structure of thermo-responsive isoporous membranes ..... 121**

5.1 Abstract .....	122
5.2 Introduction.....	122
5.3 Experimental Section .....	124
5.3.1 Materials .....	124
5.3.2 Synthesis procedures .....	124
5.3.2.1 Synthesis of PNIPAM macro-RAFT agent.....	124
5.3.2.2 Synthesis of PS- <i>b</i> -PNIPAM copolymers .....	125
5.3.3 Polymer characterization .....	125
5.3.4 Membrane preparation .....	126
5.3.5 Membrane characterization.....	126
5.3.6 Permeability measurements .....	127
5.4 Results and Discussion .....	128
5.4.1 Influence of solvent type.....	128

5.4.2 Influences of evaporation time and polymer concentration.....	131
5.4.3 Influence of solvent ratio .....	134
5.4.4 Influence of water .....	136
5.4.5 Thermo-responsive behavior .....	136
5.5 Conclusions .....	139
References .....	140
<b>Chapter 6: General Discussion .....</b>	<b>143</b>
6.1 Remarkable Materials .....	144
6.1.1 Permeability .....	145
6.1.2 Mechanical stability .....	146
6.1.3 Further characterizations .....	147
6.1.4 Lower cost solutions .....	147
6.2 Understanding the self-assembly mechanism in isoporous membrane formation.....	148
6.3 Outlook .....	150
References .....	150
<b>Summary .....</b>	<b>153</b>
<b>Özet .....</b>	<b>159</b>
<b>About the author .....</b>	<b>167</b>
<b>List of publications .....</b>	<b>169</b>
<b>Acknowledgements .....</b>	<b>171</b>
<b>Overview of completed training activities.....</b>	<b>176</b>

# CHAPTER 1

## **Introduction**

## 1.1 Scope of the thesis

---

Clean water is one of the most important resources for every living being. The world population is increasing, however clean water resources are limited. Using renewable sources is a key concept for a sustainable society. Therefore, water purification is crucial to be able to provide enough clean water. Membrane based water purification is advantageous since it is more cost-effective and less energy consuming compared to other separation methods such as disinfection and distillation which require chemical additives and thermal inputs.<sup>1</sup> Polymeric membranes are more favored over inorganic membranes since they are lower in cost and easier to produce and handle.<sup>2</sup> Moreover, with the attempts to increase the quality of human life, as the contamination by nanomaterials (e.g. proteins, drugs, hormones, viruses and inorganic nanoparticles) caused by human activities are growing, water purification at the nanoscales becomes an essential requirement.<sup>1</sup>

Fouling, the accumulation of small particles in and around the pores of a membrane, which causes a reduction in the flux and separation quality of such membranes, is one of the main challenges in membrane technology field. A promising solution is to use stimuli-responsive membranes to obtain easy-to-clean properties. In industry, since a practical parameter to control is often the temperature, it is advantageous to introduce thermo-responsive properties to the membrane.

Block copolymers (BCPs) are comprised of at least two different homopolymer blocks that are covalently bonded to each other. When the block copolymer consists of chemically distinct blocks, it can self-assemble into regular nanostructures. By combining the self-assembly behavior with the easy tunable properties of BCPs, advanced functional membranes can be obtained with desired properties such as thermo-responsivity. In this thesis, we aimed to investigate the block copolymer self-assembly concept and use the advantages of BCPs to produce thermo-responsive membranes.

## 1.2 Synthesis of block copolymers

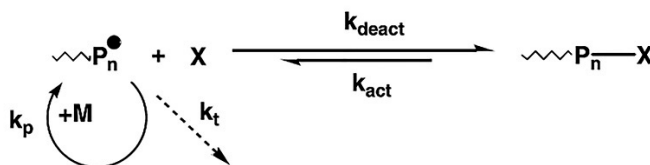
---

Polydispersity index (PDI) is a quantitative definition of the molecular weight distribution of the polymer chains and expressed as  $PDI = \bar{M}_w / \bar{M}_n$  where  $\bar{M}_n$  and  $\bar{M}_w$  are the number

average molecular weight and weight average molecular weight of the polymer, respectively. Since the success of block copolymer self-assembly is proportional to the uniformity of the block copolymer chains, we need block copolymers with a low PDI.<sup>3</sup>

To obtain a low PDI, a high control on the active chains is necessary, which is succeeded by using controlled/living polymerization (CLP) techniques. The control in CLP is mainly achieved by fast initiation, slow propagation, and without irreversible deactivation of the active centers, such as irreversible transfer and termination reactions that frequently occurs in classical free radical polymerization (FRP). Instead, for a well-controlled polymerization, the deactivation of the active centers is reversible. As an example, for comparison, 100 initiator molecules correspond to only 1 active center molecules for CLP, whereas the number of initiator molecules and active centers are both equal to 100 for FRP. This means in CLP, only one active center will propagate the polymerization reaction at a time and by reversible transfer of the radical to the other polymer chain, this active center becomes dormant and another active chain propagates the reaction. A dynamic equilibrium establishes between the growing chains and dormant chains (Scheme 1). A fast exchange with the active and the dormant chains is required for good control over the molecular weight and PDI.<sup>4</sup>

**Scheme 1.** A generalized CLP mechanism.<sup>4</sup>



### 1.2.1 Types of controlled/living polymerizations

The most common CLP's are anionic polymerization, nitroxide mediated polymerization, atom transfer radical polymerization (ATRP) and reversible-addition-fragmentation-transfer (RAFT) polymerization.

Anionic polymerization was the first living polymerization realized later due to its living character of the growing polymer chains by fast initiation and slow propagation reactions, which is carried out by using alkyl lithium initiators in non-polar solvents. Here, ion pairs are considered as dormant chains and free ions as active centers. Even though anionic

polymerization results in very well-defined polymers ( $PDI < 1.1$ ), the synthesis conditions are strict and not all the monomers can polymerize anionically.

In nitroxide mediated polymerization, alkoxyamine initiators, e.g. 2,2,6,6-tetramethyl-1-piperidinyloxy (TEMPO), form a dynamic equilibrium with actively growing chains which generate polymers with high stereochemistry and well-defined character. High temperatures ( $>110^{\circ}\text{C}$ ) are required for this polymerization method.

In ATRP, 1:1 adducts of alkyl halides and alkenes are formed, which are catalyzed by transition metal complexes. Dormant chains are activated by these transition metal complexes to produce radicals by an electron transfer. When the transition metal reaches a higher oxidation state, a dynamic equilibrium is formed which shifts to low radical concentrations. Since each growing chain has the same probability to contribute to the propagation reaction, polymer chains with similar molecular weights are obtained. Although ATRP is one of the most widely used CLP's to produce well-defined polymers in the literature, transition metals do not tolerate certain reactive monomers and transition metal complexes should be removed from the product due to its toxicity.<sup>4</sup> RAFT, as being the most recent CLP, requires a chain transfer agent to control the propagation reaction. RAFT polymerization will be explained in more detail in the next part.

### 1.2.2 Reversible-addition-fragmentation-transfer polymerization

RAFT polymerization uses dithiobenzoates, trithiocarbonates, dithiocarbonates or xanthates as chain transfer agents to acquire the controlled manner of the polymerization. The structure of the RAFT agents can be shown in a general formula as  $Z-C(=S)-S-R$  where R acts as the leaving group which initiates a new polymer chain and Z is the group responsible for reactivity and radical stability.

The reaction mechanism of RAFT is illustrated in Scheme 2. The initiation reaction is similar as in FRP. At the beginning of the polymerization, a propagating radical ( $P_n$ ) reacts with a thiocarbonylthio compound (1) which is followed by the fragmentation of the intermediate radical to a polymeric thiocarbonylthio compound and a new radical ( $R\cdot$ ) (3). This new radical reacts with monomer forming a new propagating radical ( $P_m$ ). Then a dynamic equilibrium takes place between the propagating radicals and the dormant thiocarbonyl-



RAFT polymerization is superior compared with other CLP methods, not only because there is almost no monomer limitation in this polymerization, but also conventional FRP conditions can be used. Furthermore, polymerizations can take place even in water and at low temperatures. Selection of the RAFT agent is the most crucial parameter for a successful polymerization. Drawback of this polymerization is the odor and yellow color of sulphur, which is more pronounced for low molecular weight polymers.

### 1.3 Block copolymer self-assembly

---

BCPs comprise of two or more polymer blocks that are covalently bonded to each other. When the block copolymer consists of blocks that are chemically distinct, even though they want to phase separate, the chemical bonds between the blocks prevents it. Instead of phase separation on the macroscale (macrophase separation), a microphase separation occurs on the nanoscale.<sup>6</sup> Microphase separation is driven by a tendency to minimize the interaction enthalpy that limits the number of unfavorable interactions between the blocks. By doing so, it may induce stretching of the polymer chains. This stretching reduces the conformational entropy. In effect, the system minimizes its Gibbs energy, which implies a balance between keeping the enthalpy low while trying to limit the entropy losses. When there is no solvent involved in the system, the block copolymer must fully occupy the space which also introduces an inhomogeneous stretching of the chains. By an optimization of these tendencies, BCPs can self-assemble into regular structures on the scale of 10-100 nm.<sup>3, 7</sup>

The incompatibility between the A and B blocks in the copolymer that drives the microphase separation is quantified by the Flory-Huggins parameter ( $\chi_{AB}$ ). This parameter is specified in Equation 1, wherein  $Z$  is the number of nearest neighbors per monomer;  $k_B$  is the Boltzmann constant;  $k_B T$  is thermal energy;  $\varepsilon_{AB}$ ,  $\varepsilon_{AA}$  and  $\varepsilon_{BB}$  are the interaction energies between AB, AA and BB units, respectively. In case of block copolymer melts,  $\chi_{AB}$  is expressed as  $\chi$  since there is no other effect that forms an additional  $\chi$  parameter such as solvent.

$$\chi_{AB} = \left( \frac{Z}{k_B T} \right) \left[ \varepsilon_{AB} - \frac{1}{2} (\varepsilon_{AA} + \varepsilon_{BB}) \right] \quad (1)$$

The product  $\chi N$  is the overall segregation strength of microphase separation. In this product,  $N$  is the degree of polymerization which often is referred to as the chain length.

### 1.3.1 Block copolymer phase diagram

An AB diblock copolymer (Figure 1a) can self-assemble into various nanostructures (Figure 1b) which can be predicted using a theoretical block copolymer phase diagram constructed using self-consistent field (SCF) modelling (Figure 1c).<sup>8</sup> In this plot,  $\chi N$  is the previously defined segregation strength and  $f$  is the volume ratio of the A block to the total volume of the blocks. Depending on  $\chi N$  and  $f$  values of the block copolymer, lamellar (L), spherical (S), cylindrical (C) and bicontinuous gyroid (G) phases can be obtained (Figure 1b).<sup>3</sup> Below a certain segregation strength in the phase diagram, the so-called 'critical point', no microphase segregation occurs, instead the system stays disordered. According to the modelling studies where the chain length is assumed to be infinitely long<sup>9</sup>, the critical point is located at a segregation strength of  $\chi N = 10.495$ . However, considering the critical point as a function of chain length yields a more accurate estimation, such as in Equation 2.<sup>10</sup>

$$\chi N = 10.495 + 41.022 N^{-1/3} \quad (2)$$

Experimental phase diagrams are generally found to be similar to the theoretical phase diagram except for a deviation from symmetry that may be due to polydispersity of the polymer chains<sup>8</sup> or presence of metastable phases which were detected experimentally. Furthermore, more complex structures could be identified on the experimental phase diagrams such as hexagonally perforated lamellae in the polystyrene-*b*-polyisoprene system (Figure 1d) which might as well be a metastable phase.

### 1.3.2 Mesophases obtained from block copolymers

Besides the common spherical, cylindrical and lamellar phases; many interesting mesophases can be attained from BCPs. The most prominent ones are previously mentioned gyroids i.e. single gyroid (SG) and double gyroid (DG), hexagonally perforated lamellae (HPL) phases and the double diamond (DD) phase.

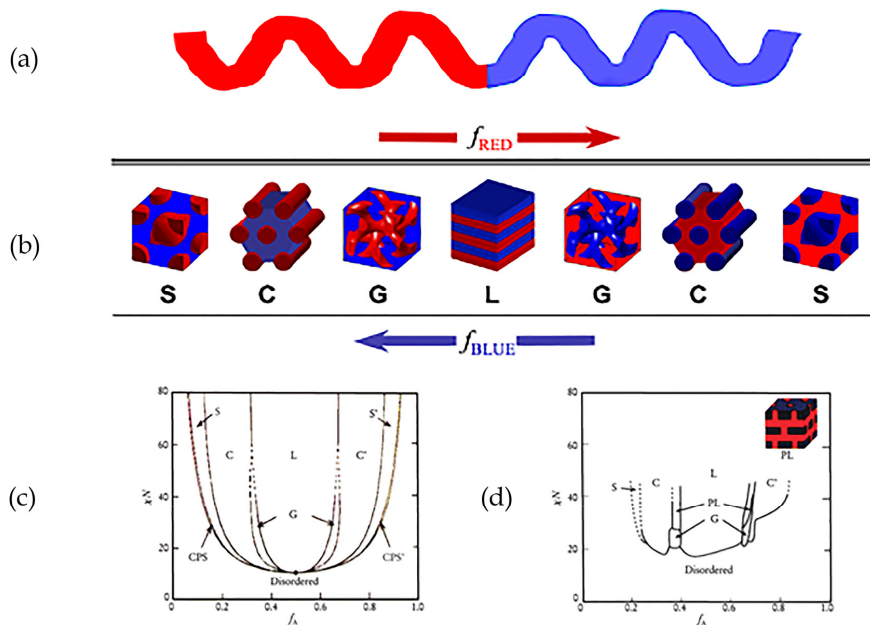


**Figure 1.** (a) Schematic representation of an AB block copolymer chain consisting of A (red) and B (blue) blocks. (b) Equilibrium phases for an AB diblock copolymer.<sup>3</sup> Segregation strength,  $\chi N$  ( $\chi$ : Flory interaction parameter,  $N$ : degree of polymerization) as a function of A block ratio ( $f_A$ ) in the (c) theoretical phase diagram of an AB diblock copolymer predicted using SCF modelling and (d) experimental phase diagram of a polystyrene-*b*-polyisoprene block copolymer. S: body centered cubic spheres, CPS: closely packed spheres, C: hexagonally packed cylinders, G: gyroid, L: lamellae, PL: hexagonally perforated lamellae (HPL).<sup>8</sup> (b) was reproduced from ref 3 with the permission of Elsevier. (c,d) were reproduced from ref 8 with the permission of the American Institute of Physics.

The **single gyroid** (space group  $I4_132$ ) was discovered in 1967 by Luzatti *et al.* in strontium soap surfactants<sup>11</sup> and identified by Alan Schoen who classified 17 such minimal surfaces, named it as gyroid or Schoen G surface<sup>12</sup> (Figure 2a). The SG structure was also detected in natural systems such as in butterfly wing scales<sup>13</sup> and in the retinal cone mitochondria of tree shrews.<sup>14</sup> The SG is a rare phase when it is compared to the DG and DD. Even though the SG was not found in diblock copolymers, because of its superior optical properties, there is a current approach to produce SG templates from a DG forming ABC BCPs such as poly(isoprene-*b*-styrene-*b*-ethylene oxide) by etching the blocks and metal deposition.<sup>15</sup>

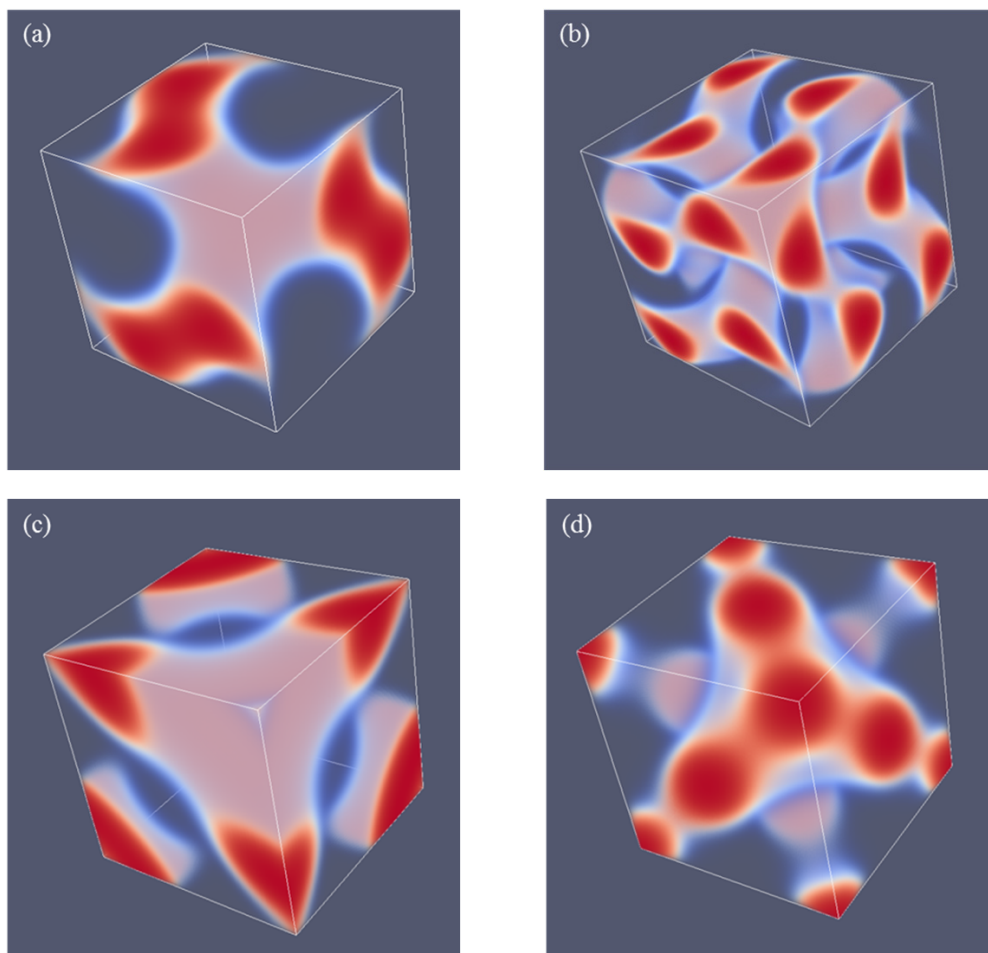


**Figure 2.** Unit cell representations of (a) the single gyroid (b) the double gyroid (c) hexagonally perforated lamellae and (d) the double diamond. Regions rich in the minority phase are given in red, the majority phase is made transparent for presentation purposes. The SCF parameters used to produce the unit cells are given in detail in Chapter 4.

The **double gyroid** (space group  $Ia\bar{3}d$ ), which consists of three continuous subvolumes with two non-intersecting SG's exhibiting the same volume and a third remaining matrix phase (Figure 2b). By gyroid, it is often meant the 'double gyroid' in the literature. It was discovered in 1986 by first being misinterpreted as the DD,<sup>16</sup> then correctly identified by two independent groups in 1994.<sup>17-18</sup> The DG was identified in various diblock,<sup>19-20</sup> ABA triblock<sup>21-22</sup> as well as ABC triblock copolymers.<sup>23</sup> There remain some points of debate

about the stability of the DG. According to the SCF calculations from Matsen and Bates,<sup>24</sup> the DG cannot be stable at strong segregation after reaching a triple point around  $\chi N=60$ , while Cochran *et al.* claim that the DG is a stable phase up to  $\chi N=100$  thereby broadening the stability window.<sup>25</sup>

**Hexagonally perforated lamellae** (space group  $R\bar{3}m$ ) (Figure 2c) were experimentally obtained in diblock copolymers<sup>26-27</sup> and were predicted to be nearly stable for diblock copolymers in the SCF calculations of Matsen *et al.*<sup>24</sup> According to Wang *et al.*, HPL is an intermediate state that occurs during cylindrical phase to the DG transition in diblock copolymers.<sup>28</sup>

Another mesophase, the **double diamond** (space group  $Pn\bar{3}m$ ) (Figure 2d) was first detected in polystyrene-polyisoprene star BCPs.<sup>16</sup> Later the DD phase was identified in diblock copolymers<sup>29</sup> and their copolymer blends with homopolymers<sup>30</sup> as well. Since the DG highly resembled the DD in TEM images, after re-examining studies, it was realized that some DD phases were actually DG.<sup>31</sup>

## 1.4 Block copolymer membranes

---

Nanoporous membranes gain more significance with the increasing contamination of nano-sized impurities in water with the increase in nanotechnological applications.<sup>1</sup> Block copolymers receive a great deal of attention in the membrane production, because they can readily microphase separate into regular structures on length scales of 10-100 nm. They result in membranes with nano-sized well-defined pores<sup>7</sup> which makes them advantageous for ultrafiltration applications where pore sizes of 10 to 100 nm are required.<sup>32</sup> Block copolymer membranes offer high pore densities, tunable pore sizes, narrow pore size distributions, tunable mechanical and chemical properties and the ability for selective functionalization such as the incorporation of stimuli-responsive functionality which can be used to produce easy-to-clean membranes.<sup>33</sup>

### 1.4.1 Block copolymer thin films

Block copolymer thin film membranes can be prepared using spin-coating the dilute block copolymer solution on a support. However, since spin-coating is a fast process, as-spun

films usually exhibit a metastable morphology with a short-range order. To achieve the desired morphology, which is generally perpendicularly oriented cylinders or bicontinuous morphologies such as the gyroid, and to improve the long-range order in the block copolymer thin films, an annealing step is required. Thermal and solvent annealing are the most common annealing methods. In both annealing methods, mobility of the polymer chains is increased, either by applying temperature over the glass transition temperature ( $T_g$ ) of the blocks or introducing solvent vapor into the thin film. As the temperature exceeds the  $T_g$ , or solvent vapor acts as a plasticizer that reduce the  $T_g$  of the block copolymer, the polymer chains are free to self-assemble to their equilibrium morphology. Although the thermal annealing method is effective, it can cause degradation of the BCPs which deteriorates the final morphology.<sup>34-42</sup> Solvent annealing does not pose the risk of polymer degradation, also by annealing with selective solvent mixtures which causes a volume fraction change in the selective block, more morphologies can be produced that cannot be attained by thermal annealing.<sup>42-45</sup> With this way, only one block copolymer is sufficient to obtain different morphologies which is time-saving, since there is no need to synthesize a new block copolymer with different molecular weight and/or block ratio for another morphology.<sup>46</sup> Plus, if perpendicular cylinders are desired, it is possible to control the orientation of the cylinders by tuning the selectivity of the solvent mixture.<sup>45, 47-49</sup>

After annealing, usually an additional step is applied for membrane production i.e. etching the minority block or removing pore forming additives to increase the permeability, even though there exists block copolymer thin films directly used as a membrane without etching any blocks as well.<sup>22</sup> Furthermore, the substrate, on which the solution is being spin-coated should be porous to readily use the material as a membrane. Otherwise the thin film needs to be transferred to a porous support afterwards, which is a delicate and time-consuming process.

### 1.4.2 Self-assembly and non-solvent induced phase separation method

A recent alternative to prepare block copolymer membranes is a phase inversion method which is referred to as self-assembly and non-solvent induced phase separation (SNIPS). For SNIPS membranes, an additional transfer of the membrane to a porous support step is

not necessary. Different from spin-coating, pores can be produced directly without the need of other steps such as etching, or rinsing the additives.<sup>50</sup>

Our method of choice in this thesis is mainly the self-assembly and non-solvent induced phase separation (SNIPS) method due to its superiority among the other methods such as fast production, easy handling plus its industrial relevance. In SNIPS (Figure 3), a viscous solution of the block copolymer is cast using a film applicator with a known gate height. The solvent in the film is evaporated for a known amount of time, which is generally less than one minute, which causes a concentration gradient perpendicular to the film surface. The film is then transferred into a non-solvent bath where the organic solvent in the polymer film and the non-solvent are exchanged which forms the final morphology.

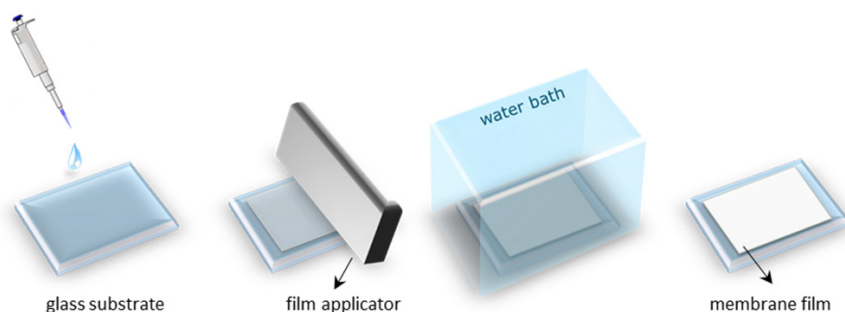


**Figure 3. Schematic representation of the SNIPS method.**

SNIPS membranes were first produced by Peinemann *et al.* from a polystyrene-*b*-poly(4-vinylpyridine) (PS-P4VP) block copolymer that resulted in a membrane with an isoporous surface and a spongy cross-section.<sup>50</sup> Isoporous surface is mainly the result of the block copolymer self-assembly mechanism during evaporation. Spongy cross-section forms because of the precipitation of the block copolymer in the non-solvent after the film was transferred to a non-solvent bath (water).<sup>50</sup> Other studies followed Peinemann's work to improve the properties of PS-P4VP membranes and SNIPS of several BCPs.<sup>51-54</sup>

Even though SNIPS is an easy and quick method to create block copolymer nanoporous membranes, many parameters should be considered for a successful membrane production. The most important parameters are polymer concentration,<sup>55</sup> evaporation time until the transfer to the non-solvent bath,<sup>55</sup> gate height of the film applicator,<sup>56</sup> selectivity of solvents,<sup>50, 57</sup> type and temperature of the non-solvent.<sup>58</sup>

### 1.4.3 Stimuli-responsive block copolymer membranes

Introduction of stimuli-responsive pores to the membrane systems is a beneficial approach to produce easy-to-clean membranes which offer advantages to decrease fouling problems in the industry.<sup>59-67</sup> When we apply a stimulus (e.g. thermal, pH, light, magnetic and electrical) to these membranes, the sizes of the pores increase which results in easy removal of the impurities (Figure 4).

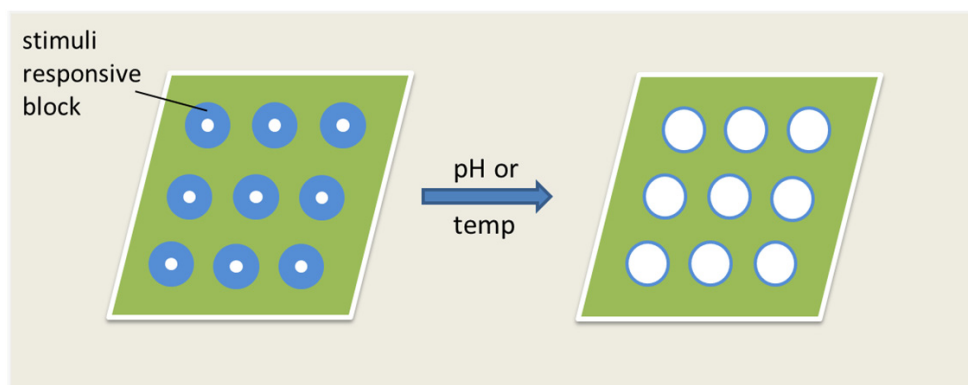


**Figure 4. Working mechanism of a stimuli-responsive membrane by the applied stimulus e.g. pH, temperature.**

Because of their high tunable character, block copolymers can be utilized to incorporate stimuli-responsive properties to the membrane, which can be achieved by introducing at least one stimuli-responsive block into the copolymer.

Thermo-responsive membranes can be produced using block copolymers which contain a thermo-responsive block with a lower critical solution temperature (LCST). When the environment reaches a temperature higher than the LCST of the block, the swollen block collapses leading to larger pores in the membrane. Since it is a reversible process, when the temperature is lowered, the thermo-responsive block swells which leads to a decrease in pore size back to its original size.

In the literature, thermo-responsive membranes were produced by spin-coating polystyrene-*b*-poly(*N*-isopropyl acrylamide)-*b*-polystyrene<sup>22</sup> and poly(ethylene glycol methyl ether methacrylate)-*b*-polystyrene-*b*-poly(ethylene glycol methyl ether methacrylate)<sup>68</sup> block co-

polymer thin films on a porous support, followed by annealing to obtain a desired morphology. Thermo-responsive properties were incorporated to PS-*b*-P4VP block copolymers by introducing poly(*N*-isopropyl acrylamide) to the membrane.<sup>52</sup>

## 1.5 Aim and outline of the thesis

---

In this thesis, we aimed to use the advantages of block copolymers in membrane applications and investigate the properties of the membranes which are produced using the SNIPS method. To reach this aim, first, the synthesis of the block polymers needed to be accomplished. Therefore, we optimized the synthesis of well-defined polystyrene-poly(*N*-isopropyl acrylamide) (PS-PNIPAM) BCPs with the desired properties for a successful membrane fabrication. We performed both experimental and theoretical investigations to gain further insight in block copolymer self-assembly behavior. Thus, we studied the self-assembly of BCPs using self-consistent field theory of Scheutjens and Fleer (SF-SCF). We worked on the several regions in the theoretical block copolymer phase diagram using SF-SCF modelling to examine the stability of some well-known mesophases and the critical point. At the same time, we investigated the self-assembly behavior of the block copolymer thin films when they were annealed in selective solvents. Finally, we fabricated free-standing membranes out of the synthesized BCPs.

In **Chapter 2**, we discuss the optimization of RAFT polymerization parameters for the synthesis of well-defined high molecular weight PS-PNIPAM BCPs where polystyrene (PS) is the matrix block as a mechanical support and poly(*N*-isopropyl acrylamide) (PNIPAM) is the thermo-responsive block. We found that the polymerization yield increased significantly when we used PNIPAM macro-RAFT agent instead of PS macro-RAFT agent while maintaining a low polydispersity. We successfully produced free-standing nanoporous fully reversible thermo-responsive membranes by SNIPS process using the solutions of high molecular weight PS-*b*-PNIPAM block copolymer prepared from the solvent mixture of *N*-methyl-2-pyrrolidone and tetrahydrofuran.

**Chapter 3** is concerned with a theoretical approach to study the self-assembly behavior of diblock copolymers. Here, we investigate the block copolymer phase diagram of diblock copolymers using self-consistent field theory of Scheutjens and Fleer (SF-SCF). Our focus is

to present chain length dependence on the critical point to confirm the accuracy of the method for block copolymer systems. Next, we examine the stability of some well-known mesophases such as single and double gyroids, hexagonally perforated lamellae and double diamond which occurs between the lamellar and hexagonal regions on the block copolymer phase diagram at intermediate segregation regime of  $\chi N=30$ . Moreover, we analyzed the stability of double gyroid at strong segregation regime of  $\chi N=120$  which is a point of debate among researchers.

In **Chapter 4**, we describe the production of PS-*b*-PNIPAM-*b*-PS BCP thin films and present the self-assembly behavior of these BCPs during solvent annealing. Thin films were annealed using solvents with different selectivity to obtain long-range order and to tune the morphology. The morphology change in the thin films were analyzed using atomic force microscopy (AFM) and *in-situ* grazing incidence X-ray scattering (GISAXS) techniques. We showed that by solvent annealing a lamellar forming PS-*b*-PNIPAM-*b*-PS block copolymer in methanol-tetrahydrofuran or methanol-toluene solvent mixtures resulted in a hexagonally ordered cylindrical morphology, having the cylinders oriented perpendicular to the substrate.

**Chapter 5** reports the tuning of the SNIPS parameters to produce nano- and isoporous thermo-responsive membranes. Here we discuss the influence of solvent, evaporation time and polymer concentration on the surface structure of the membrane. We produced nanoporous membranes using PS selective solvent mixtures, however they did not result in membranes with uniform pores. In contrast, using PNIPAM selective solvent mixtures used for SNIPS process successfully resulted in nano- and isoporous membranes while maintaining its fully reversible thermo-responsive character. We pointed out that solvent mixtures should contain a high difference in the evaporation rates to form suitable solvent concentration gradient that leads to an isoporous surface. We accomplished to fabricate free-standing membranes with nano-sized and uniform pores with a large parameter space which is not common for SNIPS process.

In **Chapter 6**, a general discussion of the thesis is presented. Even though we have demonstrated that well-defined high molecular weight PS-PNIPAM BCPs can be successfully used to produce free-standing fully thermo-responsive iso- and nanoporous membranes, there

remains plenty of room to consider for improvement. Some of these challenges and recommendations for future direction are discussed in this chapter. Finally, we will conclude with a summary of our findings at the end of the thesis.

## References

---

1. Pendergast, M. M.; Hoek, E. M. V., A review of water treatment membrane nanotechnologies. *Energy & Environmental Science* **2011**, *4* (6), 1946-1971.
2. Abetz, V., Isoporous Block Copolymer Membranes. *Macromol. Rapid Commun.* **2015**, *36* (1), 10-22.
3. Lynd, N. A.; Meuler, A. J.; Hillmyer, M. A., Polydispersity and block copolymer self-assembly. *Progress in Polymer Science* **2008**, *33* (9), 875-893.
4. Braunecker, W. A.; Matyjaszewski, K., Controlled/living radical polymerization: Features, developments, and perspectives. *Progress in Polymer Science* **2007**, *32* (1), 93-146.
5. Moad, G.; Rizzardo, E.; Thang, S. H., Living Radical Polymerization by the RAFT Process. *Australian Journal of Chemistry* **2005**, *58* (6), 379-410.
6. Bates, F. S.; Fredrickson, G. H., *Phys. Today* **1999**, *52* (2), 32.
7. Mai, Y.; Eisenberg, A., Self-assembly of block copolymers. *Chemical Society Reviews* **2012**, *41* (18), 5969-5985.
8. Matsen, M. W., Polydispersity-Induced Macrophase Separation in Diblock Copolymer Melts. *Phys. Rev. Lett.* **2007**, *99* (14), 148304.
9. Chremos, A.; Nikoubashman, A.; Panagiotopoulos, A. Z., Flory-Huggins parameter  $\chi$ , from binary mixtures of Lennard-Jones particles to block copolymer melts. *The Journal of Chemical Physics* **2014**, *140* (5), 054909.
10. Fredrickson, G. H.; Helfand, E., Fluctuation effects in the theory of microphase separation in block copolymers. *The Journal of Chemical Physics* **1987**, *87* (1), 697-705.
11. Luzzati, V.; Spegel, P. A., Polymorphism of Lipids. *Nature* **1967**, *215* (5102), 701-704.
12. Schoen, A., Infinite periodic minimal surfaces without self-intersections. *NASA Technical Note D-5541* **1970**.
13. Saranathan, V.; Osuji, C. O.; Mochrie, S. G. J.; Noh, H.; Narayanan, S.; Sandy, A.; Dufresne, E. R.; Prum, R. O., Structure, function, and self-assembly of single network gyroid (I4132) photonic crystals in butterfly wing scales. *Proceedings of the National Academy of Sciences* **2010**, *107* (26), 11676-11681.
14. Almsherqi, Z.; Margadant, F.; Deng, Y., A look through 'lens' cubic mitochondria. *Interface Focus* **2012**, *2* (5), 539-545.
15. Vignolini, S.; Yufa, N. A.; Cunha, P. S.; Guldin, S.; Rushkin, I.; Stefik, M.; Hur, K.; Wiesner, U.; Baumberg, J. J.; Steiner, U., A 3D Optical Metamaterial Made by Self-Assembly. *Adv. Mater.* **2012**, *24* (10), OP23-OP27.
16. Thomas, E. L.; Alward, D. B.; Kinning, D. J.; Martin, D. C.; Handlin, D. L.; Fetters, L. J., Ordered bicontinuous double-diamond structure of star block copolymers: a new equilibrium microdomain morphology. *Macromolecules* **1986**, *19* (8), 2197-2202.
17. Hajduk, D. A.; Harper, P. E.; Gruner, S. M.; Honeker, C. C.; Kim, G.; Thomas, E. L.; Fetters, L. J., The Gyroid: A New Equilibrium Morphology in Weakly Segregated Diblock Copolymers. *Macromolecules* **1994**, *27* (15), 4063-4075.

18. Schulz, M. F.; Bates, F. S.; Almdal, K.; Mortensen, K., Epitaxial Relationship for Hexagonal-to-Cubic Phase Transition in a Block Copolymer Mixture. *Phys. Rev. Lett.* **1994**, *73* (1), 86-89.
19. Crossland, E. J. W.; Kamperman, M.; Nedelcu, M.; Ducati, C.; Wiesner, U.; Smilgies, D. M.; Toombes, G. E. S.; Hillmyer, M. A.; Ludwigs, S.; Steiner, U.; Snaith, H. J., A Bicontinuous Double Gyroid Hybrid Solar Cell. *Nano Letters* **2009**, *9* (8), 2807-2812.
20. Ndoni, S.; Vigild, M. E.; Berg, R. H., Nanoporous Materials with Spherical and Gyroid Cavities Created by Quantitative Etching of Polydimethylsiloxane in Polystyrene-Polydimethylsiloxane Block Copolymers. *Journal of the American Chemical Society* **2003**, *125* (44), 13366-13367.
21. Dair, B. J.; Honeker, C. C.; Alward, D. B.; Avgeropoulos, A.; Hadjichristidis, N.; Fetters, L. J.; Capel, M.; Thomas, E. L., Mechanical Properties and Deformation Behavior of the Double Gyroid Phase in Unoriented Thermoplastic Elastomers. *Macromolecules* **1999**, *32* (24), 8145-8152.
22. Nykänen, A.; Nuopponen, M.; Laukkanen, A.; Hirvonen, S.-P.; Rytelä, M.; Turunen, O.; Tenhu, H.; Mezzenga, R.; Ikkala, O.; Ruokolainen, J., Phase Behavior and Temperature-Responsive Molecular Filters Based on Self-Assembly of Polystyrene-block-poly(N-isopropylacrylamide)-block-polystyrene. *Macromolecules* **2007**, *40* (16), 5827-5834.
23. Epps, T. H.; Cochran, E. W.; Bailey, T. S.; Waletzko, R. S.; Hardy, C. M.; Bates, F. S., Ordered Network Phases in Linear Poly(isoprene-b-styrene-b-ethylene oxide) Triblock Copolymers. *Macromolecules* **2004**, *37* (22), 8325-8341.
24. Matsen, M. W.; Bates, F. S., Unifying Weak- and Strong-Segregation Block Copolymer Theories. *Macromolecules* **1996**, *29* (4), 1091-1098.
25. Cochran, E. W.; Garcia-Cervera, C. J.; Fredrickson, G. H., Stability of the Gyroid Phase in Diblock Copolymers at Strong Segregation. Volume 39, Number 7, March, 14, 2006, pp 2449-2451. *Macromolecules* **2006**, *39* (12), 4264-4264.
26. Khandpur, A. K.; Foerster, S.; Bates, F. S.; Hamley, I. W.; Ryan, A. J.; Bras, W.; Almdal, K.; Mortensen, K., Polyisoprene-Polystyrene Diblock Copolymer Phase Diagram near the Order-Disorder Transition. *Macromolecules* **1995**, *28* (26), 8796-8806.
27. Tavakkoli K. G. A.; Nicaise, S. M.; Hannon, A. F.; Gotrik, K. W.; Alexander-Katz, A.; Ross, C. A.; Berggren, K. K., Sacrificial-Post Templating Method for Block Copolymer Self-Assembly. *Small* **2014**, *10* (3), 493-499.
28. Wang, C.-Y.; Lodge, T. P., Kinetics and Mechanisms for the Cylinder-to-Gyroid Transition in a Block Copolymer Solution. *Macromolecules* **2002**, *35* (18), 6997-7006.
29. Hasegawa, H.; Tanaka, H.; Yamasaki, K.; Hashimoto, T., Bicontinuous microdomain morphology of block copolymers. 1. Tetrapod-network structure of polystyrene-polyisoprene diblock polymers. *Macromolecules* **1987**, *20* (7), 1651-1662.
30. Winey, K. I.; Thomas, E. L.; Fetters, L. J., The ordered bicontinuous double-diamond morphology in diblock copolymer/homopolymer blends. *Macromolecules* **1992**, *25* (1), 422-428.
31. Meuler, A. J.; Hillmyer, M. A.; Bates, F. S., Ordered Network Messtructures in Block Polymer Materials. *Macromolecules* **2009**, *42* (19), 7221-7250.
32. Zhang, Y.; Sargent, J. L.; Boudouris, B. W.; Phillip, W. A., Nanoporous membranes generated from self-assembled block polymer precursors: Quo Vadis? *J. Appl. Polym. Sci.* **2015**, *132* (21), n/a-n/a.
33. Jackson, E. A.; Hillmyer, M. A., Nanoporous Membranes Derived from Block Copolymers: From Drug Delivery to Water Filtration. *ACS Nano* **2010**, *4* (7), 3548-3553.
34. Di, Z.; Posselt, D.; Smilgies, D.-M.; Papadakis, C. M., Structural Rearrangements in a Lamellar Diblock Copolymer Thin Film during Treatment with Saturated Solvent Vapor. *Macromolecules* **2010**, *43* (1), 418-427.

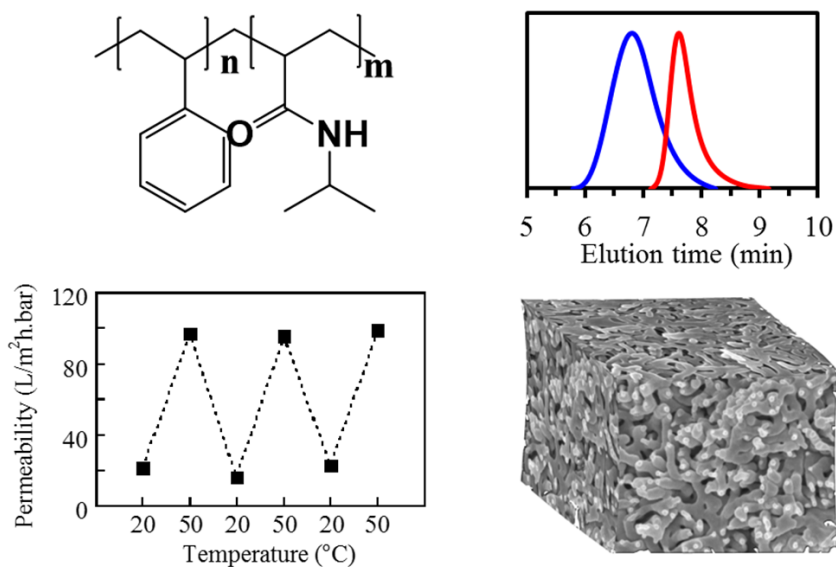
35. Kelly, J. Y.; Albert, J. N. L.; Howarter, J. A.; Kang, S.; Stafford, C. M.; Epps, T. H.; Faselka, M. J., Investigation of Thermally Responsive Block Copolymer Thin Film Morphologies Using Gradients. *ACS Applied Materials & Interfaces* **2010**, *2* (11), 3241-3248.
36. Segalman, R. A., Patterning with block copolymer thin films. *Materials Science and Engineering: R: Reports* **2005**, *48* (6), 191-226.
37. Abetz, V.; Simon, P. F. W., Phase Behaviour and Morphologies of Block Copolymers. In *Block Copolymers I*, Springer Berlin Heidelberg: 2005; Vol. 189, pp 125-212.
38. Darling, S. B., Directing the self-assembly of block copolymers. *Progress in Polymer Science* **2007**, *32* (10), 1152-1204.
39. Smilgies, D.-M.; Li, R.; Di, Z.; Darko, C.; Papadakis, C. M.; Posselt, D., Probing the Self-Organization Kinetics in Block Copolymer Thin Films. *Materials Research Society Symposium Proceedings* **2009**, *1147E*.
40. Kelly, J. Y.; Albert, J. N. L.; Howarter, J. A.; Stafford, C. M.; Epps, T. H.; Faselka, M. J., Manipulating morphology and orientation in thermally responsive block copolymer thin films. *Journal of Polymer Science, Part B: Polymer Physics* **2012**, *50* (4), 263-271.
41. Gotrik, K. W.; Hannon, A. F.; Son, J. G.; Keller, B.; Alexander-Katz, A.; Ross, C. A., Morphology Control in Block Copolymer Films Using Mixed Solvent Vapors. *ACS Nano* **2012**, *6* (9), 8052-8059.
42. Bosworth, J. K.; Paik, M. Y.; Ruiz, R.; Schwartz, E. L.; Huang, J. Q.; Ko, A. W.; Smilgies, D.-M.; Black, C. T.; Ober, C. K., Control of Self-Assembly of Lithographically Patternable Block Copolymer Films. *ACS Nano* **2008**, *2* (7), 1396-1402.
43. Sinturel, C.; Vayer, M.; Morris, M.; Hillmyer, M. A., Solvent Vapor Annealing of Block Polymer Thin Films. *Macromolecules (Washington, DC, U. S.)* **2013**, *46* (14), 5399-5415.
44. Tada, Y.; Yoshida, H.; Ishida, Y.; Hirai, T.; Bosworth, J. K.; Dobisz, E.; Ruiz, R.; Takenaka, M.; Hayakawa, T.; Hasegawa, H., Directed Self-Assembly of POSS Containing Block Copolymer on Lithographically Defined Chemical Template with Morphology Control by Solvent Vapor. *Macromolecules (Washington, DC, U. S.)* **2012**, *45* (1), 292-304.
45. Tokarev, I.; Krenek, R.; Burkov, Y.; Schmeisser, D.; Sidorenko, A.; Minko, S.; Stamm, M., Microphase Separation in Thin Films of Poly(styrene-block-4-vinylpyridine) Copolymer-2-(4'-Hydroxybenzeneazo)benzoic Acid Assembly. *Macromolecules* **2005**, *38* (2), 507-516.
46. Chavis, M. A.; Smilgies, D.-M.; Wiesner, U. B.; Ober, C. K., Widely Tunable Morphologies in Block Copolymer Thin Films Through Solvent Vapor Annealing Using Mixtures of Selective Solvents. *Adv. Funct. Mater.* **2015**, *25* (20), 3057-3065.
47. Gowd, E. B.; Marcus, B.; Manfred, S., In Situ GISAXS Study on Solvent Vapour Induced Orientation Switching in PS- b -P4VP Block Copolymer Thin Films. *IOP Conference Series: Materials Science and Engineering* **2010**, *14* (1), 012015.
48. Brendel, J. C.; Liu, F.; Lang, A. S.; Russell, T. P.; Thelakkat, M., Macroscopic Vertical Alignment of Nanodomains in Thin Films of Semiconductor Amphiphilic Block Copolymers. *ACS Nano* **2013**, *7* (7), 6069-6078.
49. Berezkin, A. V.; Papadakis, C. M.; Potemkin, I. I., Vertical Domain Orientation in Cylinder-Forming Diblock Copolymer Films upon Solvent Vapor Annealing. *Macromolecules* **2016**, *49* (1), 415-424.
50. Peinemann, K.-V.; Abetz, V.; Simon, P. F. W., Asymmetric superstructure formed in a block copolymer via phase separation. *Nat Mater* **2007**, *6* (12), 5.
51. Nunes, S. P.; Sougrat, R.; Hooghan, B.; Anjum, D. H.; Behzad, A. R.; Zhao, L.; Pradeep, N.; Pinnau, I.; Vainio, U.; Peinemann, K.-V., Ultraporous Films with Uniform Nanochannels by Block Copolymer Micelles Assembly. *Macromolecules* **2010**, *43* (19), 8079-8085.

52. Clodt, J. I.; Filiz, V.; Rangou, S.; Buhr, K.; Abetz, C.; Höche, D.; Hahn, J.; Jung, A.; Abetz, V., Double Stimuli-Responsive Isoporous Membranes via Post-Modification of pH-Sensitive Self-Assembled Diblock Copolymer Membranes. *Adv. Funct. Mater.* **2013**, *23* (6), 731-738.
53. Yu, H.; Qiu, X.; Nunes, S. P.; Peinemann, K.-V., Self-Assembled Isoporous Block Copolymer Membranes with Tuned Pore Sizes. *Angewandte Chemie, International Edition* **2014**, *53* (38), 10072-10076.
54. Clodt, J. I.; Rangou, S.; Schröder, A.; Buhr, K.; Hahn, J.; Jung, A.; Filiz, V.; Abetz, V., Carbohydrates as Additives for the Formation of Isoporous PS-b-P4VP Diblock Copolymer Membranes. *Macromol. Rapid Commun.* **2013**, *34* (2), 190-194.
55. Rangou, S.; Buhr, K.; Filiz, V.; Clodt, J. I.; Lademann, B.; Hahn, J.; Jung, A.; Abetz, V., Self-organized isoporous membranes with tailored pore sizes. *Journal of Membrane Science* **2014**, *451* (0), 266-275.
56. Phillip, W. A.; Mika Dorin, R.; Werner, J. r.; Hoek, E. M. V.; Wiesner, U.; Elimelech, M., Tuning Structure and Properties of Graded Triblock Terpolymer-Based Mesoporous and Hybrid Films. *Nano Letters* **2011**, *11* (7), 2892-2900.
57. Karunakaran, M.; Nunes, S. P.; Qiu, X.; Yu, H.; Peinemann, K.-V., Isoporous PS-b-PEO ultrafiltration membranes via self-assembly and water-induced phase separation. *Journal of Membrane Science* **2014**, *453* (0), 471-477.
58. Jung, A.; Rangou, S.; Abetz, C.; Filiz, V.; Abetz, V., Structure Formation of Integral Asymmetric Composite Membranes of Polystyrene-block-Poly(2-vinylpyridine) on a Nonwoven. *Macromolecular Materials and Engineering* **2012**, *297* (8), 790-798.
59. Tokarev, I.; Minko, S., Stimuli-responsive hydrogel thin films. *Soft Matter* **2009**, *5* (3), 511-524.
60. Pan, K.; Zhang, X.; Ren, R.; Cao, B., Double stimuli-responsive membranes grafted with block copolymer by ATRP method. *Journal of Membrane Science* **2010**, *356* (1-2), 133-137.
61. Wandera, D.; Wickramasinghe, S. R.; Husson, S. M., Stimuli-responsive membranes. *Journal of Membrane Science* **2010**, *357* (1-2), 6-35.
62. Himstedt, H. H.; Marshall, K. M.; Wickramasinghe, S. R., pH-responsive nanofiltration membranes by surface modification. *Journal of Membrane Science* **2011**, *366* (1-2), 373-381.
63. Nunes, S. P.; Behzad, A. R.; Hooghan, B.; Sougrat, R.; Karunakaran, M.; Pradeep, N.; Vainio, U.; Peinemann, K.-V., Switchable pH-Responsive Polymeric Membranes Prepared via Block Copolymer Micelle Assembly. *ACS Nano* **2011**, *5* (5), 3516-3522.
64. Mondal, S.; Wickramasinghe, S. R., Photo-induced graft polymerization of N-isopropyl acrylamide on thin film composite membrane: Produced water treatment and antifouling properties. *Separation and Purification Technology* **2012**, *90*, 231-238.
65. Chen, X.; Shi, C.; Wang, Z.; He, Y.; Bi, S.; Feng, X.; Chen, L., Structure and performance of poly(vinylidene fluoride) membrane with temperature-sensitive poly(n-isopropylacrylamide) homopolymers in membrane pores. *Polym Compos* **2013**, *34* (4), 457-467.
66. Chen, Y.-C.; Xie, R.; Chu, L.-Y., Stimuli-responsive gating membranes responding to temperature, pH, salt concentration and anion species. *Journal of Membrane Science* **2013**, *442*, 206-215.
67. Yang, Q.; Himstedt, H. H.; Ulbricht, M.; Qian, X.; Ranil Wickramasinghe, S., Designing magnetic field responsive nanofiltration membranes. *Journal of Membrane Science* **2013**, *430*, 70-78.
68. Tang, Y.; Ito, K.; Hong, L.; Ishizone, T.; Yokoyama, H., Tunable Thermo-responsive Mesoporous Block Copolymer Membranes. *Macromolecules* **2016**, *49* (20), 7886-7896.



# CHAPTER 2

## Free-standing thermo-responsive nanoporous membranes from high molecular weight PS-PNIPAM block copolymers



Published as:

Cetintas, M.; de Grooth, J.; Hofman, A. H.; van der Kooij, H. M.; Loos, K.; de Vos, W. M.; Kamperman, M. Free-standing thermo-responsive nanoporous membranes from high molecular weight PS-PNIPAM block copolymers synthesized *via* RAFT polymerization. *Polymer Chemistry* **2017**, 8 (14), 2235-2243.

## 2.1 Abstract

---

The incorporation of stimuli-responsive pores in nanoporous membranes is a promising approach to facilitate the cleaning process of the membranes. Here we present fully reversible thermo-responsive nanoporous membranes fabricated by self-assembly and non-solvent induced phase separation (SNIPS) of polystyrene-poly(*N*-isopropylacrylamide) (PS-PNIPAM) block copolymers. A variety of PS-PNIPAM block copolymers were synthesized by reversible addition-fragmentation chain transfer (RAFT) polymerization and the reaction conditions were optimized. The aimed copolymers featured: a (1) thermo-responsive PNIPAM block, (2) majority PS fraction, (3) well-defined high molecular weight, which are requirements for successful fabrication of free-standing responsive membranes using SNIPS. The resulting membranes exhibited a worm-like cylindrical morphology with interconnected nanopores. The thermo-responsive character of the membranes was studied by measuring the permeability of the membranes as a function of temperature. The permeability was found to increase by almost 400% upon going from room temperature to 50 °C and this thermo-responsive character was fully reversible.

## 2.2 Introduction

---

Fouling, both biological and colloidal in nature, can be considered as one of the biggest challenges membrane technology faces. It is the process where biomolecules, cells or suspended particles deposit reversibly or irreversibly on the membrane surface that leads to reductions in flux and/or in the separation quality, and consequently in reduced production capacity and increased operation costs. Fouling can especially be a problem for membranes with smaller pore sizes (below 20 nm), as cleaning such as back flushing is more challenging due to low shear forces that can be achieved in such small pores. To reduce this problem, by facilitating the cleaning process of the membranes, several methods have been developed.<sup>1</sup> A promising approach is the incorporation of stimuli-responsive pores into the membrane, which can be achieved by using polymers having a stimuli-responsive character.<sup>2-19</sup> Upon the application of an external stimulus, e.g. thermal, pH, light, magnetic and electrical, the size of the pores increases. This in turn allows for higher back flush speeds and thus for higher shear forces that leads to much more efficient physical cleaning.<sup>2, 9-10, 15,</sup>

20-21

Block copolymers (BCPs) are an interesting class of materials for nanoporous membrane applications, as block copolymer self-assembly can lead to monodisperse nanopores.<sup>22-31</sup> Common methods for the fabrication of block copolymer membranes include spin-coating and a method called self-assembly and non-solvent induced phase separation (SNIPS). Spin-coating of a thin block copolymer layer on a porous support, or transferring the thin film to a porous support, is followed by annealing (and possible etching of one of the blocks) resulting in porous films suitable for membrane applications.<sup>32-33</sup> Nykänen *et al.* reported that membranes prepared from a spin-coated polystyrene-*b*-poly(*N*-isopropylacrylamide)-*b*-polystyrene triblock copolymer showed thermo-responsive properties due to the poly(*N*-isopropylacrylamide) (PNIPAM) block exhibiting a lower critical solution temperature (LCST) of 32 °C.<sup>34</sup> Recently, another thermo-responsive membrane was obtained by spin-coating of poly(ethylene glycol methyl ether methacrylate)-*b*-polystyrene-*b*-poly(ethylene glycol methyl ether methacrylate) BCPs.<sup>35</sup>

In SNIPS, a viscous polymer solution is cast on a substrate with a known wet thickness, followed by solvent evaporation to densify the membrane top layer and finally transferred into a non-solvent bath to form the desired porous structure.<sup>36</sup> The major advantage compared to spin-coating is that since the films are free-standing, a transfer of the membrane to a porous support step is not necessary for SNIPS membranes. Moreover, pores can be produced directly, without the need of additional steps such as etching of one of the blocks, or removal of the additives.

Polystyrene-*b*-poly(4-vinylpyridine) (PS-*b*-P4VP) block copolymer membranes produced by the SNIPS process were studied in detail due to the polymer's ability to self-assemble into isoporous structures and its pH-responsive behavior.<sup>6-7, 16, 19-20, 37-38</sup> Despite the excellent results obtained for PS-*b*-P4VP copolymers, SNIPS is not limited to this copolymer and was extended to other responsive BCPs, including poly(isoprene-*b*-styrene-*b*-4-vinylpyridine),<sup>17-18</sup> polystyrene-*b*-poly(2-(dimethylamino)ethyl methacrylate)<sup>5, 11</sup> and poly(styrene-*co*-isoprene)-*b*-poly(*N,N*-dimethylaminoethyl methacrylate).<sup>8</sup> The poly(*N,N*-dimethylaminoethyl methacrylate) containing membranes showed both pH- and thermo-responsive behavior. This dual responsive behavior was also obtained by Clodt *et al.* by coating a PNIPAM layer onto a pH-responsive PS-*b*-P4VP membrane.<sup>3</sup>

SNIPS of isoporous membranes is based on the formation of spherical micelles which is followed by the formation of perpendicularly oriented cylinders that leads to an isoporous surface after a short solvent evaporation step (< 1 min) and subsequent transfer into the non-solvent bath.<sup>19, 22, 39</sup> A worm-like cylindrical morphology with nanopores, which occurs after longer evaporation times, is an interesting alternative to the commonly employed isoporous morphology for nanoporous membranes, because it can be produced for a wide range of parameter values.<sup>38</sup> In our study, we use BCPs containing polystyrene (PS) as the supporting block and thermo-responsive PNIPAM to produce free-standing membranes by using SNIPS. Well-defined high molecular weight PS-PNIPAM BCPs were synthesized with a minority PNIPAM fraction using reversible addition-fragmentation chain Transfer (RAFT) polymerization. RAFT polymerization was chosen since it yields well-defined polymer products using conventional free radical polymerization conditions.<sup>40</sup> RAFT is particularly attractive, because polymerization of acrylamide monomers using other controlled/living polymerization methods may result in side reactions necessitating multistep procedures.<sup>41-42</sup> The synthesized PS-PNIPAM BCPs were used for the first time in a SNIPS process and free-standing membranes were fabricated. The membranes exhibited a worm-like cylindrical morphology with nano-sized pores. By measuring the permeability values at different temperatures, it was shown that the membranes were thermo-responsive and that the thermo-responsive behavior was fully reversible.

## 2.3 Experimental Section

---

### 2.3.1 Materials

Styrene (Sigma-Aldrich, >99%) was vacuum distilled after stirring overnight over calcium hydride. *N*-isopropylacrylamide (NIPAM) (Sigma-Aldrich, 97%) was purified by recrystallization from toluene. 2,2'-Azobis(2-methylpropionitrile) (AIBN) (Sigma-Aldrich, 98%) was recrystallized from methanol. Diethylether (Biosolve B.V.) and methanol (Fisher Scientific) were used as received. Acetone, calcium hydride (95%), carbon disulphide (CS<sub>2</sub>) (anhydrous, ≥99%), chloroform (anhydrous, ≥99%), 1,4-dioxane (anhydrous, 99.8%), 2-(dodecylthiocarbonothioylthio)-2-methylpropionic acid (DTMA) (98%), hydrogen chloride

(HCl) (37%), mineral spirits, tetrabutylammonium bisulfate ( $\geq 99.0\%$ ), tetrahydrofuran (HPLC Grade,  $>99.9\%$ ), *N*-methyl-2-pyrrolidone ( $\geq 99.0\%$ ), sodium hydroxide (NaOH)(pellets, 99-100%), toluene ( $\geq 99.9\%$ ) and NMR solvents (deuterated chloroform ( $\text{CDCl}_3$ ) (99.96% D) and deuterated dimethyl sulphoxide- $\text{d}_6$  (DMSO- $\text{d}_6$ ) (99.96% D)) were purchased from Sigma-Aldrich and were used as received.

## 2.3.2 Synthesis procedures

**2.3.2.1 Synthesis of *S,S'*-bis( $\alpha,\alpha'$ -dimethyl- $\alpha''$ -acetic acid) trithiocarbonate.** A difunctional RAFT agent *S,S'*-bis( $\alpha,\alpha'$ -dimethyl- $\alpha''$ -acetic acid) trithiocarbonate (BDAT) was synthesized using the method of Lai et al<sup>43</sup> and characterized by  $^1\text{H}$  and  $^{13}\text{C}$  NMR.  $\text{CS}_2$  (4.11 g), chloroform (16.12 g), acetone (7.85 g) and tetrabutylammonium bisulfate (0.36 g) were dissolved in mineral spirits (18 mL) in a jacketed reactor and cooled with tap water under  $\text{N}_2$  atmosphere. After full dissolution, 50 wt% aqueous NaOH solution (30.24 g) was added dropwise over the course of 90 minutes to keep the temperature lower than  $25\text{ }^\circ\text{C}$ . After stirring overnight, water (135 mL) was added to dissolve the solid. To acidify the aqueous layer, concentrated HCl (18 mL) was added (*caution: corrosive gas, mercaptan odor!*). The reactor was purged with nitrogen for 30 min under continuous stirring. The solid was filtered and rinsed thoroughly with water. It was dried in a vacuum oven for two days at room temperature. The product was recrystallized from 60% acetone solution and dried in a vacuum oven for two days at room temperature giving yellow powder (1.2 g, 11%). mp:  $165\pm 3\text{ }^\circ\text{C}$  (from 60% acetone, capillary method).  $^1\text{H}$  NMR (400 MHz, DMSO- $\text{d}_6$ ):  $\delta = 1.59$  (12H, s,  $-\text{CH}_3$ ), 12.91 (2H, s,  $-\text{COOH}$ ).  $^{13}\text{C}$  NMR (400 MHz, DMSO- $\text{d}_6$ ):  $\delta = 25.76, 57.25, 176.26, 220.50$ .

**2.3.2.2 Synthesis of PS macro-RAFT agents.** Freshly distilled styrene, BDAT and AIBN were dissolved in 1,4-dioxane by stirring at room temperature. The solution was transferred to a Schlenk ampoule using syringes. After degassing by three successive freeze-pump-thaw cycles using a high vacuum Schlenk line, the solutions were heated to  $70\text{ }^\circ\text{C}$  by using a temperature controlled oil bath. The solution was allowed to polymerize for a certain amount of time. The reaction was stopped by cooling the ampoules in liquid nitrogen. The product was precipitated twice in cold methanol and dried in a vacuum oven at room temperature overnight to yield a white-yellowish powder.  $^1\text{H}$  NMR (400 MHz,  $\text{CDCl}_3$ ):  $\delta = 6.2\text{-}7.1$  (5H, m, Ph), 1.2-2.4 (3H, m,  $-\text{CH}-\text{CH}_2-$ ) (Figure S1).

**2.3.2.3 Synthesis of PS-*b*-PNIPAM-*b*-PS copolymers.** The PS macro-RAFT agent, NIPAM and AIBN were dissolved in 1,4-dioxane. The solution was degassed by three successive freeze-pump-thaw cycles and heated in a temperature controlled oil bath to 70 °C for 18 h. Then the reaction was stopped by cooling the reaction mixture in liquid nitrogen. 1,4-dioxane was removed with a rotary evaporator and dissolved in THF. The block copolymer was precipitated in diethyl ether and cold water, respectively. The precipitant obtained from diethyl ether precipitation was separated by centrifuging with PTFE centrifuge tubes and decantation. The product was separated from the homopolymer PNIPAM by centrifugation (45 min, 5000 rpm) three times. The purified copolymer was freeze-dried. <sup>1</sup>H NMR (400 MHz, CDCl<sub>3</sub>): δ = 6.2-7.1 (5H, m, Ph), 4.0 (1H, s, -NCH-), 0.8-2.5 (3H, m, -CH-CH<sub>2</sub>- for PS and 9H, m, -CH<sub>3</sub>, -CH-CH<sub>2</sub> for PNIPAM) (Figure S2).

**2.3.2.4 Synthesis of PNIPAM macro-RAFT agents.** Both a mono- and a difunctional RAFT agent were used for the synthesis of PNIPAM macro-RAFT agents, i.e. 2-(dodecylthiocarbonothioylthio)-2-methylpropionic acid (DTMA) and the previously synthesized *S,S'*-bis(*a,a'*-dimethyl-*a''*-acetic acid) trithiocarbonate (BDAT), respectively. AIBN, NIPAM and RAFT agent were dissolved in 1,4-dioxane. The solution was transferred to a Schlenk ampoule. After three freeze-pump-thaw cycles, the solution was heated to 70 °C for a certain time. The reaction was stopped by cooling the solution with liquid nitrogen. The solution was precipitated in diethyl ether and reprecipitated three times with cold ether after dissolution using a minimum amount of acetone. The product was dried overnight in a vacuum oven at room temperature. <sup>1</sup>H NMR (400 MHz, CDCl<sub>3</sub>): δ = 4.0 (1H, s, -NCH-), 0.8-2.5 (9H, m, -CH<sub>3</sub>, -CH-CH<sub>2</sub>-), 5.8-7.5 (1H, br, -NH-) (Figure S3).

**2.3.2.5 Synthesis of PS-*b*-PNIPAM block copolymers.** PNIPAM macro-RAFT agent, styrene and AIBN were dissolved in 1,4-dioxane by stirring at room temperature. Styrene was purified by vacuum distillation right before the polymerization. Samples were transferred to ampoules by using syringes. After three successive freeze-pump-thaw cycles, the solutions were heated to 70 °C by using a temperature controlled oil bath. Polymerization was allowed to proceed for 48 hours. Then the reaction was stopped by cooling in liquid nitrogen. 1,4-dioxane was evaporated using a rotary evaporator. The polymer was dissolved in THF and precipitated in cold water several times to remove unreacted PNIPAM macro-RAFT

agent until no homopolymer peak was found in the GPC elugram and precipitated twice from diethyl ether to remove unreacted styrene. The copolymers were dried in a vacuum oven at 35 °C.  $^1\text{H NMR}$  (400 MHz,  $\text{CDCl}_3$ ):  $\delta = 6.2\text{-}7.1$  (5H, m, Ph), 4.0 (1H, s, -NCH-), 0.8-2.5 (3H, m, -CH-CH<sub>2</sub>- for PS and 9H, m, -CH<sub>3</sub>, -CH-CH<sub>2</sub>-for PNIPAM) (Figure S4).

### 2.3.3 Reaction parameters

For RAFT polymerization, the molecular weight (number average molecular weight) ( $\bar{M}_n$ ) can be predicted from Equation 1. This equation is based on the assumptions that (a) the amount of polymer chains grown from the initiator is negligible and (b) the yields which were calculated using gravimetric results correspond to the monomer conversions. We used this equation to calculate the  $[\text{M}]_0/[\text{CTA}]_0$  ratio required for the polymerization to achieve the desired  $\bar{M}_n$ . Here  $[\text{M}]_0$ ,  $[\text{CTA}]_0$ ,  $m_{mon}$  and  $m_{CTA}$  correspond to the initial concentrations of monomer, chain transfer agent and molecular weights of monomer and chain transfer agent, respectively. Conversions are taken as the average gravimetric yields estimated in the previous syntheses. In case of block copolymers, the initial concentration of macro-RAFT agent was used instead of the initial concentration of chain transfer agent, and molecular weight of the macro-RAFT agent was used instead of the molecular weight of chain transfer agent (Equation 2). With the presence of polydispersity index (PDI) values, theoretical PS weight fractions found from Equation 2 and experimental PS weight fractions obtained from NMR analysis were compared to evaluate the control of the polymerization in the block copolymer. The discrepancy between the theoretical and experimental PS fractions can be attributed to material losses during purification processes. Since the calculations are based on the assumption that the yields represent the conversions, the theoretically calculated PS fractions should be taken as close estimates only.

$$\bar{M}_n = m_{CTA} + \frac{[\text{M}]_0}{[\text{CTA}]_0} \times m_{mon} \times \text{conversion} \quad (1)$$

$$\bar{M}_n = \bar{M}_{n,macroRAFT} + \frac{[\text{M}]_0}{[\text{macroRAFT}]_0} \times m_{mon} \times \text{conversion} \quad (2)$$

### 2.3.4 Membrane preparation

A 20 wt% polymer solution, which was prepared from a *N*-methyl-2-pyrrolidone-tetrahydrofuran (NMP-THF) mixture with a volume ratio of 4:6, was poured onto a glass substrate and a thin film of polymer was formed using a manual film applicator with a gate height of 200  $\mu\text{m}$ . After a certain evaporation time, the polymer film was transferred into a non-solvent bath (water). The polymer film was left in this bath for at least four hours. For AFM and SEM analysis a small portion of this film ( $1 \times 1 \text{ cm}$ ) was cut and fixed on a Si wafer with double sided tape and dried in a vacuum oven overnight at 40 °C. For permeability analysis, the membrane film was stored in demineralized water and cut into the desired dimensions just before the measurements.

### 2.3.5 Characterization

$^1\text{H}$  and  $^{13}\text{C}$  nuclear magnetic resonance (NMR) spectroscopy measurements were carried out on a Bruker AMX-400 spectrometer (400 MHz) at room temperature. The ratio between PS and PNIPAM blocks in the BCP was determined by comparing the integral of the aromatic PS protons at 6.2-7.1 ppm (5H, m, Ph) to the lone PNIPAM proton at 4.0 ppm (1H, s, -NCH-).

Gel permeation chromatography (GPC) of PS macro-RAFT agents and their copolymers was run using a set-up consisting of an Agilent Technologies 1200 series gel permeation chromatograph, a PLgel 5  $\mu\text{m}$  Mixed-D column (Mw range 200–400 000 Da, Polymer Laboratories Ltd.) and an Agilent 1200 differential refractometer. The column was calibrated using PS standards. Each polymer sample was injected into the tetrahydrofuran (THF) eluent at 30 °C and a flow rate of 1 mL/min. GPC of PNIPAM macro-RAFT agents and their copolymers was run on a Viscotek GPCmax equipped with 302 TDA model detectors, using a guard column (PSS-GRAM, 10  $\mu\text{m}$ , 5 cm) and two analytical columns (PSS-GRAM-1000/30 Å, 10  $\mu\text{m}$ , 30 cm) at a flow rate of 1 mL/min in dimethyl formamide (containing 0.01 M LiBr) at 50 °C. Poly(methyl methacrylate) standards were used for calibration of the column. Molecular weight and PDI of PNIPAM macro-RAFT agents and PDI of PS-*b*-PNIPAM block copolymers were calculated using Viscotec OmniseC software by using refractive index and light scattering signals, respectively.

For scanning electron microscopy (SEM) measurements, the samples were placed on flat aluminum stubs with double-sided adhesive, conducting carbon tape. Samples were coated with a 10-nm layer of tungsten using a Leica EM SCD 500 sputter-coater. SEM images were recorded on an FEI Magellan 400 field-emission SEM at an acceleration voltage of 2.0 kV. For the SEM of cross-sectional films, samples were fractured in liquid nitrogen and mounted onto 90° SEM stubs with the cross-section facing upwards.

The surface morphology of the films was analyzed with a Bruker Multimode 8 AFM instrument using the Nanoscope V ScanAsyst imaging mode. DNP-10 model non-conductive silicon nitride probes with a spring constant of 0.24 N/m (Bruker) were used. Images were recorded at 1.50 Hz and processed using NanoScope Analysis 1.5 software. At least three different regions on the same film sample were probed to assure that the obtained surface morphology was representative for the entire sample. Before analysis, membrane films were cut into small pieces and fixed on Si wafers of 1 × 1 cm size using double sided tape and dried in vacuum oven at 40 °C overnight.

### 2.3.6 Permeability experiments

Permeabilities of the membranes were studied using a dead-end filtration set-up by measuring the flux of Milli-Q pure water at different pressures (1-3 bar). The membrane was cut into a round shape with a diameter of 2.5 cm, and subsequently placed in an Amicon type filter cell with a volume of 40 mL. The cell was connected to a pressure vessel filled with Milli-Q pure water, where pressure was applied using compressed nitrogen. The cell and the vessel were heated to specific temperatures ranging from 20 °C to 50 °C by placing them inside larger vessels filled with water which were heated using temperature controlled heating plates. To ensure a stable temperature, the cell was stored at a specific temperature for half an hour before the measurements. For all experiments, the membranes were placed on top of a non-woven fabric that acted as an additional mechanical support. Because the non-woven fabric consists of relatively large voids and has a high permeability value ( $\sim 750,000 \text{ L}\cdot\text{m}^{-2}\cdot\text{h}^{-1}\cdot\text{bar}^{-1}$ ), we assumed that it had no influence on the results of the permeability experiments. The permeability ( $\text{L}\cdot\text{m}^{-2}\cdot\text{h}^{-1}\cdot\text{bar}^{-1}$ ) was calculated as the ratio of the flux over the applied pressure as shown in Equation 3, where  $V$  is the permeate volume (L),  $A$  is the membrane area ( $\text{m}^2$ ),  $t$  is the time in hour (h),  $J$  is the permeate flux ( $\text{L}\cdot\text{m}^{-2}\cdot\text{h}^{-1}$ ) and  $\Delta P$  is

the pressure change along the membrane (bar). For the temperatures higher than 20 °C, permeability results were corrected by multiplying the result with the dynamic viscosity of water given at the specified temperature. Error bars of the flux and permeability measurements in Figure 4 and 5 were obtained by using the standard deviations which were calculated from the average permeabilities for five different pressure values.

$$\text{Permeability} = V/(A \cdot t \cdot \Delta P) = J/\Delta P \quad (3)$$

## 2.4 Results and Discussion

---

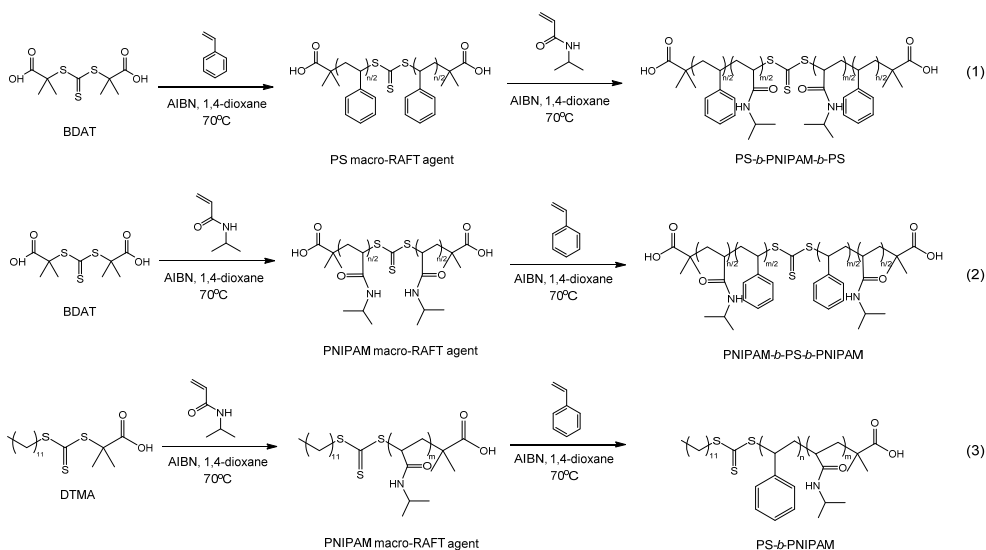
In this study, we optimized the synthesis of PS-PNIPAM BCPs to obtain high molecular weights and PS majority fractions. These features are preferential for membrane fabrication using SNIPS: a high molecular weight will ensure a suitable viscosity for the SNIPS process and both features will provide mechanical stability of the membrane. To obtain the desired polymers we compared two routes: in route 1, a PS macro-RAFT agent was extended with NIPAM and in route 2, a PNIPAM macro-RAFT agent was extended with styrene using two different types of RAFT agent. Thiocarbonyl compounds as RAFT agents can be shown in a generalized structure as Z-C(=S)-S-R where R acts as the leaving group which initiates a new polymer chain and Z is the group responsible for reactivity and radical stability; this group can also be written as SR' for the trithiocarbonate RAFT agents used in our work. The difunctional BDAT and monofunctional DTMA RAFT agents (Scheme 1) were chosen because of their suitable R and Z groups for the polymerization of styrene and NIPAM, as both give a good stability and sufficient reaction rates for each block.<sup>43</sup> Scheme 1 represents the synthesis routes that were used.

### 2.4.1 Synthesis and optimization of homopolymers and copolymers

According to the literature, the optimal route for RAFT polymerization of PS-PNIPAM BCPs using trithiocarbonates is to start with styrene polymerization and extension with NIPAM (reaction (1) in Scheme 1).<sup>34, 44-45</sup> It is reported that the polymerization of styrene from a PNIPAM macro-RAFT agent causes retardation of the styrene polymerization due to slow initiation, slow fragmentation of the intermediate radicals and/or irreversible termi-

nation reactions.<sup>44</sup> Higher PDI values were obtained in case a PNIPAM macro-RAFT agent was used for the PS-PNIPAM copolymer synthesis as compared to the use of a PS macro-RAFT agent when a dithiocarbonate RAFT agent was used.<sup>45</sup> Therefore, our initial choice was to synthesize a PS macro-RAFT agent first and subsequently polymerize NIPAM from this macro-RAFT agent to obtain PS-PNIPAM copolymers as shown in reaction (1) in Scheme 1.

**Scheme 1.** Synthesis routes of the BCPs (1) PS-*b*-PNIPAM-*b*-PS, (2) PNIPAM-*b*-PS-*b*-PNIPAM, and (3) PS-*b*-PNIPAM.



Since we aim for high molecular weight PS-PNIPAM copolymers and large PS volume fractions, the initial monomer concentration ( $[M]_0$ ), the ratio of initial monomer and chain transfer agent concentrations ( $[M]_0/[CTA]_0$ ), consequently molecular weight of PS macro-RAFT agent were increased compared to the previously reported literature on PS-PNIPAM copolymer synthesis.<sup>34</sup> The molecular weight can be as well augmented by increasing the reaction time ( $t$ ), and decreasing the ratio of initial chain transfer agent and initiator concentrations ( $[CTA]_0/[I]_0$ ). Although a decreased  $[CTA]_0/[I]_0$  value improves the rate of polymerization, this parameter also preserves the controlled manner of the polymerization reaction, therefore it should be kept at an optimum value. Since long reaction times and low  $[CTA]_0/[I]_0$  values typically result in high PDI values, a balance for these parameters had to be found to achieve a low PDI, high molecular weights and acceptable yields. This resulted

in a  $[M]_0/[CTA]_0$  ratio of 1915 and a ratio of  $[CTA]_0/[I]_0$  ratio of 10 and a reaction time of 24 h as the optimum values for the desired properties of the PS macro-RAFT agent. Table S1 lists all the synthesized PS macro-RAFT agents. Optimum conditions were reached for PS-9 having  $\bar{M}_n = 92$  kDa, PDI = 1.21 and yield = 16%.

An inherent disadvantage is that since we aim for BCPs with a large PS fraction, the chemical difference between the PS macro-RAFT agent and the copolymer became smaller when the PS fraction was increased. Thus, removal of PS macro-RAFT agent residue by precipitation became more difficult which resulted in a large decrease in the yield, plus theoretical and experimental PS fractions deviated strongly from each other. At the end, no copolymerization reaction took place (See CP-4 in Table 1). Therefore, here the second concomitant disadvantage is the difficulty for the monomers to reach the active center located at the middle of the chain due to hindrance and/or hydrophobicity of the already long active chain which inhibited the copolymerization reaction. It has been observed before by Wong et al that longer macro-RAFT agent chains decrease the reaction rate, resulting in very low reaction yields.<sup>46</sup> Since synthesis route (1) did not result in optimal yields,<sup>42, 43</sup> we switched the order and first synthesized the PNIPAM macro-RAFT agent and extended the polymer with styrene to obtain PS-PNIPAM BCPs which are shown in reactions (2) and (3) in Scheme 1.

Similar as for the PS macro-RAFT agent synthesis, for the PNIPAM macro-RAFT agent synthesis, a higher  $[M]_0$  and a higher  $[M]_0/[CTA]_0$  ratio led to higher molecular weights (Table S2). Extension of the reaction times resulted in higher PDI values due to the possible side reactions, thus four hours of reaction was selected to obtain polymers with both low polydispersity, the desired molecular weights and high yields. Hence, PNIPAM macro-RAFT agents having  $\bar{M}_n = 25-40$  kDa, PDI = 1.03-1.10 were synthesized with 80% yields, which were significantly higher than the yield of PS macro-RAFT agents that was only around 10-20%.

The extension of the PNIPAM macro-RAFT agent with styrene was optimized, using a  $[CTA]_0/[I]_0$  ratio of 10 (Table 1). However, due to slower kinetics of styrene polymerization, higher reaction times of 48 h were necessary, which resulted in acceptable yields with low polydispersity values. In addition, starting with the polymerization of PN-3, we changed

the RAFT agent from the difunctional BDAT (reaction (2) in Scheme 1) to the monofunctional DTMA (reaction (3) in Scheme 1) (Table S2). When DTMA was used as the RAFT agent, we obtained PS-*b*-PNIPAM diblock copolymers, following reaction route (3) in Scheme 1. We found that PDI values of the resulting PS-*b*-PNIPAM copolymers were decreased when DTMA was used (Compare CN-1 (BDAT) with CN-2 (DTMA) in Table 1). Thus, the yield of the polymerization of styrene from PNIPAM macro-RAFT agent was found to be significantly higher than the yields obtained for polymerization of NIPAM with PS macro-RAFT agent with more consistent PDI values of 1.3-1.4 (Table 1). Experimentally determined PS fractions match well with the theoretical PS fractions indicating a well-controlled reaction.

Typical GPC elugrams of the PS and PNIPAM macro-RAFT agents and their copolymers are given in Figure 1. These monomodal GPC curves indicate that there is no evidence of any residual PS and PNIPAM macro-RAFT agents in the copolymers and suggest homo- and block copolymers were synthesized with relatively narrow molecular weight distributions. The peaks were found to be almost symmetrical with a slight tailing in the case of PNIPAM macro-RAFT agents which is probably due to the interaction of the polymers with the column material in GPC. As PS does not interact with the column material, the tailing is less pronounced for the PS macro-RAFT agents. As a conclusion, we found that reaction route (3) is preferred, in case a high molecular weight PS-PNIPAM block copolymer with a high PS volume fraction is desired with high yields and low polydispersities.

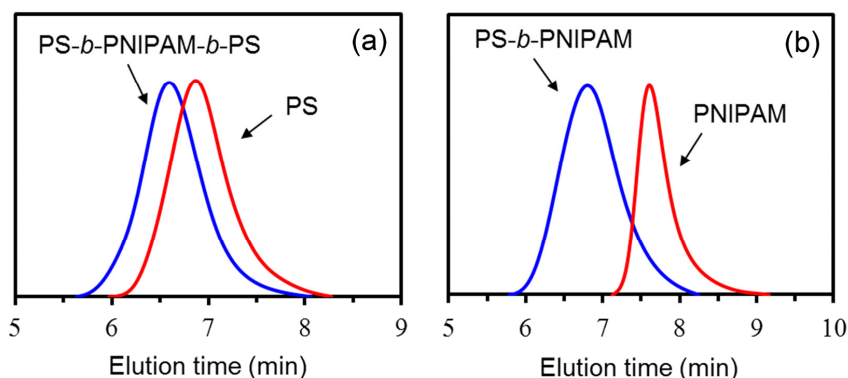


**Figure 1.** GPC elugrams of (a) CP-1 and its homopolymer PS-1, (b) CN-3 and its homopolymer PN-5.

**Table 1.** Synthesis conditions and characterization results of the obtained BCPs.

(Synthesis conditions and characterization results of the macro-RAFT agents are given in Table S1 and S2)

Copolymer	Route given in Scheme 1	Macro-RAFT	$\bar{M}_n$ Macro-RAFT (kDa)	[M] <sub>0</sub> (M)	[M] <sub>0</sub> / [MacroRAFT] <sub>0</sub>	[MacroRAFT] <sub>0</sub> / [I] <sub>0</sub>	$f_{PS}$ (wt%) (theory)	$f_{PS}$ (wt%) (NMR)	$\bar{M}_n$ BCP (kDa) (NMR)	PDI (GPC)	Yield (%)
CP-1	1	PS-1	57	0.68	750	5.8	39	45	127	1.40	30
CP-2	1	PS-1	57	0.68	35	5.8	95	89	64	1.89	13
CP-3	1	PS-8	110	0.32	204	3.5	90	69	159	1.40	1
CP-4	1	PS-9	92	0.28	177	3.5	90	100	-	-	-
CN-1	2	PN-1	41	4.35	1894	7.5	85	85	273	1.44	29
CN-2	3	PN-4	35	4.68	2656	10.0	85	87	269	1.36	18
CN-3	3	PN-5	25	4.35	1917	10.0	85	83	194	1.34	33
CN-4	3	PN-5	25	4.35	914	10.0	75	81	132	1.32	30

## 2.4.2 Membrane fabrication by SNIPS

A high molecular weight PS-PNIPAM block copolymer with high PS volume fraction is required to obtain mechanically stable free-standing membranes. Therefore, CN-3 with a  $\bar{M}_n$  of 194 kDa,  $f_{PS}$  of 83 wt% and PDI of 1.34 was selected as the most suitable block copolymer for membrane production.

A successful SNIPS process is dependent on many parameters such as block copolymer type, block length, molecular weight, polymer concentration, type of solvent/ solvent mixtures, type of non-solvent, evaporation time, temperature of polymer solution and non-solvent bath and solvent content in non-solvent bath.<sup>22</sup> The type of solvent is one of the most important parameters for SNIPS, due to the significant effects on the final material properties. *N*-methyl-2-pyrrolidone (NMP) is one of the most commonly used solvents in commercial phase inversion membrane production.<sup>47-48</sup> THF is also frequently used for the preparation of block copolymer membranes, due to its high volatility, and its ability to create ordered morphologies.<sup>11, 17-18, 20, 37, 49-51</sup> For example, for the PS-*b*-P4VP system, it is well-known that THF plays an important role in the pore formation.<sup>22</sup> Therefore, to produce the membranes we applied a solvent combination of both water miscible NMP and THF, with a volume ratio of 4:6, and water as the non-solvent.

Comparing the  $\chi$  interaction parameters of the blocks and solvents, which were calculated using Hansen solubility parameters, indicates that NMP is a PS selective and THF is a PNIPAM selective solvent (Table 2). (Details on the calculation of  $\chi$  parameters can be found in the Appendix.) According to the vapor pressure values of the solvents given in Table 2, THF will evaporate faster than NMP from the cast polymer film. For an NMP: THF volume ratio of 4:6, increasing the evaporation time will result in evaporation of more THF which consequently results in a more viscous and more PS selective solvent system. During evaporation, a PS matrix is formed and due to poor affinity of PS with water, PS precipitates when the viscous polymer film is transferred to the non-solvent.<sup>52</sup>

AFM images in Figure 2 show the morphology changes of the membrane film as a function of evaporation time. For the evaporation times of 0 and 10 seconds, the polymer solution still contained a high amount of solvent. When the film was transferred to the non-solvent bath, the remaining solvent in the cast film was exchanged with water resulting in an open

porous structure with a small number of worm-like cylinders and possibly spherical micelles underneath them.

**Table 2.** Calculated  $\chi$  parameters of the blocks and solvents and vapor pressure of the solvents

		THF	NMP
$\chi$ parameters	PS	0.78	0.92
	PNIPAM	0.46	1.35
Vapor pressure at 25 °C (kPa)		21.6	0.04

As the evaporation time was extended to 15-30 seconds, the viscosity of the polymer solution increased, the cylinders got closer, fused together and formed branched worm-like structures. Plus, the roughness of the films started to decrease. For even longer evaporation times (50-80 seconds), the distances between the worm-like cylinders became even smaller, and a compact structure with nanopores was obtained consistent with the evaporation time-dependent SNIPS results reported by Phillip *et al.*<sup>18</sup> Films prepared with long evaporation times exhibited a smoother surface than the films prepared with shorter evaporation times. In addition, more opaque films were obtained for shorter evaporation times and films became more transparent when the evaporation time was increased. This difference in transparency of the films may be due to differences in pore sizes. When the size of the pores is larger than the wavelength of visible light (380-700 nm), films appear white due to light scattering and as they are lower than the wavelengths of visible light, films appear more transparent.<sup>53</sup>

Figure 3a shows an SEM image of the membrane surface prepared using an evaporation time of 80 seconds. The image clearly indicates that a nanoporous surface is obtained. The SEM image of the cross-section of the membrane in Figure 3b demonstrates that similar worm-like cylinder characteristics and interconnected nanopores are present throughout the total thickness of the film.

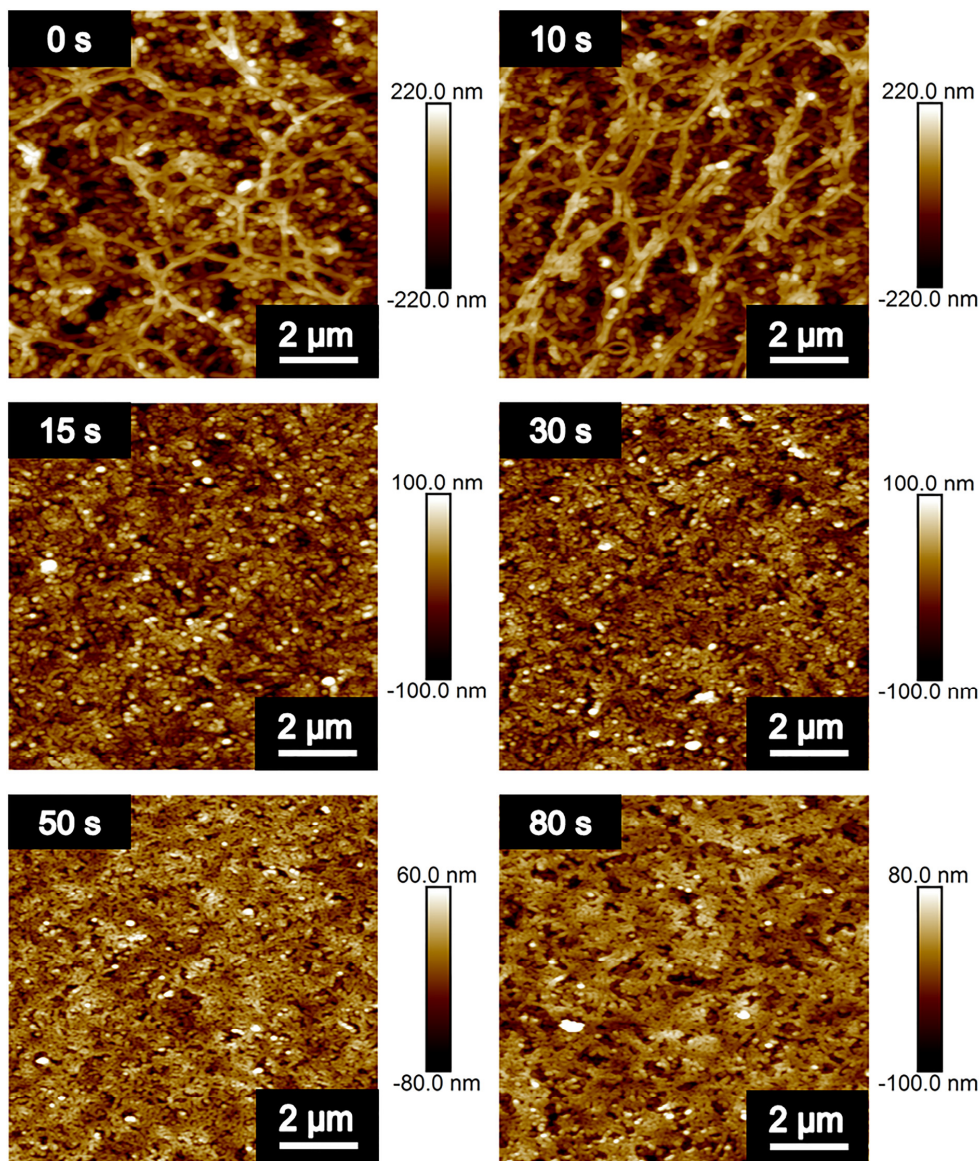
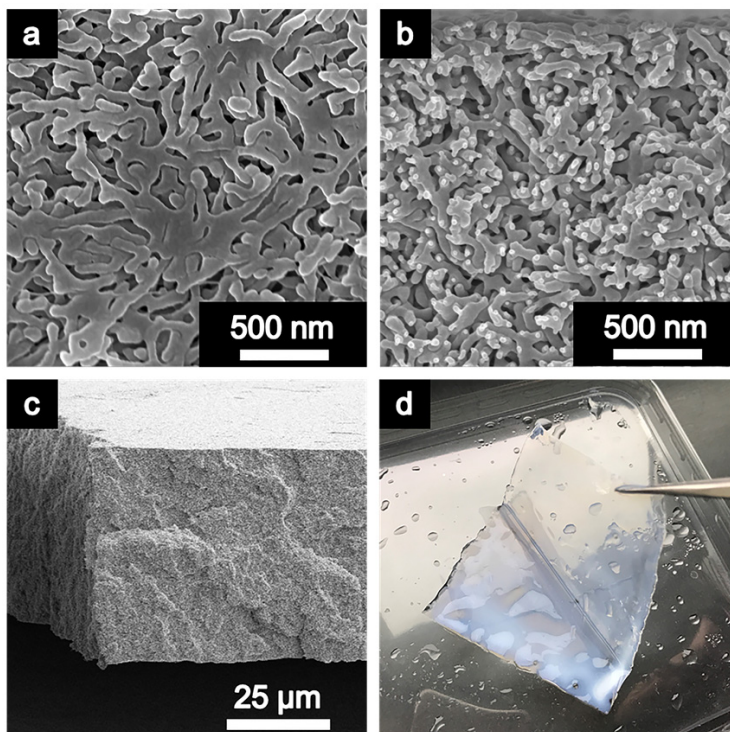


Figure 2. AFM images showing the effect of evaporation time on the membrane morphology.

These similar characteristics may be due to the long evaporation time of 80 seconds causing a large amount of solvent evaporation in the polymer solution. Therefore, the self-assembly of the BCPs also took place throughout the film to form cylindrical micelles with interconnected nanopores. The total film thickness was found to be  $50\ \mu\text{m}$  ( $\pm 5\ \mu\text{m}$ ) (Figure 3c) and the membrane was free-standing with a transparent appearance (Figure 3d).



**Figure 3.** SEM images of the membrane prepared using 80 s of evaporation time (a) the surface of the membrane, (b) the cross-section of the membrane (c) a 3D view of the membrane and (d) appearance of the membrane.

### 2.4.3 Permeability measurements

In order to investigate the thermo-responsive properties of the membrane, we first studied membrane permeability at two different temperatures, one below (at 20 °C) and one above (at 50 °C) the LCST of PNIPAM (32 °C). The water flux through a membrane is determined by the applied pressure and the membrane permeability. However, for a true comparison of the membrane permeability or pressure normalized flux for different temperatures, the permeability also needs to be normalized for the temperature-dependent changes in viscosity of the water passing through the membrane at an elevated temperature. This is analogue to the established methods of membrane resistance calculations.<sup>54</sup> Therefore, we argue that this correction is required in order to properly analyze the changes of the membrane alone. To eliminate the effect of a decreased water viscosity at 50 °C on the flux values, viscosity corrected flux values were obtained by multiplying the dynamic viscosity of

water at 50 °C with the flux values. Figure 4a shows the change in flux values at 20 °C, flux values which are viscosity corrected at 50 °C and uncorrected at 50 °C as a function of pressure. A linear flux increase is expected for all membrane systems when the pressure increases. This linear relation between flux and pressure for both temperatures demonstrates the mechanical stability of the membrane, as compaction or rupture of the membrane would have led to strong deviations from linearity. The slope of the line for viscosity corrected flux values at 50 °C was still considerably bigger than the slope at 20 °C which clearly demonstrates the thermo-responsive character of the membrane.

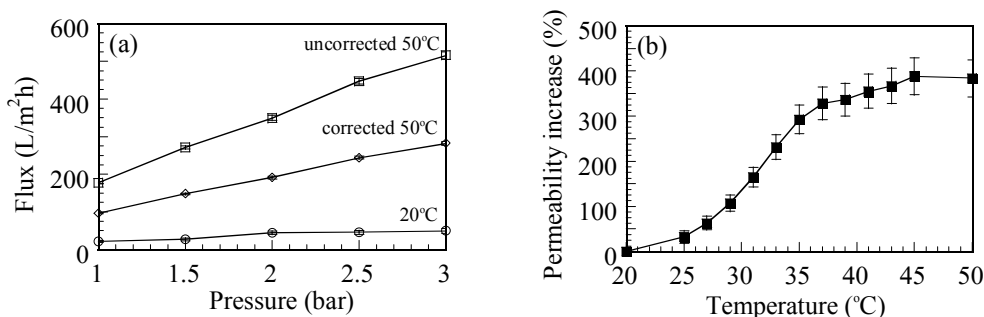


**Figure 4. (a) Flux measurements of the membrane at 20 and 50 °C as a function of pressure. Curves with circles, triangles and squares correspond to the flux values at 20 °C, viscosity corrected at 50 °C and uncorrected at 50 °C, respectively. (b) Increase in permeability as a function of temperature at 1 bar.**

We also studied the permeability increase at several temperatures between 20 °C and 50 °C at a pressure change of 1 bar as shown in Figure 4b. Here, only viscosity corrected permeability values are indicated. The transition mainly occurred between 26 °C and 38 °C, with the steepest permeability increase around the LCST of PNIPAM. These results demonstrate that the thermo-responsive behavior of the membrane is a result of the collapsing PNIPAM chains at the LCST of the polymer. This behavior also suggests that the pores of the membrane were coated with PNIPAM domains.<sup>18</sup>

Reversibility of the membranes was tested by measuring the permeability for several temperature cycles (i.e. switching between 20 and 50 °C) (Figure 5). Here, similarly as shown in Figure 4a, both viscosity corrected and uncorrected permeability values show that the

thermo-responsive behavior is an outcome of the chain collapse of PNIPAM above its LCST. Identical permeability values were obtained for each temperature cycle demonstrating that the thermo-responsive property of the membrane is fully reversible.

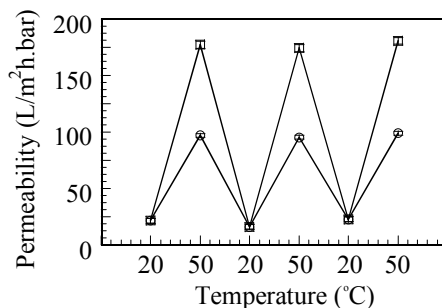


Figure 5. Reversibility of thermo-responsive behavior of the membrane showing both viscosity corrected (circles) and uncorrected (squares) permeability values.

## 2.5 Conclusions

---

Well-defined high molecular weight PS-PNIPAM BCPs with large PS volume fractions were successfully synthesized. The optimal route to obtain this copolymer is by synthesizing a PNIPAM macro-RAFT agent first and extending the chain with styrene. SNIPS method was used for the first time to produce free-standing nanoporous membranes from PS-*b*-PNIPAM copolymers. The membranes had a worm-like cylindrical morphology with nano-sized pores, and showed thermo-responsive behavior and the thermo-responsive behavior was fully reversible. To the best of our knowledge, the production of a fully reversible thermo-responsive block copolymer SNIPS membrane has not been reported before. Membranes with fully reversible thermo-responsive character offers prospects for further development of advanced easy-to-clean membrane applications.

## Acknowledgements

---

Electron microscopy work was performed at the Wageningen Electron Microscopy Centre (WEMC) of Wageningen University.

## References

---

1. Ulbricht, M., Advanced functional polymer membranes. *Polymer* **2006**, *47* (7), 2217-2262.
2. Yang, Q.; Himstedt, H. H.; Ulbricht, M.; Qian, X.; Ranil Wickramasinghe, S., Designing magnetic field responsive nanofiltration membranes. *Journal of Membrane Science* **2013**, *430*, 70-78.
3. Clodt, J. I.; Filiz, V.; Rangou, S.; Buhr, K.; Abetz, C.; Höche, D.; Hahn, J.; Jung, A.; Abetz, V., Double Stimuli-Responsive Isoporous Membranes via Post-Modification of pH-Sensitive Self-Assembled Diblock Copolymer Membranes. *Adv. Funct. Mater.* **2013**, *23* (6), 731-738.
4. Pan, K.; Zhang, X.; Ren, R.; Cao, B., Double stimuli-responsive membranes grafted with block copolymer by ATRP method. *Journal of Membrane Science* **2010**, *356* (1-2), 133-137.
5. Schacher, F.; Rudolph, T.; Wieberger, F.; Ulbricht, M.; Müller, A. H. E., Double Stimuli-Responsive Ultrafiltration Membranes from Polystyrene-block-poly(N,N-dimethylaminoethyl methacrylate) Diblock Copolymers. *ACS Applied Materials & Interfaces* **2009**, *1* (7), 1492-1503.
6. Vriezেকolk, E. J.; Nijmeijer, K.; de Vos, W. M., Dry-wet phase inversion block copolymer membranes with a minimum evaporation step from NMP/THF mixtures. *Journal of Membrane Science* **2016**, *504*, 230-239.
7. Wang, Z.; Wang, Y., Highly Permeable and Robust Responsive Nanoporous Membranes by Selective Swelling of Triblock Terpolymers with a Rubbery Block. *Macromolecules* **2016**, *49* (1), 182-191.
8. Hörenz, C.; Pietsch, C.; Goldmann, A. S.; Barner-Kowollik, C.; Schacher, F. H., Phase Inversion Membranes from Amphiphilic Diblock Terpolymers. *Adv. Mater. Interfaces* **2015**, *2* (8), n/a-n/a.
9. Mondal, S.; Wickramasinghe, S. R., Photo-induced graft polymerization of N-isopropyl acrylamide on thin film composite membrane: Produced water treatment and antifouling properties. *Separation and Purification Technology* **2012**, *90*, 231-238.
10. Himstedt, H. H.; Marshall, K. M.; Wickramasinghe, S. R., pH-responsive nanofiltration membranes by surface modification. *Journal of Membrane Science* **2011**, *366* (1-2), 373-381.
11. Schacher, F.; Ulbricht, M.; Müller, A. H. E., Self-Supporting, Double Stimuli-Responsive Porous Membranes From Polystyrene-block-poly(N,N-dimethylaminoethyl methacrylate) Diblock Copolymers. *Adv. Funct. Mater.* **2009**, *19* (7), 1040-1045.
12. Chen, Y.-C.; Xie, R.; Chu, L.-Y., Stimuli-responsive gating membranes responding to temperature, pH, salt concentration and anion species. *Journal of Membrane Science* **2013**, *442*, 206-215.
13. Tokarev, I.; Minko, S., Stimuli-responsive hydrogel thin films. *Soft Matter* **2009**, *5* (3), 511-524.
14. Wandera, D.; Wickramasinghe, S. R.; Husson, S. M., Stimuli-responsive membranes. *Journal of Membrane Science* **2010**, *357* (1-2), 6-35.
15. Chen, X.; Shi, C.; Wang, Z.; He, Y.; Bi, S.; Feng, X.; Chen, L., Structure and performance of poly(vinylidene fluoride) membrane with temperature-sensitive poly(n-isopropylacrylamide) homopolymers in membrane pores. *Polym Compos* **2013**, *34* (4), 457-467.
16. Nunes, S. P.; Behzad, A. R.; Hooghan, B.; Sougrat, R.; Karunakaran, M.; Pradeep, N.; Vainio, U.; Peinemann, K.-V., Switchable pH-Responsive Polymeric Membranes Prepared via Block Copolymer Micelle Assembly. *ACS Nano* **2011**, *5* (5), 3516-3522.
17. Gu, Y.; Wiesner, U., Tailoring Pore Size of Graded Mesoporous Block Copolymer Membranes: Moving from Ultrafiltration toward Nanofiltration. *Macromolecules* **2015**, *48* (17), 6153-6159.

18. Phillip, W. A.; Mika Dorin, R.; Werner, J. r.; Hoek, E. M. V.; Wiesner, U.; Elimelech, M., Tuning Structure and Properties of Graded Triblock Terpolymer-Based Mesoporous and Hybrid Films. *Nano Letters* **2011**, *11* (7), 2892-2900.
19. Nunes, S. P.; Sougrat, R.; Hooghan, B.; Anjum, D. H.; Behzad, A. R.; Zhao, L.; Pradeep, N.; Pinnau, I.; Vainio, U.; Peinemann, K.-V., Ultraporous Films with Uniform Nanochannels by Block Copolymer Micelles Assembly. *Macromolecules* **2010**, *43* (19), 8079-8085.
20. Tripathi, B. P.; Dubey, N. C.; Choudhury, S.; Simon, F.; Stamm, M., Antifouling and antibiofouling pH responsive block copolymer based membranes by selective surface modification. *Journal of Materials Chemistry B* **2013**, *1* (27), 3397-3409.
21. Yu, S.; Chen, Z.; Liu, J.; Yao, G.; Liu, M.; Gao, C., Intensified cleaning of organic-fouled reverse osmosis membranes by thermo-responsive polymer (TRP). *Journal of Membrane Science* **2012**, *392-393*, 181-191.
22. Peinemann, K.-V.; Abetz, V.; Simon, P. F. W., Asymmetric superstructure formed in a block copolymer via phase separation. *Nat Mater* **2007**, *6* (12), 5.
23. Nunes, S. P., Block Copolymer Membranes for Aqueous Solution Applications. *Macromolecules (Washington, DC, U. S.)* **2016**, *49* (8), 2905-2916.
24. Phillip, W. A.; Hillmyer, M. A.; Cussler, E. L., Cylinder Orientation Mechanism in Block Copolymer Thin Films Upon Solvent Evaporation. *Macromolecules* **2010**, *43* (18), 7763-7770.
25. Li, L.; Schulte, L.; Clausen, L. D.; Hansen, K. M.; Jonsson, G. E.; Ndoni, S., Gyroid Nanoporous Membranes with Tunable Permeability. *ACS Nano* **2011**, *5* (10), 7754-7766.
26. Dorin, R. M.; Sai, H.; Wiesner, U., Hierarchically Porous Materials from Block Copolymers. *Chemistry of Materials* **2014**, *26* (1), 339-347.
27. Ahn, H.; Park, S.; Kim, S.-W.; Yoo, P. J.; Ryu, D. Y.; Russell, T. P., Nanoporous block copolymer membranes for ultrafiltration: a simple approach to size tunability. *ACS nano* **2014**, *8* (11), 11745-52.
28. Hillmyer, M. A., Nanoporous Materials from Block Copolymer Precursors. In *Block Copolymers II*, Abetz, V., Ed. Springer Berlin Heidelberg: Berlin, Heidelberg, 2005; pp 137-181.
29. Jackson, E. A.; Hillmyer, M. A., Nanoporous Membranes Derived from Block Copolymers: From Drug Delivery to Water Filtration. *ACS Nano* **2010**, *4* (7), 3548-3553.
30. Zhang, Y.; Sargent, J. L.; Boudouris, B. W.; Phillip, W. A., Nanoporous membranes generated from self-assembled block polymer precursors: Quo Vadis? *J. Appl. Polym. Sci.* **2015**, *132* (21), n/a-n/a.
31. Zalusky, A. S.; Olayo-Valles, R.; Wolf, J. H.; Hillmyer, M. A., Ordered Nanoporous Polymers from Polystyrene-Polylactide Block Copolymers. *Journal of the American Chemical Society* **2002**, *124* (43), 12761-12773.
32. Park, C.; Yoon, J.; Thomas, E. L., Enabling nanotechnology with self assembled block copolymer patterns. *Polymer* **2003**, *44* (22), 6725-6760.
33. Kim, J. K.; Yang, S. Y.; Lee, Y.; Kim, Y., Functional nanomaterials based on block copolymer self-assembly. *Progress in Polymer Science* **2010**, *35* (11), 1325-1349.
34. Nykänen, A.; Nuopponen, M.; Laukkanen, A.; Hirvonen, S.-P.; Rytelä, M.; Turunen, O.; Tenhu, H.; Mezzenga, R.; Ikkala, O.; Ruokolainen, J., Phase Behavior and Temperature-Responsive Molecular Filters Based on Self-Assembly of Polystyrene-block-poly(N-isopropylacrylamide)-block-polystyrene. *Macromolecules* **2007**, *40* (16), 5827-5834.
35. Tang, Y.; Ito, K.; Hong, L.; Ishizone, T.; Yokoyama, H., Tunable Thermoresponsive Mesoporous Block Copolymer Membranes. *Macromolecules* **2016**, *49* (20), 7886-7896.
36. Scott, K., *Handbook of Industrial Membranes*. Elsevier: Oxford, UK, 1995.

37. Qiu, X.; Yu, H.; Karunakaran, M.; Pradeep, N.; Nunes, S. P.; Peinemann, K.-V., Selective Separation of Similarly Sized Proteins with Tunable Nanoporous Block Copolymer Membranes. *ACS Nano* **2013**, *7* (1), 768-776.
38. Yi, Z.; Zhang, P.-B.; Liu, C.-J.; Zhu, L.-P., Symmetrical Permeable Membranes Consisting of Overlapped Block Copolymer Cylindrical Micelles for Nanoparticle Size Fractionation. *Macromolecules* **2016**, *49* (9), 3343-3351.
39. Gallei, M.; Rangou, S.; Filiz, V.; Buhr, K.; Bolmer, S.; Abetz, C.; Abetz, V., The Influence of Magnesium Acetate on the Structure Formation of Polystyrene-block-poly(4-vinylpyridine)-Based Integral-Asymmetric Membranes. *Macromolecular Chemistry and Physics* **2013**, *214* (9), 1037-1046.
40. Chiefari, J.; Chong, Y. K.; Ercole, F.; Krstina, J.; Jeffery, J.; Le, T. P. T.; Mayadunne, R. T. A.; Meijs, G. F.; Moad, C. L.; Moad, G.; Rizzardo, E.; Thang, S. H., Living Free-Radical Polymerization by Reversible Addition-Fragmentation Chain Transfer: The RAFT Process. *Macromolecules* **1998**, *31* (16), 5559-5562.
41. Rademacher, J. T.; Baum, M.; Pallack, M. E.; Brittain, W. J.; Simonsick, W. J., Atom Transfer Radical Polymerization of N,N-Dimethylacrylamide. *Macromolecules* **2000**, *33* (2), 284-288.
42. A. Dieter Schlüter, C. H., Junji Sakamoto, *Synthesis of Polymers: New Structures and Methods*. Wiley-VCH: Weinheim, 2012.
43. Lai, J. T.; Filla, D.; Shea, R., Functional Polymers from Novel Carboxyl-Terminated Trithiocarbonates as Highly Efficient RAFT Agents. *Macromolecules* **2002**, *35* (18), 6754-6756.
44. Bivigou-Koumba, A. M.; Kristen, J.; Laschewsky, A.; Müller-Buschbaum, P.; Papadakis, C. M., Synthesis of Symmetrical Triblock Copolymers of Styrene and N-isopropylacrylamide Using Bifunctional Bis(trithiocarbonate)s as RAFT Agents. *Macromolecular Chemistry and Physics* **2009**, *210* (7), 565-578.
45. Licea-Claverie, A. V.-R. a. A., Controlled Synthesis of Block Copolymers Containing N-isopropylacrylamide by Reversible Addition-Fragmentation Chain-Transfer (RAFT) Polymerization. *Journal of the Mexican Chemical Society* **2011**, *55* (1), 21-32.
46. Wong, K. H.; Davis, T. P.; Barner-Kowollik, C.; Stenzel, M. H., Honeycomb structured porous films from amphiphilic block copolymers prepared via RAFT polymerization. *Polymer* **2007**, *48* (17), 4950-4965.
47. Kneifel, K.; Peinemann, K. V., Preparation of hollow fiber membranes from polyetherimide for gas separation. *Journal of Membrane Science* **1992**, *65* (3), 295-307.
48. Sadrzadeh, M.; Bhattacharjee, S., Rational design of phase inversion membranes by tailoring thermodynamics and kinetics of casting solution using polymer additives. *Journal of Membrane Science* **2013**, *441*, 31-44.
49. Rangou, S.; Buhr, K.; Filiz, V.; Clodt, J. I.; Lademann, B.; Hahn, J.; Jung, A.; Abetz, V., Self-organized isoporous membranes with tailored pore sizes. *Journal of Membrane Science* **2014**, *451* (0), 266-275.
50. Vriezokolk, E. J.; Nijmeijer, K.; de Vos, W. M., Dry-wet phase inversion block copolymer membranes with a minimum evaporation step from NMP/THF mixtures. *Journal of Membrane Science* **2016**, *504*, 230-239.
51. Cetintas, M.; Kamperman, M., Self-assembly of PS-b-PNIPAM-b-PS block copolymer thin films via selective solvent annealing. *Polymer* **2016**, *107*, 387-397.
52. Abetz, V., Isoporous Block Copolymer Membranes. *Macromol. Rapid Commun.* **2015**, *36* (1), 10-22.
53. Schärfl, W., *Light Scattering from Polymer Solutions and Nanoparticle Dispersions*. Springer-Verlag: Berlin Heidelberg, 2007.

## Chapter 2

54. Mulder, M., *Basic Principles of Membrane Technology*. Kluwer Academic Publishers: Dordrecht, The Netherlands, 2004.

## APPENDIX

**Table S1.** Synthesis conditions and characterization results for PS macro-RAFT agents.

PS	CTA	[M] <sub>0</sub> (M)	[M] <sub>0</sub> /[CTA] <sub>0</sub>	[CTA] <sub>0</sub> /[I] <sub>0</sub>	<i>t</i> (h)	$\bar{M}_n$ (kDa) GPC	PDI GPC	Yield (%)
PS-1	BDAT	2.20	3142	0.875	48	57	1.42	23
PS-2	BDAT	2.60	2500	10.1	72	124	1.35	11
PS-3	BDAT	4.80	1915	3.5	24	87	1.30	13
PS-4	BDAT	6.40	1915	3.5	24	101	1.28	15
PS-5	BDAT	6.40	2867	7	24	162	1.28	15
PS-6	BDAT	6.40	2867	10	24	165	1.26	11
PS-7	BDAT	6.40	1915	10	24	110	1.26	15
PS-8	BDAT	7.78	1915	10	24	110	1.22	20
PS-9	BDAT	8.04	1915	10	24	92	1.21	16
PS-10	BDAT	Bulk	1915	10	24	45	1.27	4

**Table S2.** Synthesis conditions and characterization results for PNIPAM macro-RAFT agents.

PNIPAM	CTA	$[M]_0$	$[M]_0/[CTA]_0$	$[CTA]_0/[I]_0$	$t$ (h)	$\bar{M}_n$ (kDa) GPC	PDI GPC	Yield (%)
PN-1	BDAT	1.77	260	5	48	41	1.15	82
PN-2	BDAT	1.18	216	10	24	33	1.13	83
PN-3	DTMA	1.77	216	10	4	41	1.04	84
PN-4	DTMA	1.18	162	10	3	35	1.03	77
PN-5	DTMA	1.18	145	10	4	25	1.10	81

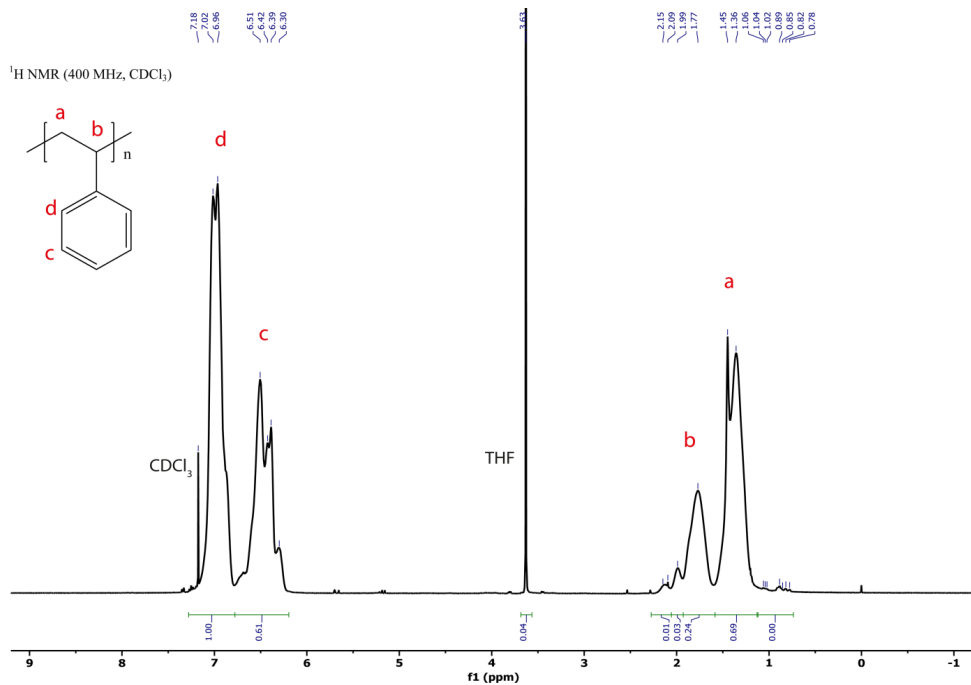


**Figure S1.** <sup>1</sup>H-NMR spectrum of PS macro-RAFT agent (PS-1).

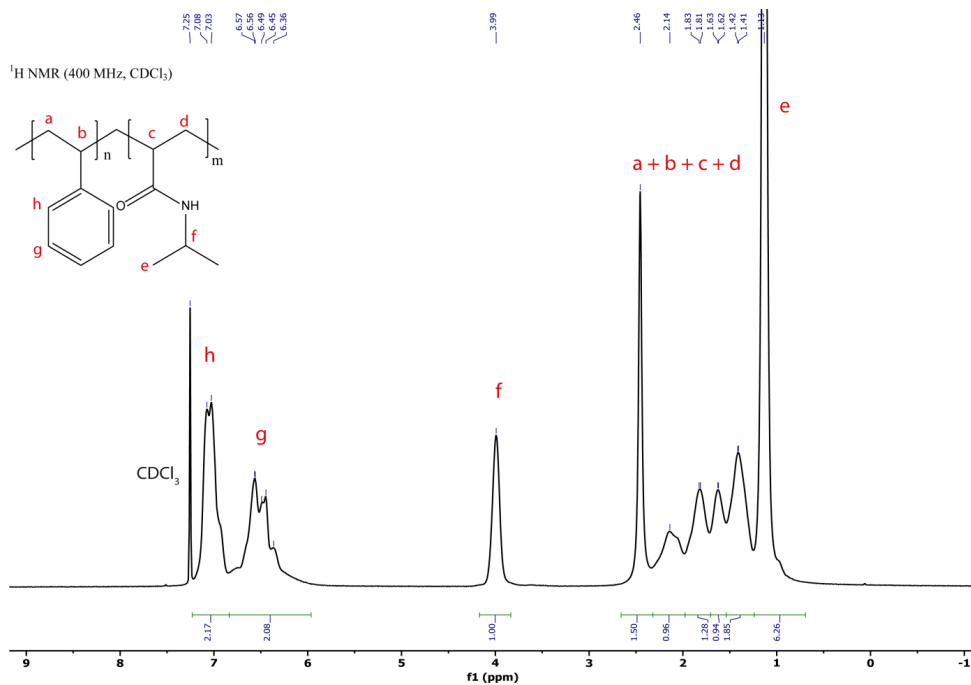


**Figure S2.** <sup>1</sup>H-NMR spectrum of PS-*b*-PNIPAM-*b*-PS copolymer (CP-1).

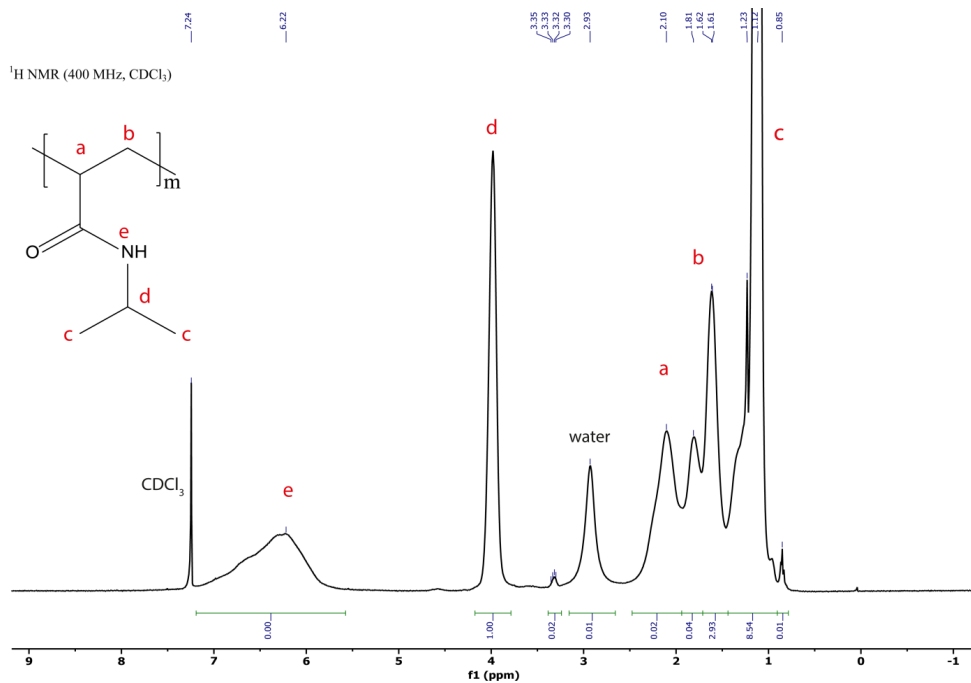


Figure S3. <sup>1</sup>H-NMR spectrum of PNIPAM macro-RAFT agent (PN-5).

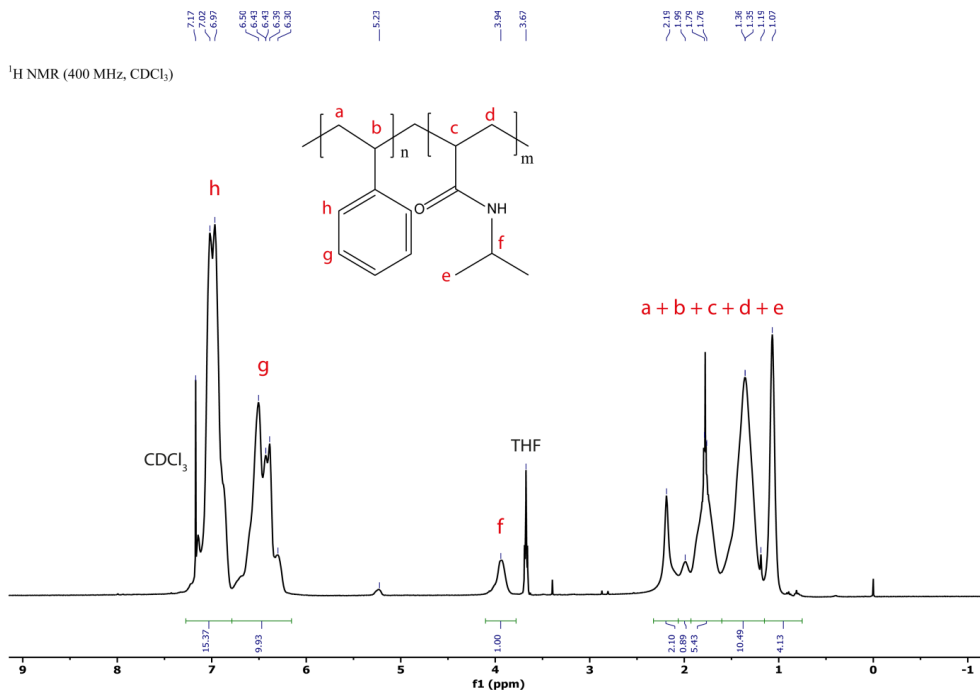


Figure S4. <sup>1</sup>H-NMR spectrum of PS-*b*-PNIPAM copolymer (CN-3).

## Calculation of Hansen solubility parameters

To compare the selectivity of the used solvents for the blocks of the copolymer, we calculated the Flory interaction parameters ( $\chi$ ) using Hansen solubility parameters.  $\chi$  parameters were calculated using Equation A1 and A2.<sup>1</sup>

$$A_{1,2} = [(\delta_{D2} - \delta_{D1})^2 + 0.25(\delta_{P2} - \delta_{P1})^2 + 0.25(\delta_{H2} - \delta_{H1})^2] \quad (\text{A1})$$

In Equation A1;  $\delta_D$ ,  $\delta_P$  and  $\delta_H$  are Hansen solubility parameters for dispersive, polar and hydrogen bonding contributions of the two blocks of the BCP, respectively.<sup>1, 2</sup> Subscript 1 stands for the solvent and 2 for the polymer block.

$$\chi_{12} = VA_{1,2}/RT \quad (\text{A2})$$

In Equation A2;  $V$ ,  $R$  and  $T$  correspond to the molar volume of the solvent, the ideal gas constant and the absolute temperature, respectively. Although some of the calculated  $\chi$  values were significantly higher than experimental values reported in the literature, for our experiments it was sufficient to compare the selectivity of the solvents between the blocks.

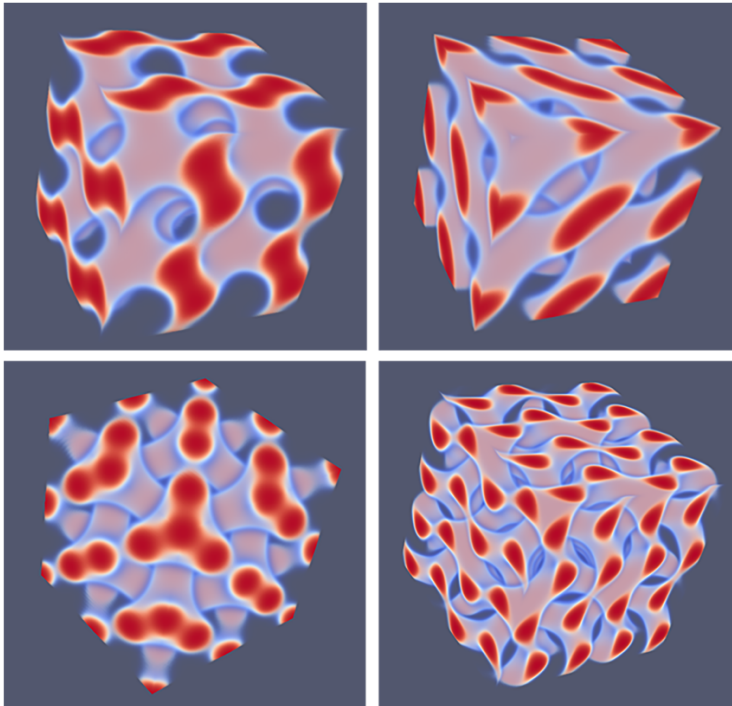
## References

1. Hansen, C. M., *Hansen Solubility Parameters: A User's Handbook*. CRC Press: U.S.A, 2000.
2. Ahmad, H. Solubility Parameter of Acrylamide Series Polymers through Its Components and Group Contribution Technique. *Journal of Macromolecular Science: Part A - Chemistry* **1982**, 17 (4), 585-600 DOI: 10.1080/00222338208062410.



# CHAPTER 3

## Microphase segregation of diblock copolymers studied by the self-consistent field theory of Scheutjens and Fleer



---

In preparation:

Cetintas M.; Kamperman, M.; Leermakers F.A.M., Microphase segregation of diblock copolymers studied by the self-consistent field theory of Scheutjens and Fleer.

### 3.1 Abstract

---

We have used the self-consistent field formalism of Scheutjens and Fleer (SF-SCF) to complement existing theoretical investigations on the phase behavior of block copolymer melts. In this paper, we discuss how the phase diagram depends on the molecular weight of the polymer in the critical region and we focus on the transition region from the hexagonal to lamellar phase at intermediate segregation  $\chi N = 30$  as well as strong segregation  $\chi N = 120$  (here  $\chi$  is the Flory-Huggins interaction parameter and  $N$  is the chain length). The lattice based SF-SCF method includes non-local contributions to the segment potentials and therefore is expected to predict finite chain length effects better than traditional methods. Implementing the freely jointed chain model, we solve the self-consistent field equations with an unbiased Hessian-free optimization scheme which relies on an initial guess and appropriate boundary conditions for its convergence to a particular segregation state. In accordance to the literature, the corrections on the well-known infinite chain length limits for features of the phase diagram (e.g. critical point) are of order  $1/N$ . In the critical regions, we report the scaling behavior of the free energy density and the density differences between the domains as a function of  $\Delta\chi = \chi - \chi^{cr}$ . The characteristic spacing  $D$  of the lamellar phase is found to accurately follow  $D = \frac{4}{3}\sqrt{N}$  at the critical conditions and therefore, for finite chain lengths, the widths of the interfaces remain finite at the critical point. We present SF-SCF predictions for the single gyroid (SG), double gyroid (DG) phases and hexagonally perforated lamellar (HPL) phase, in the region where the hexagonal phase (HEX) and lamellar (LAM) ones compete. The HPL phase consists of strongly curved layers with a hexagonal ordering of holes. At the location of a hole the two adjoining lamellae bend towards it so that the average distance between lamellae remains (close to) homogeneous. Interestingly, the HPL phase is related to the double diamond (DD) phase: when in HPL the two adjoining lamellae would merge inside a pore of a central one, the HPL transforms smoothly into DD. At  $\chi N = 30$  and  $N = 300$  we found SG, DD and HPL phases to be metastable with respect to either the lamellar or hexagonal phases. In accordance to the literature the DG was found to be stable in a narrow region of the asymmetry ratio  $f$  in the block copolymers. We present the structural evolution of the metastable HPL phase with  $f$  and this gives insight in how a system can migrate (e.g. upon addition of a selective solvent) from one microphase topology to the other. In contrast to latest literature predictions, at strong segregation ( $\chi N = 120$ ) we were unable to find any stable triply periodic phase: for chains with  $N = 300$  at such strong segregation also the DG phase is metastable with respect to the HEX or LAM phases.

---

## 3.2 Introduction

---

Typically, when two chemically different polymers with a small but positive interaction parameter  $\chi$  are mixed, when time permitted, they will demix into two macroscopic phases of which one is rich in one polymer and depleted in the other while the other phase obtains the opposite composition.<sup>1</sup> The phase diagram is characterized by a critical volume fraction and a critical interaction parameter. When the two polymers are equally long (each composed of  $N$  segments) the critical volume fraction is, for symmetry reasons,  $\varphi^{cr} = 0.5$ , while the critical interaction parameter decreases with the chain length as  $\chi^{cr} = \frac{2}{N}$ . In the critical region, one finds power-law behavior of the interfacial tension  $\gamma \propto (\Delta\chi)^\alpha = (\chi - \chi^{cr})^\alpha$ , the density difference between the phases  $\Delta\varphi \propto (\Delta\chi)^\beta$  and width of the interface  $W = (\Delta\chi)^\delta$ . The first two tend to go to zero (both  $\alpha$  and  $\beta$  are larger than zero), whereas the latter quantity diverges ( $\delta < 0$ ), upon an approach towards the critical point. In the mean field theory,  $\alpha = 3/2$ ,  $\beta = 1/2$ , and  $\delta = -1/2$ .<sup>2-3</sup>

When the two polymers are combined into a block copolymer, the tendency to demix is still present, but macrophase segregation is impossible. Instead, microphase segregation occurs. There are domains rich in one segment type and depleted in the other, while the other domains develop with opposite composition. Again, a phase diagram may be found which separates a homogeneous from a microphase segregated state. The lowest possible interaction parameter for which segregation is possible, occurs for the case that the two blocks are equally long ( $f = 0.5$ ), and again the critical interaction parameter decreases with overall chain length roughly as  $\chi^{cr} = \frac{10.5}{N}$ . In the critical region, we again should expect power-law dependences, e.g. for the free energy density (compared to the free energy of the homogeneous phases)  $-g \propto (\Delta\chi)^\alpha$ , and the difference of volume fractions in the two regions  $\Delta\varphi \propto (\Delta\chi)^\beta$  with both  $\alpha$  and  $\beta$  are positive. Below we will show that in this case,  $\alpha = 2$  and  $\beta = 1/2$ . However, as there is a finite characteristic length scale in the system (the dimension of the microphases), the width of the interface cannot diverge because it is upper bounded by this characteristic length scale.

Here we use a self-consistent field (SCF) theory with the discretization scheme of Scheutjens and Fleer (SF-SCF) to study microphase segregation.<sup>4-5</sup> Apart from the use of a lattice,

there are noticeable differences between the classical SCF models used in the literature and SF-SCF. To be more specific, SF-SCF implements besides local also non-local contributions to the contact interactions in the segment potentials (see below and Appendix for more details), whereas in the literature the non-local effects tend to be neglected for the study of microphase segregation.<sup>6-7</sup> This is a minor issue when the gradients in the densities are very small, e.g. close to the critical point, but it becomes more important when the gradients in densities are large, e.g. for strong segregation. The non-local effects are also thought to be more relevant for finite chain lengths and less important for the infinite chain length limit. Typically, within SF-SCF the focus is explicitly on finite chain lengths. The infinite chain length limit is only found by extrapolation. SF-SCF has been used successfully for modelling inhomogeneous polymer and surfactant systems, including self-assembly of surfactants and lipids in aqueous solutions,<sup>8-13</sup> however, to date the SF-SCF has not yet been used for microphase segregation of block copolymers. Therefore, it is timely to consider the applicability of SF-SCF by comparison of predictions with available data from literature. For this reason, it is natural to first focus on the critical region before addressing finite chain length effects in other parts of the phase diagram such as for the lamellar-to-hexagonal phase boundary.

Unlike in the macrophase segregation for which  $\chi^{cr} = \frac{2}{N}$ , for microphase segregation we expect that the quoted value  $\chi^{cr} = \frac{10.5}{N}$  is not the exact (mean field) result for finite chain lengths (a more accurate coefficient 10.495 is mentioned in the literature<sup>6, 14-17</sup>). In the literature, there have been few reports about possible finite chain length corrections and our results presented below are consistent with these.<sup>15</sup> From this we conclude that SF-SCF is accurate and reliable.

In practice, block copolymers are rarely found in the weak segregation limit. When interactions are stronger, the phase diagram progressively becomes richer. One can find various topologies of microstructures that results from a balance of opposite tendencies: (i) The larger is the interaction parameter  $\chi$ , the higher is the energetic cost to have an A-B interface in the system and therefore the tendency to reduce this area becomes progressively stronger. (ii) A small interfacial area per molecule will imply the brush-like stretching of the two blocks to avoid overcrowding effects. Of course, this implies a conformational entropy

loss. Hence the system will try to minimize stretching and this will increase the area per molecule. (iii) The copolymer will need to occupy the total volume and leave no voids. Therefore, the stretching of the chains cannot always be homogeneous: there may be regions in the volume which are further away from the 'interface' than others, the filling of these distant volumes require extra stretching of chain parts. Inhomogeneous stretching is avoided as much as possible.

These above set of tendencies are not easily accounted for analytically and that is why microphase segregation is the domain of numerical analysis. It is well known that the outcome depends on the fraction  $f = f_A = \frac{N_A}{N_A+N_B}$  in an  $A_{N_A}B_{N_B}$  block copolymer. At extreme values of  $f$ , we have spherical domains of the minority phase and these domains may be packed in regular order. At intermediate values, we have a cylindrical topology and these are packed in a hexagonal packing and around  $f = 1/2$  there is a lamellar phase. Depending on the strength of the interactions, other competing mesostructures are found between the hexagonal (HEX) and lamellar (LAM) phases. The most prominent examples are (double) gyroid, double diamond (DD) and hexagonally perforated lamellae (HPL).

Single gyroid (SG) (space group  $I4_132$ ) was observed for the first time in 1967 by Luzatti et al in strontium soap surfactants<sup>18</sup> and identified by Alan Schoen who classified 17 such minimal surfaces, named it as gyroid or Schoen G surface.<sup>19</sup> However now, the term gyroid is being used more commonly for double gyroid structures. In nature, SG structure was detected in butterfly wing scales. The formation of these biophotonic nanostructures, which produce the brilliant colors on butterfly wings, was explained as the deposition and polymerization of chitin on the initially formed double gyroid (DG) structure and as the cell dies air replaces cell content and a SG structure consisting of chitin and air remains.<sup>20</sup> Similar SG structures were also found in the retinal cone mitochondria of tree shrews.<sup>21</sup> SG structure was rarely observed compared to DG and DD. Even though SG was not found in diblock copolymers, a current approach is to produce SG templates from a DG forming ABC block copolymers such as poly(isoprene-*b*-styrene-*b*-ethylene oxide) by etching the blocks and metal deposition.<sup>22</sup> The double gyroid (space group  $Ia\bar{3}d$ ), which consists of three continuous subvolumes with two non-intersecting SG's with the same volume and the remaining volume as the matrix phase, was discovered in 1986 by first being misinter-

preted as DD<sup>23</sup>, then correctly identified by two independent groups in 1994.<sup>24-25</sup> DG was identified in various diblock copolymers<sup>26-27</sup>, ABA triblocks<sup>28-29</sup> as well as ABC triblock copolymers.<sup>30</sup> In the SCF calculations of Matsen et al hexagonally perforated lamellae (HPL) (space group  $R\bar{3}m$ ) phase was predicted to be nearly stable for diblock copolymers.<sup>6</sup> Wang *et al.* speculated that HPL is an intermediate state during HEX-DG transition in diblock copolymers.<sup>31</sup> Nevertheless, the metastable HPL phase could be experimentally obtained in diblock copolymers.<sup>32-33</sup> Another common mesophase, the double diamond (space group  $Pn\bar{3}m$ ) was first discovered in PS-PI star block copolymers.<sup>23</sup> DD phase was also identified for diblock copolymers<sup>34</sup> and their homopolymer blends.<sup>35</sup> After a re-examining of some of the obtained DD morphologies, it was figured out that they were only misidentified DG morphologies, since DG highly resembled DD in TEM images.<sup>36</sup>

The modelling of the stability of DG has contributed significantly to the state of the art, but to date there remain points of debate. More specifically, according to the early SCF calculations performed by Matsen and Bates<sup>6</sup>, the DG cannot be stable at strong segregation after reaching a triple point around  $\chi N = 60$ , while more recent predictions of Cochran *et al.* claim that DG is stable up to  $\chi N = 100$  with a broadening stability window.<sup>7</sup> Plus, it is still necessary to prove whether the above results are also applicable for finite chain lengths. As mentioned above, for finite chain length and strong segregation, it may be necessary to have a chain model that remains accurate when the chains become strongly stretched. The freely jointed chain (FJC) is expected to behave better than the Gaussian chain in this respect. Also for strong segregation the interfaces become more narrow and the gradients in density increase. In such situation, a theory which accounts for non-local effects in the segment potential is expected to be more accurate than theories that ignore these subtleties. It is therefore timely to use the SF-SCF method for the modeling of microphase segregation in this limit.

We have analyzed the phase boundary between HEX and LAM phases by taking the SG, DG, DD and HPL phases into account. Using the SF-SCF approach, we confirm the literature prediction that there exists a narrow region in  $f$  for which at  $\chi N = 30$  and  $N = 300$  diblock copolymers prefer the DG phase over the HEX or LAM phases. Other phases such as the DD, SG and HPL phases were found to be metastable. In contrast to the more recent

predictions, we confirm early results of Matsen and Bates<sup>6</sup> by giving evidence that at strong segregation ( $\chi N = 120$ ), the HEX phase gives directly way to the LAM phase as now also the DG is metastable. We haste to mention that this result is for finite chain length, i.e.,  $N = 300$  and the result may change when  $N$  is significantly increased. Moreover, it may not be excluded that the conclusion of metastability of mesophases at strong segregation is affected by lattice issues. The latter reservation can only be lifted when a grit refinement study is implemented. This remains work for the future.

The remainder of this paper is the following. We will first present aspects relevant for the modeling of microphase segregation of the SF-SCF approach. The idea is to give sufficient information to the reader to understand how the results were generated. Other details of the modeling are deferred to the Appendix. In the results section, we will first outline the procedures which were followed to identify the relevant results of the SF-SCF modeling. We will subsequently present our result for the near critical region of the phase diagram and then proceed with the systematic analysis of the HEX to LAM phase transition regions at intermediate and strong segregation regimes. In the discussion, we will elaborate on our expectations about how the SF-SCF method can be further used for the analysis of block copolymer self-assembly. At the end, we formulate our conclusions.

### 3.2.1 SF-SCF characteristics and parameters

The SCF machinery follows from optimizing a mean field free energy functional which is expressed in terms of segment volume fraction profiles and complementary segment potential profiles (see Appendix). Both the potentials and the segment densities are a function of the spatial coordinates. The rule how to compute the potentials from the segment densities follows from the optimization of the free energy with respect of the segment densities. The rule how to compute the segments densities from the segment potentials follows from the minimization of the free energy with respect to the segment potentials. When we follow both rules and implement the incompressibility conditions, we can evaluate the equilibrated free energy (and obtain relevant thermodynamics from this) and evaluate the relaxed structural details of the system. The input for this machinery consists of four elements. (i) Info on the molecular components. In the current system, there is only one type of molecule, namely a block copolymer  $A_{N_A}B_{N_B}$  in the system, where  $N_A$  is the degree of polymeri-

zation of the A-block and  $N_B$  is the degree of polymerization of block B. The molecules follow the FJC model for their conformational degrees of freedom. This chain model implements a finite chain extension, as all chain bonds are fixed in length. It ignores bond angle correlations. This implies that the statistical segments can go in any direction on the lattice including back folding. The latter obviously is an approximation, but we note that this excluded volume error is partially corrected by the compressibility condition. (ii) Info about the interactions. As we have no solvent, there is only one relevant interaction parameter  $\chi = \chi_{AB}$ . We thus expect that segments only feel each other when they occupy nearest neighbor sites. The number of segment-segment contacts is estimated using the well-known Bragg-Williams (mean field) approximation. (iii) A specification of the coordinate system. Mostly we consider an elementary 3-gradient ( $x$ - $y$ - $z$ ) cell, which can be used to construct the complete spatial distribution of the copolymers. For the HEX phase, we can reduce the calculations to two-gradients ( $x$ - $y$ ) while the cylinders lie in the  $z$ -direction, and for the LAM phase we consider only the direction normal to the planes ( $x$ -direction) which allows a reduction to a one-gradient calculation. (iv) Specification of the boundary conditions. In all the three-gradient cases we have implemented periodic boundaries, in the other phases we have used reflecting (mirror-like) boundaries. Below we will pay attention to both elements (iii) and (iv) for each type of calculation that is discussed.

It is important to mention the four most important differences of the SF-SCF method compared to the SCF methods typically used for microphase segregation. (A) The SF-SCF method needs an initial guess which is then iteratively adjusted using a Hessian-free optimization method (for example a steepest decent (SD) or a direct inversion in the iterative subspace (DIIS) scheme).<sup>37-38</sup> This method does not need any further input on the symmetry of the solution and the precision does not depend on e.g. the specification of test-functions of any sort. (B) We have implemented the FJC model. Within this model there exists an efficient propagator formalism to compute the volume fractions (see Appendix). The chain model is appropriate for finite chain lengths and is expected to outperform the Gaussian chain model as soon as the chains become strongly stretched. This is more of an issue at strong segregation than at weak segregation. (C) The length scale of the segments (bond length) is also used to discretize space (lattice model). Other numerical SCF methods also rely on a discretization scheme, but in SF-SCF the discretization is built in more rigidly than

in alternative approaches. (D) The SF-SCF model features segment potentials  $u(\mathbf{r})$  that include non-local contributions. The physical meaning of the segment potential is the work of bringing a segment from the reference phase (where the potentials is zero) to the coordinate  $\mathbf{r}$ . Apart from a contribution which is adjusted to obey to the incompressibility relation, there is a contribution due to the segment interactions, i.e.  $E_X(\mathbf{r})$  for segment type X at coordinate  $\mathbf{r}$ . As specified in the appendix this contribution implements the Bragg Williams approximation and typically is given for segment A by  $E_A(\mathbf{r}) = \chi\varphi_B(\mathbf{r})$  and a similar equation applies for segment type B. This local definition of the interactions is correct/accurate in the absence or vanishing gradients in the segment density. In SF-SCF one typically accounts for the gradients and the interactions are computed by  $E_A(\mathbf{r}) = \chi\langle\varphi_B(\mathbf{r})\rangle = \chi(\varphi_B(\mathbf{r}) + \frac{1}{6}\partial^2\varphi_B(\mathbf{r})/\partial\mathbf{r}^2)$  (see Appendix). The latter contribution implements information on the ‘curvature’ of the density profile. Similar ‘corrections’ are implemented in the free energy functional. The curvature correction in the segment potential is referred to as the non-local contribution because in the lattice the second derivative is implemented by using the local averaging of the segment densities around a specified coordinate (see Appendix).

### 3.3 Results

---

In the following we will first discuss how relevant SF-SCF results are obtained. Typical results for various mesophases are discussed and evaluated. This discussion is followed by a systematic analysis of the systems near the critical region. After this we report on the spacing of the LAM phase for systems that are not near the critical point. The remainder of the results is focused on the transition region between the HEX and LAM phase and more specifically to the question of (meta)stability of the DG phase.

#### 3.3.1 Box size adjustment for free energy optimization

As explained above (and in the Appendix), the SCF free energy features segment potentials and segment densities that are mutually dependent. The optimization of it leads to rules of which the fixed point is known as the SCF solution. Let us now assume we have such an SCF solution, we can evaluate the free energy using Equation A3. One can easily see that for an SCF solution, Equation A3 can be simplified resulting in:

$$G \equiv G - G^b = -n \ln \frac{q}{V} - \sum_{\mathbf{r}} \alpha(\mathbf{r}) \quad (1)$$

where the free energy of the homogeneous reference (the bulk) as the reference as usual,  $q$  is the single chain partition function, which can be computed with the propagator formalism from the segment potentials,  $V$  the system volume and  $\alpha(\mathbf{r})$  is the value of the Lagrange field which takes values such that the system is incompressible at each coordinate, i.e.  $\varphi_A(\mathbf{r}) + \varphi_B(\mathbf{r}) = 1$ . To compare systems with different size and structure to each other, it is appropriate to evaluate the free energy density for each of these systems:

$$g = \frac{G}{V} \quad (2)$$

Typically, the free energy density is negative because the microphase segregated state develops spontaneously from the homogeneous state. The system with the lowest free energy is the preferred one.

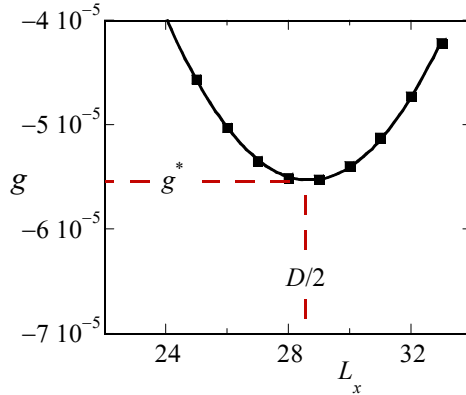


**Figure 1.** Free energy density  $g$  (in units of  $k_B T/b^3$ ) as a function of the spacing  $L_x$  for a LAM phase  $f = 0.5$ ,  $N = 1600$  and  $\chi = 0.09$ . The line is a parabolic fit through the data points. The optimal spacing  $D$  (in units  $b$ ) as well as the corresponding optimal free energy density are indicated.

Inspection of the procedure reveals that we should fix the values of  $L_x$ ,  $L_y$  and  $L_z$  before we can start solving the SCF equations. Hence, we end up with a free energy density which is a function of the specified spacing  $D$ , i.e.  $g = g(D)$ . There is no guarantee that for an arbitrary

choice of the system size, the optimized SCF free energy density is at its minimal value. Therefore, we need to vary the value of  $L_x$  in the lamellar phase, or the combination of  $L_x$  and  $L_y$  in the hexagonal phase or the value of  $L = L_x = L_y = L_z$  in (e.g.) the gyroid case to find the optimal spacing  $D = L_x^*$ . A typical result of such procedure for a lamellar phase is presented in Figure 1. The free energy that is optimized with respect to the spacing is labelled by an asterisk,  $g^*$ .

Apart from the system size we need, though the choice of the number of gradient directions and the type of boundary condition, to specify the phase of choice of considerations. To illustrate this, we will visit the topologies that are used below, namely the LAM, HEX, SG, DG, DD and HPL phases in order.

**3.3.1.1 The lamellar phase.** For a LAM phase, we reduce the calculations to the one-gradient case  $\mathbf{r} = x$  and the mean field approximation is applied in  $y$  and  $z$  directions. The system size is given by  $L_x$  and we use reflecting boundary conditions:

$$\varphi(0) = \varphi(1) \tag{3a}$$

$$\varphi(L_x + 1) = \varphi(L_x) \tag{3b}$$

All other quantities which are a function of the spatial coordinate, such as the segment potentials, the end-point distributions follow these rules. In this case, the free energy  $G$  is per unit area and the free energy density is found by  $g = G/L_x$ . Typically, we will have one A-B interface somewhere half-way in the ‘box’ (depending on  $f$ ) and the lamellar spacing is given by  $D = 2L_x$ . We select the A-rich domain to be at low  $x$ -values and the B-rich domain at high  $x$ -values by means of an initial guess for the segment potentials.

A schematic representation of the LAM phase and the optimized (with respect to the spacing) density profile are given in Figure 2a and 2b. In Figure 2a, red and blue regions belong to the A and B blocks, respectively. The spacing ( $D$ ) and width of the interface ( $W$ ) are indicated on the lamellae. The same parameters ( $D$  and  $W$ ) are defined more precisely on the density profiles  $\varphi_A(x)$  and  $\varphi_B(x)$  shown in Figure 2b. In this graph, also the density difference  $\Delta\varphi = \varphi_A - \varphi_B = 1 - 2\phi_B$  with  $\phi$  is the volume fraction midway in the A-rich phase, is indicated. As the coordinate  $x = 0$  is fixed to the position of the steepest gradients in the

density, the evaluation of the density difference takes place at  $x = -\frac{D}{4}$ :  $\phi = \varphi(-\frac{D}{4})$ . Finally, the width of the interface, as graphically illustrated in Figure 2, is computed from the profiles according to

$$W = \frac{\Delta\varphi}{\varphi_A\left(-\frac{1}{2}\right) - \varphi_A\left(\frac{1}{2}\right)} \quad (4)$$

In Figure 2b, the curves in red and blue belong to the density profiles of A and B blocks for  $\chi N = 12$  in the weak segregation regime where the optimized spacing is  $D = 42$ , whereas density profiles shown in pink and light blue belong to the A and B blocks of a copolymer in the strong segregation region of  $\chi N = 75$  with optimized spacing  $D = 64$ . For weakly segregated block copolymers,  $\Delta\varphi$  easily deviates highly from unity and its value approaches zero in the limit towards the critical point, whereas it approaches unity for strong segregation limits. From its definition (Equation 4), it is easily seen that the width of the interface  $W$  is small for strong segregation and increases upon the approach towards weak segregation. Obviously,  $W$  cannot exceed  $D/2$ .

**3.3.1.2 The hexagonal phase.** The hexagonal packing of cylindrical domains of the minority phase surrounded by the majority phase requires a two-gradient computation box. Ideally, the ratio of the box sizes in the gradient directions is  $L_x/L_y = \sqrt{3}$ . Below, we will accept small errors in the lattice dimensions and consider integer values for the system size in the  $x$ -gradient direction,  $L_x$ , and  $y$ -direction,  $L_y$  while we apply a mean field approximation in the  $z$ -direction. For a given SCF fixed point, the free energy of  $G$  is given per unit area and the free energy density follows from  $g = G/L_x L_y$ . The lattice spacing is given by  $D = \sqrt{L_x^2 + L_y^2}$ . Hence when the correct ratio is implemented we have  $D = 2L_y$ . We follow the same definition for the spacing  $D$  when integer values are used for the sizes of the system in the gradient directions. While optimizing the lattice spacing, we adjust the combinations of  $L_x$  and  $L_y$  such that the  $\sqrt{3}$  ratio is met as closely as possible (excluding the settings for which the ratio is far from the ideal value). However, there is always some imprecision remaining on the spacing values obtained for this phase and therefore we typically slightly overestimate the free energy.

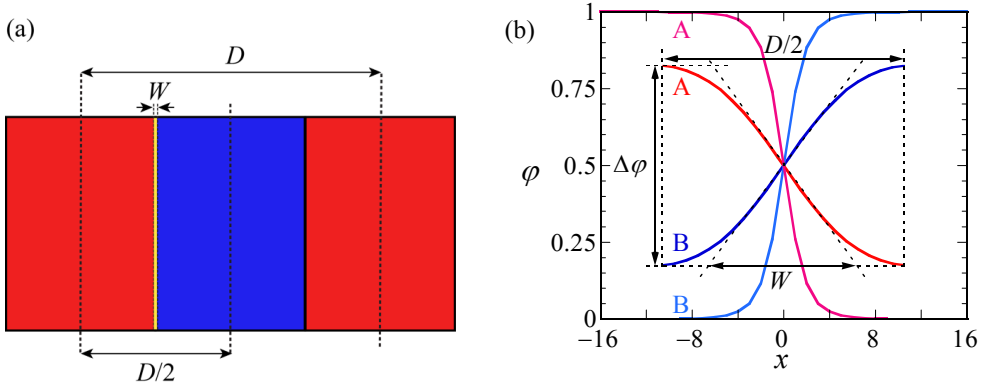


**Figure 2.** (a) Schematic representation of symmetrical LAM phase. Red and blue regions indicate blocks of A and B, respectively. The lamellar spacing  $D$  and the width of the interface  $W$  are indicated. (b) SF-SCF density profiles ( $\phi$ ) as a function of layer number  $x$  where  $x = 0$  is taken halfway the A-B interface. Parameters:  $f = 0.5$  and  $N = 1000$ ; red and blue lines are for weak segregation  $\chi N = 12$ , optimal spacing is  $\frac{D}{2} = 21$  of A and B blocks, respectively and pink and light blue lines are for strong segregation  $\chi N = 75$ ,  $\frac{D}{2} = 31$  of A and B blocks, respectively. The parameters  $\Delta\phi$ ,  $D$  and  $W$  are stated for  $\chi N = 12$ .

As in the LAM case, for the HEX phase reflecting boundary conditions are implemented. That is, both in  $x$  as  $y$  directions the densities as well as the potentials and thus the end-point distributions obey to the implementation of zero gradients across the boundaries as given in Equation 3a and 3b.

In Figure 3, a typical result for the density profile of HEX phase is given for  $D = 60$  which happens to be close to the optimal spacing for  $N = 1000$ ,  $\chi N = 30$  and  $f = 0.30$ . The two-gradient results are ‘multiplied’ 8 times in  $x$  and  $y$  directions and about 50 times in the  $z$ -directions. Here and below we give equal density color maps wherein the minority phase is given in red, while the majority phase is in blue (more intense color implies a higher density; the in between white color is the interface). In addition, the blue domain is made ‘transparent’ to allow the visualization of the cylinders in the HEX phase more clearly. It is possible to give, similarly as in the LAM phase a cross-sectional density profile. We do not show such profile because the features (apart from the fact that the interface is not centered) are very similar features to those given in Figure 2b.

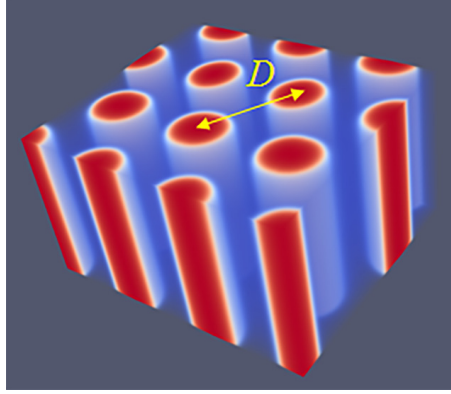


**Figure 3.** SF-SCF predictions for the density profile of HEX phase for  $D = 60$ ,  $N = 1000$ ,  $\chi N = 30$  and  $f = 0.30$ . The spacing  $D$  is indicated. Color coding is as follows. Regions rich in the minority block (segment type A) are given in red, the blue regions are rich in the majority phase (segment type B). The majority phase (blue) is made more transparent the higher is its density for presentation purposes. Mirror-like boundary conditions apply in all directions.

**3.3.1.3 Various mesophases that require three-gradient SF-SCF.** There are many three-gradient solutions of the SCF equations. Some of these, e.g. the  $Im3m$  cubic phase, requires reflecting boundary conditions.<sup>11</sup> Here our interest is in, e.g., the SG and DG structures that lack symmetry planes. For such structures, one requires periodic boundary conditions. We restrict our analysis to three-gradient SF-SCF computations with equal sizes in the three gradient directions:  $L \equiv L_x = L_y = L_z$ . The periodic boundaries are implemented by realizing that coordinates 1 and  $L$  are ‘neighbors’ where it is understood that the potentials and end-point distributions follow the same rules:

$$\begin{aligned}
 \varphi(0, y, z) &= \varphi(L_x, y, z) & \varphi(L_x + 1, y, z) &= \varphi(1, y, z) \\
 \varphi(x, 0, z) &= \varphi(x, L_y, z) & \varphi(x, L_y + 1, z) &= \varphi(x, 1, z) \\
 \varphi(x, y, 0) &= \varphi(x, y, L_z) & \varphi(x, y, L_z + 1) &= \varphi(x, y, 1)
 \end{aligned} \tag{5}$$

Next, similarly as in other systems we vary  $L$  systematically to find the optimal spacing. Here we choose the spacing  $D = L$  for which the free energy density is minimized with respect to  $L$ . The SG phase has many interesting aspects which are well documented in the literature.<sup>19-22</sup> Our result for the SG phase closely follows all these features. As mentioned

already, the SG lacks mirror symmetry. There only exists a three-fold symmetry axis along one of the diagonals of the unit cell as is easily seen from the profile given in Figure 4a. Various other features of the SG appear when we multiply the unit cell a few times. As the majority phase is made transparent, we notice spherical holes with a hexagonal pattern when viewed from the view direction given in Figure 4b. From other view directions (not shown) one can see the holes in a square packing.

As proven below, the SG is metastable as one can easily find for  $f = 0.33$  either a HEX phase or a LAM phase for which the free energy density is lower. The reason for this relatively high free energy density is clear. The majority phase fills up  $2/3$  of the volume whereas the minority phase fills the remainder of the volume in a gyroid-like. The interface in between the A and B rich domains deviates from the being a minimal surface (zero mean curvature throughout the interface), which is only expected for the SG gyroid phase with  $f = 0.5$ . Such balanced SG phase does not exist as for  $f = 0.5$  the lamellar phase is the lowest in free energy.

A typical unit cell of a DG phase is depicted in Figure 4c. The viewgraph of 8 unit cells (Figure 4d) now lacks the ‘holes’ because these ‘holes are now the place in which the second gyroidal labyrinth of the minority phase is placed. Below we show that the DG phase is a candidate ground state as it is lower in free energy than the HEX and the LAM for a small region of  $f$  values.

As compared to the SG, the DG has two gyroidal labyrinths with equal volume and the majority phase is in between the two and in this sense the symmetry is restored. From the perspective of the majority phase, the two sub-phases of the minority phase are spaced symmetrically around it even though  $f = 0.33$ . As compared to the SG the optimal spacing of the DG increased almost by a factor of two as it went up from  $D = 43$  for SG to  $D = 74$  for DG. Again, the DG has no symmetry planes and only one three-fold symmetry axis. Interestingly, the two minority phases only have three-fold junction points where three tubular domains come together. This appears sufficient to generate a so-called triply periodic structure, i.e. one can travel inside a minority phase in any of the three directions;  $x$ ,  $y$  and  $z$  throughout the system. As explained above, we do not impose a particular symmetry for a

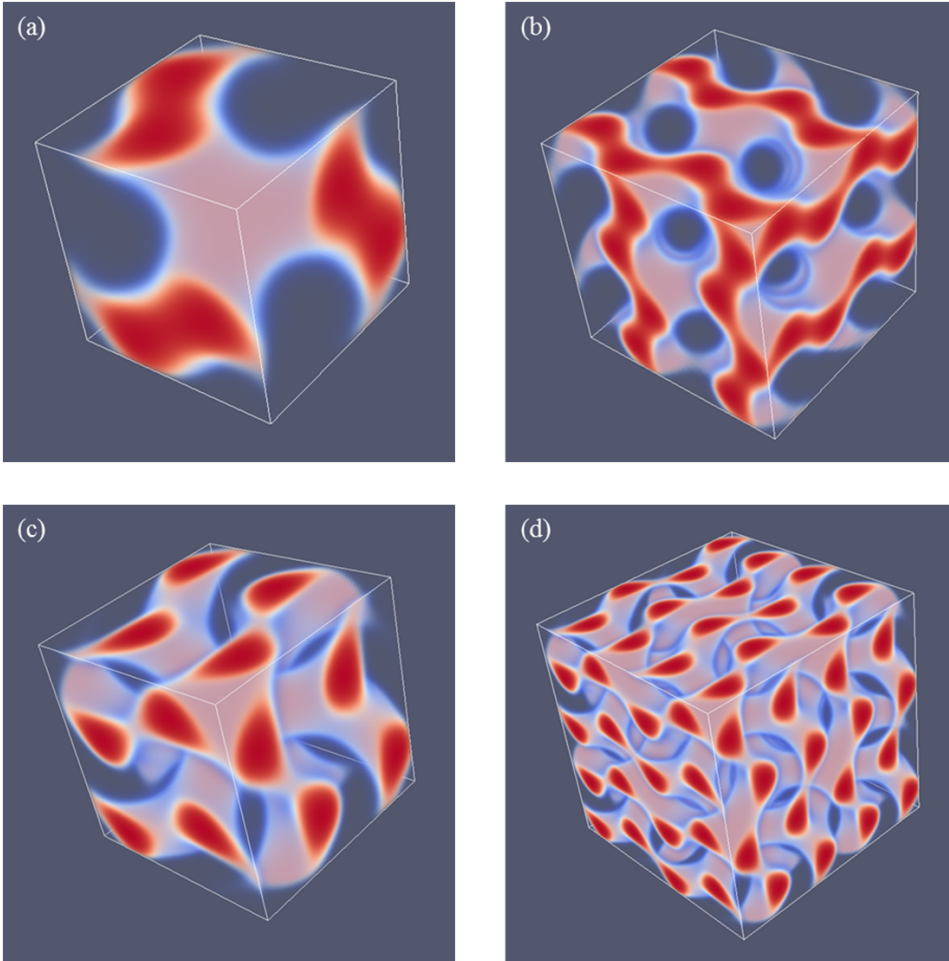


**Figure 4.** (a) SF-SCF predictions for the volume fraction profiles of a SG unit cell for  $D = 43$ ,  $N = 300$ ,  $\chi N = 30$  and  $f = 0.33$ . (b) 8 unit cells of a SG (result of (a) is doubled in each direction). (c) Volume fraction profiles of a DG unit cell for  $D = 74$ ,  $N = 300$ ,  $\chi N = 30$  and  $f = 0.34$ . (d) 8 unit cells for the DG (result of (c) is doubled in each direction). The color coding is the same as in Figure 3.

particular segregated state during the SF-SCF optimization procedure, but instead implement an initial guess and apply appropriate boundary conditions. By accident, one of the calculations targeted for a SG phase deferred to a HPL phase. A possible reason for this unforeseen result was found *posteriori* by the observation that the HPL is competitive free-energy wise with the SG for the  $f$  value that was selected in the computations (see also be-

low). Upon inspection of the HPL phase, a strong resemblance with the DD was found and therefore we present these phases side by side in Figure 5. For both phases, we employed periodic boundary conditions, and again for both phases, we have systematically varied the box size  $L$  and present the resulting structure for the optimal spacing  $D$ .

Referring to Figure 5a and 5c we present the DD morphology from two perspectives: a) a view from along one of the diagonals from which the three symmetry planes can be seen and c) a view with any of the planes of the unit cell placed perpendicular to the viewing direction. The DD morphology has often been described in the literature<sup>34-35</sup> and the phase that was predicted by SF-SCF is completely in line with this. The structure has three symmetry planes which are rotated with respect to each other by 60 degrees. Similarly as for the DG, the minority phase forms two non-intersecting triply periodic regions with opposite handedness, while the majority phase is draped in between the minority labyrinths. The morphology of DD (space group  $Pn\bar{3}m$ ) is characterized by four-fold junctions similarly as in the tetragonal C-network in diamond (or the structure of methane).

In Figures 5b and 5d, we show the typical HPL phase with an optimized spacing for an asymmetry fraction of  $f = 0.30$  for which the free energy density is lower than that of the corresponding SG (see below). The two viewgraphs show the structure from two viewpoints identical to the ones given for DD: (b) gives the view in the direction along the axis of the unit cell. For this point the three symmetry-planes can be seen, and (d) gives the view face-on with one of the planes of the unit cell perpendicular to the view direction. The comparison between panels (a), and (b) as well as (c) and (d) in Figure 5 are apparent and informative. Comparing HPL and DD, we notice that the curvatures of the interfaces are clearly similar. There are however important differences. As the DD has four-fold connections, in the HPL phase there are only three-fold connections (as in gyroids). (This is not easily recognized from the viewgraphs but this is better observed by inspection of the HPL from many viewing directions). As compared to the DD the fourth connection is 'broken'. As a consequence, the HPL phase is lamellar and not triply-periodic: one can peel off one layer after another layer from the HPL phase, which is best seen from the images of (2) and (3) in Figure 11. (2) and (3) correspond to the morphology when we have the compositions of  $f = 0.30$  and  $0.50$ , respectively. The layers together feature holes in hexagonally orga-

nized patterns. In (2) at low  $f$ , the hexagonally ordered pores are more apparent because the lower volume of the minority phase does not alter the visibility of the holes.

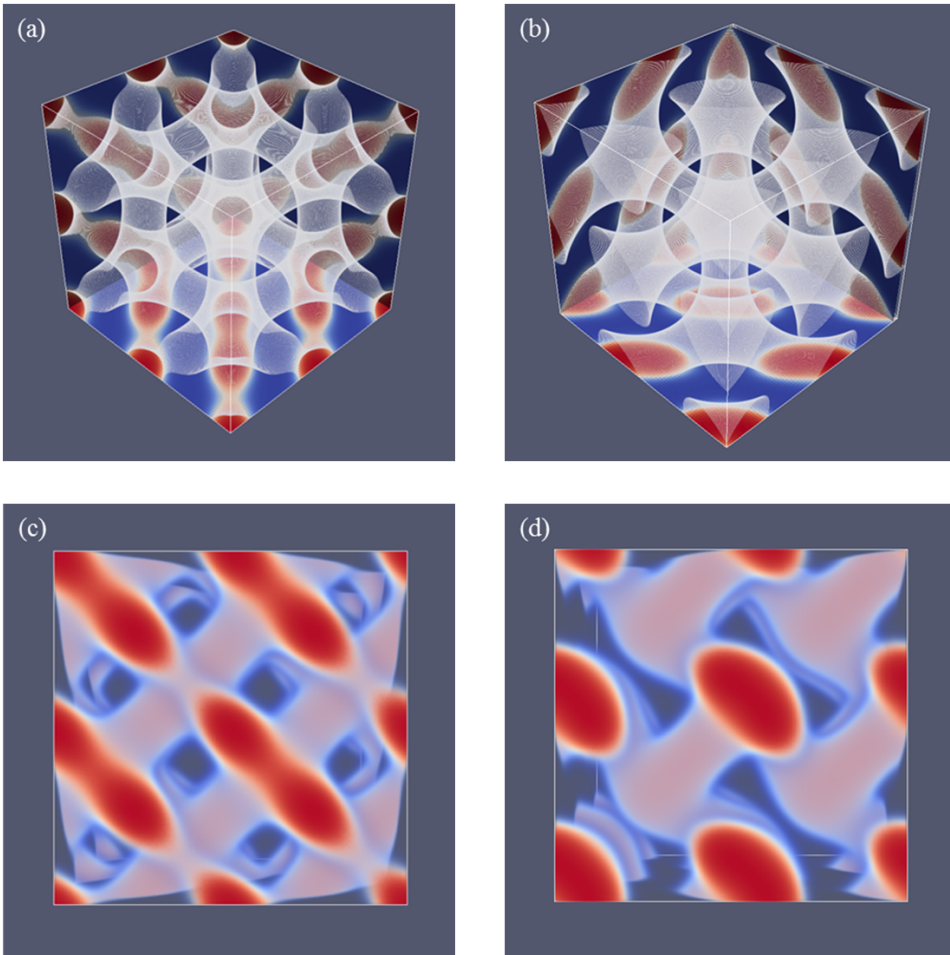


Figure 5. (a,c) Three-gradient equal density contour plots for 8 unit cells of the double diamond DD phase (b,d) Three-gradient equal density contour plots for 8 unit cells of the hexagonal perforated lamellae HPL phase. For (a) and (b), the two phases are given in the orientation that reveals the three three-fold symmetry planes. In panels (c) and (d), we present a side view of 8 unit cells (viewgraphs with  $x$ - $y$  or  $y$ - $z$  or  $x$ - $z$  planes perpendicular to the viewing direction are all similar). The color coding is similar to the one given in

Figure 3. Parameters for DD phase:  $D = 45$ ,  $N = 300$ ,  $\chi N = 30$  and  $f = 0.33$ ,

HPL phase:  $D = 43$ ,  $N = 300$ ,  $\chi N = 30$  and  $f = 0.30$ .

In between the holes, lamellae strongly bend toward a neighboring layer in the direction of the missing connector. Two neighboring lamellae have opposite bending characteristic; hence there are two types of layers in the HPL phase which alternate, each having inversed curvatures. These two types of layers resemble the two networks with opposite handedness in DG or DD phases. Characteristic for the HPL phase is that the odd layers almost touch each other across the pores of the even layers and vice versa. Indeed, if at these places the odd layers would re-establish their connection and when similar connections were made between the even layers, we restore exactly the DD phase without the need to modify the curvatures of the interfaces much (as is best seen from close inspection of the differences between Figure 5c and 5d). The reason for the HPL phase to have lamellae with locally strong curves is to ensure a homogeneous distance between the lamellae in the presence of pores in the lamellae. Such homogeneity in interlamellar distances is a desired property as this ensures homogeneous stretching of the copolymer blocks.

### 3.3.2 Systematic dependences

By examining finite chain length effects near the critical region, we are faced with a problem. In order to find  $\chi^{cr}$ , we need to have an accurate guess for the optimal spacing at the critical point, which we will refer as  $D^*$ . The latter we can only find by extrapolation. The (approximate) procedure that we followed is illustrated by referring to Figure 6a. In this graph, we present the optimal spacing of the lamellar phase with  $f = 0.5$  for a given overall chain length of  $N = 1600$  as a function of the product  $\chi N$ . Hence for this graph we varied the  $\chi$  only and each point on the graph is the result from an optimization of the box size. We find  $D^*$  by extrapolation to  $\chi N = 10.5$ . It would have been better if we would have extrapolated to the exact critical value for the chain length  $N = 1600$  (which we will find below slightly lower than 10.5), however the error in  $D^*$  that is introduced in this way is negligible. We can collect  $D^*$  as a function of chain length but which is presented later. We first analyze how the LAM phase is changed when we approach the critical point. These results are shown in Figure 6b, 6c and 6d, wherein we present the free energy density, the width of the interface and the density difference, respectively as a function of  $\Delta\chi = \chi - \chi^{cr}$  for a lamellar phase with  $f = 0.5$  for which  $D^*$  is very close to an integer number. Hence for such a case we know that in the limit of  $\Delta\chi \rightarrow 0$ , we enforce an optimal spacing to the system. For

systems away from the critical region, one possibly would have acquired slightly different  $D$  values, but this requirement cannot be implemented in a lattice model.

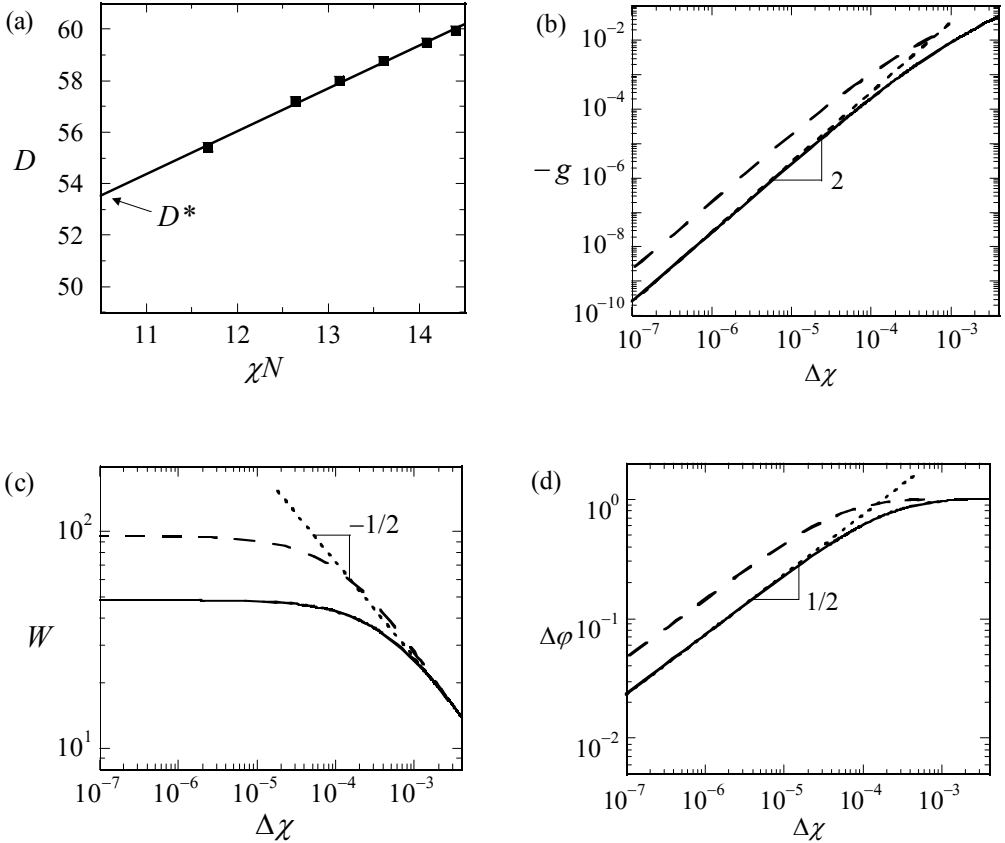


**Figure 6.** (a) The optimal spacing  $D$  in lattice units  $b$  plotted as a function for  $\chi N$  and  $N = 1600$ . Here optimal spacing at the critical point  $D^* = D(10.5)$  is obtained by the linear fit. (b) Absolute value of free energy density ( $-g$ ) (in units of  $k_B T/b^3$ ) as a function of  $\Delta\chi$  in double logarithmic coordinates. (c) The width of the interface (in units  $b$ ) as a function of  $\Delta\chi$  in double logarithmic coordinates. (d) Density difference ( $\Delta\phi$ ) as a function of  $\Delta\chi$  in double logarithmic coordinates.  $D^*/2$  values of 76 and 150 were used for  $N = 12996$  (solid lines) and 50624 (dashed lines), respectively in plots (b), (c) and (d). Dotted lines represent the fits. The slopes are indicated on the plots.

As can be seen from Figure 6b and 6d, we obtain power-law dependences for both  $-g(\Delta\chi)$  as well as  $\Delta\phi(\Delta\chi)$ . Indeed, these scaling dependences have been employed to identify  $\chi^{cr}$ :

the value of  $\chi^{cr}$  was adjusted until the best power-law scaling was observed in Figure 6b and 6d in the limit of  $\Delta\chi \rightarrow 0$ . Inspection of Figure 6b shows that we find  $-g \propto \Delta\chi^2$ . This value should be contrasted to the well-known result for the interfacial tension mentioned above for the liquid-liquid interface for macroscopic phase separation for which the coefficient is  $3/2$ . We attribute the increase in the exponent to the observation that the width of the interface does not diverge (see Figure 6c). At high value of  $\Delta\chi$  the free energy density  $-g$  tend to level of a bit as it becomes more linear dependent on  $\Delta\chi$ .

Inspection of Figure 6d shows that  $\Delta\varphi \propto \Delta\chi^{1/2}$  in the limit of  $\Delta\chi \rightarrow 0$  and goes to the constant value of unity for large values of the interaction parameter. The scaling exponent near critical is identical to the one found for macrophase segregation.

The width of the interface has a more complex behavior as illustrated in Figure 6c. It was already mentioned above that the width of the interface cannot exceed  $D^*/2$ . Hence the width should level off in the limit of  $\Delta\chi \rightarrow 0$ . In this case, the solid line is for  $N \sim 13000$  while the dashed line is for  $N \sim 50000$ . The corresponding values for  $D^*/2$  are 76 and 150, respectively. Inspection of the limiting value of the width, we notice that the width goes to approximately  $2/3$  of the value of  $D^*/2$ . Interestingly for rather high values of  $\Delta\chi$ , the width of the interface follows approximately  $W \propto \Delta\chi^{-1/2}$  similar as in the macrophase segregation problem. Apparently, as long as  $W \ll D^*/2$ , we witness an increase of the interfacial width as if the two blocks would have been disconnected.

We have collected the optimal spacing at the critical point  $D^*$  for a wide range of chain lengths and present these results in Figure 7a. To a good approximation, the results are represented by  $D^* = \frac{4}{3}\sqrt{N}$ . Next, we collected the critical interaction parameter  $\chi^{cr}$  again for a wide range of chain lengths and present the results in Figure 7b. In this graph, we have plotted  $\chi^{cr}N$  as a function of  $1/N$  and found to a good approximation as a straight line. The fitting result is indicated in the legend of Figure 7b. Within the accuracy of the fitting procedure, we thus find  $\chi^{cr}N = 10.495(1 + \frac{4}{N})$ . These results are compatible with finite chain length corrections for the critical point found in the literature.<sup>15</sup>

We may use a Flory-like argument to elaborate on the scaling of the spacing with the chain length. In this argument, we will balance the entropic penalty for stretching of the chains,

written as  $D^2/N$  (ignoring numerical coefficients) with the free energy to enlarge the contact area between the A and B blocks,  $\tilde{\gamma}a$ , where  $\tilde{\gamma}$  is the interfacial free energy associated with this surface and  $a$  is the area per molecule.

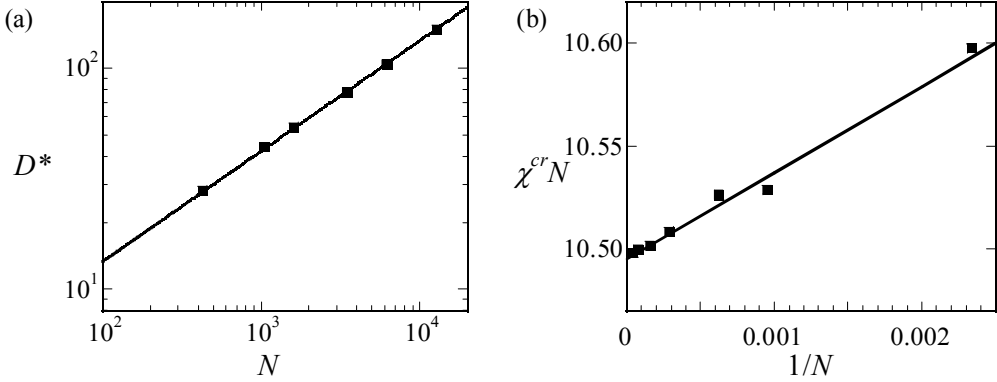


**Figure 7. (a) The spacing at the critical point  $D^*$  of a lamellar phase at  $f = 0.5$  as a function of the chain length  $N$  in double logarithmic coordinates. The fit of  $D^* = \frac{4}{3}\sqrt{N}$  is drawn to guide the eye. (b)  $N$ -dependence on the critical  $\chi N$  value. The function  $\chi N = 10.495(1 + 4/N)$  is drawn to guide the eye.**

The latter can be estimated from the filling of the system by chains, hence  $a = N/D$  and thus the free energy per chain is:

$$F = \frac{D^2}{N} + \frac{\tilde{\gamma}N}{D} \quad (6)$$

where the free energy per chain is in units of  $k_B T$  and that numerical coefficients are ignored. Optimization with respect to  $D$  gives  $D = \tilde{\gamma}^{1/3} N^{2/3}$ . The interfacial energy of an A-B interface is known to depend on the square root of the interaction energy,  $\tilde{\gamma} \propto \chi^{1/2}$ .<sup>39</sup> Using the result that at the critical point  $\chi \propto N^{-1}$ , we notice that  $D \propto \tilde{\gamma}^{1/3} N^{2/3} = N^{-1/6} N^{2/3} = \sqrt{N}$ . We can apply the same argument to systems that are not close to the critical point. In Figure 8a, we present the optimal spacing for LAM phase with  $f = 1/2$  for low, intermediate and strong segregation regions of  $\chi N = 12, 30$  and  $75$ , respectively as a function of the chain length  $N$ . Hence for each of the lines, we varied  $\chi$  such to keep  $\chi N$  fixed. Again, we find that the spacings obeyed  $D \propto \sqrt{N}$  to a good approximation. This must be contrasted to the results pre-

sented in Figure 8b. In this figure, we present the optimal spacing for the symmetric LAM phase ( $f = 1/2$ ) as a function of the chain length for fixed value of the interaction parameter. Hence in these cases, we only changed  $N$  and the interfacial energy  $\tilde{\gamma}$  was approximately constant. As a result, the spacings obeyed  $D \propto N^{2/3}$  to a good approximation.

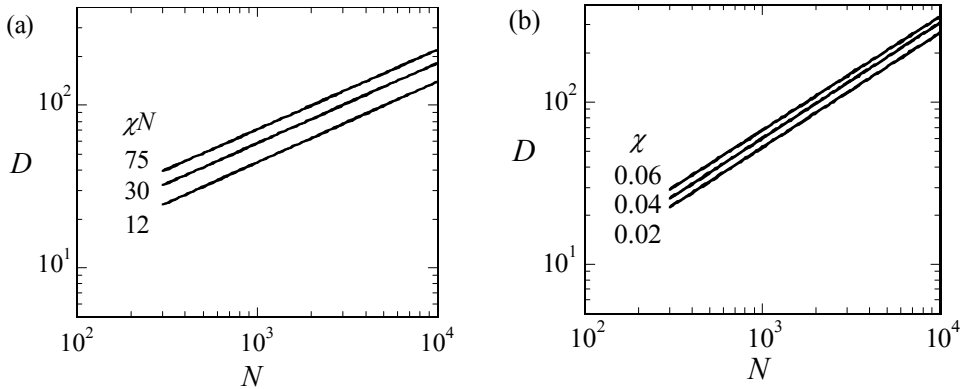


**Figure 8. (a) The optimal spacing ( $D$ ) as a function of the chain length ( $N$ ) in lamellar phase for  $\chi N$  values labelled next to the lines in double logarithmic coordinates. All lines have a slope of 1/2. (b) The optimal spacing ( $D$ ) as a function of the chain length ( $N$ ) in lamellar phase for fixed  $\chi$  values that are labelled next to the lines in double logarithmic coordinates. All lines have a slope of 2/3.**

Next, we present the optimal spacing  $D$  as a function of  $f$  for LAM and HEX in Figure 9 for a given value of  $N = 300$  and  $\chi N = 30$ . When changing  $f$ , we will pass the phase boundary around  $f = 0.34$ . Hence in Figure 9, we showed the data points of the stable phases as filled dots and squares for LAM and HEX, respectively and data points for the non-stable phases were shown as empty. With increasing  $f$ , we find an increase in the optimal spacing. For the LAM phase, the slight increase in the spacing to a plateau region was successfully fitted by  $D \propto [f^{2/3} + (1 - f)^{2/3}]$ . This is the expected dependence when the two blocks independently find the optimal width. A significantly stronger dependence for  $D(f)$  was found for the HEX phase where to a reasonable approximation  $\propto f^{1/3}$ . This result must be attributed to the decreased space occupied by the minority block in the cylindrical domains. We would have like to report on the chain length dependence of the HEX to LAM phase transition ( $f^{tr}$ ) at a finite value of  $\chi N$ . We tried to obtain such result for  $\chi N = 30$ .

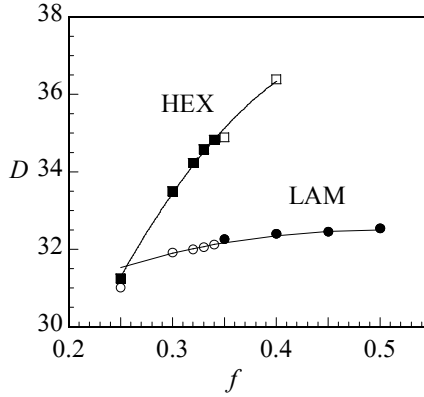


**Figure 9.** Optimal spacing ( $D$ ) of LAM and HEX phases as a function of composition ( $f$ ) for  $N = 300$  and  $\chi N = 30$ . For LAM phase, the fit of  $D \propto [f^{2/3} + (1-f)^{2/3}]$  is drawn to guide the eye. Open and closed symbols refer to the metastable and stable points, respectively.

We tested a range of chain lengths of  $N = 100$ – $1000$ . Within the numerical noise of our procedure, we could not detect the expected chain length dependence for  $f^{tr}$ . This may be attributed to the noise in the data which was amplified slightly because we could not satisfy the box dimensions for the HEX phase  $L_x/L_y = \sqrt{3}$  with enough precision. Instead, we focused on the stability of the various mesophases in the neighborhood of  $f^{tr}$ .

### 3.3.3 The stability of various mesophases

Let us focus next on the stability of various mesophases near  $f^{tr}$ . For all phases, we have computed the optimized free energy density as a function of the asymmetry ratio,  $g^*(f)$ . Plotting these free energy densities as a function of the asymmetry fractions results in lines which are nearly parallel (cf. Figure 10b). The results are more easily discussed when we take the ratio  $g^*/g_{DG}^*$  as a function of  $f$ . Obviously, this dependence results in unity for the DG phase. Recalling that the free energy densities are negative, we find that when the ratio is smaller than unity, i.e. when  $g^* < g_{DG}^*$  the DG is preferred and when  $g^* > g_{DG}^*$  the other phase is stable. In Figure 10a, we show this ratio as a function of  $f$  for the HEX, the LAM and the DG phases. Literature points to a stability domain for the DG phase between  $f = 0.320$ – $0.349$ .<sup>6</sup> We found DG as the most stable phase between  $f = 0.328$ – $0.347$ . These re-

sults are consistent with each other also considering the fact that the SF-SCF results are for a fixed chain length  $N = 300$ .

In Figure 10b, the bottom line presents the lowest free energy values that were obtained, i.e. it connects the data of the HEX phase to those of the DG and then to the LAM phase. The vertical dashed lines present the phase boundaries. The point X gives the free energy density of the DD phase which is indeed slightly larger than the DG at the same  $f$  value. The two top lines are the free energy density of the HPL and the SG phase. Both these phases are metastable as their free energy density is higher than the HEX, DG, LAM phase boundary. As shown in the inset, the free energy densities of the HPL and SG cross each other around  $f = 0.37$ . For smaller  $f$  values the HPL is preferred over SG and above this crossing point the SG is more stable.

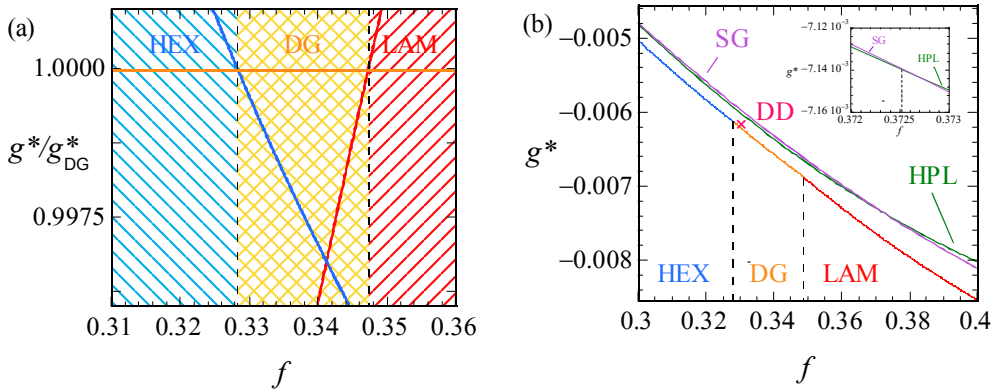
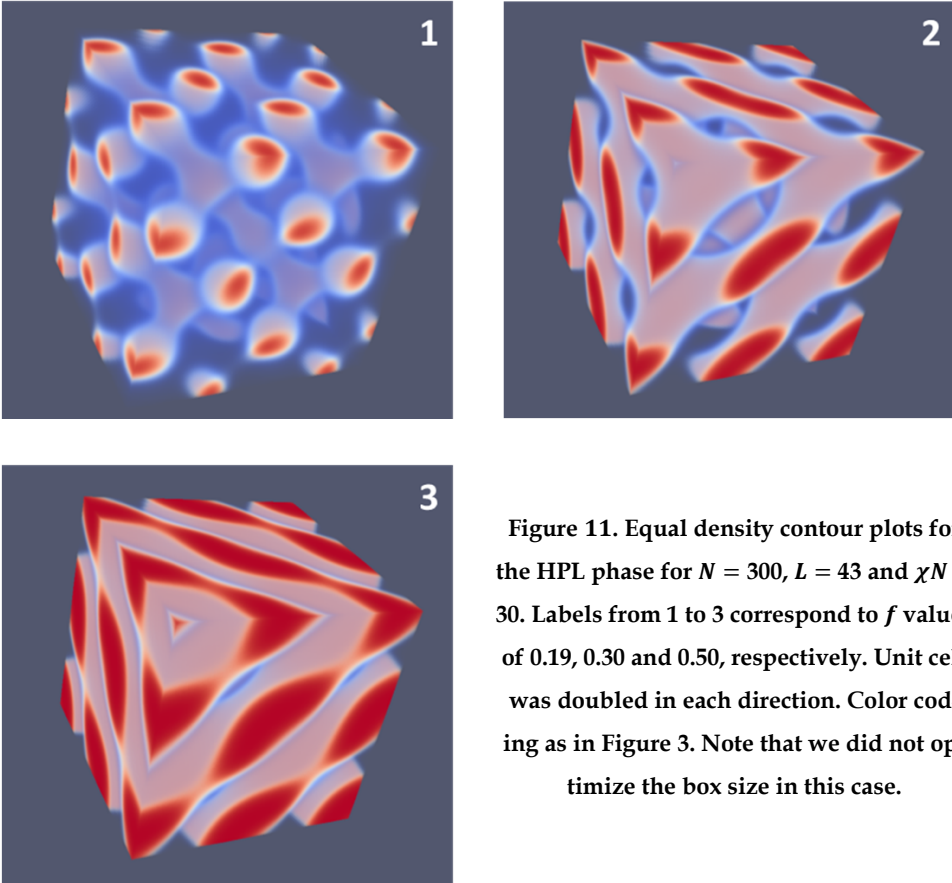


Figure 10. (a) Optimized free energy density  $g^*$  in units of  $k_B T$  of HEX (blue) and LAM (red) phases divided by the free energy density of DG ( $g^*/g_{DG}^*$ ) as a function of composition  $f$  for  $N = 300$ ,  $\chi N = 30$ . Stable phases of HEX and LAM occur when their  $g^*/g_{DG}^* > 1$ . Blue, yellow and red regions represent the HEX, DG and LAM stable regions. (b) Free energy density ( $g^*$ ) of HEX, LAM, DG, DD, SG and HPL phases as a function of composition ( $f$ ) for  $N = 300$ ,  $\chi N = 30$ . DD phase is shown in one point only. Only stable regions of HEX, DG and LAM are shown in the graph. The inset gives an expanded view near the crossing point of the HPL and SG free energy densities as a function of  $f$ .

Of all phases that we have considered the HPL phase is possibly the most novel. It turned out that the phase is computationally very robust and it was very easy to find HPL phases

for various values of  $f$  covering the whole relevant range from region where the LAM phase is stable (e.g.  $f = 0.5$ ) to near the order-disorder line for  $f < 0.2$ . In Figure 11, we put three variants of the HPL phase for  $f = 0.19, 0.3$  and  $0.5$  side by side. The first one is the HPL in the region where spherical phase is the preferred state. Number 2 is near the region where the HEX is the stable phase. Number 3 is the HPL for the case where obviously the LAM phase is the ground state. It is noticed that at large values of  $f$ , the lamellae of the HPL are close to planar ( $f = 0.5$ , i.e. nr 3) and the hexagonally ordered holes are relatively small. The holes become bigger when  $f$  decreases. At the same time the layers become more strongly curved ( $f = 0.3$ , i.e. nr 2). Now the connection points are more apparent as three cylindrical domains come together. When  $f$  is decreased even more ( $f = 0.19$ , i.e. nr 1) the cylindrical domains are no longer homogeneous in thickness. Instead the tubular fragments develop similar to spherical regions with a neck in between. This is consistent with spherical detached domains being preferred for systems with such low  $f$  values. For small  $f$  values the minority phase becomes smaller and smaller in volume and therefore the holes where the majority phase exists in the HPL phase grow larger and larger. In other words, the tubular regions which keep the layers intact become thinner and thinner. The lamellae also become more curved and the direction of the thin tubular fragments are almost perpendicular to the planar lamellae found close to  $f = 0.5$ .

In Figure 12, we present our results for the strong segregation  $\chi N = 120$ . We kept the chain length at  $N = 300$ , and thus increased the interaction parameter. Here we plot the free energy density  $g^*$  normalized by this value for the DG (similarly as in Figure 10a) as a function of the  $f$  value. Again, only when this ratio is smaller than unity we expect the DG to be stable (recall that the free energy density is negative). Inspection of Figure 12 proves that the ratios are larger than unity for both the HEX as well as the LAM phase. This proves that the DG phase is metastable for these high values of the interaction parameter. The free energy densities of the HEX and LAM phases cross at  $f \approx 0.3065$ , which is slightly below the value found for the HEX-LAM transition region for  $\chi N = 30$ . This is in line with the general knowledge of the phase diagram that the phase transitions all move slightly to smaller  $f$  values with increasing  $\chi N$ .



**Figure 11.** Equal density contour plots for the HPL phase for  $N = 300$ ,  $L = 43$  and  $\chi N = 30$ . Labels from 1 to 3 correspond to  $f$  values of 0.19, 0.30 and 0.50, respectively. Unit cell was doubled in each direction. Color coding as in Figure 3. Note that we did not optimize the box size in this case.

We note that the ratio  $\frac{g^*}{g_{DG}^*}$  are just of order 1.0015, which means that the free energy differences are minor. Nevertheless, the differences are significantly larger than the noise in the data (data point not shown are exactly on the lines) and we believe that these results are sufficiently accurate.

A typical value for the optimal  $D$  for the DG at  $\chi N = 30$ ,  $N = 300$  was  $D = 74$ . The optimal spacing for the DG at  $\chi N = 120$  for  $N = 300$  near  $f = 0.31$  was found to be  $D = 101$ . This growth with a factor 1.36 in optimal spacing is a bit larger than expected from  $D \propto \tilde{\gamma}^{1/3} N^{2/3}$ , which implies  $D \propto \chi^{1/6}$  and hence a growth by only a factor 1.26. We also investigated the free energy density of the HPL phase for the strong segregation  $\chi N = 120$ . In line with the results at lower segregation, the HPL phase is also metastable and indeed the DG phase

outperforms the HPL phase also at  $\chi N = 120$  as  $\frac{g_{HPL}^*}{g_{DG}^*} = 0.991$  (the DG free energy density  $g^* \approx -0.0583$  while that of the HPL is  $g^* \approx -0.0578$  for the corresponding  $f$  values).

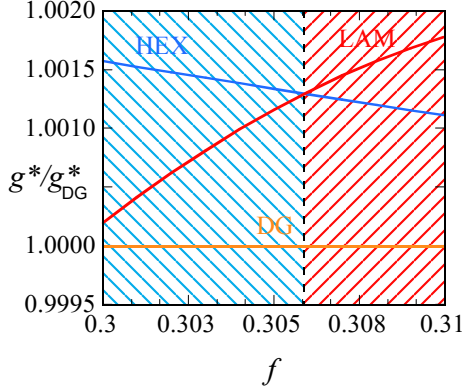


Figure 12. (a) Free energy density of HEX (blue) and LAM (red) phases divided by the free energy density of DG (orange) ( $g^*/g_{DG}^*$ ) as a function of composition  $f$  for the system  $N = 300$ ,  $\chi N = 120$ . Stable phase occurs when the corresponding phase has the value of  $g^*/g_{DG}^* > 1$ . HEX and LAM phases are stable in blue and red regions, respectively.

### 3.4 Discussion

Microphase segregation of block copolymers is a rich topic. Experimentally there are many challenges when it comes to exploit all the potential features of these systems to the best. That is why theoretical investigations are still timely. We forwarded the results of SF-SCF calculations for finite chain lengths and complement existing modeling efforts.<sup>6-7</sup> Indeed, most of the predictions mentioned above are fully in line with the common knowledge of microphase segregation. It is not necessary to re-iterate all of these, but a few of these must be mentioned once again. Most prominently we showed finite chain length corrections near the critical region are of order  $1/N$ . These corrections have been established before and it shows that the SF-SCF method is accurate and reliable.

The second aspect of microphase segregation that we focused upon was the stability of the DG phase. We found that at intermediate segregation  $\chi N = 30$  for  $N = 300$  the DG phase has a narrow region of stability in between the HEX and LAM phase. For fixed  $N$ , we

showed that a four-fold increase in  $\chi$  made the stability window to disappear. The later result is not in line with recent SCF calculations which suggested that at high  $\chi N$  the DG should remain stable. We hasten to mention that the high  $\chi N$  limit of 120 can be reached in two ways. Either the chain length is increased at fixed value of the interaction parameter, or the interaction parameter is increased at fixed chain length. We have chosen for the latter. Indeed, by increasing  $\chi$  the width of the interfaces decreases and this may have destabilized the DG phase compared to the HEX or LAM phases, which have curvature-wise more smooth surfaces. It is not excluded that when the chain length would have been increased at fixed  $\chi$ , the outcome could have been different. In such a situation, the interfacial width would have been preserved. More systematic calculations are necessary to make the situation clearer. Such works are in progress.

We may also speculate that the metastability of the DG phase at high  $\chi$  values is due to lattice artifacts. Indeed, when the interfaces sharpen to such an extent that the width of the interface is not wide compared to the discretization, the path followed by the interface may deviate from the best possible path. In other words, the interfaces follow low energy paths provided by the lattice rather than the ones dictated by stretching, area minimization and volume filling. As a result, one would overestimate the free energy density of the phases that cannot optimize the position of the interface with respect to the lattice. We believe that this is not what caused the metastability of the DG to occur in our case, but in order to exclude this option we need to implement a lattice refinement study. This work is postponed to the future.

There are several interesting aspects of the SF-SCF approach for further studying copolymer segregation. There are a number of modifications of the system, which are readily available in the existing implementations of the theory, that allow one to undertake similar studies for: (i) multi-block copolymers, (ii) polydisperse copolymers,<sup>40</sup> (iii) additions of solvents with non-trivial partitioning, (iv) branched or topologically complex chain architectures,<sup>41-42</sup> (v) including longer ranged interactions, for example electrostatic interactions.<sup>43-45</sup>

In the above, we have focused on the stability issue of DG phase, which occurs near the HEX to LAM transition. We believe that the region between spherical and HEX phases is also of interest for further investigations. We have preliminary data showing that a phase of

short dumbbells is stable at high value of  $\chi N$ . Such phases may be isotropic (dumbbells oriented in three, possibly in 6 directions e.g.  $x - y -$  and  $z$  directions as well as in three diagonal directions but also anisotropic (dumbbells oriented all parallel or ordered in two directions e.g. in planes). Such phases may have interesting optical properties when the refractive index of the minority phase is sufficiently different from the majority phase. Work in this direction is in progress.

Finally, we may reflect on the HPL results. We have seen in the calculations that this phase is very robust. We may speculate that this also has a physical interpretation. This might explain why in experimental cases, the HPL phase is relatively frequently reported as being metastable after annealing block copolymer films.<sup>32-33</sup> The HPL phase has the features close to the disconnected spheres when  $f < 0.2$ , it shows features of the hexagonal cylinders at intermediate  $f \approx 0.3$  and it is close to lamellar when  $f \approx 0.5$ . We then take this result to speculate that the HPL phase is an intermediate phase which ‘transports’ the system from one phase into the other. We have seen how it resembles, e.g. the DD when  $f = 0.3$ , we see how it can transform into lamellae when the  $f$  value is larger, or how it can transform the system into a hexagonal phase when the  $f$  value is smaller. Such transitions may be possible upon the addition of a selective solvent which effectively changes the  $f$  value in the system. Such insights may help experimentalists to further explore the micro-phase segregation phenomenon.

## 3.5 Conclusions

---

We have used the SF-SCF formalism to study microphase segregation of block copolymers. Most of our results are in line with previously undertaken SCF studies. We contributed to the problem by focusing on finite chain length effects. We believe that the SF-SCF method is appropriate to investigate microphase segregation of block copolymers and remains accurate at strong segregation because of the non-local contributions in the segment potentials are considered. We analyzed the structure of the LAM phase in the neighborhood of the critical point and reproduced the finite chain length corrections near the critical point. We found that the free energy density and the density difference scales with the distance to the critical point as a power-law. The width on the interface remains finite. We found that at

intermediate segregation the DG phase has a narrow stability region in between the HEX and LAM phases and most significantly we forwarded the prediction that for strong segregation, that is, for high  $\chi$ -values, this stability domain vanishes. We note that the computation strategy is unbiased with respect to the symmetry of the solution. We only need an initial guess and appropriate boundary conditions to focus on a particular solution. The rich structure of the HPL is an example of the type of results that one obtain by the SF-SCF method. The curvature of the lamellae as well as the size of the holes and the undulations in the connectors all vary with the asymmetry ratio  $f$  and these effects made us speculate about the role of HPL to mediate the system from one phase into another.

## Acknowledgements

---

The authors would like to thank Justin Tauber for performing single gyroid and hexagonally perforated lamellae calculations.

## References

---

1. Flory, P. J., *Principles of Polymer Chemistry*. Cornell University Press: Ithaca, NY, USA, 1953.
2. Safran, S. A., *Statistical Thermodynamics of Surfaces, Interfaces, and Membranes*. Addison Wesley: Reading, MA, USA, 1994.
3. Gennes, P.-G., *Scaling Concepts in Polymer Physics*. Cornell University Press: Ithaca, NY, USA, 1979.
4. Scheutjens, J. M. H. M.; Fleer, G. J., Statistical theory of the adsorption of interacting chain molecules. 1. Partition function, segment density distribution, and adsorption isotherms. *The Journal of Physical Chemistry* **1979**, *83* (12), 1619-1635.
5. Scheutjens, J. M. H. M.; Fleer, G. J., Statistical theory of the adsorption of interacting chain molecules. 2. Train, loop, and tail size distribution. *The Journal of Physical Chemistry* **1980**, *84* (2), 178-190.
6. Matsen, M. W.; Bates, F. S., Unifying Weak- and Strong-Segregation Block Copolymer Theories. *Macromolecules* **1996**, *29* (4), 1091-1098.
7. Cochran, E. W.; Garcia-Cervera, C. J.; Fredrickson, G. H., Stability of the Gyroid Phase in Diblock Copolymers at Strong Segregation. Volume 39, Number 7, March, 14, 2006, pp 2449–2451. *Macromolecules* **2006**, *39* (12), 4264-4264.
8. Leermakers, F. A. M.; Scheutjens, J. M. H. M.; Lykklema, J., On the statistical thermodynamics of membrane formation. *Biophysical Chemistry* **1983**, *18* (4), 353-360.
9. Meijer, L. A.; Leermakers, F. A. M.; Nelson, A., Modeling of the electrolyte ion-phospholipid layer interaction. *Langmuir* **1994**, *10* (4), 1199-1206.

10. Meijer, L. A.; Leermakers, F. A. M.; Lyklema, J., Modeling the interactions between phospholipid bilayer membranes with and without additives. *The Journal of Physical Chemistry* **1995**, *99* (47), 17282-17293.
11. Leermakers, F. A. M., Direct evaluation of the saddle splay modulus of a liquid-liquid interface using the classical mean field lattice model. *The Journal of Chemical Physics* **2013**, *138* (12), 124103.
12. Leermakers, F. A. M., Bending rigidities of surfactant bilayers using self-consistent field theory. *The Journal of Chemical Physics* **2013**, *138* (15), 154109.
13. Pera, H.; Kleijn, J. M.; Leermakers, F. A. M., Linking lipid architecture to bilayer structure and mechanics using self-consistent field modelling. *The Journal of Chemical Physics* **2014**, *140* (6), 065102.
14. Chremos, A.; Nikoubashman, A.; Panagiotopoulos, A. Z., Flory-Huggins parameter  $\chi$ , from binary mixtures of Lennard-Jones particles to block copolymer melts. *The Journal of Chemical Physics* **2014**, *140* (5), 054909.
15. Fredrickson, G. H.; Helfand, E., Fluctuation effects in the theory of microphase separation in block copolymers. *The Journal of Chemical Physics* **1987**, *87* (1), 697-705.
16. Khalatur, P. G.; Khokhlov, A. R., Nonconventional scenarios of polymer self-assembly. *Soft Matter* **2013**, *9* (46), 10943-10954.
17. Choi, E.; Park, S.; Ahn, H.; Lee, M.; Bang, J.; Lee, B.; Ryu, D. Y., Substrate-Independent Lamellar Orientation in High-Molecular-Weight Polystyrene-*b*-poly(methyl methacrylate) Films: Neutral Solvent Vapor and Thermal Annealing Effect. *Macromolecules (Washington, DC, U. S.)* **2014**, *47* (12), 3969-3977.
18. Luzzati, V.; Spegel, P. A., Polymorphism of Lipids. *Nature* **1967**, *215* (5102), 701-704.
19. Schoen, A., Infinite periodic minimal surfaces without self-intersections. *NASA Technical Note D-5541* **1970**.
20. Saranathan, V.; Osuji, C. O.; Mochrie, S. G. J.; Noh, H.; Narayanan, S.; Sandy, A.; Dufresne, E. R.; Prum, R. O., Structure, function, and self-assembly of single network gyroid (I4132) photonic crystals in butterfly wing scales. *Proceedings of the National Academy of Sciences* **2010**, *107* (26), 11676-11681.
21. Almsherqi, Z.; Margadant, F.; Deng, Y., A look through 'lens' cubic mitochondria. *Interface Focus* **2012**, *2* (5), 539-545.
22. Vignolini, S.; Yufa, N. A.; Cunha, P. S.; Guldin, S.; Rushkin, I.; Stefik, M.; Hur, K.; Wiesner, U.; Baumberg, J. J.; Steiner, U., A 3D Optical Metamaterial Made by Self-Assembly. *Adv. Mater.* **2012**, *24* (10), OP23-OP27.
23. Thomas, E. L.; Alward, D. B.; Kinning, D. J.; Martin, D. C.; Handlin, D. L.; Fetters, L. J., Ordered bicontinuous double-diamond structure of star block copolymers: a new equilibrium microdomain morphology. *Macromolecules* **1986**, *19* (8), 2197-2202.
24. Hajduk, D. A.; Harper, P. E.; Gruner, S. M.; Honeker, C. C.; Kim, G.; Thomas, E. L.; Fetters, L. J., The Gyroid: A New Equilibrium Morphology in Weakly Segregated Diblock Copolymers. *Macromolecules* **1994**, *27* (15), 4063-4075.
25. Schulz, M. F.; Bates, F. S.; Almdal, K.; Mortensen, K., Epitaxial Relationship for Hexagonal-to-Cubic Phase Transition in a Block Copolymer Mixture. *Phys. Rev. Lett.* **1994**, *73* (1), 86-89.
26. Crossland, E. J. W.; Kamperman, M.; Nedelcu, M.; Ducati, C.; Wiesner, U.; Smilgies, D. M.; Toombes, G. E. S.; Hillmyer, M. A.; Ludwigs, S.; Steiner, U.; Snaith, H. J., A Bicontinuous Double Gyroid Hybrid Solar Cell. *Nano Letters* **2009**, *9* (8), 2807-2812.

27. Ndoni, S.; Vigild, M. E.; Berg, R. H., Nanoporous Materials with Spherical and Gyroid Cavities Created by Quantitative Etching of Polydimethylsiloxane in Polystyrene–Polydimethylsiloxane Block Copolymers. *Journal of the American Chemical Society* **2003**, *125* (44), 13366-13367.
28. Dair, B. J.; Honeker, C. C.; Alward, D. B.; Avgeropoulos, A.; Hadjichristidis, N.; Fetters, L. J.; Capel, M.; Thomas, E. L., Mechanical Properties and Deformation Behavior of the Double Gyroid Phase in Unoriented Thermoplastic Elastomers. *Macromolecules* **1999**, *32* (24), 8145-8152.
29. Nykänen, A.; Nuopponen, M.; Laukkanen, A.; Hirvonen, S.-P.; Rytelä, M.; Turunen, O.; Tenhu, H.; Mezzenga, R.; Ikkala, O.; Ruokolainen, J., Phase Behavior and Temperature-Responsive Molecular Filters Based on Self-Assembly of Polystyrene-block-poly(N-isopropylacrylamide)-block-polystyrene. *Macromolecules* **2007**, *40* (16), 5827-5834.
30. Epps, T. H.; Cochran, E. W.; Bailey, T. S.; Waletzko, R. S.; Hardy, C. M.; Bates, F. S., Ordered Network Phases in Linear Poly(isoprene-b-styrene-b-ethylene oxide) Triblock Copolymers. *Macromolecules* **2004**, *37* (22), 8325-8341.
31. Wang, C.-Y.; Lodge, T. P., Kinetics and Mechanisms for the Cylinder-to-Gyroid Transition in a Block Copolymer Solution. *Macromolecules* **2002**, *35* (18), 6997-7006.
32. Khandpur, A. K.; Foerster, S.; Bates, F. S.; Hamley, I. W.; Ryan, A. J.; Bras, W.; Almdal, K.; Mortensen, K., Polyisoprene-Polystyrene Diblock Copolymer Phase Diagram near the Order-Disorder Transition. *Macromolecules* **1995**, *28* (26), 8796-8806.
33. Tavakkoli K. G. A.; Nicaise, S. M.; Hannon, A. F.; Gotrik, K. W.; Alexander-Katz, A.; Ross, C. A.; Berggren, K. K., Sacrificial-Post Templating Method for Block Copolymer Self-Assembly. *Small* **2014**, *10* (3), 493-499.
34. Hasegawa, H.; Tanaka, H.; Yamasaki, K.; Hashimoto, T., Bicontinuous microdomain morphology of block copolymers. 1. Tetrapod-network structure of polystyrene-polyisoprene diblock polymers. *Macromolecules* **1987**, *20* (7), 1651-1662.
35. Winey, K. I.; Thomas, E. L.; Fetters, L. J., The ordered bicontinuous double-diamond morphology in diblock copolymer/homopolymer blends. *Macromolecules* **1992**, *25* (1), 422-428.
36. Meuler, A. J.; Hillmyer, M. A.; Bates, F. S., Ordered Network Mesostuctures in Block Polymer Materials. *Macromolecules* **2009**, *42* (19), 7221-7250.
37. Snyman, J., *Practical Mathematical Optimization: An Introduction to Basic Optimization Theory and Classical and New Gradient-Based Algorithms*. Springer Publishing: NY, USA, 2005.
38. Ionova, I. V.; Carter, E. A., Error vector choice in direct inversion in the iterative subspace method. *Journal of Computational Chemistry* **1996**, *17* (16), 1836-1847.
39. Semenov, A. N., Theory of block copolymer interfaces in the strong segregation limit. *Macromolecules* **1993**, *26* (24), 6617-6621.
40. de Vos, W. M.; Leermakers, F. A. M., Modeling the structure of a polydisperse polymer brush. *Polymer* **2009**, *50* (1), 305-316.
41. Wijmans, C. M.; Zhulina, E. B.; Fleer, G. J., Effect of Free Polymer on the Structure of a Polymer Brush and Interaction between Two Polymer Brushes. *Macromolecules* **1994**, *27* (12), 3238-3248.
42. Leermakers, F. A. M.; Egorov, S. A., On the collapse transition of a polymer brush: the case of lateral mobility. *Soft Matter* **2013**, *9* (12), 3341-3348.
43. Lauw, Y.; Leermakers, F. A. M.; Cohen Stuart, M. A.; Borisov, O. V.; Zhulina, E. B., Coexistence of Crew-Cut and Starlike Spherical Micelles Composed of Copolymers with an Annealed Polyelectrolyte Block. *Macromolecules* **2006**, *39* (10), 3628-3641.

## Chapter 3

44. Israels, R.; Leermakers, F. A. M.; Fler, G. J., On the Theory of Grafted Weak Polyacids. *Macromolecules* **1994**, *27* (11), 3087-3093.
45. Borisov, O. V.; Zhulina, E. B.; Leermakers, F. A. M.; Müller, A. H. E., Self-Assembled Structures of Amphiphilic Ionic Block Copolymers: Theory, Self-Consistent Field Modeling and Experiment. In *Self Organized Nanostructures of Amphiphilic Block Copolymers I*, Müller, A. H. E.; Borisov, O., Eds. Springer Berlin Heidelberg: Berlin, Heidelberg, 2011; pp 57-129.

## APPENDIX

---

### Details of the Scheutjens-Fleer self-consistent field method

Let us consider lattice sites with length of  $b$  and volume of  $v = b^3$ . Below all linear lengths are given in units of  $b$ . Space is built up by a simple cubic ordering of these sites. Introducing a Cartesian coordinate system of lattice sites,  $x = 1, 2, \dots, L_x$ ,  $y = 1, 2, \dots, L_y$  and  $z = 1, 2, \dots, L_z$ . We will refer to a particular site by  $\mathbf{r} = (x, y, z)$ . The dimensionless volume of the system (box) is given by  $V = L_x L_y L_z$ . The idea of the specified volume is that it will represent a unit cell of the system of interest. To properly implement this, we need boundary conditions. As these boundary conditions depend on the type of system that is aimed for, we will pay attention to this separately below.

In this system, we introduce flexible copolymer chains which are built up by a linear string of spherically symmetric segments such that each segment occupies one lattice site. Let the composition be given by  $A_{N_A} B_{N_B}$  where segments  $s = 1, 2, \dots, N_A$  are of type A and the remainder of the segments are of type B, i.e., for  $s = N_A + 1, \dots, N$ , where the total number of segments per chain is given by  $N = N_A + N_B$ . Hence, the fraction of A segments is given by  $f = \frac{N_A}{N_A + N_B}$ . Below we will adopt the freely jointed chain (FJC) model to describe the chain statistics. In this model, two consecutive segments along the chain occupy neighboring lattice sites, but longer ranged correlations are ignored.

Below we will use a mean field approximation. In such an approach the key quantity is the probability that a site is filled with segment type A or B and will be given by volume fractions of the  $\varphi_A$  and  $\varphi_B$ , respectively. One way to envision such volume fractions is that we consider not just one box, but an ensemble of boxes and that the focus is on the ensemble average.

It is a good approximation to consider most liquids as incompressible. This also applies to copolymer melts. We therefore implement an incompressibility condition on each site. This means that we are only interested in the solution for which at each coordinate  $\mathbf{r}$ , when  $\varphi_A(\mathbf{r}) + \varphi_B(\mathbf{r}) = 1$ .

### Chapter 3

It is convenient to define so-called site averages, e.g. for the segment density, which is denoted by angular brackets and encompasses an average of the volume fractions over the nearest neighbor coordinates:

$$\begin{aligned} \langle \phi(x, y, z) \rangle = \frac{1}{6} [ & \phi(x - 1, y, z) + \phi(x + 1, y, z) + \phi(x, y - 1, z) \\ & + \phi(x, y + 1, z) + \phi(x, y, z - 1) + \phi(x, y, z + 1) ] \end{aligned} \quad (\text{A1})$$

It is known that in the limit of small lattice spacings (weak gradients) the site average accounts for the local density as well as the curvature of the density in three directions:

$$\langle \phi(\mathbf{r}) \rangle = \phi(\mathbf{r}) + \frac{1}{6} \nabla^2 \phi(\mathbf{r}) \quad (\text{A2})$$

In an exact lattice theory, the sites are filled either by a segment A or B and the local segment interactions should be evaluated accordingly to the instantaneous surroundings. Within mean field approximations, the exact counting of contacts is replaced by an estimated counting using probabilities that sites are filled, e.g. based on the volume fractions. This simplifies the evaluation of the partition function because it then boils down to the evaluation of the so-called single chain partition functions,  $q$ , wherefore the molecules feel the surroundings by potential fields. Hence, in the mean field theory there are, complementary to the volume fractions, so called segment potentials  $u_A(\mathbf{r})$  and  $u_B(\mathbf{r})$ , 'felt' by the A and B segments, respectively. It can be shown that the mean field free energy ( $G$ ) in terms of the volume fraction and segment potentials can be written as below which is specified in units of the thermal energy  $k_B T$ .

$$\begin{aligned} G = -\ln \frac{q^n}{n!} - \sum_{\mathbf{r}} \{ & u_A(\mathbf{r}) \varphi_A(\mathbf{r}) + u_B(\mathbf{r}) \varphi_B(\mathbf{r}) \} + \sum_{\mathbf{r}} \frac{1}{2} \chi [ \varphi_A(\mathbf{r}) \langle \varphi_B(\mathbf{r}) \rangle \\ & + \varphi_B \langle \varphi(\mathbf{r}) \rangle ] + \sum_{\mathbf{r}} \alpha(\mathbf{r}) \{ \varphi_A(\mathbf{r}) + \varphi_B(\mathbf{r}) - 1 \} \end{aligned} \quad (\text{A3})$$

Here,  $n = V/N$  is the number of copolymers in the volume. The factor  $\frac{1}{2}$  is present to correct for the double counting as the two terms within the square brackets are the same after summation over  $\mathbf{r}$  has taken place. The incompressibility constraint is added to the mean field free energy through the use of a Lagrange parameter  $\alpha(\mathbf{r})$ . This will allow for an easier

differentiation of the mean field free energy. It turns out that we need a saddle point of  $G$ , that is we need a maximum of  $G$  with respect to the segment potentials and the Lagrange field and a minimum with respect to the volume fractions. The search for such a saddle point leads to the self-consistent field protocol, which specifies (i) the rule how to compute the segment potentials from the volume fraction, (ii) the rule how to compute the volume fractions from the potentials and finally (iii) how to find the value for the Lagrange field. These rules will be discussed in the following sections. After the free energy is optimized we can simplify it and make sure that it is normalized such that when the system turns homogenous, the free energy vanishes. We will return to this below.

When we take the derivative of Equation A3 with respect to the volume fractions and set the result to zero we find an equation for the segment potential. The result for segment type A is

$$\frac{\partial G}{\partial \varphi_A(\mathbf{r})} = -u_A(\mathbf{r}) + \alpha(\mathbf{r}) + \chi \langle \varphi_B(\mathbf{r}) \rangle = 0 \quad (\text{A4})$$

Note that in the segment potentials, the interaction term is including curvature information through the angular brackets. Again, when the curvature in the volume fractions is minor we find that  $u_A(\mathbf{r}) = \alpha(\mathbf{r}) + \chi \varphi_B(\mathbf{r})$ , and this form of the potential is used classically in the field of block copolymer self-assembly. Typically, we will normalize the potentials such that when the system is homogeneous, the potentials are zero, hence in practice we use

$$u_A(r) = \alpha(r) + \chi (\langle \varphi_B(r) \rangle - (1 - f)) \quad (\text{A5a})$$

$$u_B(r) = \alpha(r) + \chi (\langle \varphi_A(r) \rangle - f) \quad (\text{A5b})$$

The optimization of the mean field free energy with respect to the segment potentials lead to the rule how to compute the volume fractions:

$$\frac{\partial G}{\partial u_A(\mathbf{r})} = -\frac{n \partial \ln q}{\partial u_A(r)} - \varphi_A(\mathbf{r}) = 0 \quad (\text{A6})$$

Hence, we need the evaluation of the molecular partition function  $q$ . It turns out that subsequent differentiation of the  $\ln q$  is not needed because the propagator formalism gives besides the value of  $q$  also the volume fractions.

### Chapter 3

It is convenient to introduce the Boltzmann weights  $G_A(\mathbf{r}) = \exp -u_A(\mathbf{r})$  and  $G_B(\mathbf{r}) = \exp -u_B(\mathbf{r})$ . Next, we introduce so-called free segment distribution functions  $G(\mathbf{r}, s) = G_A(\mathbf{r})$  when segment  $s = 1, 2, \dots, N_A$  is of type A and  $G(\mathbf{r}, s) = G_B(\mathbf{r})$  otherwise. These quantities are used to compute so-called end-point distribution functions  $G(\mathbf{r}, s|1)$  or  $G(\mathbf{r}, s|N)$  with the propagator equations

$$G(\mathbf{r}, s|1) = G(\mathbf{r}, s)\langle G(\mathbf{r}, s-1|1) \rangle \quad (\text{A7a})$$

$$G(\mathbf{r}, s|N) = G(\mathbf{r}, s)\langle G(\mathbf{r}, s+1|N) \rangle \quad (\text{A7b})$$

which are started by realizing that at the ends of the chain, we can use the free segment distributions:

$$G(\mathbf{r}, 1|1) = G(\mathbf{r}, 1) \quad (\text{A8a})$$

$$G(\mathbf{r}, N|N) = G(\mathbf{r}, N) \quad (\text{A8b})$$

In passing we note that when we Taylor expand the free segment distribution function  $G(\mathbf{r}, s) = 1 - u(\mathbf{r}, s)$  and replace the angular brackets as in Equation A3 with the local end-point distribution plus the curvature contribution, we can rewrite the right-hand side of Equation A7 and obtain 4 terms on the right-hand side. Neglecting the product of the potentials and the second derivative (both should be small) we can arrange the result and obtain the Edwards diffusion equation.<sup>1</sup>

$$\frac{\partial G}{\partial s} = \frac{1}{6} \nabla^2 G - uG \quad (\text{A9})$$

Note that the latter equation is applicable for Gaussian chains, whereas the propagators are representing FJC's. There is only a noticeable difference between the Gaussian chain and the FJC when the chains become strongly stretched in the limit of their contour length. This will not easily occur for block copolymer self-assembly.

The partition function can now be computed by:

$$q = \sum_{\mathbf{r}} G(\mathbf{r}, N|1) = \sum_{\mathbf{r}} G(\mathbf{r}, 1|N) \quad (\text{A10})$$

and the combination of two complementary end-point distribution functions leads to the segment densities:

$$\varphi(\mathbf{r}, s) = \frac{n G(\mathbf{r}, s|1)G(\mathbf{r}, s|N)}{q G(\mathbf{r}, s)} \quad (\text{A11})$$

In this equation, the division by  $G(\mathbf{r}, s)$  is needed to prevent that the statistical weight for the segment  $s$  is counted twice. Finally, the volume fractions of the segment types become:

$$\varphi_A(\mathbf{r}) = \sum_{s=1}^{N_A} \varphi(\mathbf{r}, s) \quad (\text{A12a})$$

$$\varphi_B(\mathbf{r}) = \sum_{s=N_A+1}^N \varphi(\mathbf{r}, s) \quad (\text{A12b})$$

Optimization of the free energy (Equation 3) to the Lagrange parameter  $\alpha(\mathbf{r})$  gives the compressibility constraint (Equation 1). Below we discuss the iteration scheme, but part of this is the need to know the Lagrange field. This quantity is updated at iteration  $k$  simply by adding the constraint:

$$\alpha(\mathbf{r})^{(k)} = \alpha(\mathbf{r})^{(k-1)} + \eta(\varphi_A(\mathbf{r})^{(k)} + \varphi_B(\mathbf{r})^{(k)} - 1) \quad (\text{A13})$$

The idea behind Equation A13 is the following. When the local volume fractions do not add up to unity, the value of the Lagrange field should be adjusted. When the overall volume fraction (density) exceeds unity, we need to push segments away from that coordinate. This is done by increasing  $\alpha$ . Inversely, when the volume fraction is less than unity we need to attract segments to this site. We do this by decreasing  $\alpha$ . Equation A13 exactly will do this. In Equation A13,  $\eta < 1$  is a damping parameter. Typically, a value of 0.1 is needed to find smooth convergence.

The above set of equations is closed. As mentioned already, we need an iteration to find the fixed point. Let's define the interaction term,  $E_A(\mathbf{r}) = u_A(\mathbf{r}) - \alpha(\mathbf{r})$  and  $E_B(\mathbf{r}) = u_B(\mathbf{r}) - \alpha(\mathbf{r})$ . According to Equation 5, we can compute this interaction term when the volume fractions are available. Let's assume that at iteration of  $k - 1$ , we have the interaction terms  $E_A(\mathbf{r})^{(k-1)}$  and  $E_B(\mathbf{r})^{(k-1)}$  as well as the potentials  $u_A(\mathbf{r})^{(k-1)}$  and  $u_B(\mathbf{r})^{(k-1)}$ . The latter ones

are used to compute volume fractions (cf Equation A12)  $\varphi_A(r)^{(k)}$  and  $\varphi_B(r)^{(k)}$ . With these we may evaluate  $E_A(r)^{(k)}$  and  $E_B(r)^{(k)}$ . Next, we use Equation A13 to find an update for the Lagrange field  $\alpha(r)^{(k)}$  and update the segment potentials, e.g. for segment type A, according to the Pikar mixing:

$$u_A(r)^{(k)} = \alpha(r)^{(k)} + \eta E_A(r)^{(k)} + (1 - \eta) E_A(r)^{(k-1)} \quad (\text{A14})$$

Now the loop is closed and we can continue until the potential fields as well as the segment volume fractions between two consecutive iterations differ less than a tolerance value. We typically continue until we have 7 significant digits. Note that is Pikar-like iteration does not require the storage of a large matrix and hence can be used also for three-gradient applications.

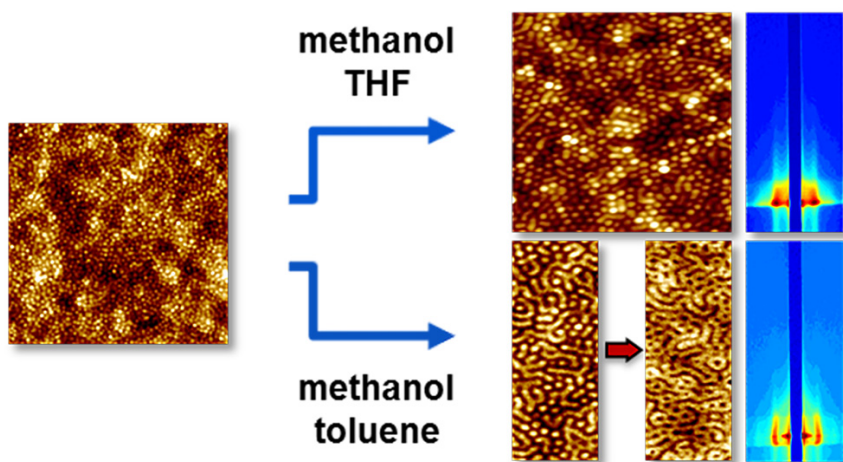
In practice, we do not use this Pikar scheme because it needs relatively many iterations. Instead we use target functions specified by Evers *et al.*<sup>2</sup> and use the DIIS algorithm<sup>3</sup> to find the fixed point. The method is remarkable fast and typically requires only an order of 100 iterations and even for 3-gradient applications one obtains solutions within a few minutes CPU time. When necessary the procedure can be implemented on graphical cards which for large enough systems can lead to improvements in wall time by a factor of 5 to 10.

## References

1. Edwards, S. F., The statistical mechanics of polymers with excluded volume. *Proceedings of the Physical Society* **1965**, 85 (4), 613.
2. Evers, O. A.; Scheutjens, J. M. H. M.; Fleer, G. J., Statistical thermodynamics of block copolymer adsorption. 1. Formulation of the model and results for the adsorbed layer structure. *Macromolecules* **1990**, 23 (25), 5221-5233.
3. Ionova, I. V.; Carter, E. A., Error vector choice in direct inversion in the iterative subspace method. *Journal of Computational Chemistry* **1996**, 17 (16), 1836-1847.

# CHAPTER 4

## Self-assembly of PS-*b*-PNIPAM-*b*-PS block copolymer thin films *via* selective solvent annealing



---

Published as:

Cetintas, M.; Kamperman, M. Self-assembly of PS-*b*-PNIPAM-*b*-PS block copolymer thin films *via* selective solvent annealing. *Polymer* **2016**, *107*, 387-397.

## 4.1 Abstract

---

Block copolymer (BCP) thin films are interesting material systems for nanofabrication since they can form well-defined periodic nanostructures by microphase separation. However, attaining a specific morphology with the required orientation can be challenging. In this study, we investigated the morphological behavior of polystyrene-*b*-poly(*N*-isopropylacrylamide)-*b*-polystyrene (PS-*b*-PNIPAM-*b*-PS) BCP thin films by using atomic force microscopy (AFM) and *in-situ* grazing-incidence X-ray scattering (GISAXS) during selective solvent annealing. Thin films of a lamellar BCP were annealed by using various solvents with different selectivity for the blocks, such as PNIPAM-selective methanol, non-selective tetrahydrofuran (THF) and PS-selective toluene. Solvent annealing using methanol: THF 1:2 (v:v) or methanol: toluene 1:1 (v:v) resulted in the formation of hexagonally ordered perpendicular cylinders, whereas no sustained long-range order was found when only one type of solvent was used. PS-*b*-PNIPAM-*b*-PS BCP thin films that have hexagonally ordered perpendicular cylinders are promising for applications where thermo-responsiveness is desired, such as nanofiltration and biomedical applications.

## 4.2 Introduction

---

Block copolymer (BCP) thin films having a hexagonally ordered cylindrical morphology, with the cylinders oriented perpendicular to the substrate, are attractive for many applications such as nanoporous membranes<sup>1</sup>, pattern transfer<sup>2</sup> and nanolithography<sup>3</sup>. These applications often require that the films are well-ordered and maintain perpendicular orientation over large areas, which can be obtained by using annealing techniques. The most widely used annealing techniques are thermal and solvent annealing. In these techniques, either the temperature of the thin film is increased over the glass transition temperature ( $T_g$ ) of the blocks or solvent vapor acts as a plasticizer on the BCP and reduces the  $T_g$  of the blocks below room temperature which causes an increase in chain mobility. As a consequence, the lateral ordering of the BCP microdomains is significantly promoted. Although thermal annealing is an effective method to create ordered morphologies<sup>4-11</sup>, application of high temperatures to BCP thin films may result in the degradation of one or more blocks, causing the final morphology to deteriorate.<sup>12-20</sup> This can also bring a loss to the long-range ordering of the morphology.<sup>16-17, 21</sup>

Solvent annealing, does not pose any risk of polymer degradation, is faster<sup>22-23</sup> and introduces structures which are not approachable using thermal annealing.<sup>18-20, 24-27</sup> Solvent annealing also offers the possibility to choose solvents selective for one of the blocks in the copolymer.<sup>19, 26, 28-36</sup> A selective solvent swells one block more than the other block(s) causing an increase in the effective volume fraction of that block during the annealing process. In this way, it is possible to shift through the BCP phase diagram to different regions which correspond to different morphologies without changing the molecular weight or block ratio of the copolymer.<sup>20, 23, 37-38</sup> Thus, selective solvent annealing is a useful approach to achieve non-equilibrium morphologies without the need of more than one BCP.<sup>35</sup> For example, Chavis *et al.* used one poly(2-hydroxyethyl methacrylate)-*b*-poly(methyl methacrylate) (PHEMA-*b*-PMMA) BCP to create four different morphologies including hexagonally ordered cylinders by using selective solvent annealing<sup>31</sup>. Precise control of selective solvents was also used to shift to different morphologies during annealing of polystyrene-*b*-poly(2-vinylpyridine) (PS-P2VP) BCPs as reported by Park *et al.*<sup>33</sup>

An additional interesting feature of using selective solvents is that the orientation of the cylindrical morphologies may be modified.<sup>26, 36, 38-40</sup> For PS-*b*-P4VP BCPs, parallel cylinders were obtained using the non-selective solvent chloroform whereas cylinders oriented perpendicularly in case of using the PS block selective solvent 1,4-dioxane.<sup>38-39</sup> Brendel *et al.* showed a perpendicular cylindrical morphology for a semiconductor BCP by annealing with a selective solvent which was not possible to attain with thermal annealing methods.<sup>40</sup> Similarly, Berezkin *et al.* reported that a certain selectivity of the annealing solvents is necessary for perpendicular orientation of the cylinders while thermal annealing was only able to produce parallel cylinders.<sup>26</sup>

In this work, we study the effect of selective solvent annealing on a stimuli-responsive BCP system. Stimuli-responsive thin films are used in various applications such as stimuli-responsive nanoporous membranes<sup>41</sup>, chemical sensors for microelectromechanical systems (MEMS), drug release systems, actuators in biomedical applications<sup>42-43</sup>, nanolithography<sup>44</sup> and cell adhesion.<sup>45</sup> Stimuli-responsive thin films are often prepared by grafting a stimuli-responsive polymer to the surface. However, the use of BCPs, containing one or more responsive blocks, forms an interesting alternative.<sup>43</sup>

There exist several solvent annealing studies of BCPs containing pH responsive blocks, including polyacrylic acid (PAA)<sup>46</sup>, P2VP and P4VP<sup>28, 33, 38, 47-51</sup>, and pH and temperature dual-responsive blocks, including poly(*N,N'*-dimethylaminoethylmethacrylate) (PDMAEMA) and poly(*N,N'*-diethylaminoethylmethacrylate) (PDEAEMA).<sup>52</sup> One of the most widely used thermo-responsive blocks in BCPs is poly(*N*-isopropylacrylamide) (PNIPAM) which has a lower critical solution temperature (LCST) at 32 °C. Thomas *et al.* investigated the morphological properties of bulk films of protein-PNIPAM BCPs using selective solvent annealing.<sup>53</sup> In addition, PS-PNIPAM BCPs were successfully used for thermo-responsive nanofiltration purposes<sup>1</sup>, cell adhesion and growth studies for biomedical applications.<sup>54</sup> However, to the best of our knowledge, there is no systematic study for solvent annealing for PS-*b*-PNIPAM-*b*-PS BCP thin films using selective solvent systems.

In our study, we fabricated PS-*b*-PNIPAM-*b*-PS BCP thin films which were annealed using various selective solvents. The morphologies of the thin films were analyzed using Atomic force microscopy (AFM) and *in-situ* grazing incidence X-ray scattering (GISAXS) techniques. We show that by solvent annealing in methanol-THF or methanol-toluene solvent mixtures, a hexagonally ordered cylindrical morphology, with the cylinders oriented perpendicular to the substrate, can be obtained from a lamellar BCP thin film. Having the ability to control the order and to maintain the perpendicular orientation of temperature-responsive BCP thin films is particularly promising for membrane applications.

## 4.3 Experimental Section

---

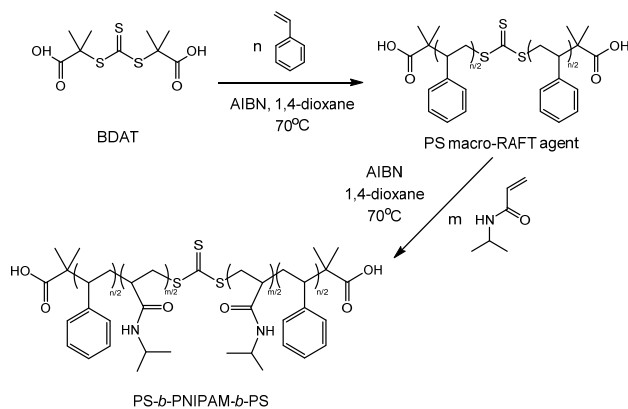
### 4.3.1 Materials

Styrene (Sigma-Aldrich, >99%) was vacuum distilled after stirring overnight over calcium hydride. *N*-isopropylacrylamide (NIPAM, Sigma-Aldrich, 97%) was purified by recrystallization from toluene. 2,2'-Azobis(2-methylpropionitrile) (AIBN, Sigma-Aldrich, 98%) was recrystallized from methanol. Diethylether (Biosolve), methanol (Fisher Scientific), tetrahydrofuran (THF), 1,4-dioxane and toluene (Sigma-Aldrich) were used without further purification.

### 4.3.2 Synthesis

**4.3.2.1 Synthesis of PS macro-RAFT agent.** A difunctional RAFT agent *S,S'*-bis(*a,a'*-dimethyl-*a''*-acetic acid) trithiocarbonate (BDAT) was synthesized by using the method reported by Lai *et al.*<sup>55</sup> and characterized by <sup>1</sup>H NMR and <sup>13</sup>C NMR. The synthesis of the PS macro-RAFT agent and the copolymer were based on the procedure reported by Nykänen *et al.*<sup>1</sup> BDAT (0.7 mM, 14 mg), freshly distilled styrene (2.2 M, 16 g) and AIBN (0.8 mM, 9.2 mg) were dissolved in 70 mL of 1,4-dioxane by stirring at room temperature. The solution was transferred to a Schlenk ampoule by using syringes. After degassing with three successive freeze-pump-thaw cycles by using a high vacuum Schlenk line, the solutions were heated to 70 °C with a temperature controlled oil bath. The solution was allowed to polymerize for 48 hours. The reaction was stopped by cooling the ampoules in liquid nitrogen. The product was precipitated twice in cold methanol and dried in a vacuum oven at room temperature overnight to give a white-yellowish powder (22% yield). <sup>1</sup>H NMR (CDCl<sub>3</sub>): 6.2-7.1 (Ar-5H), 1.2-2.4 (3H, PS backbone). GPC:  $M_n = 57$  kDa, PDI = 1.42.

**4.3.2.2 Synthesis of PS-*b*-PNIPAM-*b*-PS copolymers.** The PS macro-RAFT agent (3 g, 1.2 mM), NIPAM (6 g, 0.9 M) and AIBN (1.99 mg, 0.206 mM) were dissolved in 60 mL of 1,4-dioxane. The solution was degassed by three successive freeze-pump-thaw cycles and heated in a temperature controlled oil bath to 70 °C for 18 h. The reaction was stopped by cooling the reaction mixture in liquid nitrogen. 1,4-dioxane was removed with a rotary evaporator after which the BCP was dissolved in THF. The BCP was reprecipitated from diethyl ether and cold water, respectively. The precipitant obtained from diethyl ether precipitation was separated by centrifuging with PTFE centrifuge tubes and decantation. The product was separated from the homopolymer PNIPAM by centrifugation (45 min, 5000 rpm) three times. The purified copolymer was freeze-dried giving 41% yield. The molar ratio of the PS:PNIPAM blocks is equal to 0.90 which was calculated from the NMR data. This corresponds to a PS weight fraction 0.45 and a PS volume fraction ( $f_{PS}$ ) of 0.44 (using  $\rho_{PS} = 1.05$  g/cm<sup>3</sup>,<sup>56</sup> and  $\rho_{PNIPAM} = 1.10$  g/cm<sup>3</sup>,<sup>57</sup>). <sup>1</sup>H NMR (CDCl<sub>3</sub>): 6.2-7.1 (Ar-5H), 4.0 (1H, -NCH-), 0.8-2.5 (3H, PS backbone and 9H, PNIPAM -CH<sub>3</sub> and the backbone). GPC:  $M_n = 127$  kDa, PDI = 1.40.

**Scheme 1.** Synthesis route of PS-*b*-PNIPAM-*b*-PS BCP

### 4.3.3 Polymer characterization

$^1\text{H}$  NMR measurements were carried out on a Bruker AMX-400 spectrometer (400 MHz) at room temperature. The ratio between PS and PNIPAM blocks in the BCP was determined by comparing the integral of the aromatic PS protons at 6.2–7.1 ppm (5H, Ar-H) to the lone PNIPAM proton at 4.0 ppm (1H, -NCH). Gel permeation chromatography (GPC) of the polymers was carried out by using a set-up consisting of an Agilent Technologies 1200 series gel permeation chromatograph, a PLgel 5  $\mu\text{m}$  Mixed-D column (Mw range 200–400,000 Da, Polymer Laboratories Ltd.) and an Agilent 1200 differential refractometer. The column was calibrated by using PS standards. An amount of 100  $\mu\text{L}$  of each sample was injected into the THF eluent at 30  $^\circ\text{C}$  and a flow rate of 1 mL/min.

### 4.3.4 Bulk film preparation

A 3 wt% copolymer solution in THF was prepared and stirred overnight for full dissolution. The solution was poured into a PTFE beaker. This beaker was transferred to a desiccator, containing a beaker full of THF, which forms the desired solvent atmosphere, and solvent annealed for 2 weeks. After annealing, the THF beaker was taken out and the film was transferred to a vacuum oven where vacuum was applied slowly for 6 hours at room temperature. Then the temperature of the vacuum oven was increased stepwise first to 40  $^\circ\text{C}$  and then to 60  $^\circ\text{C}$ . The beaker was kept under vacuum at 60  $^\circ\text{C}$  for at least 18 hours. Then

Self-assembly of PS-*b*-PNIPAM-*b*-PS thin films *via* selective solvent annealing cooled to room temperature after which the vacuum was released, yielding a solid film without any air bubbles.

#### 4.3.5 Thin film preparation

Films were deposited from 2 wt% solutions of copolymer by spin-coating on Si wafers at 3500 rpm for 15 seconds with a Laurell WS-650MZ-23NPP spin-coater in N<sub>2</sub> atmosphere. 1 × 1 cm and 2 × 2 cm sized Si wafers were used for solvent annealing experiments in the desiccator and for *in-situ* GISAXS experiments, respectively. Solvent annealing was stopped by fast quenching, which was executed by opening the cap of the desiccator and removing all the solvent from the desiccator. Si wafers were pre-treated with piranha solution (*attention: highly oxidizing!*) and stored in a methanol-water solution and rinsed with acetone just before use. THF was used as the solvent for the preparation of the solutions for spin-coating unless stated otherwise. The thickness of the films was measured with spectroscopic ellipsometry (Sentech Instruments GmbH) at an incidence angle of 70° with a wavelength of 632.8 nm and was found to be around 100 nm. The spin-coated films that were not used for *in-situ* GISAXS experiments were annealed at room temperature in a desiccator saturated with solvent or with a solvent mixture for a certain amount of time.

#### 4.3.6 Atomic force microscopy (AFM)

The surface morphology of the films was analyzed with a Bruker Multimode 8 AFM instrument using the Nanoscope V ScanAsyst imaging mode. DNP-10 model non-conductive silicon nitride probes with a spring constant of 0.24 N/m (Bruker) were used. Images were recorded at a frequency of 1.50 Hz and NanoScope Analysis 1.5 software was used for the processing of the data. At least three different regions on the same thin film sample were probed to assure that the obtained surface morphology was representative for the entire sample.

#### 4.3.7 Small angle X-ray scattering (SAXS)

Small angle X-ray scattering measurements were performed on a SAXSLAB GANESHA 300 XL SAXS system equipped with a GeniX 3D Cu Ultra Low Divergence micro focus sealed tube source. The wavelength  $\lambda$  was 1.54 Å at a flux of  $1 \times 10^8$  photons/s. A Pilatus 300K sili-

con pixel detector with  $487 \times 619$  pixels and a size of  $172 \times 172 \mu\text{m}$  was placed at a sample-to-detector distance of 1513 mm. Silver behenate was used for calibration of the beam center and the  $q$ -range. The calibrated detector response function was used together with the known sample-to-detector distance, measured incident and transmitted beam intensities, to bring the two-dimensional SAXS patterns to an absolute intensity scale. The corrected SAXS patterns were azimuthally averaged to obtain one dimensional SAXS profiles. SAXS-GUI v2.13 software was used to analyze the data.

### 4.3.8 Grazing incidence small angle X-ray scattering (GISAXS)

*In-situ* GISAXS experiments were carried out at beamline D1 at the Cornell High Energy Synchrotron Source (CHESS) at Cornell University, Ithaca, New York, USA. The wavelength  $\lambda$  was 0.1162 nm and the beam size  $0.5 \text{ mm} \times 0.1 \text{ mm}$ . A CCD camera with a pixel size of  $46.9 \mu\text{m}$  was used as detector and placed at a sample-to-detector distance of 1825 mm. The sample was placed in a custom-made annealing chamber having a volume of 110 mL. 3 mL of solvent was injected into the chamber. Two or three exposures were taken before injection of the solvent and every 5 minutes during the annealing process. The sample was being moved to a previously unexposed area after around 10 exposures to avoid beam damage of the sample. The annealing chamber was connected to a flowmeter which was used to control the evaporation rate of the solvent inside the chamber.<sup>58</sup> It was equipped with a FilMetrics F30 optical spectroscopic reflectometer for monitoring the thickness of the films during the annealing process. The spots where the thickness was measured were not exposed to X-rays.

ProcessGIXS 8 software was used to analyze the data. Error bars in Figure 7 and Figure 10 were calculated by taking the standard deviation between the second order polynomial fit and the raw data of around 20 data points. Since the resulting error bars were smaller than the size of the marker on the graph, they were not plotted in the figures.

## 4.4 Results and Discussion

---

In this work, we aim to fabricate PS-*b*-PNIPAM-*b*-PS thin films having a cylindrical morphology with hexagonal perpendicular alignment by using solvent annealing. We explore

Self-assembly of PS-*b*-PNIPAM-*b*-PS thin films *via* selective solvent annealing the effect of several selective solvents and combinations of them on the ordering of the BCP thin films. Common laboratory solvents were selected, i.e. THF, methanol and toluene. The vapor pressures of all solvents are similar except for toluene, which has a lower vapor pressure as shown in Table 1.<sup>59</sup> Since slow drying of the swollen film will often lead to changes in the final morphology of the block copolymer thin film,<sup>27</sup> we rapidly quenched the films to kinetically trap the morphology.<sup>58</sup>

To compare the selectivity of these solvents for the blocks of the copolymer, we calculated the Flory interaction parameters ( $\chi$ ) using Hansen solubility parameters.  $\chi$  parameters were calculated using Equation 1 and 2.<sup>60</sup>

$$A_{1,2} = [(\delta_{D2} - \delta_{D1})^2 + 0.25(\delta_{P2} - \delta_{P1})^2 + 0.25(\delta_{H2} - \delta_{H1})^2] \quad (1)$$

In Equation 1;  $\delta_D$ ,  $\delta_P$  and  $\delta_H$  are Hansen solubility parameters for dispersive, polar and hydrogen bonding contributions of the two blocks of the BCP, respectively.<sup>60-61</sup> Subscript 1 stands for the solvent and 2 stands for the polymer block.

$$\chi_{12} = VA_{1,2}/RT \quad (2)$$

In Equation 2;  $V$ ,  $R$  and  $T$  correspond to the molar volume of the solvent, the ideal gas constant and the absolute temperature, respectively. The calculated results, given in Table 1, indicate that methanol is a better solvent for PNIPAM than for PS, while toluene is a better solvent for PS. THF can be considered as a neutral solvent for both blocks. Although some of the calculated  $\chi$  values were significantly higher than experimental values reported in the literature, for our experiments it was sufficient to compare the selectivity of the solvents between the blocks.

**Table 1.** Calculated  $\chi$  parameters and vapor pressures

		methanol	THF	toluene
$\chi$ parameters	PS	2.14	0.78	0.74
	PNIPAM	1.13	0.46	1.21
Vapor pressure at 25°C (kPa)		16.9	21.6	3.79

### 4.4.1 Bulk morphology

The triblock PS-*b*-PNIPAM-*b*-PS copolymer with a total molecular weight of  $M_n = 127\text{kDa}$ , PDI = 1.40 and  $f_{\text{PS}} = 0.44$  was successfully synthesized by RAFT polymerization (CP-1 in Chapter 2). The bulk morphology of the copolymer was characterized by using SAXS and AFM, after solvent annealing of the bulk copolymer film. As shown in Figure 1a, the intensity profile of the SAXS data shows a well-defined first-order peak and a higher order reflection at a  $q$  spacing ratio of  $3q^*$ . The AFM image, shown in Figure 1b, shows a lamellar morphology perpendicularly aligned to the surface with an average interlayer distance of 59 nm (+/- 2 nm). This interlayer distance is in agreement with the SAXS data from which an interlayer distance of 59.3 nm was obtained. In the SAXS traces, no clear second order peak at  $q$  spacing ratio of  $2q^*$  was observed, which can indicate that the lamellae of the two blocks are similar in thickness.<sup>62</sup> This is consistent with the almost equal volume fractions of the polymer blocks.

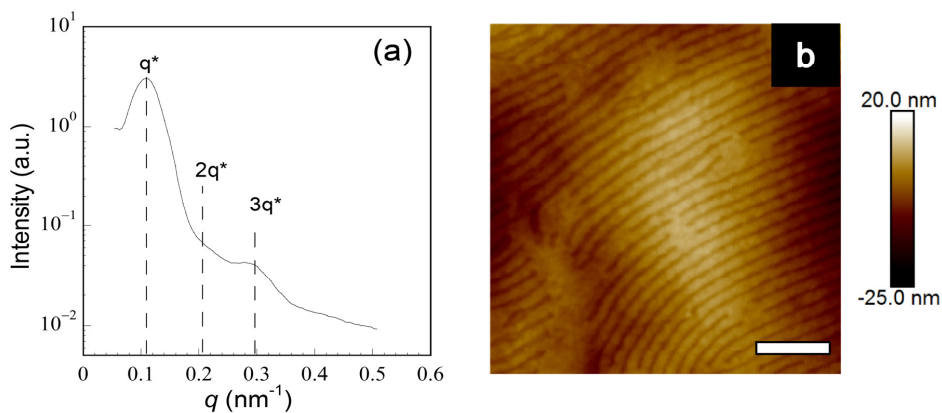


**Figure 1. Bulk film characterization. (a) Intensity profile of the SAXS data. Peak positions as expected for a lamellar morphology are indicated. (b) AFM height image. Scale bar = 400 nm.**

### 4.4.2 As-spun samples

Copolymer thin films with a thickness of around 100 nm were prepared by spin-coating from PS-*b*-PNIPAM-*b*-PS solutions in THF or methanol: THF 2:1 (v:v) solvent mixtures. The variation in thickness for a set of samples annealed with a particular solvent (mixture) was +/- 10 nm. Methanol is a more selective solvent for PNIPAM than for PS. THF is almost

Self-assembly of PS-*b*-PNIPAM-*b*-PS thin films *via* selective solvent annealing neutral for both blocks. The AFM images in Figure 2 show a disordered micellar morphology for both types of solvent systems. The light regions in the images correspond to PS and the dark regions correspond to the PNIPAM part of the block copolymer. The micelles can either indicate spheres or perpendicular cylinders. The GISAXS images in Figure SI show a weak first-order peak and confirm that there is only short-range ordering in the lateral direction with domain spacings of 62.8 nm for THF and 40 nm for methanol-THF. This relatively large difference in domain size, may be due to the poor solubility of PS in methanol. Since the obtained as-spun morphologies are metastable due to the rapid solvent evaporation during spin-coating, collapse of the PS chains in solution may cause a decrease in domain size. Both the AFM and the GISAXS data indicate that the methanol-THF solvent mixture slightly improved the uniformity of the domains. Therefore, the use of selective solvents improved the morphology.<sup>51</sup>

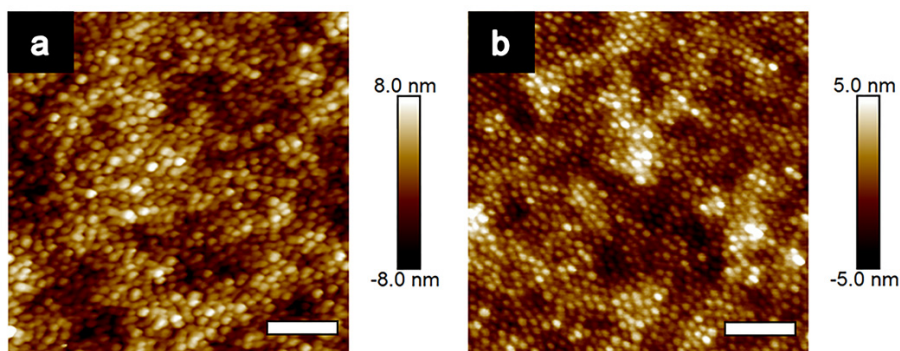


**Figure 2.** AFM topography images of as spun thin films prepared by spin coating solutions of the BCP in (a) THF and (b) methanol-THF. Scale bars = 400 nm.

### 4.4.3 Solvent annealing

#### 4.4.3.1 Solvent annealing with pure solvents

We solvent annealed as-spun BCP thin films using three different pure solvents: THF, methanol and toluene, and studied the morphological behavior using *in-situ* GISAXS and AFM. The GISAXS analysis was performed on films swollen with solvent and AFM analysis on quenched dry thin films after solvent annealing. The as-spun morphology for solvent annealing was always disordered micellar as shown in Figure 2. In all solvent annealing

experiments, including with pure solvents and solvent mixtures, there was always an initial first order peak in the dry state which immediately disappeared when it came into contact with the solvent vapor. The occurrence and disappearance of this initial peak will not be mentioned for each system separately.

Toluene is a good solvent for PS, but a poor solvent for PNIPAM. For toluene, a weak first order peak was observed for a short time, after which the film became and stayed disordered during the solvent annealing process (Figure 3a). GISAXS images of the integrated plots in Figure 3 can be found in Figure SII. While the thickness of the film increased by 50% (from ~100 to 150 nm) there was apparently insufficient plasticization to induce any reordering of the BCP domains. The initial weak first order peak may be lost due to a small screening effect by the toluene of the non-favorable interactions between the blocks.

For both THF and methanol annealing, a stable and well-defined first order peak was obtained, as can be seen in Figure 3b and 3c, respectively. For THF the film could be swollen up to 363% relative to its original film thickness, but no higher order peaks were obtained during the process. Since THF is an almost non-selective solvent for the PS-PNIPAM system increasing the solvent content in the film not only increases the chain mobility but also leads to an increased screening of the non-favorable interactions between the blocks. Therefore, the lack of higher order may also indicate that the solvent concentration during *in-situ* GISAXS was too high to obtain well-defined morphologies. To complement the swelling data, we performed separate AFM studies on solvent annealed films that were rapidly quenched by removing the samples from the annealing desiccator. According to the AFM images in Figure 4, after 60 minutes of THF annealing there was almost no change in the morphology of as-spun samples and after 120 minutes, worm-like micelles were formed. After 240 minutes, there was a mixed morphology of parallel lamellae and either parallel cylinders or perpendicular lamellae. Although phase transitions could be observed with AFM, none of the images showed order over large areas, in agreement with the GISAXS data.

For solvent annealing with methanol a final film thickness of 171% the original film thickness was reached. This value lies between the final thickness of toluene and THF, which is due to a combined effect of vapor pressure and solvent quality of the respective solvents.

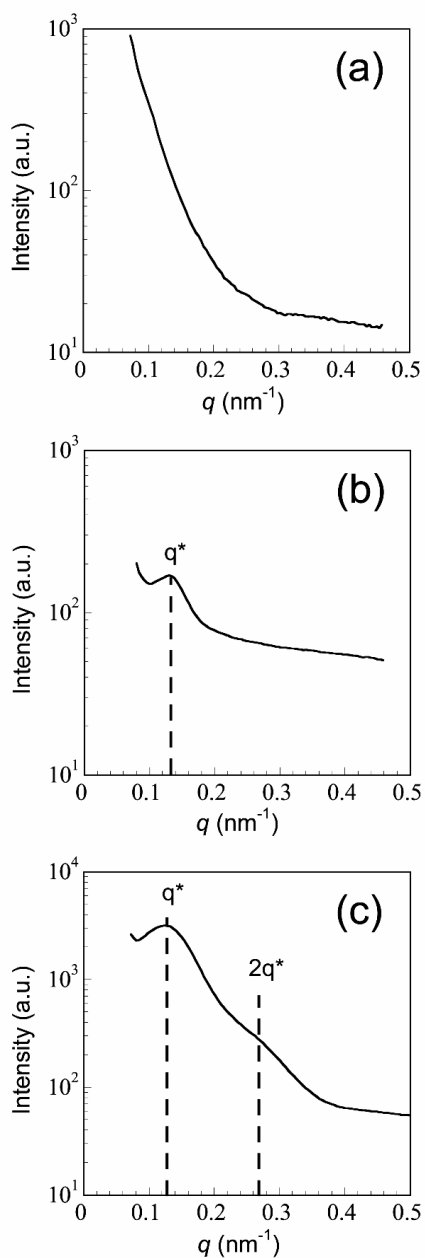


Figure 3. In-plane GISAXS profiles obtained during solvent annealing in (a) toluene, (b) THF and (c) methanol vapor. Polymer fractions for toluene, THF and methanol were 0.84, 0.53 and 0.37, respectively. Corresponding 2D GISAXS data can be found in the appendix in Figure SII.

Methanol has higher interactions parameters with the polymer blocks than THF and toluene, but toluene has a low vapor pressure. At similar conditions (temperature and air flow) the low vapor pressure of toluene results in a lower driving force for the toluene to diffuse into the film as compared to more volatile solvents. *In-situ* GISAXS data showed that next to a well-defined first order peak, a second order shoulder at  $2q^*$  was observed during solvent annealing upon reaching a polymer fraction of 0.47. The peak intensities increased until a polymer fraction of 0.37 was reached at the end of the experiment. The improved order obtained in GISAXS for methanol-annealing as compared to THF-annealing may be explained by the fact that methanol is a more selective solvent than THF and the screening effect of non-favorable interactions will be less pronounced. The complementary AFM study, as shown in Figure 5, only indicated micelles with short-range order even after 2 hours of solvent annealing. Apparently, quenching of the methanol swollen films leads to loss of long-range order.

#### 4.4.3.2 Solvent annealing with selective solvent mixtures

After establishing that no sustained long-range order was found by using pure solvents, we continued with selective solvent mixtures.

##### 4.4.3.2.1 Methanol-tetrahydrofuran

Figure 6a shows a series of in-plane GISAXS profiles that were collected during annealing of a BCP thin film using a 1:2 (v:v) methanol-THF mixture. The corresponding 2D GISAXS image for a polymer fraction of 0.44 is given in Figure 6b and the rest of the 2D images are given in Figure SIII. During the annealing process the thickness of the film was monitored and Figure 7 shows the domain spacing as a function of the polymer volume fraction  $\phi_{\text{BCP}}$ . The polymer volume fraction is determined by the ratio of the dry polymer film thickness,  $t_0$ , over the swollen film thickness,  $t$ :

$$\phi_{\text{BCP}} = \frac{t_0}{t} \quad (3)$$

Similar as with the pure solvent systems, the as-spun morphology for solvent annealing was always disordered micellar. Upon swelling of the film the first order peak was initially lost.

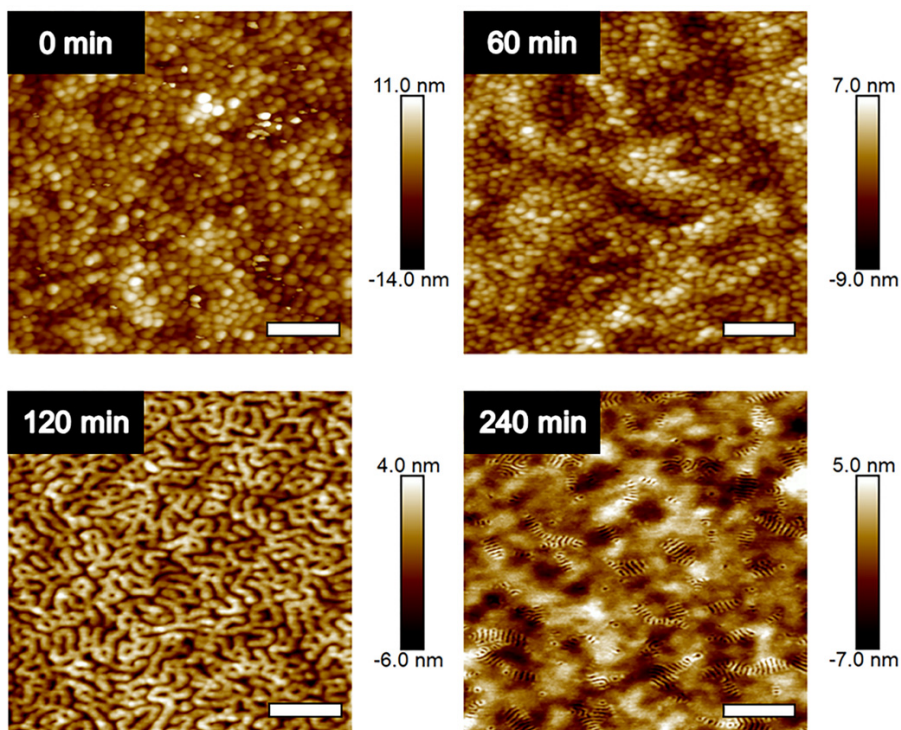


Figure 4. AFM images of time dependent solvent annealing using THF. Scale bars = 400 nm for 0, 60 and 120 minutes and scale bar = 1  $\mu\text{m}$  for 240 minutes.

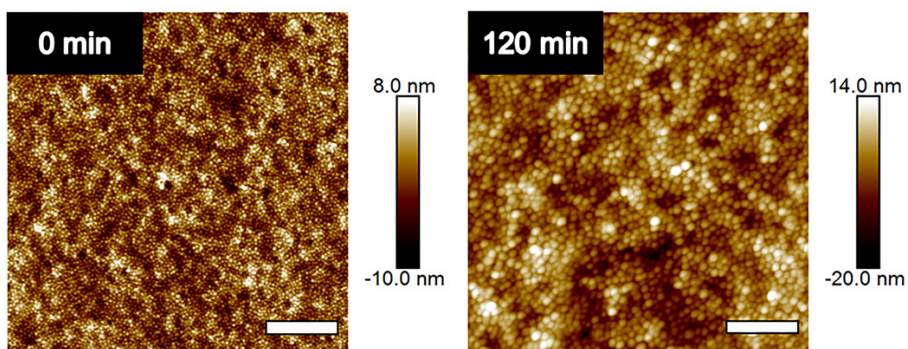
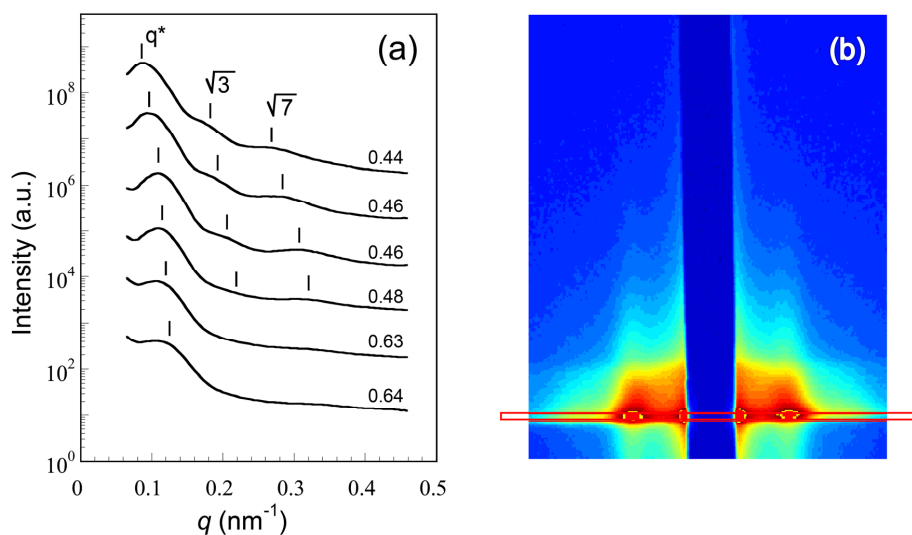


Figure 5. AFM images of time dependent solvent annealing with methanol. Scale bar = 1  $\mu\text{m}$  for 0 minutes and scale bar = 400 nm for 120 minutes.

A well-defined first order peak, corresponding to a domain spacing of 55.1 nm, reappeared when the films started to show significant reorganization at a polymer fraction of 0.66. Higher order reflections at  $q$  spacing ratios of  $\sqrt{3}q^*$  and  $\sqrt{7}q^*$  started to become visible after reaching a polymer fraction of 0.48 and after the domain spacing had shifted to 57.1 nm. This profile is consistent with hexagonally ordered perpendicular cylinders. The peaks sharpened and intensified upon further swelling (from a polymer fraction of 0.46 to 0.44) and the perpendicular orientation of the cylinders was maintained. Due to the selectivity of methanol for PNIPAM it is expected that the PNIPAM forms the majority matrix phase surrounding PS perpendicular cylinders. During the annealing process the thickness of the film increased by 123% (reaching a polymer volume fraction of 0.44) and the domain spacing started at 55.1 and shifted to 69.8 nm.



**Figure 6. (a) In-plane GISAXS profiles collected during annealing of a BCP thin film using a 1:2 (v:v) methanol: THF mixture. Polymer volume fractions are indicated next to the profiles. (b) Corresponding 2D GISAXS images for a polymer fraction of 0.44. The red box indicates the integrated area.**

The domain spacing did not constantly increase with polymer fraction, as is indicated in Figure 7. An increasing domain spacing is indicated by green data points and a decrease by red data points. An increase in domain spacing indicates that the film is simply taking up

Self-assembly of PS-*b*-PNIPAM-*b*-PS thin films *via* selective solvent annealing more solvent, whereas a decrease in domain spacing (despite the solvent-uptake) usually results from relaxation of the BCP chain at the interface due to the increase in screening of the non-favorable interactions.

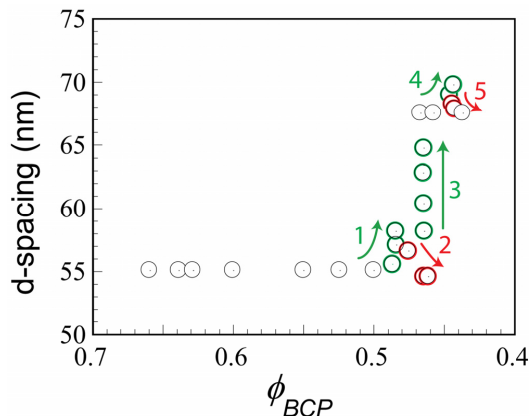


**Figure 7. Domain spacing as a function of the polymer volume fraction for methanol: THF (v:v) 1:2 solvent annealing Green data points and arrows indicate an increasing trend in d-spacing and red data points a decreasing d-spacing. Error bars are smaller than the size of the markers and are therefore not shown in the graph**

The GISAXS study was again combined with a separate AFM study. Figure 8 shows that disordered micelles started to gain some mobility after 20 minutes of solvent annealing. Ordering improved after 40 minutes and after 70 minutes of solvent annealing, well-defined hexagonally ordered perpendicular cylinders were observed. Upon further increase of the solvent annealing time, it was observed that cylinders tend to align parallel to the substrate. After 120 minutes of solvent annealing, all cylinders showed a parallel alignment. These observations that hexagonally ordered perpendicular cylinders are obtained for short annealing times and cylinders start to align parallel after longer annealing times are in agreement with several reports in the literature.<sup>2, 63</sup> However, no change in orientation of the cylinders was observed during the *in-situ* GISAXS experiments.

In addition to varying the annealing time, we also changed the methanol-THF volume ratio and studied the morphological behavior with AFM after annealing in the vapor of 1:1 and 2:1 (v:v) solvent mixtures (see Figure SIV).

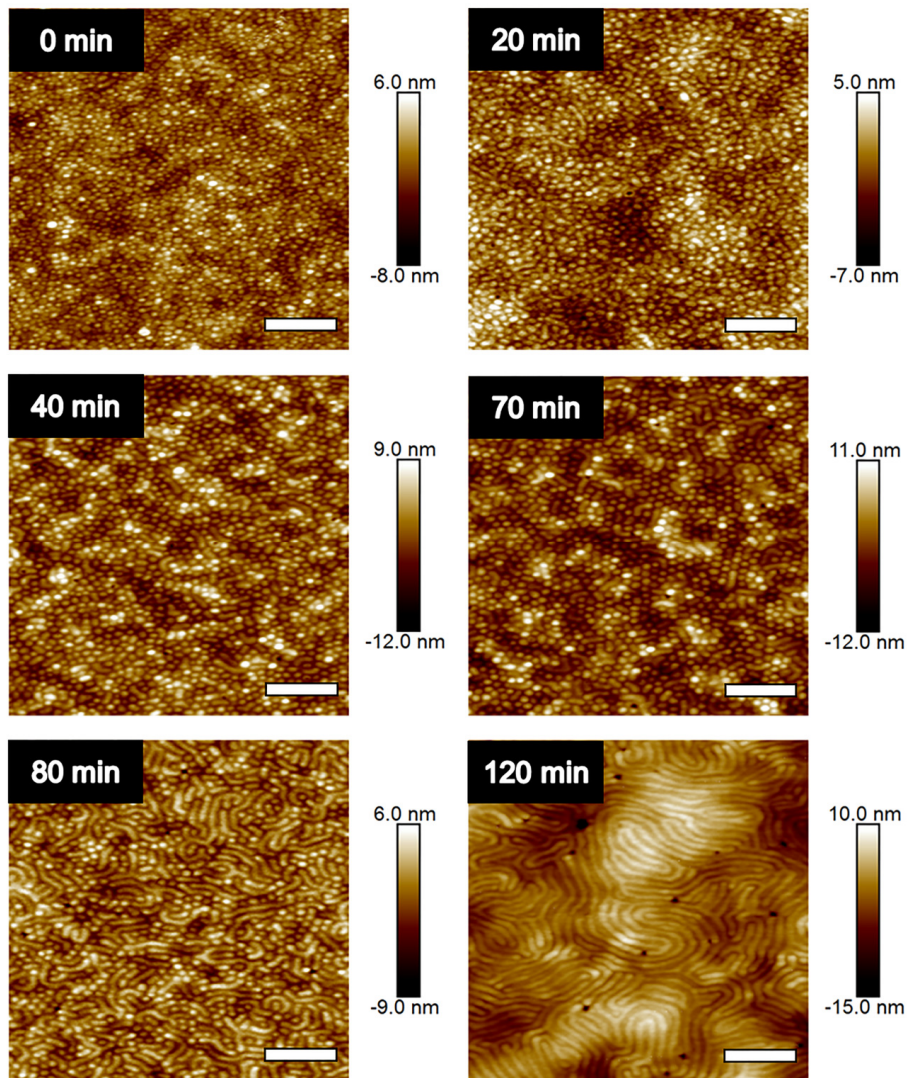


Figure 8. AFM images of time dependent solvent annealing using methanol: THF (v:v) 1:2 solvent mixture. Scale bars = 600 nm.

Upon increasing the amount of methanol in the solvent mixture from 1:2 (Figure 8) to 1:1 (Figure SIV) the morphological rearrangements occurred after a longer annealing time. Whereas for the 1:1 volume ratio, small grains with hexagonally ordered perpendicular cylinders were obtained, for the 2:1 volume ratio no long-range ordering was observed (Figure SIV). The delayed rearrangement of the BCP chains is consistent with the data of Park *et al.*

Self-assembly of PS-*b*-PNIPAM-*b*-PS thin films *via* selective solvent annealing where the presence of a poor solvent was also found to increase the annealing time before well-ordered nanostructures were obtained.<sup>29</sup> The reduction in ordering is attributed to the poor solubility of PS in methanol, resulting in a lower mobility of the chains.

#### 4.4.3.2 Methanol-toluene

Solvent annealing using methanol-toluene mixtures is expected to be considerably different from the use of methanol-THF mixtures, since both solvents are selective. As shown in Table 1, toluene and methanol are selective for PS and PNIPAM, respectively. The volume ratio of methanol: toluene solvent mixture that we used was 1:1.

*In-situ* GISAXS analysis of the annealing process, presented by in-plane profiles in Figure 9a, showed the reappearance of a broad first-order peak after an initial disappearance at the start of the annealing process. The corresponding 2D GISAXS images for a polymer fraction of 0.50 and 0.22 are given in Figure 9b and 9c and the rest of the 2D images are given in Figure SV. The first-order peak reappeared at a polymer volume fraction of 0.55. A sharpening of the first-order peak and broad higher order reflections at  $q$  spacing ratios of  $\sqrt{3}q^*$  and  $\sqrt{7}q^*$  started to become visible when the polymer volume fraction was 0.50. This profile is consistent with hexagonally ordered perpendicular cylinders. However, close inspection of the 2D GISAXS images revealed that the order and orientation of the cylinders did not reach the same level as for methanol-THF annealing. In addition, we noted differences in the 2D GISAXS images in the  $q_z$ -direction at polymer volume ratios of 0.50 and 0.22 (Figure 9b and 9c, respectively). The vertical stripes in the 2D GISAXS image of Figure 9b were found to be more curved than those of Figure 9c which is an indication that the orientation of the cylinders is not fully perpendicular to the substrate.<sup>34</sup>

A surprising feature was the fact that although the polymer volume fraction decreased to 0.22 during the annealing process, the domain spacing of the film did not change significantly and stayed 60.4 nm during the entire solvent annealing procedure, as shown in Figure 10.

Moreover, at a polymer volume fraction of 0.49 the higher order reflections disappeared and during the course of solvent annealing these peaks reappeared at their original positions at a polymer volume fraction of 0.24. The disappearance and reappearance of the

peaks in the GISAXS profiles may indicate that the system was passed through the order-disorder transition into the disordered state, after which it returned to the ordered state.

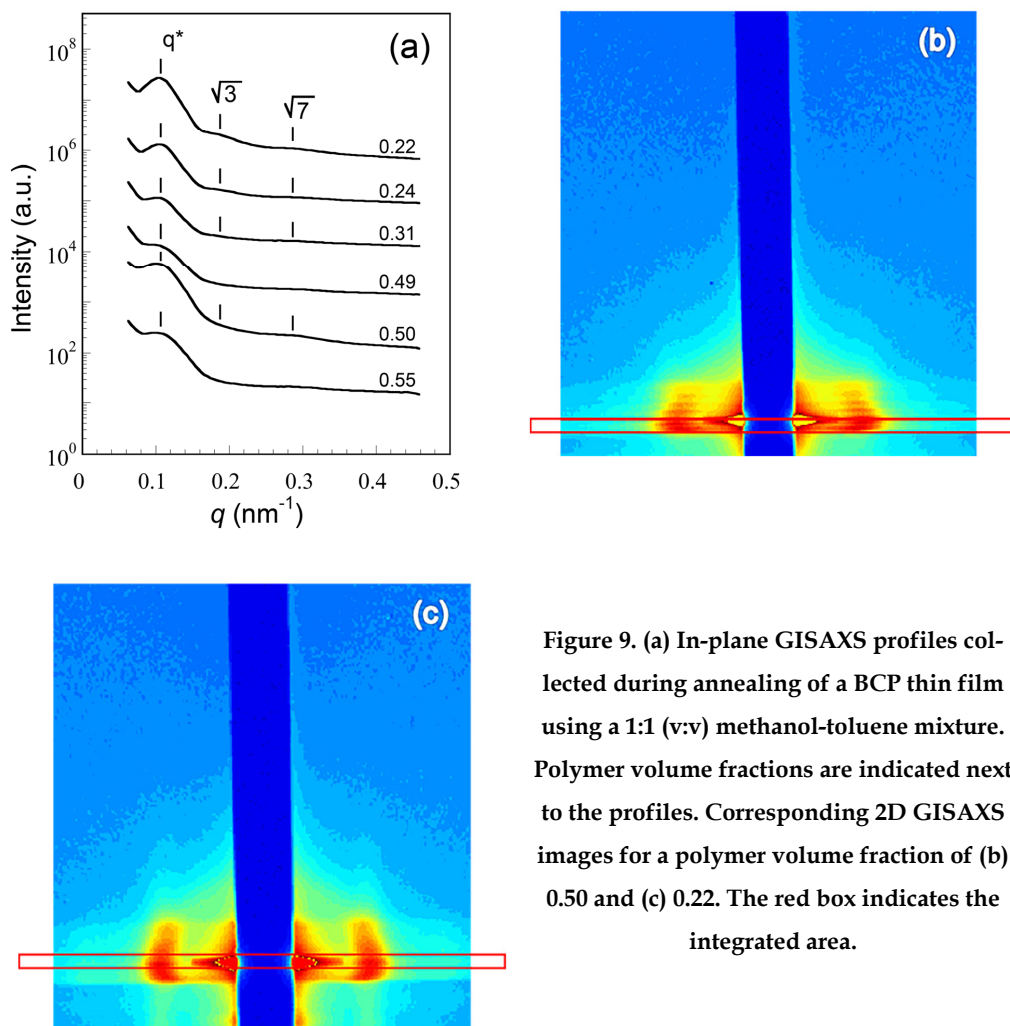


**Figure 9.** (a) In-plane GISAXS profiles collected during annealing of a BCP thin film using a 1:1 (v:v) methanol-toluene mixture. Polymer volume fractions are indicated next to the profiles. Corresponding 2D GISAXS images for a polymer volume fraction of (b) 0.50 and (c) 0.22. The red box indicates the integrated area.

However, since the solvent concentrations did not decrease during the course of these events, reappearance of the order can only occur if the solvent mixture volume ratio in the film was altered. This may occur, because vapor pressure and solvent quality differences may result in solvent composition variations within the film. At short annealing times, at a polymer volume fraction of 0.50 (see Figure 10), the film will be rich in methanol and will create a more selective environment for PNIPAM, resulting in PS cylinders surrounded by

Self-assembly of PS-*b*-PNIPAM-*b*-PS thin films *via* selective solvent annealing a PNIPAM matrix. At a polymer volume fraction of 0.49, the higher order peaks disappeared in GISAXS, which indicates that the system rearranged and long-range order was lost. When the polymer volume fraction decreased to 0.24 the ratio of methanol-toluene vapor changed in favor of toluene. We attribute this to the outlet of the solvent chamber, through which more of the solvent with the higher volatility, i.e. methanol, will leave the system. At this point, the amount of toluene in the film may have dominated the amount of methanol, causing the PS domains to swell and the PNIPAM domains to shrink their volume. In the presence of a solvent fraction of 0.76, the effective volume fraction of PS domains (including the PS selective solvent) can be as large as 0.85, for which the inverse cylindrical morphology, consisting of PNIPAM cylinders within a PS matrix, is expected to be the most stable morphology. This would mean that the morphology is inverted without a change in domain spacing.

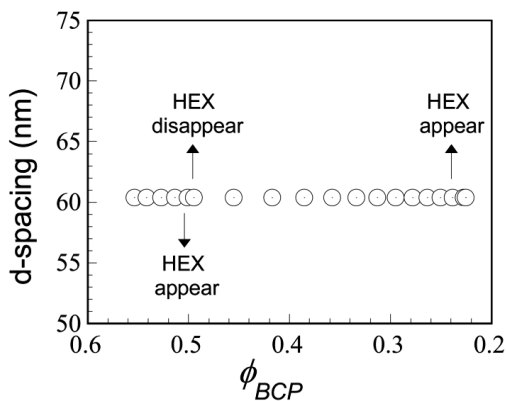


**Figure 10. Domain spacing as a function of the polymer volume fraction for methanol: toluene (v:v) 1:1 solvent annealing. The appearance and the disappearance of the higher order peaks are indicated with arrows. Error bars are smaller than the size of the markers and are therefore not shown in the graph.**

The AFM study of quenched morphologies after annealing in the vapor of a 1:1 (v:v) methanol: toluene mixture is shown in Figure 11. After 40 minutes the micelles started to become mobile. Between 40 and 60 minutes of annealing, a cylindrical morphology was formed with no preferred orientation of the cylinders and only short-range order. After 90 minutes of solvent annealing, however, the cylindrical morphology seemed inverted. As explained

above for the GISAXS study this may occur, because vapor pressure and solvent quality differences give rise to solvent composition variations within the films. Even though perpendicular cylinder formation was observed both in GISAXS and in AFM for the methanol-toluene solvent annealing system, the ordering did not reach the same level as for methanol-THF solvent annealing.

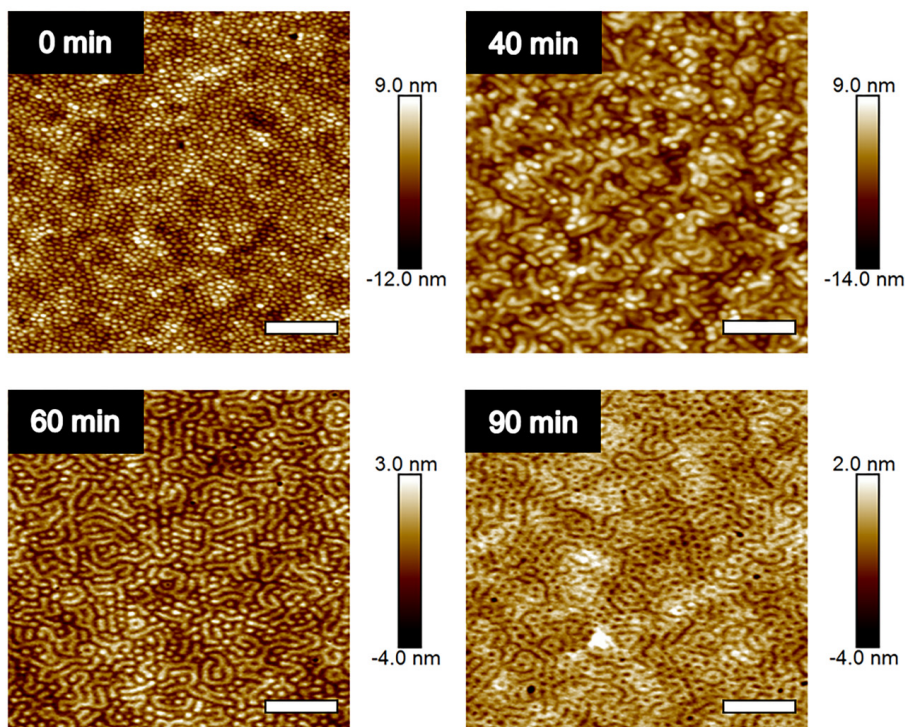


Figure 11. AFM images of time dependent solvent annealing using methanol: toluene (v:v) 1:1 solvent mixture. Scale bars = 600 nm.

## 4.5 Conclusions

We studied the morphological behavior of PS-*b*-PNIPAM-*b*-PS BCP thin films upon solvent annealing using selective solvents by means of *in-situ* GISAXS and AFM. The influence of solvent type, solvent ratio and annealing time were investigated. PS-*b*-PNIPAM-*b*-PS was found to form hexagonally ordered perpendicular cylinders, when annealed with selective solvent mixtures of methanol-THF and methanol-toluene. However, solvent annealing with

Self-assembly of PS-*b*-PNIPAM-*b*-PS thin films *via* selective solvent annealing methanol-THF resulted in a higher degree of order than with methanol-toluene. This morphology could not be obtained when only one type of solvent was used, showing the importance of using selective solvents for direct tuning to a specific morphology. PS-*b*-PNIPAM-*b*-PS BCPs hexagonally ordered perpendicular cylinders may find use in BCP thin film applications where thermo-responsiveness is required, such as MEMS, biomedical and nanoporous membrane applications.

## Acknowledgements

---

The authors are grateful to Detlef-M. Smilgies for his help with the GISAXS experiments and Ilja Voets for performing the SAXS experiments. This work is based upon research conducted at the Cornell High Energy Synchrotron Source (CHESS) which is supported by the National Science Foundation and the National Institutes of Health/National Institute of General Medical Sciences under NSF award DMR-1332208.

## References

---

1. Nykänen, A.; Nuopponen, M.; Laukkanen, A.; Hirvonen, S.-P.; Rytelä, M.; Turunen, O.; Tenhu, H.; Mezzenga, R.; Ikkala, O.; Ruokolainen, J., Phase Behavior and Temperature-Responsive Molecular Filters Based on Self-Assembly of Polystyrene-block-poly(N-isopropylacrylamide)-block-polystyrene. *Macromolecules* **2007**, *40* (16), 5827-5834.
2. Vayer, M.; Hillmyer, M. A.; Dirany, M.; Thevenin, G.; Erre, R.; Sinturel, C., Perpendicular orientation of cylindrical domains upon solvent annealing thin films of polystyrene-*b*-polylactide. *Thin Solid Films* **2010**, *518* (14), 3710-3715.
3. Bang, J.; Jeong, U.; Ryu, D. Y.; Russell, T. P.; Hawker, C. J., Block Copolymer Nanolithography: Translation of Molecular Level Control to Nanoscale Patterns. *Adv. Mater. (Weinheim, Ger.)* **2009**, *21* (47), 4769-4792.
4. Jung, H.; Woo, S.; Choe, Y.; Ryu, D. Y.; Huh, J.; Bang, J., Single Step Process for Self-Assembled Block Copolymer Patterns via in Situ Annealing during Spin-Casting. *ACS Macro Letters* **2015**, *4* (6), 656-660.
5. Kim, S. Y.; Gwyther, J.; Manners, I.; Chaikin, P. M.; Register, R. A., Metal-Containing Block Copolymer Thin Films Yield Wire Grid Polarizers with High Aspect Ratio. *Adv. Mater.* **2014**, *26* (5), 791-795.
6. Bates, C. M.; Maher, M. J.; Janes, D. W.; Ellison, C. J.; Willson, C. G., Block Copolymer Lithography. *Macromolecules* **2014**, *47* (1), 2-12.
7. Fitzgerald, T. G.; Farrell, R. A.; Petkov, N.; Bolger, C. T.; Shaw, M. T.; Charpin, J. P. F.; Gleeson, J. P.; Holmes, J. D.; Morris, M. A., Study on the Combined Effects of Solvent Evaporation and Polymer Flow upon Block Copolymer Self-Assembly and Alignment on Topographic Patterns. *Langmuir* **2009**, *25* (23), 13551-13560.

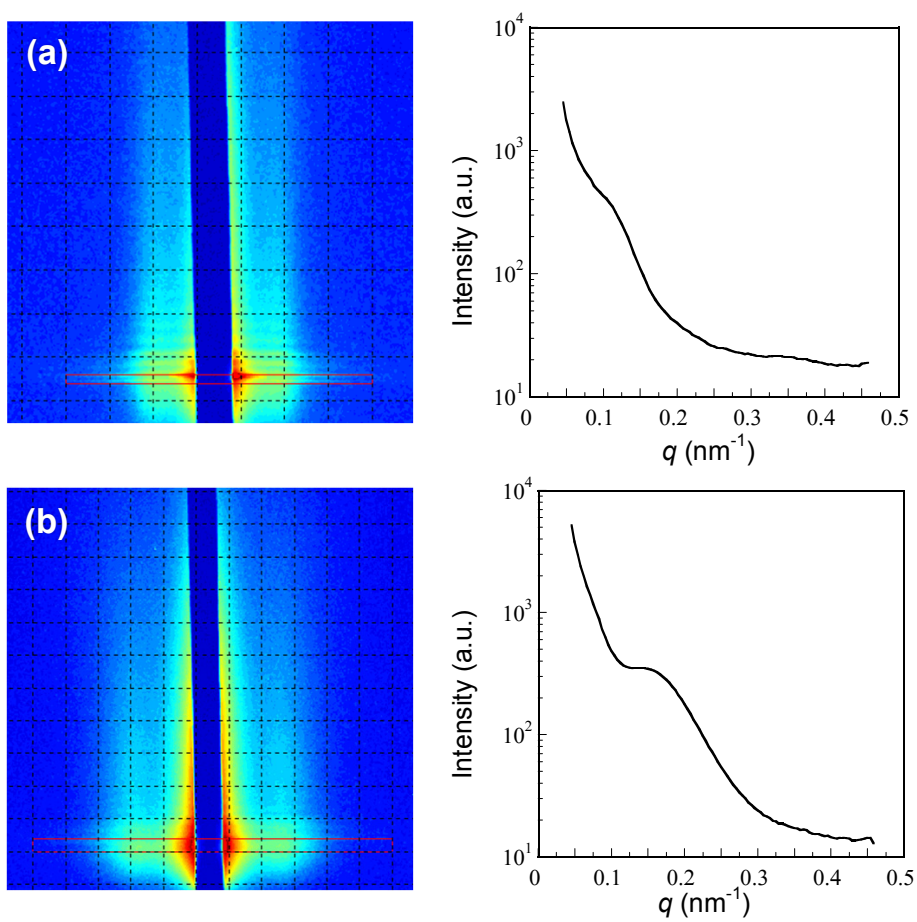
8. Ahn, D. U.; Sancaktar, E., Fabrication of well-defined block copolymer nano-cylinders by controlling the thermodynamics and kinetics involved in block copolymer self-assembly. *Soft Matter* **2008**, *4* (7), 1454-1466.
9. Yang, S. Y.; Ryu, I.; Kim, H. Y.; Kim, J. K.; Jang, S. K.; Russell, T. P., Nanoporous Membranes with Ultrahigh Selectivity and Flux for the Filtration of Viruses. *Adv. Mater.* **2006**, *18* (6), 709-712.
10. Kim, D. H.; Lau, K. H. A.; Joo, W.; Peng, J.; Jeong, U.; Hawker, C. J.; Kim, J. K.; Russell, T. P.; Knoll, W., An Optical Waveguide Study on the Nanopore Formation in Block Copolymer/Homopolymer Thin Films by Selective Solvent Swelling. *The Journal of Physical Chemistry B* **2006**, *110* (31), 15381-15388.
11. Jeong, U.; Ryu, D. Y.; Kho, D. H.; Kim, J. K.; Goldbach, J. T.; Kim, D. H.; Russell, T. P., Enhancement in the Orientation of the Microdomain in Block Copolymer Thin Films upon the Addition of Homopolymer. *Adv. Mater.* **2004**, *16* (6), 533-536.
12. Di, Z.; Posselt, D.; Smilgies, D.-M.; Papadakis, C. M., Structural Rearrangements in a Lamellar Diblock Copolymer Thin Film during Treatment with Saturated Solvent Vapor. *Macromolecules* **2010**, *43* (1), 418-427.
13. Kelly, J. Y.; Albert, J. N. L.; Howarter, J. A.; Kang, S.; Stafford, C. M.; Epps, T. H.; Faselka, M. J., Investigation of Thermally Responsive Block Copolymer Thin Film Morphologies Using Gradients. *ACS Applied Materials & Interfaces* **2010**, *2* (11), 3241-3248.
14. Segalman, R. A., Patterning with block copolymer thin films. *Materials Science and Engineering: R: Reports* **2005**, *48* (6), 191-226.
15. Abetz, V.; Simon, P. F. W., Phase Behaviour and Morphologies of Block Copolymers. In *Block Copolymers I*, Springer Berlin Heidelberg: 2005; Vol. 189, pp 125-212.
16. Darling, S. B., Directing the self-assembly of block copolymers. *Progress in Polymer Science* **2007**, *32* (10), 1152-1204.
17. Smilgies, D.-M.; Li, R.; Di, Z.; Darko, C.; Papadakis, C. M.; Posselt, D., Probing the Self-Organization Kinetics in Block Copolymer Thin Films. *Materials Research Society Symposium Proceedings* **2009**, *1147E*.
18. Kelly, J. Y.; Albert, J. N. L.; Howarter, J. A.; Stafford, C. M.; Epps, T. H.; Faselka, M. J., Manipulating morphology and orientation in thermally responsive block copolymer thin films. *Journal of Polymer Science, Part B: Polymer Physics* **2012**, *50* (4), 263-271.
19. Gotrik, K. W.; Hannon, A. F.; Son, J. G.; Keller, B.; Alexander-Katz, A.; Ross, C. A., Morphology Control in Block Copolymer Films Using Mixed Solvent Vapors. *ACS Nano* **2012**, *6* (9), 8052-8059.
20. Bosworth, J. K.; Paik, M. Y.; Ruiz, R.; Schwartz, E. L.; Huang, J. Q.; Ko, A. W.; Smilgies, D.-M.; Black, C. T.; Ober, C. K., Control of Self-Assembly of Lithographically Patternable Block Copolymer Films. *ACS Nano* **2008**, *2* (7), 1396-1402.
21. Park, C.; Yoon, J.; Thomas, E. L., Enabling nanotechnology with self assembled block copolymer patterns. *Polymer* **2003**, *44* (22), 6725-6760.
22. Gu, X.; Gunkel, I.; Hexemer, A.; Gu, W.; Russell, T. P., An In Situ Grazing Incidence X-Ray Scattering Study of Block Copolymer Thin Films During Solvent Vapor Annealing. *Adv. Mater. (Weinheim, Ger.)* **2014**, *26* (2), 273-281.
23. Sinturel, C.; Vayer, M.; Morris, M.; Hillmyer, M. A., Solvent Vapor Annealing of Block Polymer Thin Films. *Macromolecules (Washington, DC, U. S.)* **2013**, *46* (14), 5399-5415.
24. Wan, L.; Ji, S.; Liu, C.-C.; Craig, G. S. W.; Nealey, P. F., Directed self-assembly of solvent-vapor-induced non-bulk block copolymer morphologies on nanopatterned substrates. *Soft Matter* **2016**, *12* (11), 2914-2922.

25. Albert, J. N. L.; Young, W.-S.; Lewis, R. L.; Bogart, T. D.; Smith, J. R.; Epps, T. H., Systematic Study on the Effect of Solvent Removal Rate on the Morphology of Solvent Vapor Annealed ABA Triblock Copolymer Thin Films. *ACS Nano* **2012**, *6* (1), 459-466.
26. Berezkin, A. V.; Papadakis, C. M.; Potemkin, I. I., Vertical Domain Orientation in Cylinder-Forming Diblock Copolymer Films upon Solvent Vapor Annealing. *Macromolecules* **2016**, *49* (1), 415-424.
27. Son, J. G.; Gotrik, K. W.; Ross, C. A., High-Aspect-Ratio Perpendicular Orientation of PS-*b*-PDMS Thin Films under Solvent Annealing. *ACS Macro Letters* **2012**, *1* (11), 1279-1284.
28. Gunkel, I.; Gu, X.; Sun, Z.; Schaible, E.; Hexemer, A.; Russell, T. P., An in situ GISAXS study of selective solvent vapor annealing in thin block copolymer films: Symmetry breaking of in-plane sphere order upon deswelling. *J. Polym. Sci. Part B: Polym. Phys.* **2016**, *54* (2), 331-338.
29. Park, W. I.; Choi, Y. J.; Yun, J. M.; Hong, S. W.; Jung, Y. S.; Kim, K. H., Enhancing the Directed Self-assembly Kinetics of Block Copolymers Using Binary Solvent Mixtures. *ACS Applied Materials & Interfaces* **2015**, *7* (46), 25843-25850.
30. Kim, J. M.; Kim, Y. J.; Park, W. I.; Hur, Y. H.; Jeong, J. W.; Sim, D. M.; Baek, K. M.; Lee, J. H.; Kim, M.-J.; Jung, Y. S., Eliminating the Trade-Off between the Throughput and Pattern Quality of Sub-15 nm Directed Self-Assembly via Warm Solvent Annealing. *Adv. Funct. Mater.* **2015**, *25* (2), 306-315.
31. Chavis, M. A.; Smilgies, D.-M.; Wiesner, U. B.; Ober, C. K., Widely Tunable Morphologies in Block Copolymer Thin Films Through Solvent Vapor Annealing Using Mixtures of Selective Solvents. *Adv. Funct. Mater.* **2015**, *25* (20), 3057-3065.
32. Bai, W.; Yager, K. G.; Ross, C. A., In Situ Characterization of the Self-Assembly of a Polystyrene-Polydimethylsiloxane Block Copolymer during Solvent Vapor Annealing. *Macromolecules (Washington, DC, U. S.)* **2015**, *48* (23), 8574-8584.
33. Park, W. I.; Tong, S.; Liu, Y.; Jung, I. W.; Roelofs, A.; Hong, S., Tunable and rapid self-assembly of block copolymers using mixed solvent vapors. *Nanoscale* **2014**, *6* (24), 15216-15221.
34. Di, Z.; Posselt, D.; Smilgies, D.-M.; Li, R.; Rauscher, M.; Potemkin, I. I.; Papadakis, C. M., Stepwise Swelling of a Thin Film of Lamellae-Forming Poly(styrene-*b*-butadiene) in Cyclohexane Vapor. *Macromolecules* **2012**, *45* (12), 5185-5195.
35. Jeong, J. W.; Park, W. I.; Kim, M.-J.; Ross, C. A.; Jung, Y. S., Highly Tunable Self-Assembled Nanostructures from a Poly(2-vinylpyridine-*b*-dimethylsiloxane) Block Copolymer. *Nano Letters* **2011**, *11* (10), 4095-4101.
36. Cavicchi, K. A.; Berthiaume, K. J.; Russell, T. P., Solvent annealing thin films of poly(isoprene-*b*-lactide). *Polymer* **2005**, *46* (25), 11635-11639.
37. Tada, Y.; Yoshida, H.; Ishida, Y.; Hirai, T.; Bosworth, J. K.; Dobisz, E.; Ruiz, R.; Takenaka, M.; Hayakawa, T.; Hasegawa, H., Directed Self-Assembly of POSS Containing Block Copolymer on Lithographically Defined Chemical Template with Morphology Control by Solvent Vapor. *Macromolecules (Washington, DC, U. S.)* **2012**, *45* (1), 292-304.
38. Tokarev, I.; Krenek, R.; Burkov, Y.; Schmeisser, D.; Sidorenko, A.; Minko, S.; Stamm, M., Microphase Separation in Thin Films of Poly(styrene-*b*-4-vinylpyridine) Copolymer-2-(4'-Hydroxybenzeneazo)benzoic Acid Assembly. *Macromolecules* **2005**, *38* (2), 507-516.
39. Gowd, E. B.; Marcus, B.; Manfred, S., In Situ GISAXS Study on Solvent Vapour Induced Orientation Switching in PS-*b*-P4VP Block Copolymer Thin Films. *IOP Conference Series: Materials Science and Engineering* **2010**, *14* (1), 012015.
40. Brendel, J. C.; Liu, F.; Lang, A. S.; Russell, T. P.; Thelakkat, M., Macroscopic Vertical Alignment of Nanodomains in Thin Films of Semiconductor Amphiphilic Block Copolymers. *ACS Nano* **2013**, *7* (7), 6069-6078.

41. Mondal, S.; Wickramasinghe, S. R., Photo-induced graft polymerization of N-isopropyl acrylamide on thin film composite membrane: Produced water treatment and antifouling properties. *Separation and Purification Technology* **2012**, *90*, 231-238.
42. F. Montagne, R. P., A. M. Popa, A. Hoogerwerf, T. Overstolz, H. Heinzelmann, Stimuli-Responsive Polymers in MEMS Devices. In *NSTI-Nanotech 2008*, Vol. 2, pp 653-656.
43. Tokarev, I.; Minko, S., Stimuli-responsive hydrogel thin films. *Soft Matter* **2009**, *5* (3), 511-524.
44. Wang, X.; Wang, X.; Fernandez, R.; Yan, M.; Rosa, A. L., Nanolithography on responsive materials. *Journal of Nanoscience Letters* **2012**, *2* (23), 1-16.
45. Rusen, L.; Dinca, V.; Mitu, B.; Mustaciosu, C.; Dinescu, M., Temperature responsive functional polymeric thin films obtained by matrix assisted pulsed laser evaporation for cells attachment–detachment study. *Applied Surface Science* **2014**, *302*, 134-140.
46. Xu, C.; Fu, X.; Fryd, M.; Xu, S.; Wayland, B. B.; Winey, K. I.; Composto, R. J., Reversible Stimuli-Responsive Nanostructures Assembled from Amphiphilic Block Copolymers. *Nano Letters* **2006**, *6* (2), 282-287.
47. Wu, S.; Bubeck, C., Macro- and Microphase Separation in Block Copolymer Supramolecular Assemblies Induced by Solvent Annealing. *Macromolecules (Washington, DC, U. S.)* **2013**, *46* (9), 3512-3518.
48. Li, X.; Peng, J.; Wen, Y.; Kim, D. H.; Knoll, W., Morphology change of asymmetric diblock copolymer micellar films during solvent annealing. *Polymer* **2007**, *48* (8), 2434-2443.
49. Liang, C.; Hong, K.; Guiochon, G. A.; Mays, J. W.; Dai, S., Nanoporous films: Synthesis of a large-scale highly ordered porous carbon film by self-assembly of block copolymers. *Angewandte Chemie, International Edition* **2004**, *43* (43), 5785-5789.
50. Jeon, S.-M.; Lee, S. H.; Yoo, S. I.; Sohn, B.-H., Ordered Complex Nanostructures from Bimodal Self-Assemblies of Diblock Copolymer Micelles with Solvent Annealing. *Langmuir* **2011**, *27* (19), 12191-12196.
51. Park, S.; Wang, J.-Y.; Kim, B.; Chen, W.; Russell, T. P., Solvent-Induced Transition from Micelles in Solution to Cylindrical Microdomains in Diblock Copolymer Thin Films. *Macromolecules* **2007**, *40* (25), 9059-9063.
52. Bousquet, A.; Ibarboure, E.; Papon, E.; Labrugère, C.; Rodríguez-Hernández, J., Structured multistimuli-responsive functional polymer surfaces obtained by interfacial diffusion of amphiphilic block copolymers. *J. Polym. Sci. A Polym. Chem.* **2010**, *48* (9), 1952-1961.
53. Thomas, C. S.; Xu, L.; Olsen, B. D., Kinetically Controlled Nanostructure Formation in Self-Assembled Globular Protein–Polymer Diblock Copolymers. *Biomacromolecules* **2012**, *13* (9), 2781-2792.
54. Yu, Q.; Zhang, Y.; Chen, H.; Zhou, F.; Wu, Z.; Huang, H.; Brash, J. L., Protein Adsorption and Cell Adhesion/Detachment Behavior on Dual-Responsive Silicon Surfaces Modified with Poly(N-isopropylacrylamide)-block-polystyrene Copolymer. *Langmuir* **2010**, *26* (11), 8582-8588.
55. Lai, J. T.; Filla, D.; Shea, R., Functional Polymers from Novel Carboxyl-Terminated Trithiocarbonates as Highly Efficient RAFT Agents. *Macromolecules* **2002**, *35* (18), 6754-6756.
56. Tanaka, H.; Hasegawa, H.; Hashimoto, T., Ordered structure in mixtures of a block copolymer and homopolymers. 1. Solubilization of low molecular weight homopolymers. *Macromolecules* **1991**, *24* (1), 240-251.
57. Schild, H. G., Poly(N-isopropylacrylamide): experiment, theory and application. *Progress in Polymer Science* **1992**, *17* (2), 163-249.

58. Paik, M. Y.; Bosworth, J. K.; Smilges, D.-M.; Schwartz, E. L.; Andre, X.; Ober, C. K., Reversible Morphology Control in Block Copolymer Films via Solvent Vapor Processing: An in Situ GISAXS Study. *Macromolecules (Washington, DC, U. S.)* **2010**, *43* (9), 4253-4260.
59. Lide, D. R., *Handbook of Organic Solvents*. CRC Press: Boca Raton, FL, USA, 1995.
60. Hansen, C. M., *Hansen Solubility Parameters: A User's Handbook*. CRC Press: U.S.A, 2000.
61. Ahmad, H., Solubility Parameter of Acrylamide Series Polymers through Its Components and Group Contribution Technique. *Journal of Macromolecular Science: Part A - Chemistry* **1982**, *17* (4), 585-600.
62. Zhang, J.; Posselt, D.; Smilgies, D.-M.; Perlich, J.; Kyriakos, K.; Jaksch, S.; Papadakis, C. M., Lamellar Diblock Copolymer Thin Films during Solvent Vapor Annealing Studied by GISAXS: Different Behavior of Parallel and Perpendicular Lamellae. *Macromolecules* **2014**, *47* (16), 5711-5718.
63. Phillip, W. A.; Hillmyer, M. A.; Cussler, E. L., Cylinder Orientation Mechanism in Block Copolymer Thin Films Upon Solvent Evaporation. *Macromolecules* **2010**, *43* (18), 7763-7770.

## APPENDIX



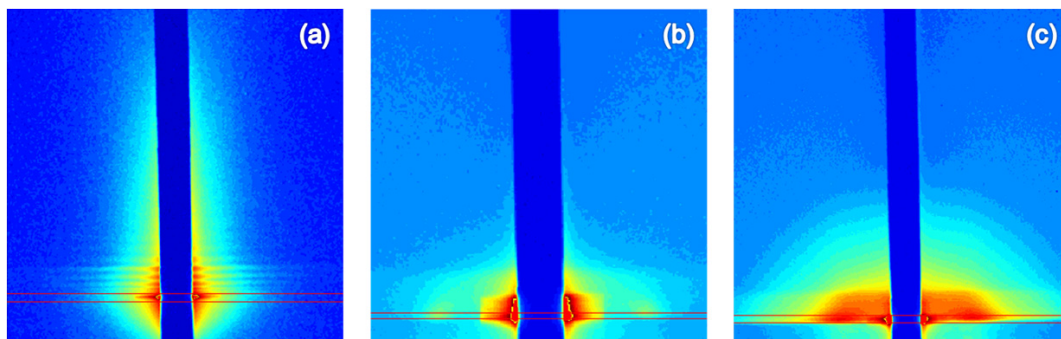


Figure SII. 2D GISAXS images collected during annealing of a BCP thin film using (a) toluene, (b) THF and (c) methanol. The red boxes indicate the integrated area.

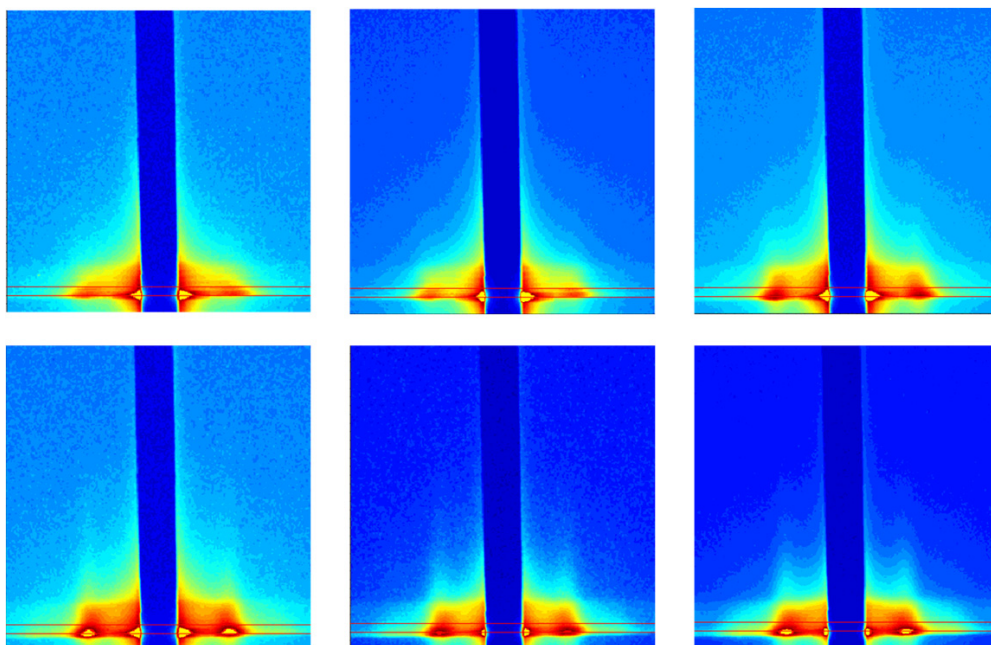


Figure SIII. Corresponding 2D GISAXS images for the integrated profiles as shown in Figure 6 for methanol-THF solvent annealing. The red boxes indicate the integrated area.

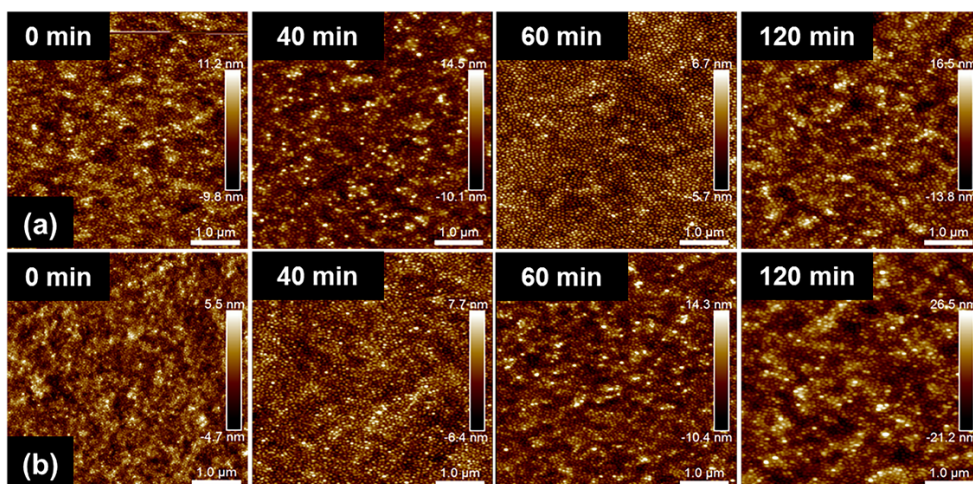


Figure SIV. AFM images of time dependent solvent annealing using methanol: THF (v:v) (a) 1:1 and (b) 2:1.

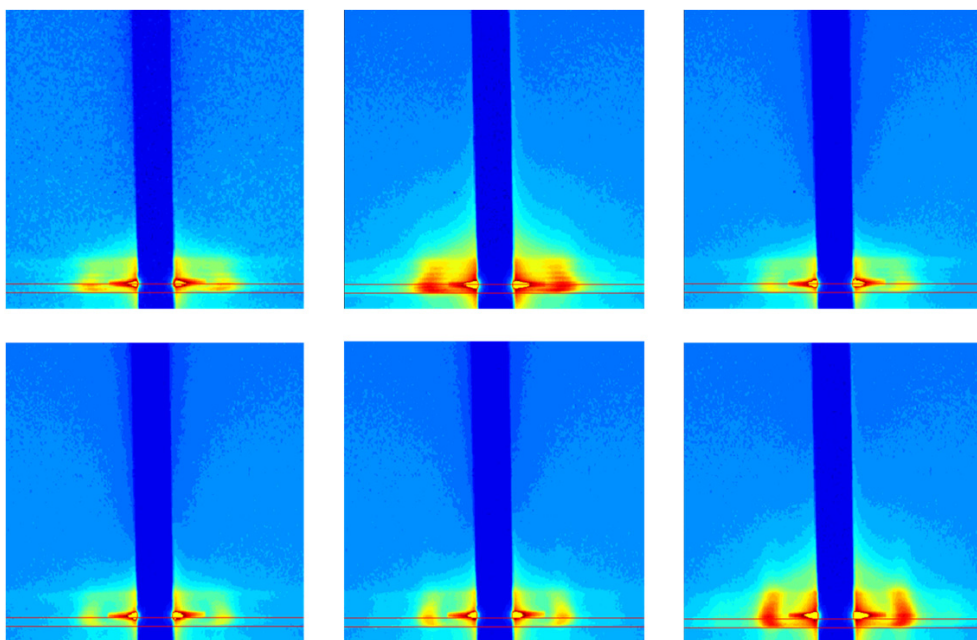
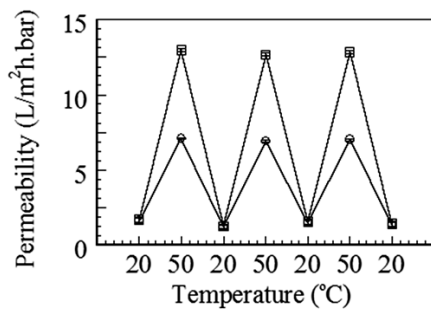
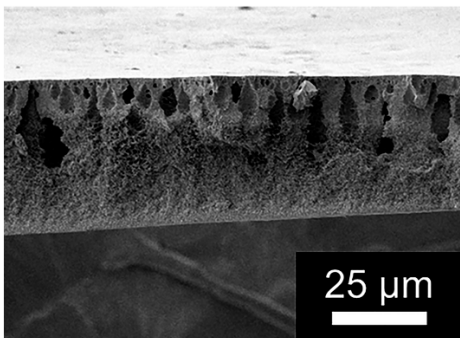
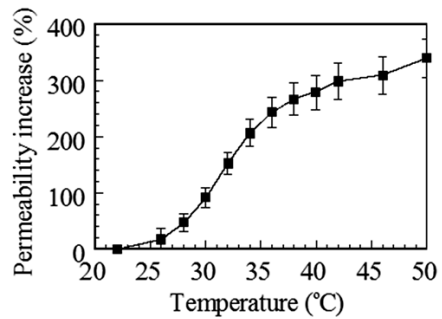
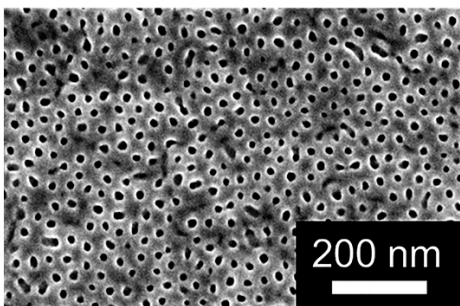


Figure SV. Corresponding 2D GISAXS images for the integrated profiles as shown in Figure 9 for methanol-toluene solvent annealing. The red boxes indicate the integrated area.

# CHAPTER 5

## Systematic variation of membrane casting parameters to control the structure of thermo-responsive isoporous membranes



In preparation:

Cetintas, M.; Wahdat, H; van der Kooij, H. M.; Kamperman, M., Systematic variation of membrane casting parameters to control the structure of thermo-responsive isoporous membranes.

## 5.1 Abstract

---

Fouling is a critical issue in membrane process operation as it greatly compromises the efficiency of the treatment processes. A promising approach to overcome this problem is to produce of easy-to-clean membranes by incorporating stimuli-responsive pores. In this study, we fabricated thermo-responsive polystyrene-*b*-poly(*N*-isopropylacrylamide) (PS-*b*-PNIPAM) block copolymer membranes using the self-assembly and non-solvent induced phase separation (SNIPS) method and systematically varied several membrane casting parameters i.e. evaporation time, polymer concentration, solvent type and water content to obtain nano- and isoporous membranes. Whereas, isoporous membranes were obtained when the block copolymers were dissolved in PNIPAM (poly(*N*-isopropylacrylamide)) (minority block) selective solvent mixtures, membranes with a disordered surface were obtained for polystyrene (PS) selective solvents. Using 1,4-dioxane-tetrahydrofuran mixtures resulted in isoporous membranes for a large parameter space, indicating the robustness of structure formation in the PS-*b*-PNIPAM system. Permeability tests at various temperatures demonstrated fully reversible thermo-responsive behavior of the membranes.

## 5.2 Introduction

---

Nanoporous membranes are essential materials that are used in water filtration to separate nano-sized impurities such as proteins and viruses. Block copolymers receive a great deal of attention in this field, since they can microphase separate into regular structures on length scales of 10-100 nm and have the ability to form membranes with uniform nano-sized pores.<sup>1</sup> Block copolymer membranes offer high pore densities, tunable pore sizes, narrow pore size distributions, tunable mechanical and chemical properties and the ability for selective functionalization such as stimuli-responsivity.<sup>2</sup>

Introducing stimuli-responsive pores in the membrane is a promising approach to create easy-to-clean membranes<sup>3-11</sup>, since fouling, the accumulation of impurities on the membrane surface, is one of the most important problems in membrane technology. When a stimulus (e.g. temperature, pH, light, magnetism and electricity) is applied, the size of the pores increases and accumulated impurities can be removed. A stimuli-responsive character can be acquired by fabricating membranes using block copolymers that possess a stimuli-responsive character. The most commonly used stimuli-responsive block copolymers for

Membrane casting parameters to control the structure of isoporous membranes membrane production are polystyrene-*b*-poly(4-vinylpyridine) (PS-*b*-P4VP)<sup>7, 12-14</sup> and poly(isoprene-*b*-styrene-*b*-4-vinylpyridine)<sup>15-16</sup> due to their pH-responsive character and their ability to produce well-ordered isoporous membranes. PS-*b*-P4VP block copolymer membranes were also modified to attain thermo-responsivity in addition to pH-responsivity.<sup>17</sup> Thermo-responsivity was also directly obtained using polystyrene-poly(*N*-isopropyl acrylamide) (PS-PNIPAM) block copolymers either in a spin-coating process<sup>18</sup> or using a phase inversion method (as discussed in Chapter 2).<sup>19</sup> Other pH and thermo-responsive membranes were produced from polystyrene-*b*-poly(2-(dimethylamino)ethyl methacrylate)<sup>20-21</sup> and block copolymer consisting of polystyrene and poly(ethylene glycol methyl ether methacrylate).<sup>22</sup>

Recently, block copolymer membranes are produced by a phase inversion method, also referred to as self-assembly and non-solvent-induced phase separation (SNIPS). In the SNIPS process, a film is formed from a viscous solution of the block copolymer by using a doctor blade with a known gate height. The solvent in the film is evaporated for a certain period, often less than one minute, which causes a concentration gradient perpendicular to the film surface. This is the main step where self-assembly occurs. The film is then transferred into a non-solvent bath where the organic solvent in the polymer film and the non-solvent are exchanged. This ends the self-assembly process and results in the formation of the porous structure.<sup>12</sup> SNIPS membranes are free-standing and additional transfer of the membrane to a porous support step can be omitted. Different from other methods, pores are produced directly without the need of additional steps such as etching or additive removal.

Although SNIPS is an easy and quick method, there are many parameters in the process that should be considered and chosen carefully, since they strongly affect the final structure and properties of the membrane. The main parameters that influence the membrane structure are solvent type(s) and ratio, polymer concentration, evaporation time, and type of non-solvent. For a successful SNIPS process, all parameters should be optimized. In our previous study, we produced membranes from PS-*b*-PNIPAM block copolymers by using SNIPS. Whereas the films exhibited fully reversible thermo-responsive behavior, the obtained pore sizes were not uniform (Chapter 2).<sup>19</sup> In this work, we aimed to improve the surface structures of the membranes by systematically tuning the membrane casting pa-

rameters. We investigated the effect of casting solution composition and evaporation time of the SNIPS process and produced nano- and isoporous membranes from a PS-*b*-PNIPAM block copolymer. The membranes with uniform nanopores were obtained for a relatively large range of parameters. The membranes exhibited thermo-responsive behavior and this behavior was found to be fully reversible.

## 5.3 Experimental Section

---

### 5.3.1 Materials

Styrene (Sigma-Aldrich, >99%) was vacuum distilled after stirring overnight over calcium hydride. *N*-isopropylacrylamide (NIPAM) (Sigma-Aldrich, 97%) was purified by recrystallization from toluene. 2,2'-Azobis(2-methylpropionitrile) (AIBN, Sigma-Aldrich, 98%) was recrystallized from methanol. Diethylether (Biosolve B.V.) and methanol (Fisher Scientific) were used as received. 2-(dodecylthiocarbonothioylthio)-2-methylpropionic acid (DTMA) (98%), calcium hydride (CaH<sub>2</sub>) (95%), 1,4-dioxane (anhydrous, 99.8%), tetrahydrofuran (THF) (anhydrous, ≥99.9%), *N*-methyl-2-pyrrolidone (NMP) (≥99.0%), acetone and deuterated chloroform (CDCl<sub>3</sub>) (99.96% D) were purchased from Sigma-Aldrich and were used as received.

### 5.3.2 Synthesis procedures

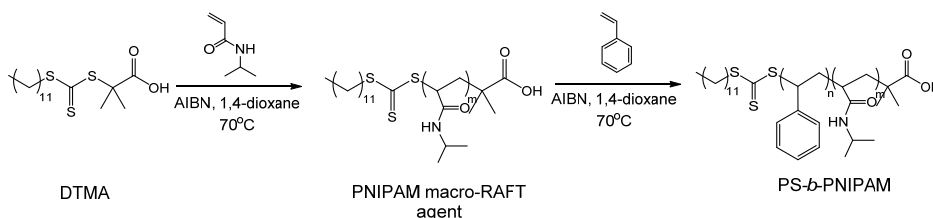
**5.3.2.1 Synthesis of PNIPAM macro-RAFT agent.** A monofunctional RAFT agent 2-(Dodecylthiocarbonothioylthio)-2-methylpropionic acid (DTMA) was used for the synthesis of PNIPAM macro-RAFT agent. AIBN, NIPAM and DTMA were dissolved in 40 mL 1,4-dioxane. The initial monomer concentration ( $[M]_0$ ), the ratio of initial monomer and chain transfer agent concentrations ( $[M]_0/[CTA]_0$ ) and the ratio of initial chain transfer agent and initiator concentrations ( $[CTA]_0/[I]_0$ ) were 1.18 mol/L, 145 and 10, respectively. The solution was transferred to a Schlenk ampoule by using syringes. After three freeze-pump-thaw cycles, the solution was heated to 70 °C by using a temperature controlled oil bath for 4 hours. The reaction was stopped by cooling the solution with liquid nitrogen. The solution was reprecipitated in diethyl ether after dissolution using a minimum amount of acetone.

Membrane casting parameters to control the structure of isoporous membranes

The product was dried overnight in a vacuum oven at room temperature (Yield: 81%).  $^1\text{H}$  NMR (400 MHz,  $\text{CDCl}_3$ ):  $\delta = 4.0$  (1H, s, -NCH-), 0.8-2.5 (9H, m,  $-\text{CH}_3$ ,  $-\text{CH}-\text{CH}_2-$ ), 5.8-7.5 (1H, br, -NH-).  $M_n = 25$  kDa, PDI = 1.10 (GPC)

**5.3.2.2 Synthesis of PS-*b*-PNIPAM copolymer.** PNIPAM macro-RAFT agent, styrene and AIBN were dissolved in 90 mL 1,4-dioxane by stirring at room temperature. Styrene was purified by vacuum distillation just before the polymerization. The initial monomer concentration ( $[\text{M}]_0$ ), the ratio of initial monomer and PNIPAM macro-RAFT agent concentrations ( $[\text{M}]_0/[\text{macro-RAFT}]_0$ ) and the ratio of initial PNIPAM macro-RAFT agent and initiator concentrations ( $[\text{macro-RAFT}]_0/[\text{I}]_0$ ) were 4.35 mol/L, 1917 and 10, respectively. The solution was transferred to a Schlenk ampoule by using syringes. After three successive freeze-pump-thaw cycles, the solutions were heated to 70 °C by using a temperature controlled oil bath. The polymerization reaction took place for 48 hours. Then the reaction was stopped by cooling the reaction solution in liquid nitrogen. 1,4-dioxane was evaporated using a rotary evaporator. The polymer was dissolved in THF and precipitated in cold water to remove unreacted PNIPAM macro-RAFT agent until no homopolymer peak was found in the GPC elugram and precipitated twice from diethyl ether to remove unreacted styrene. The copolymers were dried in a vacuum oven at 35°C (Yield: 33%).  $^1\text{H}$  NMR (400 MHz,  $\text{CDCl}_3$ ):  $\delta = 6.2$ -7.1 (5H, m, Ph), 4.0 (1H, s, -NCH-), 0.8-2.5 (3H, m,  $-\text{CH}-\text{CH}_2-$  for PS and 9H, m,  $-\text{CH}_3$ ,  $-\text{CH}-\text{CH}_2-$  for PNIPAM).  $f_{\text{PS}} = 0.83$  (NMR),  $M_n = 194$  kDa (NMR), PDI = 1.34 (GPC)

**Scheme 1.** Synthesis route of PS-*b*-PNIPAM block copolymer



### 5.3.3 Polymer characterization

$^1\text{H}$  NMR measurements were carried out on a Bruker AMX-400 spectrometer (400 MHz) at room temperature. Gel permeation chromatography (GPC) was performed on a Viscotek GPCmax equipped with 302 TDA model detectors, using a guard column (PSS-GRAM, 10

$\mu\text{m}$ , 5 cm) and two analytical columns (PSS-GRAM-1000/30 Å, 10  $\mu\text{m}$ , 30 cm) at a flow rate of 1 mL/min in dimethyl formamide (containing 0.01 M LiBr) at 50 °C. Poly(methyl methacrylate) standards were used for calibration of the column. Molecular weight and PDI of PNIPAM macro-RAFT agent and PDI of PS-*b*-PNIPAM block copolymer were calculated using Viscotec Omnisec software by using refractive index and light scattering signals, respectively. The molecular weight of the block copolymer was calculated using the molecular weight of PNIPAM-macro RAFT agent and the block ratio found from NMR. The ratio between the PS and PNIPAM blocks in the BCP was determined by comparing the integral of the aromatic PS protons at 6.2-7.1 ppm (5H, m, Ph) to the lone PNIPAM proton at 4.0 ppm (1H, s, -NCH-).

### 5.3.4 Membrane preparation

A polymer solution was poured onto a glass substrate and a thin film of polymer was formed using a manual film applicator with a gate height of 200  $\mu\text{m}$ . The polymer film was transferred into the non-solvent bath after a certain evaporation time. Water was used as a non-solvent for all the membranes except the one prepared from toluene-THF solutions. Ethanol was used as a non-solvent for that system due to immiscibility of toluene in water. Polymer films were kept in the non-solvent bath for at least 4 hours. For atomic force microscopy (AFM) and scanning electron microscopy (SEM) analyses, a small portion of this film (1 × 1 cm) was cut and fixed on a Si wafer with double sided tape and dried in a vacuum oven for at least two days at 40 °C. For permeability analysis, the membrane films were stored in demineralized water and cut into the desired dimensions just before the measurements.

Humidity might have an influence on the morphology especially because PNIPAM is hygroscopic. However, a significant difference was not observed, therefore we did not report the results. Nevertheless, all samples presented here were prepared at a constant humidity of 40% RH.

### 5.3.5 Membrane characterization

The surface morphology of the films was analyzed with a Bruker Multimode 8 AFM instrument using the Nanoscope V ScanAsyst imaging mode. DNP-10 model non-conductive

Membrane casting parameters to control the structure of isoporous membranes silicon nitride probes with a spring constant of 0.24 N/m (Bruker) were used. Images were recorded at 1.50 Hz and processed using NanoScope Analysis 1.5 software. At least three different regions on the same thin film sample were probed to assure that the obtained surface morphology was representative for the entire sample. Before analysis, membrane films were cut into small pieces and fixed on Si wafers of 1 × 1 cm size using double sided tape and dried in a vacuum oven at 40 °C overnight.

For SEM measurements, the samples were placed on flat aluminum stubs with double-sided adhesive, conducting carbon tape. Samples were coated with a 10-nm layer of tungsten using a Leica EM SCD 500 sputter-coater. SEM images were recorded on an FEI Magellan 400 field-emission SEM at an acceleration voltage of 2.0 kV. For the SEM of cross-sectional films, samples were fractured in liquid nitrogen and mounted onto 90° SEM stubs as the cross-section facing upwards.

### 5.3.6 Permeability measurements

The permeability of the membranes was carried out by using a dead-end filtration set-up by measuring the flux of Milli-Q pure water at different pressures (1-3 bar). The membrane was cut in a round shape with a diameter of 2.5 cm. It was placed in a filter holder cell having a volume of 40 mL. The cell was connected to a vessel filled with Milli-Q pure water, pressure was applied using compressed nitrogen. The cell and the vessel were heated to 20 and 50 °C by dipping them inside vessels filled with water which were heated using temperature controlled heating plates. In all experiments, the membranes were placed on top of a non-woven that acted as an additional mechanical support. Because the non-woven consists of relatively large voids and because of its high permeability value ( $\sim 750,000 \text{ L}\cdot\text{m}^{-2}\cdot\text{h}^{-1}\cdot\text{bar}^{-1}$ ), we assumed that the non-woven used has no influence on the results of the permeability experiments. For the temperatures higher than 20 °C, permeability results were corrected by multiplying the result with viscosity of water at the specified temperatures. The permeability ( $\text{L}\cdot\text{m}^{-2}\cdot\text{h}^{-1}\cdot\text{bar}^{-1}$ ) was calculated as the ratio of the flux over the applied pressure as shown in Equation 1, where  $V$  is the permeate volume (L),  $A$  is the membrane area ( $\text{m}^2$ ),  $t$  is the time (h),  $J$  is the permeate flux ( $\text{L}\cdot\text{m}^{-2}\cdot\text{h}^{-1}$ ) and  $P$  is the pressure (bar). Error bars of permeability measurements in Figure 8a were obtained by calculating the standard deviation of the repetitive measurements at 20 °C and in Figure 8b error bars for 50 °C were

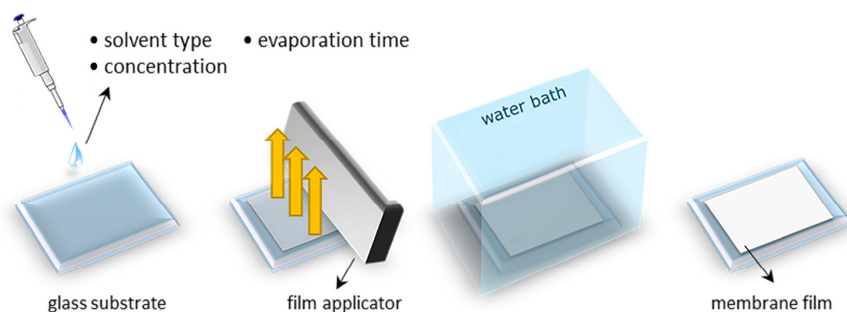
obtained by using the standard deviations that are calculated from the repetitive permeability measurements at 50 °C.

$$\text{Permeability} = V/(A \cdot t \cdot \Delta P) = J/\Delta P \quad (1)$$

## 5.4 Results and Discussion

In this study, we aimed to obtain isoporous PS-*b*-PNIPAM membrane surfaces by systematically varying various parameters that are critical in the SNIPS process (see Scheme 2). PS-*b*-PNIPAM used in this study is a high molecular weight block copolymer ( $M_n = 194$  kDa, PDI = 1.34) that consists of a major PS and a minor PNIPAM block ( $f_{PS} = 0.83$ ,  $f_{PNIPAM} = 0.17$ ) (CN-3 in Chapter 2). First, we varied the type and ratio of solvent mixtures to attain the desired solvent combination. Following this, the influence of the evaporation time, polymer concentration and water content were investigated.

**Scheme 2.** Representation of the SNIPS process. Modified SNIPS parameters are indicated on top.



### 5.4.1 Influence of solvent type

We compared the morphological behavior of the membranes prepared from the following solvent combinations: toluene-tetrahydrofuran (THF), *N*-methyl-2-pyrrolidone (NMP)-THF, methanol-THF and 1,4-dioxane (DOX)-THF. The selectivity of the solvents was estimated by comparing the Flory interaction parameters ( $\chi$ ) of the solvents and the blocks.  $\chi$  parameters were calculated using Hansen solubility parameters<sup>23-24</sup> (see Table 1). If the difference is a positive number, the solvent is PNIPAM selective; if the number is negative it is a PS selective solvent. Although the  $\chi$  parameters were moderately higher than some of the

Membrane casting parameters to control the structure of isoporous membranes experimental values reported in the literature, these calculations were sufficient to compare the affinities of the solvents with the blocks qualitatively.

**Table 1.** Calculated  $\chi$  parameters for the copolymer blocks and the solvents.

Block	NMP	DOX	THF	toluene	methanol	water	ethanol
PS	0.92	0.40	0.78	0.74	2.14	3.06	2.11
PNIPAM	1.35	0.21	0.46	1.21	1.13	2.09	0.85
$4\chi$	-0.43	0.19	0.32	-0.47	1.01	0.96	1.27

The ratios of PS selective solvent combinations were toluene: THF (v:v) 6:4, NMP: THF 8:2 and 4:6. The polymer concentration was kept constant at 20 wt%. Water was used as the non-solvent, except for the membranes prepared from toluene-THF. For this solution, ethanol was used as a non-solvent due to immiscibility of toluene and water.

Membranes prepared from the toluene: THF (6:4) solution resulted in a spherical micellar morphology for a range of evaporation times as observed by AFM imaging. Figure 1a shows a representative morphology of a membrane prepared with an evaporation time of 10 seconds. It is probable that these spheres exhibited a core-shell morphology with a PNIPAM core and a PS shell, to avoid undesired interactions of the PNIPAM chains with the highly PS selective solvent toluene.

The other PS selective solvent mixture, NMP-THF, was investigated in two volume ratios i.e. 4:6 and 8:2. For the mixture with the 8:2 ratio similar, but smaller micelles were formed (Figure 1b) as compared to the toluene-THF casting solution. Another noticeable difference was the height profile of the AFM images of the membrane surfaces shown in Figure 1a and 1b. The situation for the NMP: THF (4:6) casting solution was different: cylindrical instead of spherical micelles formed with an interconnected structure (Figure 1c). This casting solution was less PS selective, which reduced the difference in swelling of the two blocks, which may have favored cylinder formation. Overall, no isoporous membranes were obtained when PS selective solutions were used.

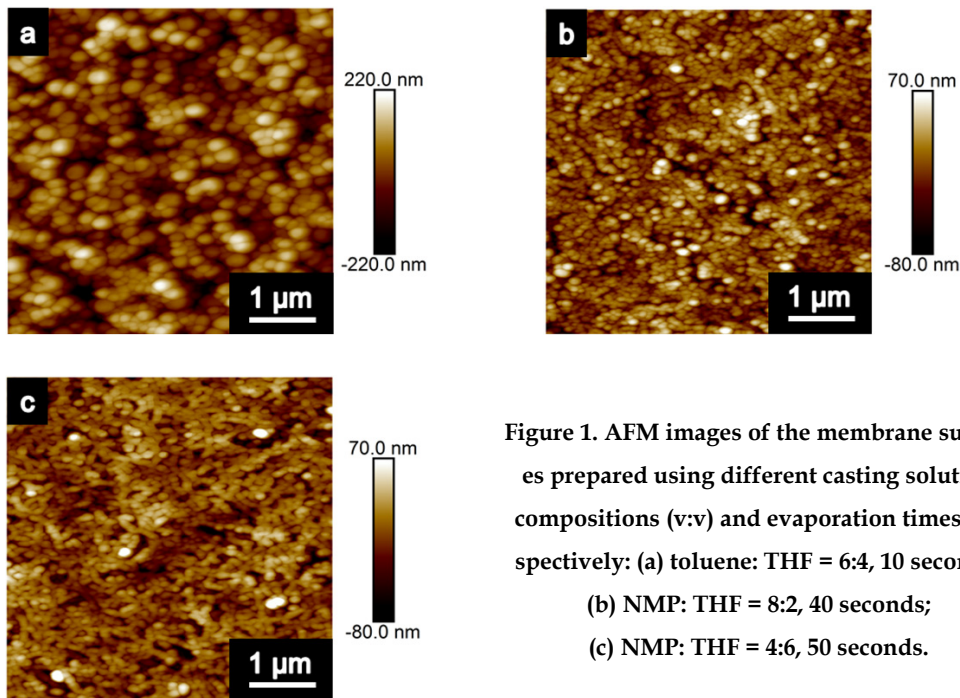


**Figure 1.** AFM images of the membrane surfaces prepared using different casting solution compositions (v:v) and evaporation times, respectively: (a) toluene: THF = 6:4, 10 seconds; (b) NMP: THF = 8:2, 40 seconds; (c) NMP: THF = 4:6, 50 seconds.

The results for PNIPAM selective solutions, i.e. methanol: THF (5:5) and DOX: THF (7:3), again with water being as the non-solvent and with 20 wt% polymer solutions, were significantly different than the results for PS selective solutions. Height differences of AFM images were lower as compared to PS selective solutions and the surface structure was found to be more interconnected. For membranes prepared using a methanol: THF (5:5) casting solution ill-defined pores were observed when using an evaporation time of 5 seconds (Figure 2a), however, this morphology was lost when the evaporation time was extended to 15 seconds. Parallel features or cracks were obtained instead of pores (Figure 2b). We speculate that due to the highly volatile character of both methanol and THF, the evaporation is so fast that it disrupts the self-assembly process.

Using DOX-THF casting solutions, pore formation was more distinct and uniform spherical pores were obtained at an evaporation time of 40 seconds. The presence of spherical pores is a strong indication of cylindrical micelles aligned perpendicular to the surface as previously reported in block copolymer membrane literature.<sup>12</sup>

Membrane casting parameters to control the structure of isoporous membranes

The mechanism of cylindrical pore formation is a complicated combination of thermodynamic and kinetic factors and is not completely understood. We speculate that, during the SNIPS process, the selectivity of the solvent composition induces micelle formation. Fast evaporation of mainly THF results in a gradient in concentration and in solvent composition. Because of this reason THF is a commonly used solvent that helps to obtain regular structures.<sup>25-28</sup> In the top layer, both the polymer concentration and the incompatibility of the PS with the solvent system are increased. This decreases the mobility and results in packing of the micelles. The DOX will evaporate at a much lower rate and limits the reduction in mobility to ensure structure formation. If the concentration gradient is steep enough, this will result in perpendicular cylindrical pores with PNIPAM lining the pore walls.<sup>29</sup> Since DOX-THF was the only solvent mixture that resulted in membranes with uniform pores in our initial experiments, we continued the optimization studies using this solvent mixture. A more detailed look at the morphological behavior of this system will be given in the next sections.

#### **5.4.2 Influence of evaporation time and polymer concentration**

The amount of time between film casting and transfer to the non-solvent bath, i.e. the time in which solvents are allowed to evaporate is probably the most crucial phase in the entire SNIPS process since this is the main step where self-assembly of the block copolymer takes place and therefore substantially determines the morphology of the membrane.

Here we examine the effect of evaporation time and polymer concentration in parallel. In Figure 3, SEM images of membranes prepared using a DOX: THF (7:3) casting solution are given for different evaporation times (20, 40, 80, 120, 160 and 200 seconds) when the polymer concentration was kept at 22 wt%. Figure 4 shows SEM images of membranes that were prepared using the same solvent mixture with a constant evaporation time of 40 seconds, but using different polymer concentrations (20, 22, 25 and 30 wt%). At short evaporation times (20 seconds), a rough irregular porous morphology was formed (Figure 3a). At that point in time, a large amount of solvent is still left in the wet film, resulting in polymer chains that are still too swollen and too mobile for a well-defined morphology to form. When the evaporation time was prolonged to 40 seconds, regular pores were observed (Figure 3b).

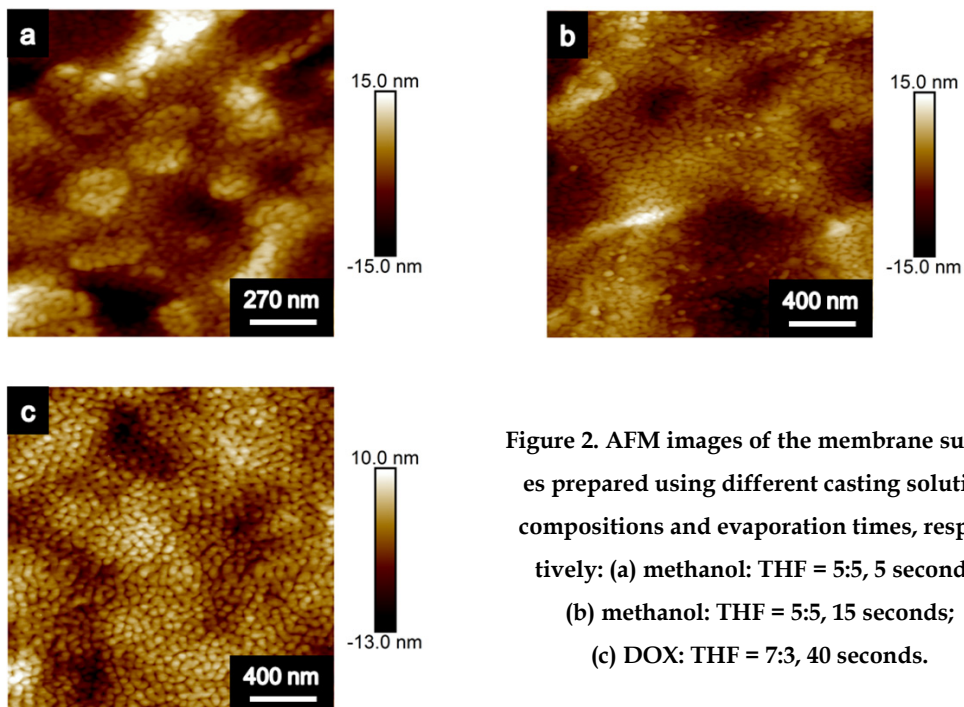


**Figure 2.** AFM images of the membrane surfaces prepared using different casting solution compositions and evaporation times, respectively: (a) methanol: THF = 5:5, 5 seconds; (b) methanol: THF = 5:5, 15 seconds; (c) DOX: THF = 7:3, 40 seconds.

Since the concentration of the polymer and/or the evaporation times were increased, the solution viscosity was higher so that the chains could arrange in a more ordered morphology in a more compact environment. Similar results were obtained for membranes prepared from polymer concentrations between 20 and 22 wt% (while keeping the evaporation time constant at 40 seconds) as shown in Figure 4a and 4b, respectively.

For longer evaporation times or higher polymer concentrations (Figure 3c, 3d and Figure 4c) a combination of spherical pores and worm-like features are obtained. We believe that these worm-like features are cylinders that are aligned parallel to the surface. DOX is a slowly evaporating solvent which results in a low solvent concentration gradient after some of the THF has evaporated. A low gradient reduces the driving force for the cylinders to align perpendicular, so for longer evaporation times the perpendicular cylinders may align parallel to the surface.

Even longer evaporation times (160-200 seconds) (Figure 3e, 3f) or even higher polymer concentrations (30 wt%) (Figure 4d) resulted in fewer pores and eventually dense films

Membrane casting parameters to control the structure of isoporous membranes were obtained. Since pores mainly form when the polymer film is transferred into the non-solvent, i.e. upon the exchange of the remaining solvent and the non-solvent, after long evaporation times (or high concentrations) there will be almost no solvent left to exchange with the non-solvent bath.

From these results, we conclude that when using DOX: THF (7:3) casting solutions the optimum concentration lies between 20-25% and evaporation times should be kept between 30-80 seconds. Using this relatively large window of casting parameters, membranes with uniform pores can be produced.

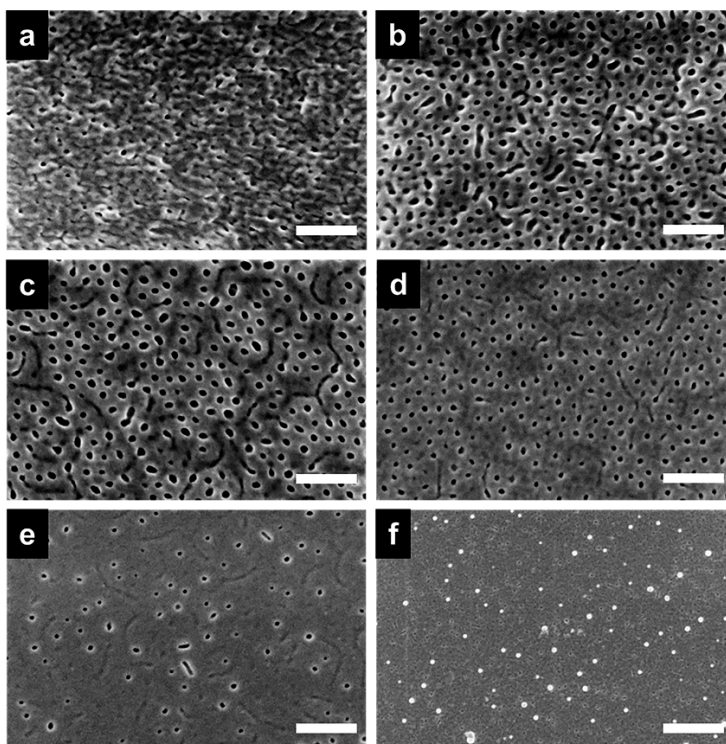


**Figure 3.** SEM images of membrane surfaces obtained with different evaporation times: (a) 20, (b) 40, (c) 80, (d) 120, (e) 160 and (f) 200 seconds. SNIPS conditions: DOX: THF (v:v) = 7:3, polymer concentration = 22 wt%. Scale bars (a-e) = 200 nm and (f) = 500 nm.

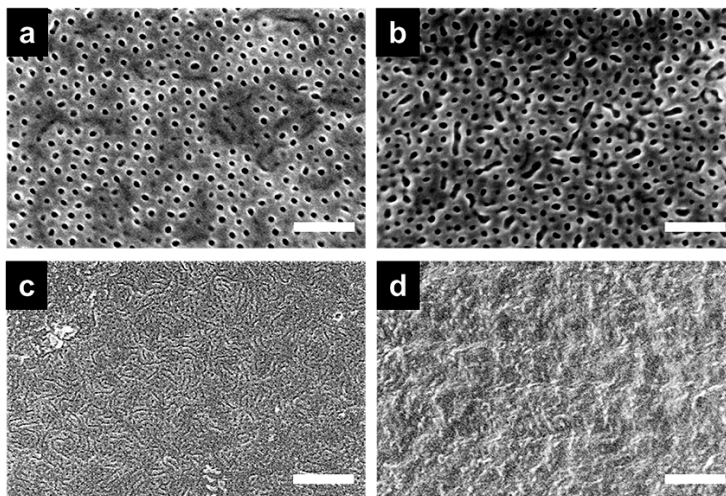


**Figure 4.** SEM images of membrane surfaces obtained using different polymer concentrations: (a) 20, (b) 22, (c) 25 and (d) 30 wt%. SNIPS conditions: DOX: THF (v: v) = 7:3, evaporation time = 40 seconds. Scale bars (a,b) = 200 nm and (c,d) = 500 nm

### 5.4.3 Influence of solvent ratio

The set of SEM images in Figure 5 provides information about the influence of solvent ratio on the membrane morphology with increasing evaporation time. When the DOX: THF ratio was high, i.e. 8:2, the evaporation time required to obtain pores was short. Uniform pores were already obtained at evaporation times of 20 seconds (Figure 5a). For the 7:3 ratio it took 40 seconds to reach a similar morphology (Figure 5f). However, this trend was not clearly observed for higher THF ratios.

Another effect of the use of high DOX: THF ratios was that the morphology switched from perpendicularly aligned cylinders to parallel aligned cylinders at shorter evaporation times as compared to lower DOX: THF ratios. Whereas, parallel features occurred for the 8:2 ratio at an evaporation time of 40 seconds (Figure 5b), for the 7:3 ratio the same structures were observed at an evaporation time of 80 seconds (Figure 5h). For the 6:4 ratio, probably an even longer evaporation time is required to obtain a morphology of parallel features. Interestingly, there were almost no parallel cylinders observed for the 3:7 ratio (Figure 5m-p). This apparent faster formation of the different morphologies upon increasing the relative

Membrane casting parameters to control the structure of isoporous membranes amount of DOX to THF, may be due to the increased incompatibility of the PS with the solvent system.

For intermediate DOX: THF ratios (7:3 and 6:4) more well-defined pores were obtained between for evaporation times of 40-60 seconds (Figure 5f, g, j, k). For the DOX: THF 3:7 ratio, fewer pores were obtained at an evaporation time of 60 seconds and at 80 seconds few, less uniform pores were obtained (Figure 5o, p). Apparently, a high amount of THF in the casting solution limits the range in which well-defined pores can be obtained. We speculate that this is due to the limited selectivity of THF for one of the blocks, which results in highly swollen polymers and low density micelles.

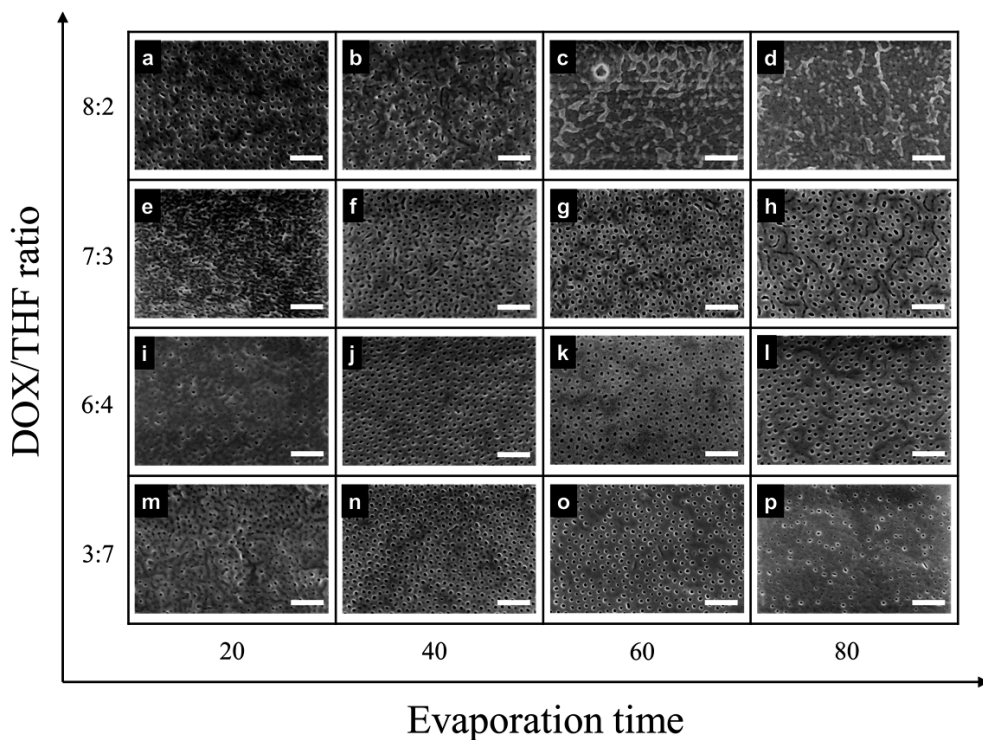


Figure 5. SEM images of the membrane surfaces cast using 22 wt% polymer solutions with evaporation times of 20-80 seconds for DOX: THF ratios of 8:2, 7:3, 6:4 and 3:7. Scale bar = 200 nm.

#### 5.4.4 Influence of water

We found that the water content in the block copolymer solution decreased the evaporation time necessary to obtain uniform pores. When no water was used in the polymer solution, an evaporation time of 20 seconds was not sufficient for proper rearrangement of the chains to obtain uniform nanopores (Figure 6a). However, in the presence of 1 vol% water, uniform nanopores were already formed after 20 seconds (Figure 6d). Parallel features occurred after 80 seconds when no water was added to the polymer solution (Figure 6c), however in the presence of 1% water, the same features were already obtained after 60 seconds (Figure 6e). These changes in evaporation times to obtain uniform pores are analogous as using a higher DOX: THF ratio. The high selectivity of water for the minority PNIPAM block affects the self-assembly behavior in favor of uniform pore formation. The theoretical estimation of  $\chi$  between PNIPAM and water (Table 1) is probably too high, because water is a good solvent for PNIPAM when  $T < 32$  °C. Therefore, the selectivity difference between PS and PNIPAM in water is probably considerably higher than the selectivity difference between the blocks in DOX. In addition, the size of the pores was found to be larger in case 1% water was added to the polymer solution (Compare the pore sizes between Figure 6b and 6d and between Figure 6c and 6e), which is also caused by the fact that PNIPAM will swell more in a more PNIPAM selective solvent mixture. We note that the differences in pore sizes were not significant when a high amount of DOX was used in the solution.

#### 5.4.5 Thermo-responsive behavior

We studied the thermo-responsive behavior of the membranes prepared using the 22 wt% DOX: THF (7:3) solution at an evaporation time of 60 seconds. The SEM images in Figure 7a show that the membrane exhibited an isoporous surface with cross-sections that have channel-like structures and large voids (Figure 7b and 7c). Film exhibited a white-opaque appearance (Figure 7d) with a total film thickness of 50  $\mu\text{m}$  (+/-5  $\mu\text{m}$ ).

To investigate the thermo-responsive properties, we measured the permeability of the membranes prepared at the same SNIPS conditions at several temperatures between 20 and 50 °C at a pressure of 1 bar (Figure 8a). For a true comparison of membrane permeability at

Membrane casting parameters to control the structure of isoporous membranes different temperatures, the permeability values need to be corrected for the temperature-dependent changes in viscosity of the water passing through the membrane. This correction is necessary to precisely analyze the temperature-dependent changes that occur only due to the thermo-responsive character of the membrane. This is achieved by multiplying the dynamic viscosity of water at a given temperature with the measured permeability values.

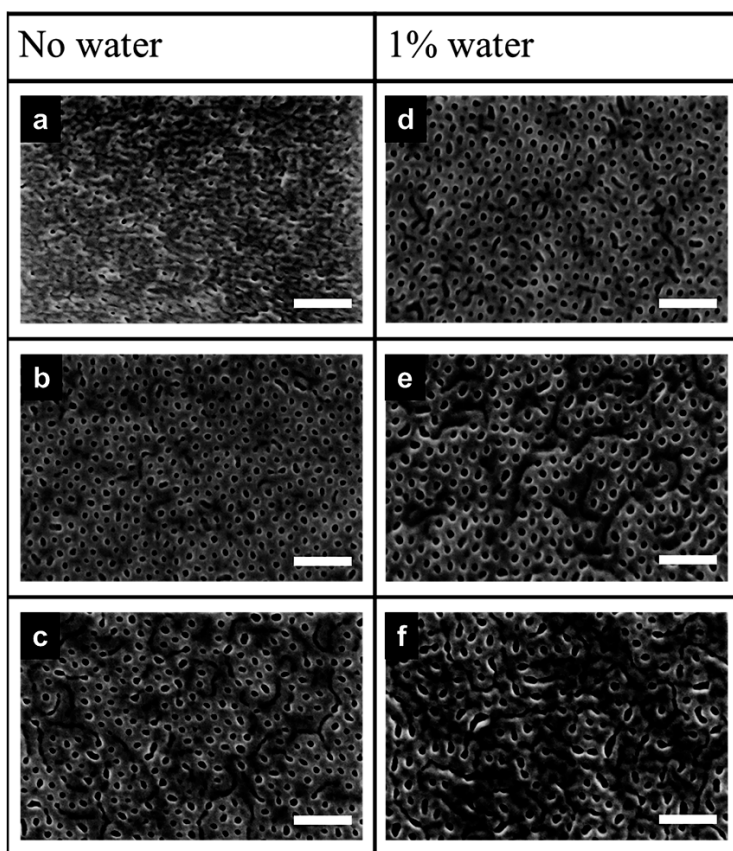
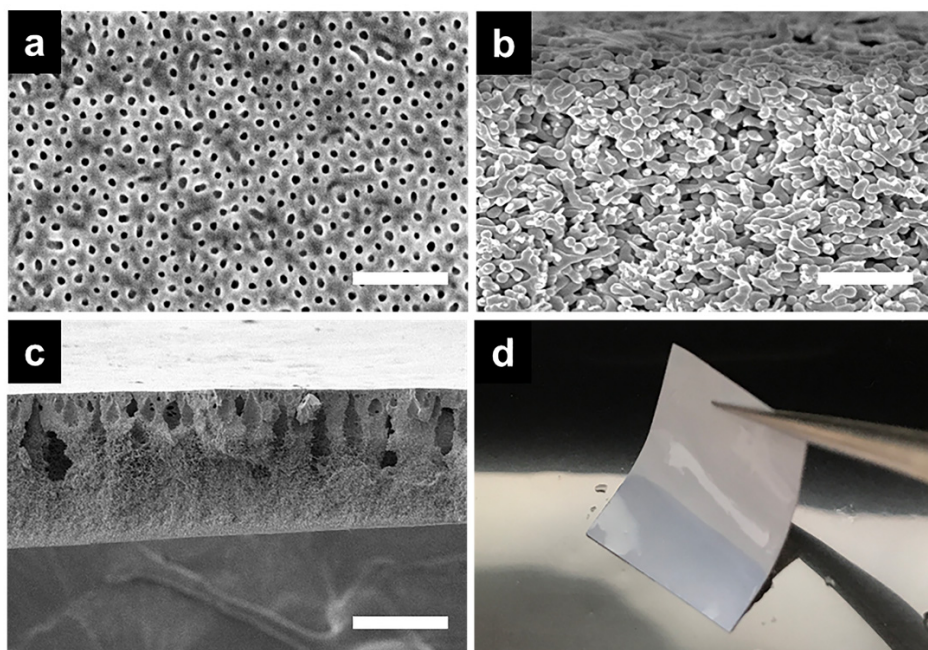


Figure 6. SEM images of the membranes from 22 wt% DOX: THF = 7: 3 solutions (a-c) without water and (d-f) with 1 vol% water added to the DOX-THF solution, for evaporation times of (a,d) 20 (b,e) 60 and (c,f) 80 seconds. Scale bar = 200 nm.

In Figure 8a, only viscosity corrected permeability values were used to illustrate the permeability increase as a function of temperature. The transition primarily occurred between 26 and 38 °C with the steepest increase around the LCST of PNIPAM (~32 °C). This result demonstrates that the thermo-responsive behavior of the membrane is a result of the col-

lapsing PNIPAM chains above the LCST. This behavior strongly suggests that the pores were coated with PNIPAM domains.<sup>16</sup>



**Figure 7.** SEM images of the (a) surface, (b-c) cross-section of the membrane. (d) Appearance of the membrane used for thermo-responsive permeability measurements. SNIPS conditions: 22 wt% polymer solution from DOX: THF = 7:3 with an evaporation time of 60 seconds. Scale bars for (a) = 200 nm, (b) = 1  $\mu\text{m}$  and (c) = 25  $\mu\text{m}$ .

Reversibility of the membranes was analyzed by measuring the permeability for several temperature cycles (i.e. switching between 20 °C and 50 °C). In Figure 8b, both uncorrected and viscosity corrected permeability values are indicated to observe the contribution of the membrane in the permeability change at 50 °C. When we compare uncorrected and viscosity corrected permeability values, viscosity corrected permeability values prove that the permeability increase is only a result of the thermo-responsive character of the membrane at elevated temperatures without contribution of any other parameters that participate to the experiment. Identical permeability values were obtained at each cycle which confirms that the thermo-responsive property of the membrane is fully reversible. Consequently, we can conclude that these membranes can be repetitively used at room temperature for filtra-

Membrane casting parameters to control the structure of isoporous membranes for various applications. These fully reversible thermo-responsive membranes offer prospects to produce industrially valuable easy-to-clean membranes.

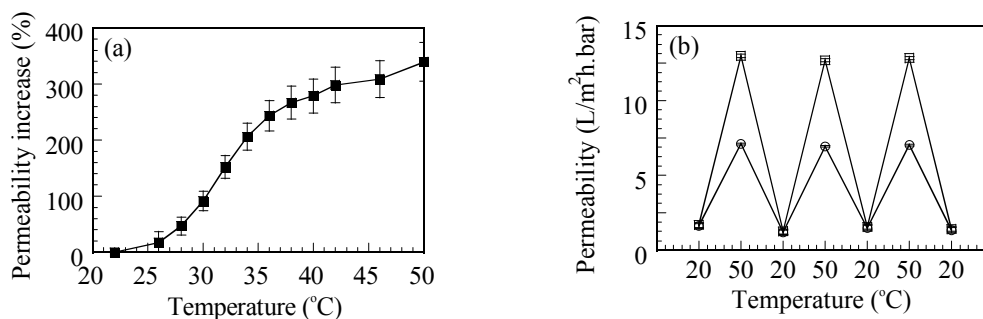


**Figure 8. (a) Permeability increase as a function of temperature. (b) Reversibility of the permeability as a function of temperature cycles. SNIPS conditions: 22 wt% polymer solution from DOX: THF = 7:3 with an evaporation time of 60 seconds.**

## 5.5 Conclusions

We fabricated nanoporous membranes from PS-*b*-PNIPAM block copolymers by using a SNIPS process. We investigated the influence of the solvent type, evaporation time and polymer concentration to attain nano- and isoporous membranes. Isoporous membranes could be obtained at a relatively large window of the SNIPS parameters, i.e. 20-25 wt% polymer concentration, evaporation time of 20-80 seconds. We obtained uniform pores when we used solvent mixtures selective for the minority block, i.e. PNIPAM, in the copolymer. The membranes exhibited thermo-responsive behavior and this behavior was found to be fully reversible which is advantageous for future industrial easy-to-clean membrane applications. The combination of casting parameter optimization and permeability measurements described here demonstrates the ability to systematically design structures in block copolymer derived ultrafiltration membranes.

## Acknowledgements

Electron microscopy work was performed at the Wageningen Electron Microscopy Centre (WEMC) of Wageningen University.

## References

---

1. Mai, Y.; Eisenberg, A., Self-assembly of block copolymers. *Chemical Society Reviews* **2012**, *41* (18), 5969-5985.
2. Jackson, E. A.; Hillmyer, M. A., Nanoporous Membranes Derived from Block Copolymers: From Drug Delivery to Water Filtration. *ACS Nano* **2010**, *4* (7), 3548-3553.
3. Tokarev, I.; Minko, S., Stimuli-responsive hydrogel thin films. *Soft Matter* **2009**, *5* (3), 511-524.
4. Pan, K.; Zhang, X.; Ren, R.; Cao, B., Double stimuli-responsive membranes grafted with block copolymer by ATRP method. *Journal of Membrane Science* **2010**, *356* (1-2), 133-137.
5. Wandera, D.; Wickramasinghe, S. R.; Husson, S. M., Stimuli-responsive membranes. *Journal of Membrane Science* **2010**, *357* (1-2), 6-35.
6. Himstedt, H. H.; Marshall, K. M.; Wickramasinghe, S. R., pH-responsive nanofiltration membranes by surface modification. *Journal of Membrane Science* **2011**, *366* (1-2), 373-381.
7. Nunes, S. P.; Behzad, A. R.; Hooghan, B.; Sougrat, R.; Karunakaran, M.; Pradeep, N.; Vainio, U.; Peinemann, K.-V., Switchable pH-Responsive Polymeric Membranes Prepared via Block Copolymer Micelle Assembly. *ACS Nano* **2011**, *5* (5), 3516-3522.
8. Mondal, S.; Wickramasinghe, S. R., Photo-induced graft polymerization of N-isopropyl acrylamide on thin film composite membrane: Produced water treatment and antifouling properties. *Separation and Purification Technology* **2012**, *90*, 231-238.
9. Chen, X.; Shi, C.; Wang, Z.; He, Y.; Bi, S.; Feng, X.; Chen, L., Structure and performance of poly(vinylidene fluoride) membrane with temperature-sensitive poly(n-isopropylacrylamide) homopolymers in membrane pores. *Polym Compos* **2013**, *34* (4), 457-467.
10. Chen, Y.-C.; Xie, R.; Chu, L.-Y., Stimuli-responsive gating membranes responding to temperature, pH, salt concentration and anion species. *Journal of Membrane Science* **2013**, *442*, 206-215.
11. Yang, Q.; Himstedt, H. H.; Ulbricht, M.; Qian, X.; Ranil Wickramasinghe, S., Designing magnetic field responsive nanofiltration membranes. *Journal of Membrane Science* **2013**, *430*, 70-78.
12. Peinemann, K.-V.; Abetz, V.; Simon, P. F. W., Asymmetric superstructure formed in a block copolymer via phase separation. *Nat Mater* **2007**, *6* (12), 5.
13. Tripathi, B. P.; Dubey, N. C.; Choudhury, S.; Simon, F.; Stamm, M., Antifouling and antibiofouling pH responsive block copolymer based membranes by selective surface modification. *Journal of Materials Chemistry B* **2013**, *1* (27), 3397-3409.
14. Yi, Z.; Zhang, P.-B.; Liu, C.-J.; Zhu, L.-P., Symmetrical Permeable Membranes Consisting of Overlapped Block Copolymer Cylindrical Micelles for Nanoparticle Size Fractionation. *Macromolecules* **2016**, *49* (9), 3343-3351.
15. Gu, Y.; Wiesner, U., Tailoring Pore Size of Graded Mesoporous Block Copolymer Membranes: Moving from Ultrafiltration toward Nanofiltration. *Macromolecules* **2015**, *48* (17), 6153-6159.
16. Phillip, W. A.; Mika Dorin, R.; Werner, J. r.; Hoek, E. M. V.; Wiesner, U.; Elimelech, M., Tuning Structure and Properties of Graded Triblock Terpolymer-Based Mesoporous and Hybrid Films. *Nano Letters* **2011**, *11* (7), 2892-2900.
17. Clodt, J. I.; Filiz, V.; Rangou, S.; Buhr, K.; Abetz, C.; Höche, D.; Hahn, J.; Jung, A.; Abetz, V., Double Stimuli-Responsive Isoporous Membranes via Post-Modification of pH-Sensitive Self-Assembled Diblock Copolymer Membranes. *Adv. Funct. Mater.* **2013**, *23* (6), 731-738.
18. Nykänen, A.; Nuopponen, M.; Laukkanen, A.; Hirvonen, S.-P.; Rytelä, M.; Turunen, O.; Tenhu, H.; Mezzenga, R.; Ikkala, O.; Ruokolainen, J., Phase Behavior and Temperature-Responsive

Molecular Filters Based on Self-Assembly of Polystyrene-block-poly(N-isopropylacrylamide)-block-polystyrene. *Macromolecules* **2007**, *40* (16), 5827-5834.

19. Cetintas, M.; de Groot, J.; Hofman, A. H.; van der Kooij, H. M.; Loos, K.; de Vos, W. M.; Kamperman, M., Free-standing thermo-responsive nanoporous membranes from high molecular weight PS-PNIPAM block copolymers synthesized via RAFT polymerization. *Polymer Chemistry* **2017**, *8* (14), 2235-2243.
20. Schacher, F.; Rudolph, T.; Wieberger, F.; Ulbricht, M.; Müller, A. H. E., Double Stimuli-Responsive Ultrafiltration Membranes from Polystyrene-block-poly(N,N-dimethylaminoethyl methacrylate) Diblock Copolymers. *ACS Applied Materials & Interfaces* **2009**, *1* (7), 1492-1503.
21. Schacher, F.; Ulbricht, M.; Müller, A. H. E., Self-Supporting, Double Stimuli-Responsive Porous Membranes From Polystyrene-block-poly(N,N-dimethylaminoethyl methacrylate) Diblock Copolymers. *Adv. Funct. Mater.* **2009**, *19* (7), 1040-1045.
22. Tang, Y.; Ito, K.; Hong, L.; Ishizone, T.; Yokoyama, H., Tunable Thermo-responsive Mesoporous Block Copolymer Membranes. *Macromolecules* **2016**, *49* (20), 7886-7896.
23. Ahmad, H., Solubility Parameter of Acrylamide Series Polymers through Its Components and Group Contribution Technique. *Journal of Macromolecular Science: Part A - Chemistry* **1982**, *17* (4), 585-600.
24. Hansen, C. M., *Hansen Solubility Parameters: A User's Handbook*. CRC Press: U.S.A, 2000.
25. Cetintas, M.; Kamperman, M., Self-assembly of PS-b-PNIPAM-b-PS block copolymer thin films via selective solvent annealing. *Polymer* **2016**, *107*, 387-397.
26. Jung, A.; Rangou, S.; Abetz, C.; Filiz, V.; Abetz, V., Structure Formation of Integral Asymmetric Composite Membranes of Polystyrene-block-Poly(2-vinylpyridine) on a Nonwoven. *Macromolecular Materials and Engineering* **2012**, *297* (8), 790-798.
27. Karunakaran, M.; Nunes, S. P.; Qiu, X.; Yu, H.; Peinemann, K.-V., Isoporous PS-b-PEO ultrafiltration membranes via self-assembly and water-induced phase separation. *Journal of Membrane Science* **2014**, *453* (0), 471-477.
28. Vriezokolk, E. J.; Nijmeijer, K.; de Vos, W. M., Dry-wet phase inversion block copolymer membranes with a minimum evaporation step from NMP/THF mixtures. *Journal of Membrane Science* **2016**, *504*, 230-239.
29. Phillip, W. A.; Hillmyer, M. A.; Cussler, E. L., Cylinder Orientation Mechanism in Block Copolymer Thin Films Upon Solvent Evaporation. *Macromolecules* **2010**, *43* (18), 7763-7770.



# CHAPTER 6

## **General Discussion**

## 6.1 Remarkable Materials

---

Block copolymers (BCPs) exhibit a special ability to self-assemble to form regular nanostructures that can easily be tuned for specific applications. In this thesis, we aimed to use BCPs to develop thermo-responsive nanoporous membranes that can be used to incorporate easy-to-clean properties to the membrane.

We showed that well-defined high molecular weight polystyrene-*b*-poly(*N*-isopropyl acrylamide) (PS-*b*-PNIPAM) BCPs can be successfully synthesized and used to produce free-standing thermo-responsive nanoporous membranes via a non-solvent induced phase separation (SNIPS) process. We found that SNIPS of PS-*b*-PNIPAM BCPs required parameter settings that were much 'broader' than the isoporous SNIPS membranes reported in the literature.<sup>1</sup> This feature may offer advantages to produce isoporous membranes in less controlled production conditions. We confirmed that these membranes exhibited fully reversible thermo-responsive behavior, which makes them interesting for industrial applications. Fully thermo-responsive behavior was not obtained in any SNIPS membrane before.

We also prepared polystyrene-*b*-poly(*N*-isopropylacrylamide)-*b*-polystyrene (PS-*b*-PNIPAM-*b*-PS) triblock copolymer thin films and investigated their morphological properties when these were annealed with solvents of different selectivity. This systematic analysis allowed us to find the conditions that were needed to produce thin films with hexagonally ordered perpendicular cylinders. Similar solvent annealing studies may be of use in a wider context of thin film research e.g., when there is a need to attain different morphologies using a given block copolymer. In addition, stimuli-responsive block copolymer thin films have advantages over stimuli-responsive grafted films, since a 3D network is more stable than grafted brushes. For example, thin films can be transferred from one substrate to another and depending on the thickness they can be used as standing film as well.<sup>2</sup> In general, as compared to grafted brushes, more complex nanostructured features can be achieved in BCP thin films and additional modification reaction steps such as 'grafting' are not necessary.

In the process of the thesis work, new insights were obtained and a number of problems were solved but at the same time various new questions and new ideas for future research

directions emerged. The purpose of this chapter is to highlight these. The idea is to discuss how we can improve the properties of block copolymer membranes, so that they will meet the requirements for (more) industrial applications.

### 6.1.1 Permeability

As mentioned above, we succeeded to produce isoporous membranes by carefully tuning the SNIPS parameters. Still, the permeability values can be further improved to meet the values that are used in industry. To further increase the permeability of these isoporous membranes, the pore sizes should be increased. In the literature, one typically finds that pore formation is highly dependent on the minority block of the copolymer. More specifically, the size of the pores is proportional to the volume of the minority block. Therefore, when the volume of the minority block is increased, consequently, the pores of the membrane which are surrounded by PNIPAM will be larger after the collapse of PNIPAM chains. Hence this requires PS-PNIPAM block copolymer with a higher PNIPAM percentage. Indeed, Abetz et al. showed that they reached larger pore sizes with a higher percentage of minority block with the same block copolymer molecular weight.<sup>3</sup> Alternatively, one can blend homopolymers of the type of the minority block with the block copolymer to increase the volume ratio of the minority block.<sup>4</sup>

Another way to tune the volume ratio of the PNIPAM block is to make use of selective solvents. It may prove feasible to use a solvent mixture which is even more PNIPAM selective than the solvent mixtures we used to prepare block copolymer solutions reported in Chapter 5. Our studies confirmed that a more PNIPAM selective solvent mixture (water addition) resulted in isoporous membranes with increased pore sizes (Chapter 5), because the more PNIPAM selective solvent resulted in more swollen PNIPAM-rich regions. During the attempts to increase the volume ratio of PNIPAM, it is important to take into account that the morphology can shift to other regions of the block copolymer phase diagram (Chapter 1). For example, one may go from a hexagonally packed cylinder phase to a lamellar phase. Such a shift should be avoided because generally a lamellar morphology is not useful for membranes with filtering capabilities. Hence, one should aim specifically to remain in the cylindrical phase or more favorably to reach bicontinuous phases such as the double gyroid

(Chapter 3), since for this phase, a perpendicular alignment of the structures will not be necessary to target.

Among the mentioned solutions to tune the domain size of the PNIPAM rich regions, we speculate that the selective solvent approach is the most practical one, since the synthesis of new BCPs for each pore size is a time-consuming process. Moreover, the solvent selectivity can be changed significantly with a small adjustment of the solvent ratios. Furthermore, common laboratory solvents are much less expensive than the use of expensive compounds i.e. homopolymers. Plus, one can easily find plenty of information in the literature on the selectivity of the common solvents for the respective polymer blocks.<sup>5</sup>

Furthermore, there are reports in the literature stating that shorter evaporation times result in membranes with a thinner selective layer and a larger spongy cross-section.<sup>6</sup> That is why the permeability of the resulting membranes can also be increased by reducing the evaporation time of the cast film. Nevertheless, during such optimization one should carefully consider the changes in the membrane surface structure. In our own studies, our membranes did not result in an isoporous surface at short evaporation times. Possibly, with a more PNIPAM selective solvent mixture, one can improve the surface structures at short evaporation times, since in our own investigations it was observed that the isoporous morphology occurs earlier at higher PNIPAM selective conditions (see the results of 1,4-dioxane: THF (8:2) solvent combination and 1% water addition in polymer solution in Chapter 5).

In addition, when membranes are needed for applications where isoporosity is not a strict requirement, the membranes prepared using NMP-THF solutions, reported in Chapter 2, can be readily used for higher permeability values while preserving their fully thermo-responsive behavior.

### **6.1.2 Mechanical stability**

Membranes fabricated using PS-*b*-PNIPAM BCPs exhibited in an acceptable strength for our characterizations. However, for industrial applications, higher mechanical strengths may be required especially during the handling and transfer of the membranes. To incorporate a higher mechanical strength to these membranes, the overall molecular weight of the copolymer can be increased. In case the brittle character of the PS matrix still causes a

drawback, when highly ductile membranes are desired, incorporating a rubbery block to the copolymer, such as polybutadiene and polyisoprene offers a favorable solution.<sup>4, 7</sup> In this situation, the synthesis methods must be adjusted. The addition of such blocks to the copolymer may require polymerization methods other than RAFT e.g. anionic polymerization which requires concomitantly more strict reaction conditions.

### 6.1.3 Further characterization

Before membranes can be used in real-life applications, extensive characterization tests are mandatory. One of such tests involves *mechanical strength* measurements which include tensile strength testing and dynamic mechanical analysis. The result of such mechanical characterization will inform us on the limitations of use for a particular membrane. We know from the literature that both stimuli-responsive membranes<sup>8-13</sup> as well as the presence of a hydrophilic component on the membrane surface,<sup>14</sup> such as PNIPAM,<sup>9, 11</sup> results in low-fouling properties. Nevertheless, a solid confirmation of the low-fouling properties of our membranes remains to be obtained. Hence it is necessary to execute *fouling studies*. In a typical fouling study, change in the water flux is monitored after the membrane is fouled using commercial protein solutions (e.g. bovine serum albumin).<sup>10, 15</sup> If the membrane is low-fouling, the flux should increase when the temperature is increased above the LCST of the block polymer. *Rejection tests* will be also helpful to confirm the sizes of the uniform nanopores observed in SEM images of the membrane surface and to precisely determine the filtration range of a membrane. Furthermore, since the membranes exhibit fully thermo-responsive properties, the confirmation of the *long-term usage* of the membrane should be also on the program. When the membranes are used for a long time, there is a high possibility that bacteria will accumulate on the membrane surface, therefore the *measurement of antimicrobial properties* is another necessity to fully confirm that these membranes are suitable for long-term industrial applications.

### 6.1.4 Lower cost solutions

Even though the number of industrial attempts to use controlled/living synthesis methods to produce well-defined polymers in large quantities is increasing,<sup>16</sup> these controlled polymers including BCPs remain expensive materials.

To decrease the material cost, one possibility may be to blend the block copolymer with cheaper additives such as carbohydrates,<sup>17</sup> Cu<sup>2+</sup> or Mg<sup>2+</sup> salts<sup>18-19</sup> which increases the solution viscosity that leads to more compact structures with a minimum amount of block copolymer to attain an isoporous surface.

Another solution is to prepare thin film membranes, since it requires rather less material than for SNIPS. We know from literature that the thin film should be spin-coated on a porous substrate or on a support membrane and annealed to obtain long-range ordering and the desired morphology, such as perpendicular hexagonal cylinders that we obtained for PS-*b*-PNIPAM-*b*-PS BCPs in Chapter 4. These materials can be directly used as a membrane where it is hypothesized that PS plays a role as physical crosslinks<sup>20</sup> or the permeability can be further increased by etching the cylinder forming block.<sup>21</sup> However, in the second case, since cylinders consist of PS and PNIPAM being the matrix phase, an additional cross-linking reaction might be necessary to maintain the mechanical strength of the membrane. It should be kept in mind that these extra steps necessary in thin film fabrication may increase the product costs as well which finally can result in total costs being even more expensive than the cost of block copolymer necessary in SNIPS process, therefore, a good balance should be constituted to choose the optimum conditions.

## 6.2 Understanding the self-assembly mechanism in isoporous membrane formation

---

Since SNIPS is a relatively new membrane production process that involves block copolymers, the role of block copolymer self-assembly on the pore formation mechanism is not yet fully elucidated. Systematic modelling of the process will shed more light on the pore formation mechanism. We discussed above that typically selective solvent mixtures will be used in SNIPS to direct a desired morphology to the block copolymer at a given evaporation time. The modeling of the dynamics of this process is highly challenging as we will need to predict how the change in the amounts of solvent(s) in the system effects the microphase segregation of the block copolymers. In general, this calls for theories that can account for systems that are off-equilibrium. However, as a first step we may rely on the in-

formation that can be obtained from an equilibrium theory. We may use the SF-SCF method once again and extend the analysis to block copolymer self-assembly in the presence of one or more (selective) solvents. By fixing the solvent amounts, the system can be modelled at a specific moment during the membrane formation process. Of course, as compared to the results of Chapter 3, the parameter space increases significantly and hence it complicates the effective phase diagram. It is however expected that a detailed study on the effects of selective solvents on the block copolymer morphology will help us to understand what happens in the dynamical system. Here in line with the simulations, *in-situ* characterization of the membrane formation can be investigated using X-ray scattering measurements. Grazing incidence small angle X-ray spectroscopy (GISAXS) has been successfully used for the membrane formation of PS-*b*-P4VP BCPs.<sup>22</sup> Similar *in-situ* characterization of PS-*b*-PNIPAM block copolymer using GISAXS will give insights about the instant morphologies of film occurring during evaporation. When we know which phase to expect at given conditions, we will have the opportunity to design the process that will lead to better and more well-defined membranes.

In a systematic study, one should subsequently couple the equilibrium SF-SCF results to the membranes in a dynamic practical situation. The idea is that SNIPS is a dynamic process and the self-assembly of the block copolymer can be stopped at a desired morphology which occurs before the equilibrium is reached. Thus, we can precisely identify the phases that occur in the system upon the approach toward full equilibrium. These kinetically trapped systems observed, e.g. in GISAXS measurements, can be compared to the SCF predictions at given solvent compositions. Such a study will extend the results of Chapter 3 wherein the morphology of the hexagonally perforated lamellar phase (HPL) was followed as a function of the block ratio. Including solvents to such an analysis may lead to a deeper understanding of the block copolymer phase transition dynamics. The investigation of the solvent concentration gradient that occurs on the membrane surface during evaporation may be yet another challenge. Possibly the SF-SCF theory for microphase segregation can be extended to account for chemical potential gradients of the solvent across the modelling volume.<sup>23-25</sup> In parallel, it was claimed that during solvent evaporation the possible formation of metastable phases such as HPL, also studied in Chapter 3, may play a role in pore

formation thereby further investigation of such phases is promising to unveil the pore formation mechanism of SNIPS membranes.<sup>26</sup>

## 6.3 Outlook

---

In this thesis, we successfully synthesized well-defined high molecular weight PS-PNIPAM BCPs and produced fully reversible thermo-responsive nano- and isoporous membranes. We have contributed to the block copolymer literature by proposing a better way for the *synthesis* of block copolymers, by studying the *self-assembly* process and by taking steps towards *membrane applications*. We are convinced that the thermo-responsive character of our BCPs will be a key factor for practical membrane applications, however before our type of membranes will be on the market, more research is needed. We hope that this thesis will inspire many researches to step in and solve the remaining puzzles so that we will soon have durable thermo-responsive, easy-to-clean membranes that will allow us to produce nice, clean drinking water for generations to come.

## References

---

1. Abetz, V., Isoporous Block Copolymer Membranes. *Macromol. Rapid Commun.* **2015**, *36* (1), 10-22.
2. Tokarev, I.; Minko, S., Stimuli-responsive hydrogel thin films. *Soft Matter* **2009**, *5* (3), 511-524.
3. Rangou, S.; Buhr, K.; Filiz, V.; Clodt, J. I.; Lademann, B.; Hahn, J.; Jung, A.; Abetz, V., Self-organized isoporous membranes with tailored pore sizes. *Journal of Membrane Science* **2014**, *451* (0), 266-275.
4. Phillip, W. A.; Mika Dorin, R.; Werner, J. r.; Hoek, E. M. V.; Wiesner, U.; Elimelech, M., Tuning Structure and Properties of Graded Triblock Terpolymer-Based Mesoporous and Hybrid Films. *Nano Letters* **2011**, *11* (7), 2892-2900.
5. Hansen, C. M., *Hansen Solubility Parameters: A User's Handbook*. CRC Press: U.S.A, 2000.
6. Peinemann, K.-V.; Abetz, V.; Simon, P. F. W., Asymmetric superstructure formed in a block copolymer via phase separation. *Nat Mater* **2007**, *6* (12), 5.
7. Hörenz, C.; Pietsch, C.; Goldmann, A. S.; Barner-Kowollik, C.; Schacher, F. H., Phase Inversion Membranes from Amphiphilic Diblock Terpolymers. *Adv. Mater. Interfaces* **2015**, *2* (8), n/a-n/a.
8. Himstedt, H. H.; Marshall, K. M.; Wickramasinghe, S. R., pH-responsive nanofiltration membranes by surface modification. *Journal of Membrane Science* **2011**, *366* (1-2), 373-381.
9. Mondal, S.; Wickramasinghe, S. R., Photo-induced graft polymerization of N-isopropyl acrylamide on thin film composite membrane: Produced water treatment and antifouling properties. *Separation and Purification Technology* **2012**, *90*, 231-238.

10. Yu, S.; Chen, Z.; Liu, J.; Yao, G.; Liu, M.; Gao, C., Intensified cleaning of organic-fouled reverse osmosis membranes by thermo-responsive polymer (TRP). *Journal of Membrane Science* **2012**, *392–393*, 181-191.
11. Chen, X.; Shi, C.; Wang, Z.; He, Y.; Bi, S.; Feng, X.; Chen, L., Structure and performance of poly(vinylidene fluoride) membrane with temperature-sensitive poly(*n*-isopropylacrylamide) homopolymers in membrane pores. *Polym Compos* **2013**, *34* (4), 457-467.
12. Tripathi, B. P.; Dubey, N. C.; Choudhury, S.; Simon, F.; Stamm, M., Antifouling and antibiofouling pH responsive block copolymer based membranes by selective surface modification. *Journal of Materials Chemistry B* **2013**, *1* (27), 3397-3409.
13. Yang, Q.; Himstedt, H. H.; Ulbricht, M.; Qian, X.; Ranil Wickramasinghe, S., Designing magnetic field responsive nanofiltration membranes. *Journal of Membrane Science* **2013**, *430*, 70-78.
14. Jung, A.; Filiz, V.; Rangou, S.; Buhr, K.; Merten, P.; Hahn, J.; Clodt, J.; Abetz, C.; Abetz, V., Formation of Integral Asymmetric Membranes of AB Diblock and ABC Triblock Copolymers by Phase Inversion. *Macromol. Rapid Commun.* **2013**, *34* (7), 610-615.
15. Clodt, J. I.; Bajer, B.; Buhr, K.; Hahn, J.; Filiz, V.; Abetz, V., Performance study of isoporous membranes with tailored pore sizes. *Journal of Membrane Science* **2015**, *495*, 334-340.
16. Grishin, D. F.; Grishin, I. D., Controlled radical polymerization: Prospects for application for industrial synthesis of polymers (Review). *Russian Journal of Applied Chemistry* **2011**, *84* (12), 2021-2028.
17. Clodt, J. I.; Rangou, S.; Schröder, A.; Buhr, K.; Hahn, J.; Jung, A.; Filiz, V.; Abetz, V., Carbohydrates as Additives for the Formation of Isoporous PS-*b*-P4VP Diblock Copolymer Membranes. *Macromol. Rapid Commun.* **2013**, *34* (2), 190-194.
18. Nunes, S. P.; Behzad, A. R.; Hooghan, B.; Sougrat, R.; Karunakaran, M.; Pradeep, N.; Vainio, U.; Peinemann, K.-V., Switchable pH-Responsive Polymeric Membranes Prepared via Block Copolymer Micelle Assembly. *ACS Nano* **2011**, *5* (5), 3516-3522.
19. Gallei, M.; Rangou, S.; Filiz, V.; Buhr, K.; Bolmer, S.; Abetz, C.; Abetz, V., The Influence of Magnesium Acetate on the Structure Formation of Polystyrene-*block*-poly(4-vinylpyridine)-Based Integral-Asymmetric Membranes. *Macromolecular Chemistry and Physics* **2013**, *214* (9), 1037-1046.
20. Nykänen, A.; Nuopponen, M.; Laukkanen, A.; Hirvonen, S.-P.; Rytelä, M.; Turunen, O.; Tenhu, H.; Mezzenga, R.; Ikkala, O.; Ruokolainen, J., Phase Behavior and Temperature-Responsive Molecular Filters Based on Self-Assembly of Polystyrene-*block*-poly(*N*-isopropylacrylamide)-*block*-polystyrene. *Macromolecules* **2007**, *40* (16), 5827-5834.
21. Phillip, W. A.; Hillmyer, M. A.; Cussler, E. L., Cylinder Orientation Mechanism in Block Copolymer Thin Films Upon Solvent Evaporation. *Macromolecules* **2010**, *43* (18), 7763-7770.
22. Marques, D. S.; Dorin, R. M.; Wiesner, U.; Smilgies, D.-M.; Behzad, A. R.; Vainio, U.; Peinemann, K.-V.; Nunes, S. P., Time-resolved GISAXS and cryo-microscopy characterization of block copolymer membrane formation. *Polymer* **2014**, *55* (6), 1327-1332.
23. Scheinhardt-Engels, S. M.; Leermakers, F. A. M.; Fler, G. J., Steady-state analysis of polymer adsorption at and transport across an interface between two polymer phases. *Faraday Discussions* **2005**, *129* (0), 315-326.
24. Scheinhardt-Engels, S. M.; Leermakers, F. A. M.; Fler, G. J., Lattice mean-field method for stationary polymer diffusion. *Phys. Rev. E* **2003**, *68* (1), 011802.
25. Scheinhardt-Engels, S. M.; Leermakers, F. A. M.; Fler, G. J., Stationary dynamics approach to analytical approximations for polymer coexistence curves. *Phys. Rev. E* **2004**, *69* (2), 021808.
26. Nunes, S. P., Block Copolymer Membranes for Aqueous Solution Applications. *Macromolecules (Washington, DC, U. S.)* **2016**, *49* (8), 2905-2916.



# Summary

## Summary

Block copolymers (BCPs) are attractive materials because of their high tunability and self-assembling ability into regular morphologies in the range of 10-100 nm. They can be used for nanotechnological applications as surfactants, thin films for nanolithography, biomedicine and nanoporous membranes. In this thesis, we aimed to fabricate thermo-responsive iso- and nanoporous membranes that can be used to purify water from nano-sized impurities, also to gain a good understanding on the self-assembly properties of the BCPs.

In the introduction of the thesis, given in **Chapter 1**, we present our scope and aim of the research and introduce the literature about the synthesis and self-assembly of block copolymers. Next, we report the fundamentals of block copolymer membranes including the block copolymer thin films, the SNIPS (self-assembly and non-solvent induced phase separation) process and stimuli-responsive block copolymer membranes.

In **Chapter 2**, we synthesized well-defined polystyrene-poly(*N*-isopropylacrylamide) (PS-PNIPAM) BCPs using reversible-addition-fragmentation-transfer polymerization to produce the desired membranes. Poly(*N*-isopropylacrylamide) (PNIPAM) is thermo-responsive which exhibits a lower critical solution temperature (LCST) of around 32 °C. This means that at temperatures lower than the LCST, the block is hydrophilic and therefore swollen in aqueous environment and when the temperature is increased above the LCST the block becomes hydrophobic and collapses. When we have the membranes, the pore sizes of the membrane should increase at temperatures above the LCST of PNIPAM, due to collapsing of the PNIPAM chains. The second block of the copolymer, polystyrene (PS), acts as the matrix thereby preventing the block copolymer from dissolving in water and maintaining mechanical stability of the membrane.

We optimized the synthesis conditions to obtain BCPs with a high percentage of PS, a high yield and a low polydispersity index (PDI), which are required to produce thermo-responsive iso- and nanoporous membranes with a suitable mechanical stability. According to the literature, the best strategy to synthesize PS-PNIPAM block copolymers was suggested as first synthesizing the PS macro-RAFT agent and extending it with NIPAM monomer. However, following this route we found that when PS was chosen as the majority phase, the obtained yield of this block copolymer was rather low or even zero. Instead, when we synthesized the PNIPAM macro-RAFT agent first and extend it with styrene monomers, we

obtained PS-PNIPAM block copolymers with higher yields while maintaining the low PDI values. We used two different RAFT agents to attain block copolymers with various architectures such as AB, ABA and BAB types. We used an AB type block copolymer to produce membranes. The membranes were fabricated using a SNIPS process using a 20 wt% block copolymer solution in *N*-methyl-2-pyrrolidone (NMP) and tetrahydrofuran (THF) with a volume ratio of 4:6. We found that by increasing the evaporation time from 10 to 80 seconds the membrane surface became more interconnected with smaller pore sizes. Permeability measurements performed from 20 to 50°C showed that the membranes were thermo-responsive and this property was found to be fully reversible when several temperature cycles of 20 and 50°C were applied.

To get a deeper insight on the block copolymer self-assembly, we theoretically and experimentally investigated the behavior of block copolymers. Our theoretical work, presented in **Chapter 3**, employed the self-consistent field method of Scheutjens and Fler (SF-SCF) which consisted of two parts. As the SF-SCF technique was not yet used for the microphase segregation of block copolymers, we benchmarked the calculations. For this reason, we focused on the chain length dependence of the critical point in the block copolymer phase diagram. In the critical region, we report the scaling behavior of the free energy density and the density differences between the domains as a function of  $\Delta\chi = \chi - \chi^{cr}$  where  $\chi$  is the Flory-Huggins interaction parameter and  $\chi^{cr}$  is the Flory interaction parameter at the critical point. We found that the characteristic spacing ( $D$ ) of the lamellar phase is found to accurately follow  $D = \frac{4}{3}\sqrt{N}$  at the critical conditions. The chain length ( $N$ ) dependence as a for the critical strength of interactions was found to obey  $\chi^{cr}N = 10.495(1 + \frac{4}{N})$  which is consistent with results obtained by complementary approaches found in the literature. We also report on the spacing of the lamellar phase as a function of chain length for systems that are not near the critical point and obtained that the spacings obeyed  $D \propto N^{2/3}$  to a good approximation for fixed  $\chi$ ; whereas for fixed  $\chi N$ , the relation was found to be  $D \propto N^{1/2}$ .

The second issue we addressed was the stability of some common mesophases that occur in the transition region between lamellar and hexagonal phases in the block copolymer phase diagram, which is the preferred region to obtain isoporous membranes. These mesophases include the gyroid i.e. single gyroid (SG) and double gyroid (DG), hexagonally perforated

## Summary

lamellae (HPL) and double diamond (DD). These mesophases were investigated at the intermediate segregation regime i.e.  $\chi N = 30$  for  $N = 300$ . The structural evolution of the metastable HPL phase with increasing block ratio ( $f$ ) gave insights about how a phase can migrate to the next one. We also analyzed the stability of the DG at strong segregation regime i.e.  $\chi N = 120$  which is still a point of debate. The DG was found to be metastable for a fixed chain length of  $N = 300$ .

In **Chapter 4**, we present an experimental investigation on block copolymer self-assembly. We worked on the solvent annealing of polystyrene-*b*-poly(*N*-isopropylacrylamide)-*b*-polystyrene (PS-*b*-PNIPAM-*b*-PS) block copolymer thin films. In this approach, common solvents i.e. methanol, toluene and tetrahydrofuran with various ratios were used to tune the selectivity of the solvent mixtures to the blocks in the copolymer. We used atomic force microscopy (AFM) and *in-situ* grazing incidence small angle X-ray scattering (GISAXS) characterization methods to follow the morphological changes of the BCPs during solvent annealing. With AFM, the surface of the film was probed with a high resolution on the order of a nanometer, while with GISAXS the morphology of the bulk film was monitored. The combination of the two techniques proved that we obtained hexagonally ordered cylinders throughout the thickness of the film.

More specifically, we obtained a hexagonally ordered perpendicular cylinder morphology from a lamellar forming block copolymer using the solvent mixtures methanol: THF (v:v) 1:2 or methanol: toluene (v:v) 1:1. In contrast, no sustained long-range order was found when only one type of solvent was used. The annealing times to attain hexagonally ordered perpendicular cylinders were found to be longer when the amount of methanol was increased in the methanol-THF solvent mixture. These thermo-responsive block copolymer thin films are promising materials to produce nanoporous membranes. We also speculated that these materials can be used in cell adhesion and growth studies for biomedical applications and microelectromechanical systems. To the best of our knowledge, there was no systematic study achieved for solvent annealing for PS-*b*-PNIPAM-*b*-PS BCP thin films using selective solvent systems.

Finally, in **Chapter 5**, we report our work to improve the surface of PS-*b*-PNIPAM block copolymer membranes fabricated by using the SNIPS process. In this chapter, we aimed to

obtain isoporous membrane surfaces by optimizing the casting parameters. We focused on the influences of solvent, polymer concentration and evaporation time.

To prepare casting solutions we used solvent mixtures with different selectivities. When we used a highly PS selective toluene: THF (6:4) (v:v) solution, core-shell micelles were obtained where most likely PS was the core and PNIPAM was the corona. NMP: THF solutions were prepared with two different ratios, i.e. 8:2 and 4:6 (v:v). The 8:2 ratio resulted in similar core-shell micelles but smaller in size compared to the toluene-THF solution due to less PS selectivity of the NMP-THF solvent mixture. When the ratio of NMP was lowered from 8 to 4 (NMP: THF = 4:6), the solvent mixture was less PS selective which resulted in worm-like cylinders which fused together to form an interconnected surface. However, the pores formed on these films were not uniform.

When PNIPAM selective solvent mixtures of methanol: THF (5:5) and 1,4-dioxane(DOX): THF (7:3) were used well-defined pore formation was observed. For a methanol-THF solvent mixture, these well-defined pores were lost after a short time, most probably due to fast evaporation rates of both methanol and THF. In DOX-THF solvent mixtures, however, the stability of the well-defined pores was higher. A suitable solvent concentration gradient is thought to be formed using this solvent combination which leads to perpendicular cylinder formation and thereby isoporous surfaces. Since isoporous membranes could be obtained only with DOX-THF solvent mixtures, we further investigated the influence of evaporation time, solvent ratio and polymer concentration using this solvent mixture.

At short evaporation times and low polymer concentrations, there still is a high amount of solvent in the polymer film, and more solvent-non-solvent exchange will take place. These conditions resulted in rough irregular porous morphologies. At intermediate evaporation times and polymer concentrations, the formation of uniform pores was observed. For longer evaporation times or higher polymer concentrations worm-like features were obtained. These features are likely cylinders that are aligned parallel to the surface. Even longer evaporation times or even higher polymer concentrations led to dense films with almost no pores, since no solvent was left to exchange with the non-solvent. High amount of DOX or presence of water in the solution led to uniform pore formation at shorter evaporation times. We found that the presence of more PNIPAM selective solvents affects the self-

## Summary

assembly behavior in favor of uniform pore formation. Besides, larger pore sizes were obtained when 1 vol% water was added to the solution. We produced isoporous membranes with polymer concentrations between 20 and 25 wt%, evaporation times between 20 and 80 seconds, and by varying DOX and THF ratios from 7:3 to 3:7. This is a relatively large parameter space that was not achieved for a SNIPS process before. Similar to the membranes reported in Chapter 2, these isoporous membranes also exhibited thermo-responsive behavior and this behavior was found to be fully reversible. These materials are promising for industrial easy-to-clean membrane applications.

In **Chapter 6**, we present a general discussion of the research and conclude that PS-PNIPAM block copolymers can be successfully used to attain free-standing fully reversible thermo-responsive membranes with uniform and nano-sized pores. This makes them excellent candidates for easy-to-clean advanced membrane systems. In this chapter, we also discussed how to improve the properties of these membranes to be able to use them in industrial applications and suggested some future recommendations. We also report our recommendations to get a better understanding of the self-assembly mechanism in isoporous membrane formation.

# Özet

## Özet

Blok kopolimerler (BKP'ler) farklı kimyasal özelliklerdeki iki veya daha fazla polimerin birbirine kovalent bağ gibi bir kimyasal bağ ile bağlanmasından oluşan yapılardır. BKP'ler, bloklarının kimyasal farklılıklarından dolayı fazlara ayrılmak istemeleri ama yapılarındaki kovalent bağdan dolayı zeytinyağı-su örneğinde olduğu gibi makro ölçüde fazlara ayrışamazlar. Bunun yerine blok kopolimerin blok yüzdesine bağlı olarak, 10-100 nm boyutlarında farklı şekillerde düzenli yapılar oluştururlar, buna BKP'nin 'kendiliğinden bir araya gelme'si (self-assembly) olayı olarak isimlendirilir. BKP'lerin bu özelliği ve blokların uygulamaya göre istenen şekilde seçilebilmesi bu malzemeleri çekici kılmaktadır.

Tezin **1. Bölümü**'nde verilen Giriş kısmında; çalışmanın kapsamı ve amacı belirtilmiş, BKP'lerin sentezi ve yukarıda bahsedilen kendiliğinden bir araya gelme özelliği hakkında mevcut literatür sunulmuştur. Daha sonra BKP ince filmler ve bir membran üretim yöntemi olan 'kendiliğinden bir araya gelme ve çöktürücü tesirli faz ayrımı' (SNIPS) işlemi dahil olmak üzere, BKP membranlar hakkında temel bilgiler verilmiştir.

**2. Bölüm**'de, istenen özelliklerde BKP membranları elde etmek için, tersinir eklenme-parçalanma zincir transferi (RAFT) polimerizasyonu ile polistiren-poli(*N*-izopropil akrilamid) (PS-PNIPAM) BKP'lerin sentezi verilmiştir. Poli(*N*-izopropil akrilamid) (PNIPAM) sıcaklığa duyarlı bir polimer olup 32°C civarında düşük kritik çözelti sıcaklığına (LCST) sahiptir. Bunun anlamı, polimer bu sıcaklıktan daha düşük sıcaklıklarda suda çözünebilir hâldeyken; bu sıcaklıktan daha yüksek sıcaklıklarda su sevmeyen özellik göstererek suda çözünmez hâle gelir. Bu polimerden oluşmuş membranlarımızın olması durumunda, LCST sıcaklığının üzerinde PNIPAM zincirlerinin suda çözünmez hale gelerek çökmesinden ötürü membran gözeneklerinin genişlemesini bekleriz. BKP'nin ikinci bloğu olan polistiren (PS), anafaz olarak davranır ve BKP'nin suda çözünmesine mâni olmakla beraber membranın mekanik dayanımının artmasına yardımcı olur.

RAFT sentez koşullarını; yüksek yüzdeli PS, yüksek verim ve polimerin zincir uzunluklarının benzer olmasının ifadesi olan düşük polidispersite indisi (PDI) elde edecek şekilde ayarladık. Bu sayılan koşullar; sıcaklığa duyarlı, birbiri ile aynı ve nano boyutlarda gözeneklere ve yeterli mekanik dayanıma sahip membranlar elde etmek için gerekli koşullardır. Mevcut literatür, PS-PNIPAM BKP'ler elde etmek için önce PS makro-RAFT ajanı sentezini ve daha sonra *N*-izopropil akrilamid monomeriyle polimer zincirinin

uzatılmasını tavsiye etmektedir. Ancak biz yüksek yüzdeli PS içeren BKP'ler sentezlemek için bu yöntemi kullandığımızda, reaksiyon verimini çok düşük ve hatta bazı durumlarda sıfır olarak elde ettik. Bu sebeple, bu yöntem yerine sentezi PNIPAM makro-RAFT ajanından başlayıp stiren monomeriyle polimer zincirini uzatarak gerçekleştirdiğimizde, daha yüksek verim elde ettiğimiz ve PDI değerlerinin de düşük değerlerde kalmasını sağladığımız için bu yöntemi tavsiye etmekteyiz. AB, ABA ve BAB tipi BKP'ler elde edebilmek için iki farklı RAFT ajanı kullandık. Membran üretimi için AB tipi bir BKP kullandık. Membranlar yukarıda bahsedilen SNIPS işlemi ile ağırlıkça %20 polimer ve çözücü olarak hacimce 4:6 oranında *N*-metil-2-pirolidon (NMP) ve tetrahidrofuran (THF) içeren çözelti kullanarak hazırlanmıştır. SNIPS işleminde kullanılan buharlaşma süresinin 10 saniyeden 80 saniyeye çıkarılmasıyla membran yüzeyinin daha birbirine bağlı yapıda olduğu ve gözenek boyutlarının küçüldüğü gözlenmiştir. 20'den 50°C'ye kadar olan sıcaklıklarda yapılan geçirgenlik ölçümleriyle membranın sıcaklığa duyarlı yapıda olduğu ve membrana 20 - 50°C sıcaklık devirleri uygulandığı zaman sıcaklığa duyarlı yapının tam tersinir olduğu görülmüştür.

BKP'lerin kendiliğinden bir araya gelme özelliğini daha detaylı incelemek maksadıyla, teorik ve deneysel çalışmalar gerçekleştirdik. **3. Bölüm'**de sunulan teorik çalışmamız 'Scheutjens ve Fleer'in kendinden tutarlı alan kuramı' (SF-SCF) olarak isimlendirilen yöntemi içermekte olup iki kısma ayrılmaktadır. SF-SCF yöntemiyle daha önceden BKP'lerin kendiliğinden bir araya gelme olayı incelenmemiş olduğu için öncelikle hesaplamalarımızı doğruluğunu değerlendirmeyi amaçladık. Bunun için öncelikle polimerin zincir uzunluğunun (*N*) BKP faz diyagramında bulunan kritik noktaya etkisini inceledik. Kritik bölgede, serbest enerji yoğunluğu ile bölgeler arasında yoğunluk farkının Flory-Huggins etkileşim parametre farkının ( $\Delta\chi$ ) birer fonksiyonu olduğunu gösterdik. Flory-Huggins etkileşim parametre farkı  $\Delta\chi = \chi - \chi^{cr}$  olarak tanımlanmakta olup burada  $\chi$  ve  $\chi^{cr}$  sırayla belli bir noktadaki ve kritik noktadaki Flory-Huggins etkileşim parametrelerini ifade etmektedir.

Kritik koşullarda tabakalı (lamellar) fazın karakteristik aralık değerinin (*D*) zincir uzunluğuna fonksiyonunun  $D = \frac{4}{3}\sqrt{N}$  olduğunu bulduk. Kritik noktadaki etkileşim gücünün ( $\chi^{cr}N$ ) zincir uzunluğu ile olan ilişkisi  $\chi^{cr}N = 10.495 \cdot (1 + \frac{4}{N})$  bulunmuş olup, bu

## Özet

sonuç daha önceden yayınlanmış literatür sonuçlarıyla tutarlıdır. Ayrıca, sabit  $\chi$  değerlerinde kritik noktadan uzak olan bölgelerde tabakalı fazın aralık değerinin zincir uzunluğuna fonksiyonu  $D \propto N^{2/3}$ , aynı ilişki sabit  $\chi N$  değerleri için  $D \propto N^{1/2}$  olarak bulunmuştur.

Çalışmanın ikinci kısmında tabakalı ve altıgen fazların arasında bulunan geçiş bölgesinde görülen bazı yaygın arafazların kararlılıkları incelenmiştir. Bu bölge özellikle aynı boyutta gözenekli membranlar elde etmek için önem teşkil etmektedir. Bu arafazlar; tek gyroid (TG) ve çift gyroid (ÇG) olarak gyroid'ler, altıgen delikli tabakalar (ADT) and çift elmas (ÇE) olarak sayılabilir. Bu arafazlar  $\chi N = 30$  gibi orta düzey ayrışma bölgelerinde ve  $N = 300$ 'de incelenmiştir. Yarı kararlı olan ADT fazının artan blok oranı ( $f$ ) ile yapısal gelişimi bir fazın diğerine nasıl geçiş yapabildiği hakkında fikirler vermektedir. Ayrıca hala görüş birliğine varılamamış olan  $\chi N = 120$  gibi yüksek bir ayrışma bölgesinde ÇG fazının kararlılığını araştırdık.  $N = 300$  sabit zincir uzunluğu için ÇG fazının yarı kararlı bir faz olduğu bulduk.

**4. Bölüm'**de BKP'lerin kendiğinden bir araya gelme özelliğini deneysel olarak inceledik. Burada ABA tipi polistiren-*b*-poli(*N*-izopropil akrilamid)-*b*-polistiren (PS-*b*-PNIPAM-*b*-PS) BKP ince filmlerin çözücü ile tavlama işlemi çalışılmış olup çözücü olarak metanol, toluen ve tetrahidrofuran gibi genel laboratuvar çözücüleri kullanılmıştır. Çözücülerin kopolimerdeki bloklara seçicilikleri, çözücü miktarları ve birbirlerine olan oranları değiştirilerek ayarlanmıştır. Tavlama sonucunda BKP'de oluşan yapısal değişikliklerin takibi için atomik kuvvet mikroskobu (AFM) ve anlık geliş açılı X-ışını saçılması (GISAXS) yöntemlerini kullandık. AFM ile nanometre boyutundaki yüksek çözünürlükle filmin yüzeyi araştırılırken, GISAXS ile filmin tüm kalınlığındaki anlık yapısı izlenebilmektedir. Bu iki yöntemin kullanılmasıyla filmin tüm kalınlığında altıgen olarak sıralanmış silindirler elde ettiğimiz kanıtlanmıştır.

Daha detaylı belirtmek gerekirse, seçici olmayan çözücüde denge halinde tabakalı yapı oluşturabilen bir BKP'den metanol: THF 1:2 (hacimce) veya metanol: toluen 1:1 (hacimce) seçici çözücü karışımları kullanılarak tavlama işlemiyle altıgen olarak sıralanmış silindir yapı elde edilmiştir. Buna karşın tek tip çözücü kullanıldığında sürdürülebilir düzenli bir yapı elde edilememiştir. Metanol-THF karışımındaki metanol miktarı arttırıldığında altıgen olarak sıralanmış silindir yapı elde etmek için gerekli süre artmıştır. Bu sıcaklığa duyarlı

BKP ince filmler nanoboyutta gözenekli membran üretmek için gelecek vaad eden malzemelerdir. Ayrıca bu malzemelerin hücre yapışma-büyüme çalışmaları gibi biyomedikal uygulamalarda ve mikro-elektro-mekanik sistemlerde de kullanılabileceğini düşünmekteyiz. Bildiğimiz kadarıyla, PS-*b*-PNIPAM-*b*-PS BKP'lerin seçici çözücüler kullanılarak sistematik olarak çözücü tavlama işleminin incelenmesi daha önceden gerçekleştirilmemiştir.

Son olarak, **5. Bölüm**'de SNIPS yöntemiyle üretilen PS-*b*-PNIPAM BKP membranların yüzeyini iyileştirmek için yaptığımız çalışmayı sunmaktayız. Bu bölümde, film döküm değişkenlerini en uygun şekilde seçerek aynı boyutlarda gözenekler içeren membran yüzeyleri elde etmeyi amaçladık. Bu değişkenlerden özellikle çözücü, polimer konsantrasyonu ve buharlaşma süresinin etkileri üzerinde durduk.

Film oluşturmak için hazırlanan döküm çözeltisinde farklı seçiciliklere sahip çözücü karışımları kullandık. Yüksek PS seçiciliğine sahip toluen: THF (6:4) (hacimce) karışımı kullanıldığında yüksek ihtimalla çekirdeği PNIPAM'dan ve çeperi PS'den oluşan çekirdek-çeper (core-shell) miseller elde edildi. Ayrıca çözücü karışımı olarak 8:2 ve 4:6 olmak üzere iki farklı oranda NMP-THF karışımı da kullanıldı. NMP:THF 8:2 oranında toluen-THF karışımında elde edilene benzer çekirdek-çeper yapılar oluşurken, bu yapılar NMP-THF çözücü karışımının daha düşük PS seçiciliğinden ötürü daha küçük boyutlarda kalmıştır. NMP'nin karışımdaki oranı 8'den 4'e düşürüldüğünde (NMP: THF = 4:6), çözücü karışımının daha az PS seçici olması birbirleri ile bütünleşen solucan benzeri silindirlerin oluşumuna bu da sonuç olarak birbiri ile daha bağlantılı bir yüzey elde edilmesine sebep olmuştur. Buna rağmen elde edilen bu filmin üzerinde oluşan gözenekler aynı boyutlarda değildir.

PNIPAM seçici olan metanol: THF (5:5) ve 1,4-dioksan (DOX): THF (7:3) çözücü karışımları kullanıldığı zaman sınırları daha iyi tanımlı gözeneklerin oluşumu gözlemlenmiştir. Metanol-THF çözücü karışımı için bu iyi tanımlı gözenekler, büyük olasılıkla hem metanolün hem THF'nin hızlı buharlaşma hızından ötürü kısa sürede kaybolmuştur. Buna rağmen DOX-THF çözücü karışımının kullanılmasıyla iyi tanımlı gözeneklerin daha yüksek kararlılıkta olduğu görülmüştür. Bu çözücü birleşiminde ortaya çıkan uygun 'çözücü konsantrasyon meyili'nin kopolimerin yapısında oluşan silindirlerin yüzeye dik

## Özet

açıda yönlemesine, bunun da aynı boyutlarda gözenekli yüzey oluşumuna sebep olduğu düşünülmektedir. Aynı boyutlarda gözenekli membranlar kararlı olarak sadece DOX-THF karışımında elde edildiği için; buharlaşma süresi, çözücü oranı ve polimer konsantrasyonu gibi değişkenlerin etkisinin incelenmesi bu çözücü karışımında gerçekleştirilmiştir.

Kısa buharlaşma süresi ve düşük polimer konsantrasyonlarında, polimer filmde halen yüksek miktarda çözücü olmasından dolayı çöktürücü banyosunda daha fazla çözücü-çöktürücü değişimi gerçekleşmiştir. Bu koşullar kaba ve düzensiz gözenekli yapıların oluşumuna sebep olmuştur. Orta düzeyde buharlaşma süresi ve polimer konsantrasyonlarında aynı boyutlu gözeneklerin oluşumu gözlenmiştir. Daha uzun buharlaşma süreleri ve yüksek polimer konsantrasyonlarında silindirik benzeri oluşumlar elde edilmiştir. Bu oluşumlar yüzeye paralel olarak sıralanmış silindirikler gibi gözükmektedir. Buharlaşma sürelerinin daha da uzatılması veya polimer konsantrasyonun daha fazla artırılması, çöktürücü banyosunda gerçekleşen çözücü-çöktürücü değişimi için gereken çözücünün filmde çok az miktarda olmasından dolayı neredeyse hiç gözenek içermeyen geçirimsiz yapılar oluşmuştur. Çözeltide yüksek miktarda DOX veya suyun varlığında daha kısa buharlaşma sürelerinde aynı boyutlu gözenekler elde edilmiştir. Çözeltide daha fazla PNIPAM seçici çözücü kullanımının, BKP'nin kendiliğinden bir araya gelme davranışını aynı boyutlu gözenek oluşumu lehine etkilediğini tespit ettik. Ayrıca, çözücü karışımına hacimce %1 su eklendiğinde gözenek boyutlarının büyüdüğü gözlemlenmiştir. %20 ile 25 polimer konsantrasyonları, 20 ile 80 saniye buharlaşma süreleri ve 7:3'ten 3:7'ye değişen DOX: THF oranları kullanılarak aynı boyutlu gözenekli membranlar üretmeyi başardık. Bu aralıklar oldukça geniş olup daha önceden hiçbir SNIPS işlemi için bu kadar geniş değişken aralıkları elde edilmemiştir. 2. Bölüm'de verilen membranlar gibi bu aynı boyutlu gözenekli membranlar da sıcaklığa duyarlı özellikte olup bu özellik yine tam tersinirdir. Bu malzemeler kolay temizlenebilir membran uygulamalarında gelecek vaad etmektedir.

**6. Bölüm'de,** yapılan çalışmaların genel bir tartışması sunulmakta olup sonuç olarak PS-PNIPAM BKP'lerin kendiliğinden destekli, birbirine aynı ve nano boyutta gözeneklere sahip, tam tersinir olarak sıcaklığa duyarlı membranlar elde etmek için kullanılabildiği belirtildi. Bu özellikler, bu BKP'leri kolay temizlenebilir ileri düzeyde membranlar elde

etmek için mükemmel adaylar hâline getirmektedir. Bu bölümde ayrıca elde edilen membranların sanayide kullanımına uygunluğunu arttırmak için özelliklerinin daha fazla nasıl iyileştirilebileceğini tartıştık ve bazı ileriye yönelik önerilerde bulunduk. Ayrıca kendiliğinden bir araya gelme mekanizmasının aynı boyutlu gözenek oluşumundaki etkisinin daha iyi anlaşılması için bazı öneriler sunduk.



## About the author

Merve Mocan Çetintaş was born on 30<sup>th</sup> of August, 1984 in Istanbul, Turkey. Her interest in science started in primary school times when she wanted to become an astronaut. After ten years, she thought it is also fine to be a chemical engineer for a start and she graduated from Chemical Engineering Department in Istanbul University with a first-class honors degree in 2006. A few months after the graduation, she started working in a polymer company, Polychem, as a quality control engineer, however she realized that she more curious about what was really happening inside of the polyurethane and polyester reactors. Therefore, after an almost two year of work experience, she started her masters in Polymer Science and Technology Department in Istanbul Technical University. Her research subject was polymer-organoclay nanocomposites where she synthesized polymers and prepared organoclays. During that time and with the nice polymer courses she took, she discovered that she loves polymer synthesis. During MSc, she was accepted as a research assistant in Department of Chemistry at the same university. After this, besides research, she was also responsible in teaching chemistry to the bachelor students. She gained strong relations and instructive experiences with the students, research assistants, technical staff and professors in the department and of course during working in the lab. Later on, she decided to push her limits a bit more by doing a PhD in a university outside of her own country to see what was going on out of her comfort zone. Thereafter she was accepted to Wageningen University, Physical Chemistry and Soft Matter Lab to produce water filtration membranes from home-made block copolymers and started working on March 2013 under the supervision of Marleen Kamperman and Frans Leermakers. Here also she met many nice people and gain a lot of experience about polymers, research and living abroad in the beautiful city called Wageningen. The book you are holding is the product of this four-year PhD work. Time will show the next adventure.



# List of Publications

- Cetintas, M. and Kamperman, M. Self-assembly of PS-*b*-PNIPAM-*b*-PS block copolymer thin films via selective solvent annealing. *Polymer* **2016**, 107, 387-397.
- Cetintas, M.; de Groot, J.; Hofman, A. H.; van der Kooij, H. M.; Loos, K.; de Vos, W. M. and Kamperman, M., Free-standing thermo-responsive nanoporous membranes from high molecular weight PS-PNIPAM block copolymers synthesized *via* RAFT polymerization, *Polymer Chemistry* **2017**, 8 (14), 2235-2243.
- Cetintas, M.; Wahdat, H.; van der Kooij, H. M. and Kamperman, M., Systematic variation of membrane casting parameters to control the structure of thermo-responsive isoporous membranes, *in preparation*.
- Cetintas, M.; Kamperman, M. and Leermakers F. A. M., Microphase segregation of diblock copolymers studied by the self-consistent field theory of Scheutjens and Fleer, *in preparation*.



# Acknowledgements

When I first stepped out of the bus 88 with Cenap with our big luggages, I knew I would like the place that I will live during my PhD. I started to live in a room in Marijkeweg, then moved to a nice apartment in Rijnveste. I believed I adapted to my new home and work place rather quick because of the beautiful nature, trees, peace and quietness of Wageningen and friendly attitude of the people both in the lab and in the city. First Mirmur then Cenap joined to our new home. As a single child, I enjoyed working in the lab 1010 in my very own messy fumehood, at the same time I liked sharing ideas with my lab mates. I gained experience more than I could if I stayed in my hometown and I am thankful to the ones who caused it. Without noticing how the years have passed, now it's time to graduate. This part is for those who contributed to my life experience in these fruitful four years.

First of all, I am grateful to Marleen and Frans for choosing me as the PhD student for their project. At the end, I hope you were happy that you offered the job to me. *Marleen*, thank you for coming all the way to Ithaca with me for my measurements and you never wanted to go back to hotel yourself and never left me to do my own experiments even it was late at night (did we see 4 am?), thank you for spending the weekend with my experiments when you could spend it with your family. Thank you for waiting in front of your computer at 3 am for me to finish the paper submission (did we work more with you at night?). You always tried your best to respond all my many emails, carefully reviewed my many documents at the same time. Thank you for believing in me, even when I stopped doing it and perfectly balancing your support when I was stuck and leaving enough space to help me to become an independent researcher. I appreciated your calmness in any difficulty that came across, even when you missed your plane. It was a pleasure to work with both a kind and inspiring person like you.

*Frans*, I am very happy that you were my promotor. I would like to thank all the help and support in my studies and during writing my thesis. Maybe no one would believe this, but I enjoyed our deep conversions very much about our research which took many hours in your office when we tried to identify the phases by looking all kinds of literature including crystallography, minerology, surfactant etc. fields even when it was 9 pm in the evening. I remember once you screamed late in the evening when we were again trying to solve a puzzling question and it was funny when people taught there was a fire or something. Beyond research, I liked to find out your hidden kindness towards every PhD student in the lab. Plus, I admired your energy also when you were cycling uphill!

*Wiebe de Vos*, from University of Twente, thanks for letting us to use Amicon cell for permeability measurements and for your contribution to my membrane articles. *Joris de Grooth*, we appreciate the permeability measurements you did and taught us. *Detlef-M. Smilgies* from Cornell University, thanks for your support for helping us to use D-line GISAXS, coming to help us at the weekend and special thanks for the delicious bagel you ordered for me. *Roy L'Abée* from Sabic, I appreciated your kind help on the clearance procedures and never giving up your motivating comments in every clearance you made in four years. I'd like to thank to *Anton Hofman*, current postdoc in our lab, and his former supervisor *Katja Loos*, for the help measuring GPC-LS of my several polymers and contributions in my papers.

*Josie*, thank you for all hugs and positiveness, plus inviting me and Cenap to your house for tea and nice chat. First Mara and we miss your presence in the lab. *Mara*, the lab can survive for some time

without us but without you, even for a short time, it's impossible! Thank you for all your effort to order the chemicals as quick as possible, plus, thanks for your understanding when I changed my plane ticket several times to find the cheapest option. But that was worth at the end, wasn't it? *Anita*, thank you for all your help for financial matters of the project. *Bert*, thank you for very quickly arranging my payments and preparing my thesis copies. *Remco*, thanks for instructing me to use several instruments such as ellipsometer, DLS. *Hannie*, thank you for your AFM instructions and always worrying about me during my research. *Rene*, thank you for your help to modify my schedule when I realized that I needed to take a course during my teaching period. Btw, you never believed that I was in the lab on time and actually doing fine, did you? *Anton*, thank you for your instructions on several instruments and for your support during my submission process. *Mieke*, thank you for showing mechanical AFM analysis and discussions during the group meetings. *Joris, Jasper, Renko* and *Joshua* thanks for sharing your supportive ideas in group meetings. *Hans*, it was always exciting for me to see you in the lab and I will remember you with your kind attitude every time we meet. *Diane*, you were my first office mate and the flower of the lab 1010. Thank you for worrying about me during my PhD and patiently keep telling me to wear lab goggles, now I really do! I appreciate the help the people of Organic Chemistry Department; *Elbert* and *Frank* for GPC and MS, *Pijpen* and *Barend* for FTIR and NMR instructions and *Tom Wennekes* for the discussions about my experimental setup.

*Hares*, I am glad you were the MSc student I worked with. You were very hardworking even coming at the weekends when we were running out of time and you never complained for working more. I think both of us learned a lot from each other. I believe nothing is on your way to success and happiness if you keep your motivation high and when you understand the meaning of your surname by heart. *Juan*, I didn't only like working in the same lab with you, but also I liked shopping, eating sushi, buying all kinds of Asian food without knowing how we will carry all the stuff till the bus stop, bugging me in the office only when you were available and of course Tingting wasn't around. I still appreciate your technical and motivational support from abroad. Wish you and Ran happiness and success with your dear Ivan! *Inge*, my dear neighbor, thank you for taking care of Mirmir when we were away, thanks for the delicious makronen and cookies, for going to shopping, to the sandsculpture museum together and tips you gave to me to earn more gold in Hugo game during our AFM analyses and still for your support about thesis submission and printing process. I already missed your presence in the apartment building. *Thao*, my dear office mate, I met you first time when you were almost finishing your PhD, now I know why you were acting like crazy those times, later on I think I did the same too! Thanks to you for all tips to survive PhD and still for your supports even from Singapore. *Tingting*, I always liked your cheerful attitude lighting up our office, your elegant gifts and discussions about being a single child. You are a perfect couple with Huanhuan and you are perfect parents for your sweet Leo, Dudu and Wei. *Huanhuan*, it was so sweet when you were bringing lunch to Tingting's desk every single day and I appreciated when you kindly worried about me and my family when there were conflicts in my country. *Yunus*, you were the first person I met in Wageningen when I came for my first interview. Hearing a similar arrival history to the Netherlands like mine, I was happy for the motivation you gave me that time. Even though we were working at different floors or research areas it was nice when you were still around. *Hande*, thank you for helping me to bring and carry the huge exercise bike to our home with your car, patiently answering all the visa and thesis related questions or just chatting and delicious dinners you prepared for us and good moments in a Turkish restaurant or in 'çiğköftelim'

when Pamuk was small enough to be carried like a baby. Special thanks for the thesis template. I wish you and Eric a beautiful and successful life with your snowball. *Kamuran*, I was happy that you were in our lab in my first years. Thank you for all your help when I was moving to my new apartment by picking up all the laminates with your car, even carrying them to upstairs. It was fun to learn about CO<sub>2</sub> cycle in the earth and life in the Netherlands and in Aydın. *Gosia*, I like your kindness to people even in difficult situations. Mirmur said he liked you very much and would like to purr you again. Wish you a happy life together with Kamuran! *Hanne*, thanks for your support for SEM characterization of my membrane samples and your answers to my all kinds of weird Kaledigraph questions and I really appreciated your quick working style and your contributions on my papers. Apart from those, thank you for your never-changing nice attitude, I believe which is something much harder than doing a PhD. *Jan Bart*, it was fun to work with you in the same lab in our first years but I always appreciated when you lowered down the volume of the radio. *Sabine*, I liked your fun and sociable character and thanks for all the activities you organized for all of us. *Kris*, thanks to your endless questions about almost everything. I hope I could help you a bit to satisfy your curiosity. I like your music very much. *Antsje*, thank you for the chats during teaching. I should remind you that you still didn't bring one of your tasty cakes which you keep on posting in facebook! *Gosia with horse*, I admired your high motivation for doing the things you find necessary. *Jan Maarten*, I appreciated your long try to save my accidently deleted data from my USB stick. *Rui*, thanks for your positive energy that you always brought to the lab and for your beautiful night sky photos.

It was fun to go to UK with you guys, I'd like to thank to the organizing committee: *Hanne*, *Gosia*, *Wolf*, *Natalia* and *Maarten* for such a nice organization. I enjoyed when we wandered in London together and afterwards Indian food that I had together with Inge, Wolf, Jan Bart and Jan Maarten. I was wondering why Jan Bart and Wolf were crying and eating at the same time while I was enjoying my non-spicy Indian food with yoghurt sauce.

Also thanks to the people I met in my last periods of my PhD. *Ilse*, thank you for sharing the office with me and your understanding for all my last year forgetfulnesses. I enjoyed your concerts a lot. I appreciated your help to introduce Dutch culture to me including every single detail that I asked to you. *Aljasha*, you made me get used to eat no-milk chocolate, I learned from you that vegan dish can indeed be very delicious and when I try to say something emotional I won't forget you saying: "C'mon, get over it!". *Marco*, it was nice to share our office for a while, I enjoyed our discussions about polymers and chat about Italian food and football, thanks for the tips to make a good pizza dough. *Pieter*, I liked your kindness to everyone around you. Thanks *Joanne* for the 'gezellig' chats we made. *Marcel*, I wish you and Ana a happy life with Emma and a lot of success. *Lione*, thank you for inviting us to your nice house for barbeque. *Ruben*, thanks for all your fun games. *Ties*, I will remember you with your "helluuu" greeting. *Camilla* and *Julia*, I liked your joyful attitude, you are almost like sisters. *Vittorio*, thanks for the link to low pixel games. *Niek*, thanks for giving the coloring book to me in Sinterklaas, I still need to color it. *Justin*, thanks for the SCF calculations you did in your MSc which is included in my modelling chapter. *Qimeng*, *Ram*, *Junior* and *Raisa*, I very much would like to have more time to share with you. Many thanks to *Jeroen*, *Johan*, *Maria*, *Helene*, *Soumi*, *Surender*, *Prachi*, *Duc*, *Armando*, *Harke*, *Junyou*, *Nadia*, *Celine* for making our lab more beautiful and enjoyable. I wish our new PhD candidates, postdocs and staff members a lot of luck and success.

I would like to express my gratitude to my former supervisors and professors in Turkey Gülten Gürdağ, Nurseli Uyanık, Candan Erbil and Nermin Orakdöğen who always supported me and believed in me.

Sevgili Anneciğim ve Babacığım; ömrüm boyunca bana göstermiş olduğunuz sonsuz sabır, anlayış ve sevginin karşılığını ödemem mümkün değil. Türkiye’den gönderdiğiniz yiyecekler, buraya geldiğinizde de Hollanda’yı gezmek yerine evi düzene sokmayı tercih etmenizden ve ne zaman nerede olursak olalım sadece ve sadece birlikte olmanın zevkini yaşatmanızdan dolayı size teşekkür ederim. Hep birlikte nice sağlıklı, huzurlu ve mutlu yıllar diliyorum.

Özer babacığım ve Safiye anneciğim; bana göstermiş olduğunuz bitmeyen sevgi ve anlayışınız, bize duraksız ettiğiniz dualarınız için; sevgiyle ve emekle hazırladığınız harika yemekleriniz için size ne kadar teşekkür etsem az. İyi ki Cenap gibi bir vefalı, merhametli ve sevgi dolu bir evlat yetiştirmişsiniz. Özer babacığım, siz ne yaparsam yapayım, her zaman benim en büyük destekçim oldunuz. Sınav sırasında da ve hayatım boyunca da kalbimde benimle birlikte olacağınıza inanıyorum.

Sevgili anneannem, dedem, Sevin halam, Gülten, Sunay ve Ayşegül teyzelerim, Hasan eniştem, Salih dayım, Nevin yengem, Gamze, Gökhan, Umut, Sema, Zeynep İlke, Aykut, Burcu, Melih, Yeşim abla, Bilun, İlsu, Derin, Ceylan abla, Lara, Hakan abi varlığınıza ve sağlığınıza duacıyım. Sizleri özleyorum ve çok seviyorum.

Zor zamanlarımda bana aile gibi olan Ramazan dedeme, gönülleri ferahlatıcı sohbetleri ve kitaplarıyla Cemalnur Sargut ve Taşkın Tuna hocalarıma saygılarımı ve hürmetlerimi sunarım.

Last but not the least, it is not easy to express my gratitude to best friend and my dear husband Cenap with a few words. Although you joined me to our new home later, my life became more beautiful after your arrival. Thank you for your endless support to me to continue in science even from the beginning. Thank you for your patience and understanding even in my crazy times and always giving constructive advices. Thank you for joining me to the weekend lab experiments and having breakfasts in the office, 24/7 IT support and of course for all your delicious food. I enjoyed creating many nice travel memories with you at many places in the Netherlands, Belgium, Germany, Italy and France. Thank you for always just being there for me at any condition.

Finally, during my PhD, I wouldn't forget when my country has gone through difficult times such as Gezipark, coup attempt and terror attacks but I could not be there. Those times were difficult to concentrate and continue working. I was heartbroken when I couldn't go to my own country for a polymer congress, I'd like to thank to the friends who showed their support to me in those times. Thankfully, me and my country managed to go on and hopefully we will keep on going on the straight path.

Merve Mocan Çetintaş, Wageningen, 2017

# Overview of completed training activities

## Conferences and Meetings

Controlled/Living Polymerization Symposium*	Antalya, TR	2014
Aachener Membran Kolloquium	Aachen, GER	2014
Dutch Polymer Days*	Lunteren, NL	2015
Euromembrane Conference*	Aachen, GER	2015
Frontiers in Polymer Science*	Riva del Garda, IT	2015
CHAINS: the Dutch Chemistry Conference*§	Veldhoven, NL	2015
Dutch Polymer Days*§	Lunteren, NL	2016
EUPOC: Block Copolymers for Nanotechnology Applications§	Gargnano, IT	2016
Dutch Polymer Days*	Lunteren, NL	2017
APME 2017: Advanced Polymers via Macromolecular Engineering*	Ghent, BE	2017

## Discipline Specific Courses

Colloid Science Course	Wageningen, NL	2013
RPK-C: Polymer Properties	Utrecht, NL	2013
RPK-B: Polymer Physics	Utrecht, NL	2014
Membrane Course for Water Technologies	Aachen, GER	2015

## General Courses

Competence Assessment	Wageningen, NL	2013
VLAG PhD Week <sup>§</sup>	Baarlo, NL	2013
Voice Matters <sup>§</sup>	Wageningen, NL	2014
Project and Time Management	Wageningen, NL	2014
High-Impact Writing in Science	Wageningen, NL	2015
Scientific Writing	Wageningen, NL	2016
Scientific Artwork with Photoshop and Illustrator	Wageningen, NL	2016

## Optionals

Group meetings and Colloquia <sup>§</sup>	Wageningen, NL	2013-2017
Social Dutch for Employees	Wageningen, NL	2013
Journal Club	Wageningen, NL	2014-2017
VLAG Dutch Course	Wageningen, NL	2014-2015
PhD Trip <sup>*§</sup>	London, UK	2015
PhD Workshop Carousel	Wageningen, NL	2015
PhD Workshop Carousel	Wageningen, NL	2016

\*poster presentation, <sup>§</sup>oral presentation.

This research forms part of the research program of the Dutch Polymer Institute (DPI),  
P.O. Box 902, 5600 AX Eindhoven, the Netherlands, project #766n

Cover design: Merve Mocan Çetintaş

Printed by GVO drukkers & vormgevers B.V., Ede, the Netherlands